UNIVERSITÀ DI PARMA

UNIVERSITA' DEGLI STUDI DI PARMA

DOTTORATO DI RICERCA IN
SCIENZA E TECNOLOGIA DEI MATERIALI

CICLO XXXVII

Reprocessable self-diagnostic covalent adaptable networks and liquid crystal elastomers

Coordinatore:
Prof. Enrico Dalcanale

Tutore:
Prof. Roberta Pinalli

Dottorando: Alessandro Torri

2021/2022-2023/2024

Contents

Nomenclature

CAN	covalent adaptable network
DGEBA	bisphenol A diglycidyl ether
CB[8]	cucurbit[8]uril
PDMS	polydimethylsiloxane
CNS	carbon nanostructures
CVL	crystal violet lactone
CVL^+	opened crystal violet
MWCNT	multi-walled carbon nanotube
SWCNT	single-walled carbon nanotube
GO	graphene-oxide
PMMA	poly(methyl methacrylate)
SEM	scanning electron microscope
TEM	transmission electron microscope
$CDCl_3$	chloroform-d
DLS	dynamic light scattering
Tween-80	Polyethylene glycol sorbitan monooleate
THF	tetrahydrofuran
Et_3N	triethylamine
TLC	thin layer chromatography
DCM	dichloromethane
NMR	nuclear magnetic resonance
AIBN	α, α'-Azoisobutyronitrile
ESI-MS	electrospray ionization mass spectrometry
PE	polyethylene
PE-HEMA	poly (ethylene-*co*-(2-hydroxyethyl methacrylate))
TGA	thermogravimetric analysis
DMTA	dynamic mechanical thermal analysis
DSC	differential scanning calorimetry
ACN	acetonitrile
K_2CO_3	potassium carbonate
KI	potassium iodide
EtOAc	ethyl acetate
Hex	hexane
EtOH	ethanol
DBTL	dibutyltin dilaurate
TMSPEDA	N,N'-Bis(3-(trimethoxysilyl)propyl)ethylenediamine
X_{cr}	degree of crystallinity
T_m	melting temperature
E'	Storage Modulus (tension)

G'	Storage Modulus (shear)
G''	Loss Modulus (shear)
E	Young Modulus
UTS	Ultimate Tensile Strength
POM	polarized light optical microscope
DMSO-d_6	dimethyl sulfoxide-d_6
BPO	benzoyl peroxide
MeOD-d_4	methanol-d_4
DMF	dimethyl formamide
HMDI	hexamethylene diisocyanate
TEG	tetraethylene glycol
PEG	polyethylene glycol
MEK	methyl ethyl ketone
PFAS	per and poly-fluoroalkyl substances
ITO	indium tin oxide
HCl	hydrochloric acid
$SOCl_2$	thionyl chloride
DMF	dimethylformamide
NaN_3	sodium azide
PPh_3	triphenyl phosphine
NaOH	sodium hydroxide
CsF	cesium fluoride
EDOT	(2,3-dihydrothieno[3,4-b][1,4]dioxin-2-yl)methanol
TBAHFP	tetrabutylammonium hexafluorophosphate
CV	cyclic voltammetry
GC	glassy carbon electrode
N-MePy	N-methyl pyrrole
PFOA	sodium perfluorooctanoate
$FeCl_3$	iron(III) chloride
$MgSO_4$	magnesium sulphate
GC-MS	gas-chromatography and mass spectrometry

Summary

Polymeric materials can be categorized into two main classes: thermoplastics and thermosetting polymers, each possessing distinct advantages and limitations. Thermoplastics, characterized by non-crosslinked polymer chains, derive their mechanical properties from chain entanglement. While they exhibit good mechanical properties, often inferior to those of thermosetting polymers, their non-crosslinked nature enables melting and reprocessing. In contrast, thermosetting polymers possess a covalent crosslinked network, conferring superior mechanical properties but compromising their reprocessability. Once cured, thermosetting materials cannot be melted or reshaped. Consequently, the end-of-life disposal options for thermosetting materials are limited to landfill disposal, incineration for energy recovery, or grinding into fine particles for use as fillers in new materials. In the modern era, characterized by a circular economy perspective which takes into account the entire product lifecycle, these options are clearly unsustainable.

In recent years, covalent adaptable networks (CANs) have emerged as an intriguing solution to the limitations of traditional thermosetting polymers. These materials behave like thermosets at their working temperature but can undergo dynamic crosslink exchange reactions at elevated temperatures, enabling reprocessing. However, CANs are susceptible to the formation of microfractures due to minor mechanical stresses, which can compromise their long-term mechanical properties leading to catastrophic failures. Therefore, developing materials provided by self-diagnostic properties able to detect micro-damages at their early stage represents a precious tool.

This thesis aims to develop innovative smart materials that incorporate probes to achieve self-diagnostic properties within dynamic covalent matrices. This approach enables the autonomous detection of microfractures caused by minor mechanical stresses, while the matrix made of a covalent adaptable network allows the material reprocessing extending the material lifespan.
The work begins with the study of the main matrices characterized by a dynamic crosslinking network and the primary methods used for self-diagnostics. This allows for careful selection of the best combination between dynamic polymer matrix and the method for identifying mechanical stress.

Chapter 2 presents the development of a self-diagnostic and reprocessable system characterized by core-shell nanocapsules containing crystal violet lactone (CVL) as fluorescent probe. CVL emission can be turned on through interaction with a hydrogen donor group and subsequently switched off via thermal treatment. The work involved the synthesis of core-shell polymethyl methacrylate (PMMA) nanocapsules encapsulating CVL, followed by their characterization using dynamic light scattering (DLS), scanning electron microscopy (SEM), and transmission electron microscopy (TEM). The ability of these

nanocapsules to release the fluorophore upon rupture was subsequently demonstrated. The released CVL interacts with carboxylic acid groups on graphene oxide (GO) nanostructures, triggering the transition from the non-emissive CVL to the emissive form of CVL^+. To assess the self-diagnostic capabilities of this system within a solid matrix, the nanocapsule-GO system was initially incorporated as additives into an epoxy resin model system. Upon successful demonstration of damage detection, the additives were introduced into a matrix characterized by a dynamic covalent crosslinking network based on disulfide bonds. This integration enabled the material to both identify microfractures and undergo reprocessing and reuse. Nanocapsules and GO were dispersed in the polymer matrix, then the application of a mechanical stress caused capsule rupture releasing CVL. The interaction of CVL with graphene-oxide triggered the switch on of the fluorophore emission thus detecting the mechanical damage. Subsequent heating deactivated the fluorophore and initiated the healing process which resulted to be only partial. The material could then be subjected to further mechanical stress, triggering another round of damage detection.

The developed system, however, presents a limitation: each capsule can only provide a single damage detection. Upon rupture and fluorophore release, the capsule becomes non-functional. Chapter 3 introduces a system that addresses this limitation by utilizing mechanophores as damage detection probes. Mechanophores are molecules that undergo a reversible transition between a non-emissive and an emissive form through the breaking and reforming of a labile bond. When incorporated as crosslinkers within a polymeric matrix, mechanophores respond to mechanical stress applied to the material, leading to bond breakage and subsequent emission switch on. Thermal treatment can reverse this process, restoring the non-emissive form and enabling repeated cycles of damage detection and repair. The chapter demonstrates how, by appropriately functionalizing a derivative of rhodamine 6G with silyl ether groups, it is possible to obtain a mechanophore that can be used as a crosslinker to create a material that is both self-diagnostic and characterized by a dynamic covalent crosslinking network, making it reprocessable. Upon mechanical solicitation, the labile lactam ring of the rhodamine breaks, triggering fluorescence emission. Subsequent thermal treatment quenches the fluorescence and repairs the material. This cycle of damage detection, repair, and reuse can be repeated multiple times without compromising the material's self-diagnostic or mechanical properties.

Another approach to achieve high mechanical properties while maintaining reprocessability involves the use of supramolecular crosslinking through hydrogen bonds. At operating temperatures, these hydrogen bonds provide sufficient crosslinking to enhance the material's mechanical properties. However, upon heating, the H-bonds break, enabling the material to be reprocessed like a thermoplastic. Cooling the material facilitates the reformation of hydrogen bonds, restoring the crosslinked state.

Chapter 4 explores the synthesis of photoactivated liquid crystal elastomers suitable for electrospinning, incorporating a reversible supramolecular crosslinking *via* hydrogen bonding. Initial efforts focused on side-chain liquid crystalline materials, where the mesogen, photoactuator, and hydrogen bond crosslinker were attached as side groups to the polymer backbone. However, these approaches did not yield materials with the desired properties. Subsequently, the focus shifted to polyurethane-based materials with a main-chain geometry. In this design, the mesogen and the photoactuator are incorporated into the polymer backbone, while the urethane groups act as hydrogen bond donors and acceptors. The abundance of hydrogen bonds ensures strong interchain interactions, facilitating electrospinning and locking in the orientation of liquid crystalline monomers during fiber formation. The first synthesized material, utilizing a mesogen with a two-ring aromatic core, exhibited excellent electrospinnability and photoactuation properties but lacked the desired liquid crystalline behavior. To address this, a mesogen with a three-ring aromatic core was employed. This modification led to materials with improved liquid crystalline properties. Further investigation is underway to evaluate the electrospinnability and photoactuation properties of these materials.

Per- and polyfluoroalkyl substances (PFAS) are a class of emerging pollutants known for their environmental persistence and detrimental health effects. The scientific community has actively developed innovative methodologies to detect and remove these substances from various environmental matrices, including soil, wastewater, and drinking water. Chapter 5 explores the potential of supramolecular organic receptors, quinoxaline cavitands, to complex small organic molecules, enabling their application in PFAS detection and removal. To develop a PFAS sensor, the cavitand was incorporated into a conductive polymer matrix. This approach aimed to leverage the host-guest complexation within the cavity as a trigger for generating a sensor response. To achieve this goal two novel quinoxaline cavitands, functionalized with thiophene and pyrrole units at the upper rim, were synthesized for electropolymerization. While the thiophene-functionalized cavitand resulted unsuitable for the polymerization reaction, the pyrrole-functionalized cavitand was successfully copolymerized with N-methyl pyrrole. However, attempts to create a functional sensor were unsuccessful, as exposure to both blank and pollutant-containing matrices resulted in inconsistent signal variations. Subsequently, the pyrrole-functionalized cavitand was copolymerized with N-methyl pyrrole to create a membrane for PFOA removal. The strategy involved exploiting the oxidation of the conductive polymer matrix to generate positive charges, enabling dual interactions with the pollutant: ion pair formation between the positively charged matrix and negatively charged PFOA, coupled with host-guest complexation of the PFOA lipophilic tail within the hydrophobic cavity. While the material demonstrated good PFOA removal capabilities its performances resulted to be lower when compared with control material poly-N-methyl pyrrole alone.

Chapter 1

Fundamentals

1. Introduction

In recent decades, the global consumption of polymeric materials has grown exponentially, driven by their unique properties and extensive range of applications. Specifically, the use of thermoplastic and thermosetting polymers has seen significant growth across various industrial sectors, including construction, automotive, aerospace, packaging, and electronics.

This increase can be attributed to the distinctive characteristics of polymeric materials, which are versatile, lightweight, durable, and easy to process. Furthermore, polymers are relatively inexpensive to produce compared to materials such as metals and ceramics, making them an attractive option for many industries. However, the growing consumption of polymeric materials has raised environmental concerns, as most polymers are non-biodegradable and can persist in the environment for decades, if not centuries. Additionally, the production of polymers often involves the use of non-renewable resources and generates greenhouse gas emissions. Currently, less than 15% of all plastic waste is globally recycled (Figure 1).[1]

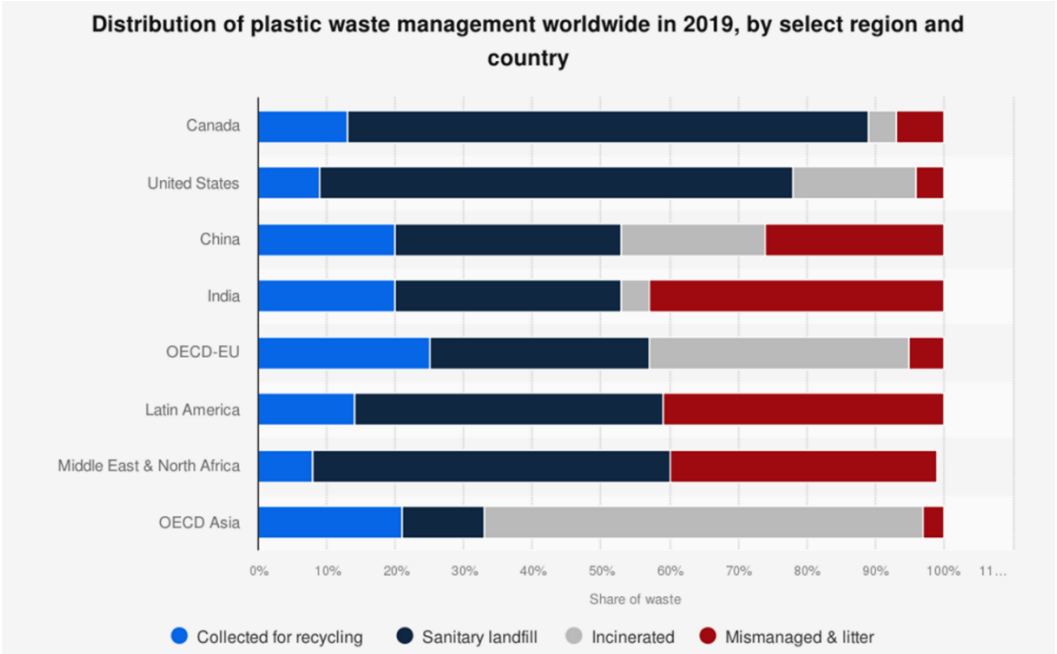

Figure 1. Histogram representing the percentage of plastic wastes which have been mismanaged and uncollected (red trace); disposed in landfills (dark blue trace); incinerated (grey trace) and recycled (light blue trace).[1]

While the majority of plastics are technically recyclable, the process becomes significantly more complex when dealing with mixtures which are difficult to separate. Moreover, in some materials, plasticizers may account for up to 30% of their weight, as is the case with phthalates in PVC. Thus, efficient recycling requires extensive sorting, separation, and cleaning, which drastically increase the cost of mechanical recycled plastic with inferior purity and properties compared to virgin materials. Consequently, there is a clear need to develop materials with extended lifespans that can be efficiently recycled or reprocessed.

Polymeric materials are generally classified into two categories (Figure 2): thermosets and thermoplastics, depending on their thermal behaviour and, in the case of thermoplastics, the absence of cross-linking. Thermoplastic polymers derive their mechanical properties from polymer chain *entanglements* and weak intermolecular forces, allowing for recyclability. In contrast, thermosets possess a highly cross-linked structure that imparts rigidity and prevents melting without undergoing chemical degradation. Today, thermosets are widely used in applications demanding high performance due to their dimensional stability, chemical resistance, and stiffness. However, their molecular architecture renders them non-recyclable; at best, thermoset waste can be utilized as filler in construction materials.

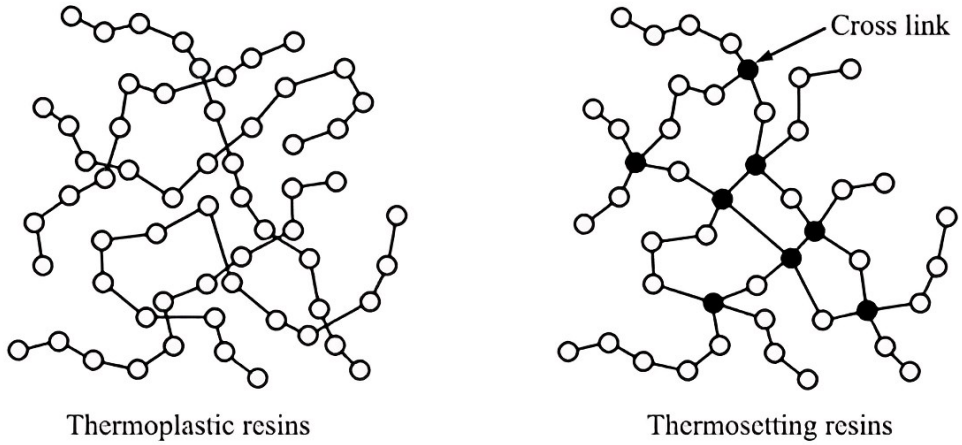

Figure 2. Schematic representation of thermoplastics (left) and thermosetting (right) polymers.[2]

A major scientific challenge is to develop polymer networks with robust, highly cross-linked structures that are also recyclable. One of the most straightforward yet intriguing chemical strategies for transforming cross-linked polymer networks into recyclable materials involves the incorporation of dynamic covalent bonds. When a sufficient number of reactive bonds are introduced, the polymer forms a covalent adaptable network (CAN), a concept pioneered by Wudl and Bowman.[3-4].

In covalent adaptable networks (CANs), the rearrangement of cross-linked bonds can proceed via two mechanisms: dissociative and associative.[5] In dissociative networks (Figure 3), the cross-linked bonds are broken during reprocessing, followed by the formation of new covalent cross-links at different sites.

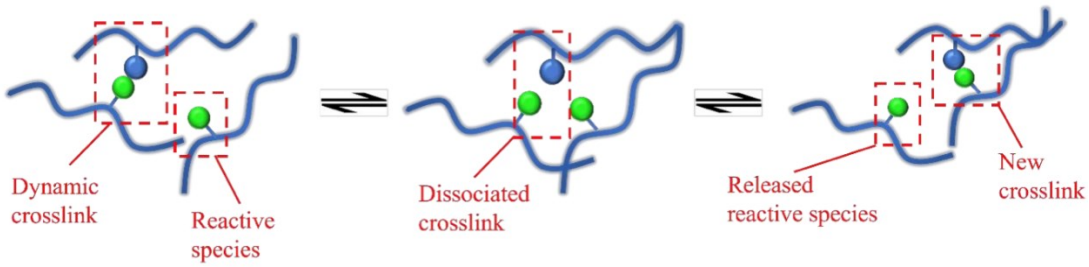

Figure 3. Schematic representation of dissociative mechanism.[5]

On the other hand, associative mechanism (Figure 4) involves the simultaneous formation of a new bond and the breaking of an existing one, via an associative intermediate. This class of materials is particularly appealing because the exchange process preserves the total number of cross-links.

Expanding on Wudl's and Bowman work, Leibler designed polymer systems with a permanent network connectivity that can be rearranged at elevated temperatures.[6] In

particular, Leibler developed a material utilizing the well-established chemistry of epoxides, wherein diglycidyl ether of bisphenol A (DGEBA) was reacted with a mixture of di and tricarboxylic fatty acids with an epoxy:COOH 1:1 ratio, resulting in the formation of both ester crosslinks and free hydroxyl functionalities. Additionally, zinc acetate [$Zn(ac)_2$], a known catalyst for transesterification reactions, was incorporated into the material. At room temperature, the material exhibited a covalent crosslinking network characteristic of elastomeric materials. However, upon increasing the temperature, the presence of zinc acetate facilitated transesterification reactions involving the free hydroxyl groups and pre-existing ester functionalities, making the crosslinking network dynamic. In general, these CANs are particularly suited to circular economy principles, as they combine the high-performance properties of thermosets with the recyclability of thermoplastics.

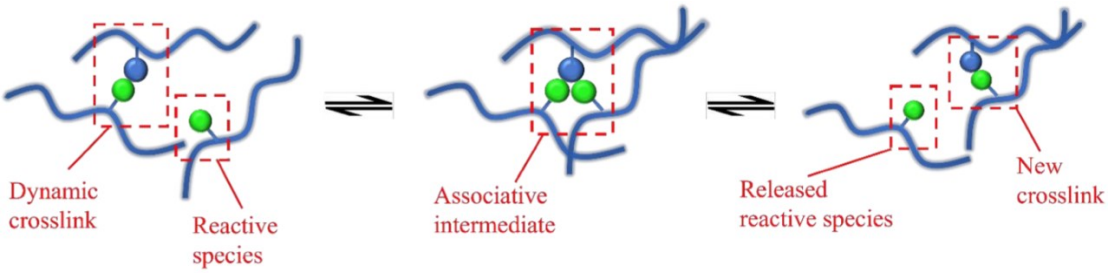

Figure 4. Schematic representation of associative mechanism.[6]

The primary parameter governing the rate of bond exchange in CANs is temperature. At operational temperatures, these materials behave as thermosets, but when heated beyond a certain threshold, they transition into thermoplastics. In particular, covalent adaptable networks exhibit a viscosity-temperature relationship that follows the Arrhenius equation (Figure 5), similar to glass, and the rate of dynamic bond exchange dictates the material's viscous flow. To describe the viscous flow of a covalent adaptable network, two critical temperatures must be considered: the glass transition temperature (T_g) and the topological freezing temperature (T_v). The T_g, a common parameter in all amorphous polymers, corresponds to the onset of large-scale polymer chain segment movements, while the T_v is unique to CANs and relates to the rate of exchange reactions within the network. Conventionally, T_v is placed at the solid to liquid transition point where a viscosity of 10^{12} Pa*s is reached.[7]

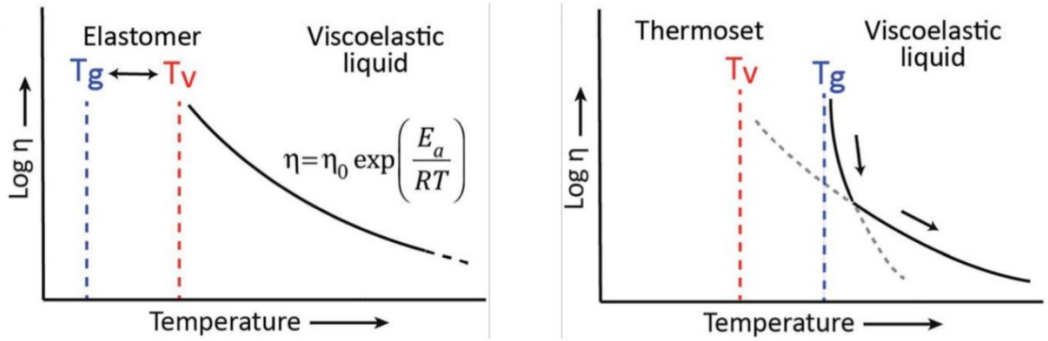

Figure 5. Schematic representation of covalent adaptable networks viscoelastic behaviour when $T_g < T_v$ (Left). Increasing temperature, the material evolves from glassy solid ($T < T_g$) to elastomer ($T_g < T < T_v$) and to viscoelastic liquid ($T > T_v$) following Arrhenius's law. When the covalent adaptable network evolves form glassy solid state to a viscoelastic liquid, its viscosity is firstly controlled by diffusion (WLF) and then by the exchange kinetic (Arrhenius).[8]

Above T_v, the covalent adaptable network behaves as a viscoelastic liquid with rheological properties conducive to plastic processing. Once reprocessing is complete, cooling the material below T_v "freezes" the new network configuration.
In most cases, covalent adaptable networks exhibit a T_v higher than T_g, resulting in a viscosity decrease that follows Arrhenius' law (Figure 5, left). In these instances, the material's topology remains unchanged until the bond exchange reactions become sufficiently rapid. Less frequently, covalent adaptable network systems may exhibit a T_v lower than T_g. In such cases, bond exchange reactions are suppressed due to limited chain mobility until T_g is reached. Once T_g is surpassed, exchange reactions proceed rapidly, and the initial viscosity-temperature relationship can be described by the Williams-Landel-Ferry (WLF) model, before transitioning to Arrhenius behavior at higher temperatures (Figure 5, right). T_v thus represents both the material's upper operational limit and the minimum temperature required for recycling.

With respect to the chemistry of the dynamic bonds used in covalent adaptable network cross-linking, numerous systems have been developed, utilizing various functional groups and reactive mechanisms (Figure 6).[5] Our research group has as already demonstrated the exchange chemistry on networks incorporating vinylogous urethane and silyl ether bonds, which have been employed to synthesize polyethylene-based covalent adaptable networks from suitably functionalized polyethylene.[9,10]

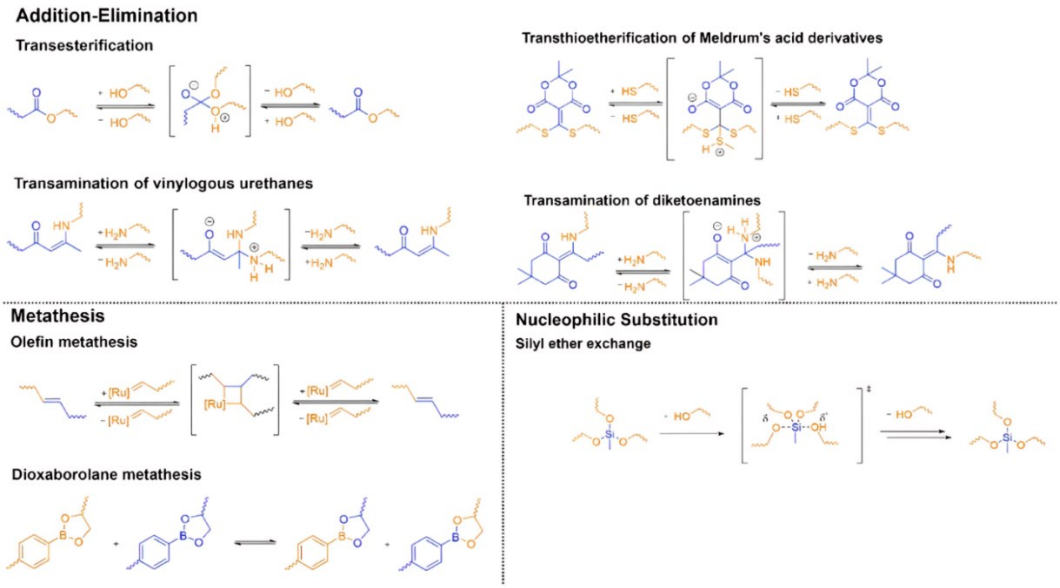

Figure 6. Notable examples of dynamic chemistry for covalent adaptable networks.[5]

Like all materials, covalent adaptable networks are susceptible to degradation and damages under minor mechanical stresses, fatigue, or strain, and these micro-damages are often invisible to the naked eye. Monitoring the formation of microcracks in polymeric materials is crucial for preventing catastrophic failures, such as material fracture.[11] Therefore, non-destructive detection of microcracks in polymers is essential for preventing structural failures and extending materials lifespan. Self-diagnostic polymers, capable of autonomously sensing mechanical stress, offer an ideal solution to this challenge. Mechanical damage or excessive strain can be signalled through optical responses, based on a variety of systems.[12] Most examples of self-diagnostic materials reported in the literature rely on mechanochemistry, wherein mechanophores—molecular units embedded in the polymer matrix—detect zones of mechanical stress.[13] Mechanophores undergo structural changes in response to external mechanical stimuli, leading to shifts in their UV-vis absorption spectrum, thereby signalling excessive strain.

One key class of mechanophores developed involves supramolecular mechanophores, which rely on weak interactions. These mechanophores offer the advantage of requiring activation forces 2-3 orders of magnitude lower than covalent-bond-based systems (from pN to fN). Dalcanale and collaborators have reported two examples of supramolecular mechanophores, one used in an elastomeric matrix[14] and the second one in a thermoset polymer based on epoxy resin and carbon fiber.[15] In the latter case, the mechanophore is a ternary complex comprising cucurbit[8]uril (CB[8]) as the host and two distinct guests. CB[8] is particularly suited to incorporation in polar matrices, such as epoxy resins, due to its capacity to form highly stable complexes in polar environments (Figure 7).

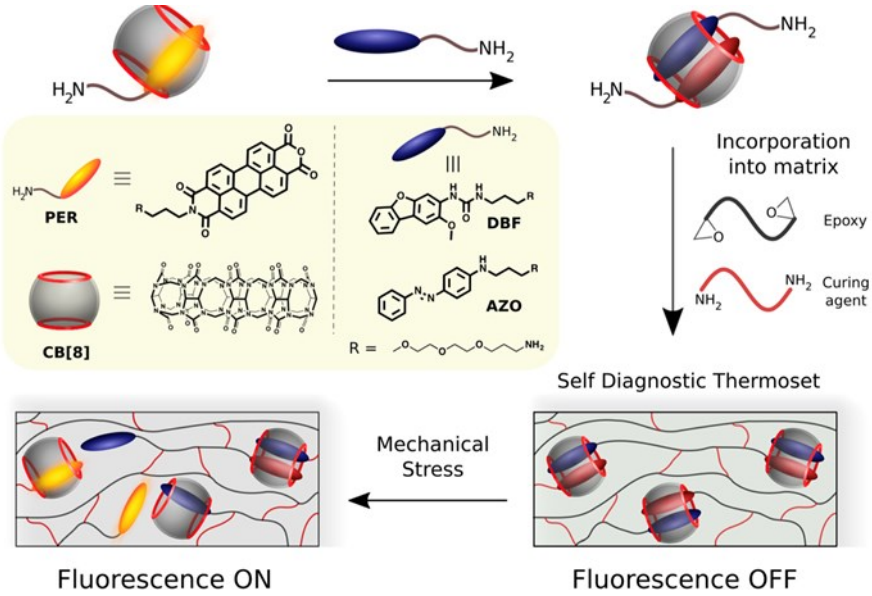

Figure 7. Supramolecular probe for stress detection made of CB[8] heteroternary complex with a fluorophore and its quencher.[15]

As depicted in Figure 7, the system is designed such that CB[8] encapsulates two molecules — a fluorophore and a quencher — forming a non-fluorescent heteroternary complex (via static quenching). Upon mechanical stress, the weak supramolecular interactions within the polymer matrix are disrupted, leading to dissociation of the ternary complex. Once the host-guest complex dissociates, the spatial proximity between the quencher and fluorophore is lost, allowing the fluorophore to resume emission. However, this system is not reversible, as the supramolecular complex cannot be reconstituted after dissociation due to the high rigidity and low molecular mobility provided by the epoxy matrix.

Weder and colleagues[16] demonstrated a notable example of stress-detection utilizing supramolecular chemistry. They developed a ternary blend of polyurethane elastomers capable of emitting blue, green, and orange photoluminescence upon mechanical stimulation. Each polyurethane incorporated a unique rotaxane structure, comprising a fluorophore-functionalized receptor and a macrocycle-complexed quencher. Mechanical stress induced decomplexation of the quencher, leading to fluorescence activation of the dye (Figure 8).

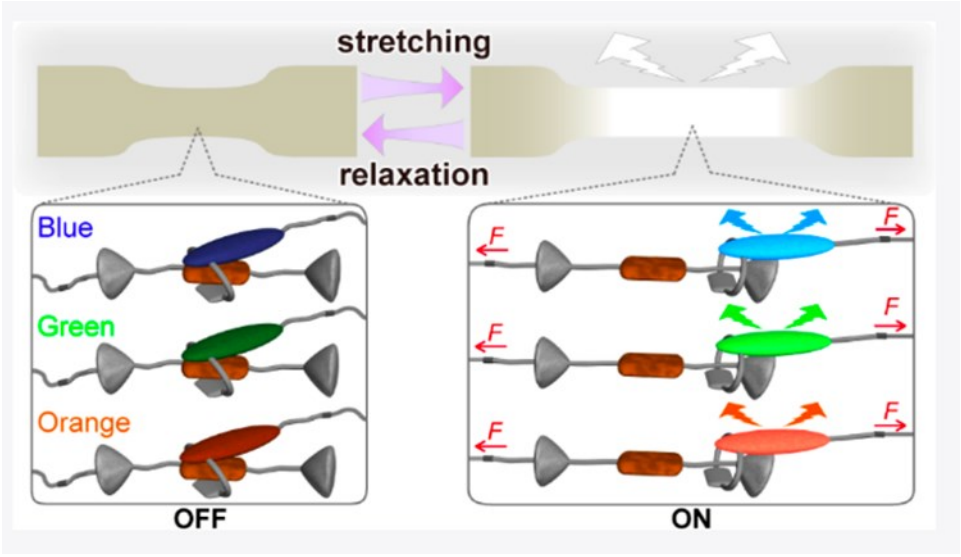

Figure 8. Werder's self-diagnostic system based on rotaxanes.[16]

Supramolecular self-diagnostic systems exhibit notably low activation energies. While this confers high sensitivity, it can also lead to false positives due to weak mechanical solicitations insufficient to induce microcracks that compromise mechanical integrity. Additionally, the synthesis and compatibility of these systems with polymer matrices can pose significant challenges.

Another highly effective method for endowing materials with self-diagnostic properties involves encapsulating dyes within microcapsules dispersed throughout the polymer matrix. Calvino et al. developed a self-diagnostic system that combines the concept of aggregation-induced excimer formation of a fluorescent dye, together with the controlled release through the rupture of specific microcapsules embedded within the matrix.[17]
The system consists of poly(urea-formaldehyde) microcapsules filled with a solution of a cyano-OPV derivative, 1,4-bis(α-cyano-4-(2-ethylhexyloxystyryl))-2,5-dimethoxybenzene (BCEDB), in hexyl acetate, dispersed within a poly(dimethylsiloxane) matrix. When subjected to mechanical stress, such as scratching, impact, or tensile strain, the microcapsules break apart releasing the dye into the damaged area. Upon release, the dye tends to aggregate, leading to excimer formation and a subsequent change in fluorescence (Figure 9).

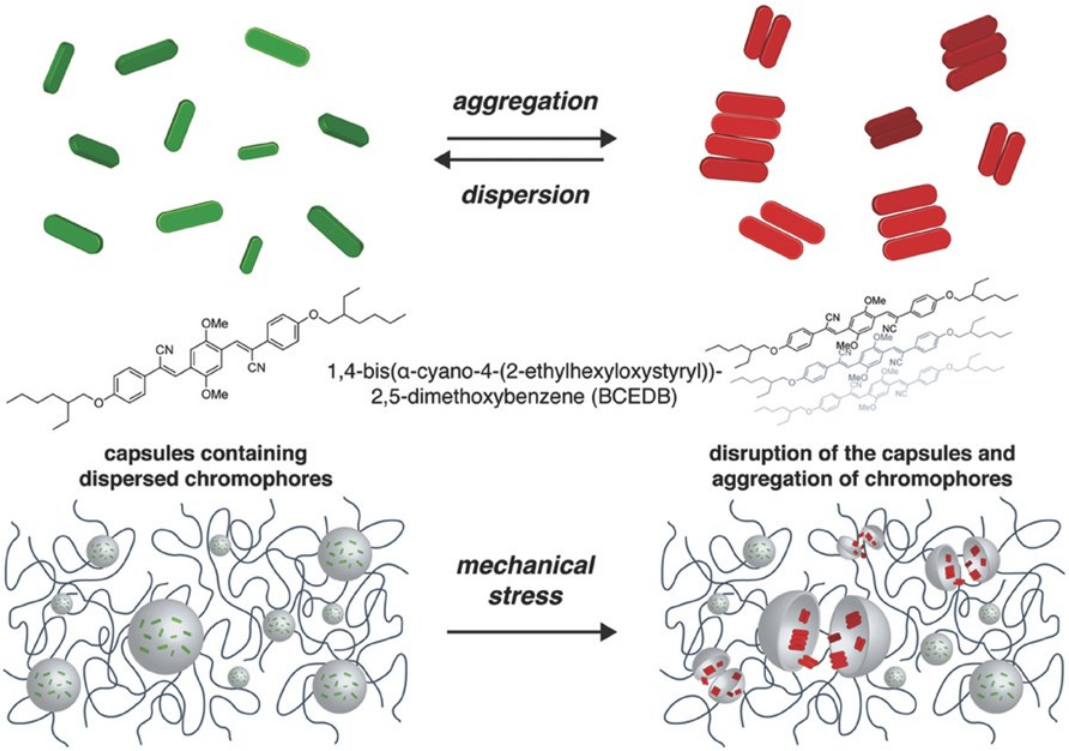

Figure 9. Schematic representation of the working principle of the designed self-diagnostic material.[17]

This method offers two significant advantages: (1) damage detection is based on a change in fluorescence, rather than an on-off switch (e.g., appearance/disappearance of color), enabling a ratiometric response and self-calibration, allowing for direct, quantitative assessment of damage; and (2) this method is applicable to a wide range of polymer matrices, facilitating the evaluation of structural integrity in composite materials containing these microcapsules as an additive. However, they can only serve once thus only useful to indicate that a part is damaged and needs to be changed.

Mechanochromophores, which rely on the reversible breakage and reformation of labile covalent bonds to control fluorescence, offer a potentially more advantageous approach. Spiropyran, one of the earliest examples of reversible mechanochromophores, demonstrates a structural transformation from a yellow closed form to a purple open form, known as merocyanine. This conversion, accompanied by a colour change, is driven by the cleavage and restoration of the labile C-O bond at the spiro-junction (Figure 10).[18]

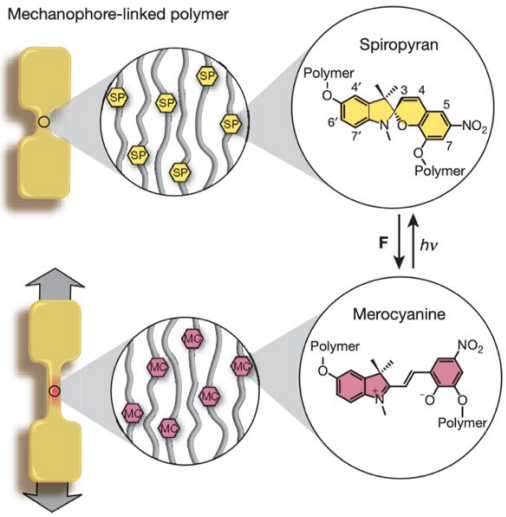

Figure 10. Spiropyran (yellow) - merocyanine (purple) upon tensile mechanical stress.[18]

When spiropyran is covalently incorporated within a polymer matrix, mechanical stress applied to the material can induce the conversion from the closed to the open form.[19] The subsequent reversion from merocyanine to spiropyran can be triggered by external stimuli such as elevated temperature or ultraviolet-visible light exposure. [19]

Efficient transmission of mechanical stress from the polymer matrix to the labile C-O bond of the spiropyran probe is crucial for maximizing mechanophore opening.[20] To this end, the spiropyran should be covalently linked to the polymer matrix via either the indole moiety (C1-C4) and the benzopyranic residue (C5-C10) (Figure 11). Additionally, the presence of electron-withdrawing groups stabilizes the merocyanine intermediate, facilitating the opening process.

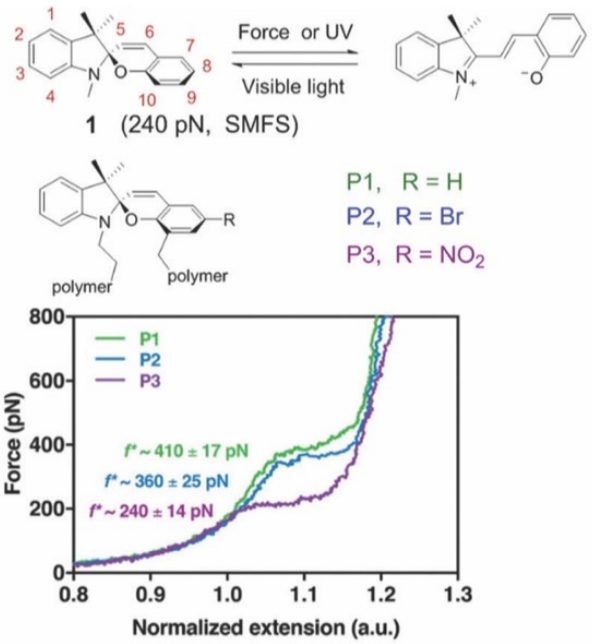

Figure 11. On top: the activation of spiropyran by mechanical forces or UV light, the reverse reaction is accelerated by visible light. At the bottom: three differently substituted spiropyrans, the graph shows the mechanical strength necessary for their opening to their respective merocyanine.[20]

Other interesting mechanophores characterized by a ring-opening process are rhodamine[21] and naphthopyran.[22]

Rhodamine (Figure 12) is a well-established dye, widely employed in biochemistry due to its high quantum yield, and it offers exceptional sensitivity and spatial resolution. Like spiropyran, the labile C-N bond at the spiro-junction can be cleaved to form a planar zwitterion under mechanical stress, while the reverse reaction can be induced by increasing temperature. As with spiropyran, efficient transmission of mechanical stress from the polymer matrix to the probe is crucial for enhancing stress-detection. In the case of rhodamine, covalent linkage of the polymer chain to both the lactam ring and the opposite side of the scaffold (Figure 12) is necessary to activate the fluorophore.[21]

Wang et al. developed a system incorporating a rhodamine derivative functionalized with three acrylate groups, serving as cross-linking sites in a photopolymerization reaction. Two acrylate groups were positioned on the xanthene scaffold, while one was attached to the lactam ring. The resulting material exhibited remarkable mechanochromic properties when subjected to tensile stress, characterized by a noticeable fluorescent color change from pale blue to red upon stretching. This color change was visually apparent, as the sample transitioned from colorless to bright pink. The observed color change was attributed to force-induced isomerization of rhodamine, shifting from its closed lactam form to its open zwitterionic form, resulting in a red-shift in the molecule's absorption band.[21]

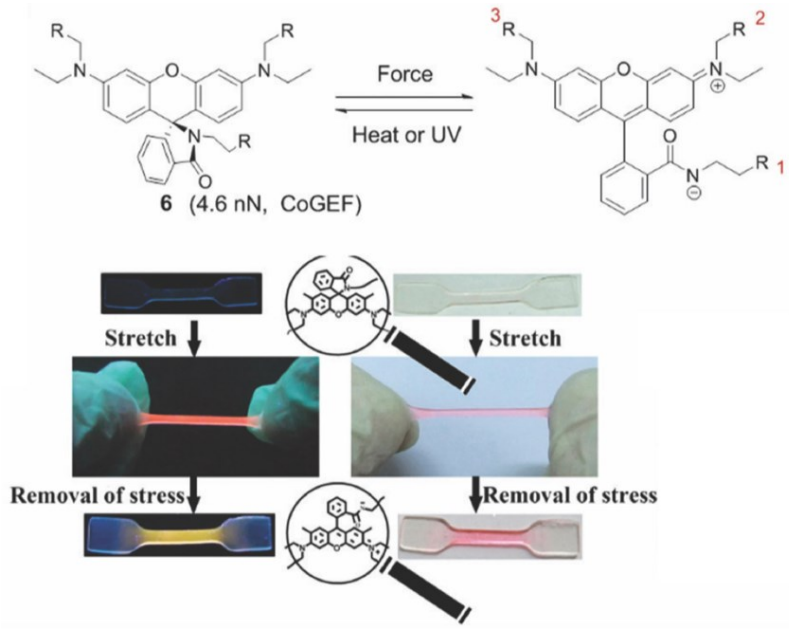

Figure 12. On top: activation of rhodamine by mechanical stress and the reversible process by applying an external trigger as temperature increase or a UV irradiation (R substituent represents the polymer chain). At the bottom: rhodamine used as crosslinker which can be activated upon mechanical stretching and the colouration is maintained when the stress is released.[21]

Versaw et al. demonstrated the ability to modify naphthopyran-based mechanophores to precisely control the exhibited coloration and decay kinetics following mechanical activation.[22] The various naphthopyran-based scaffolds were functionalized with acrylate groups for use as cross-linkers in a polydimethylsiloxane (PDMS) matrix (Figure 13).

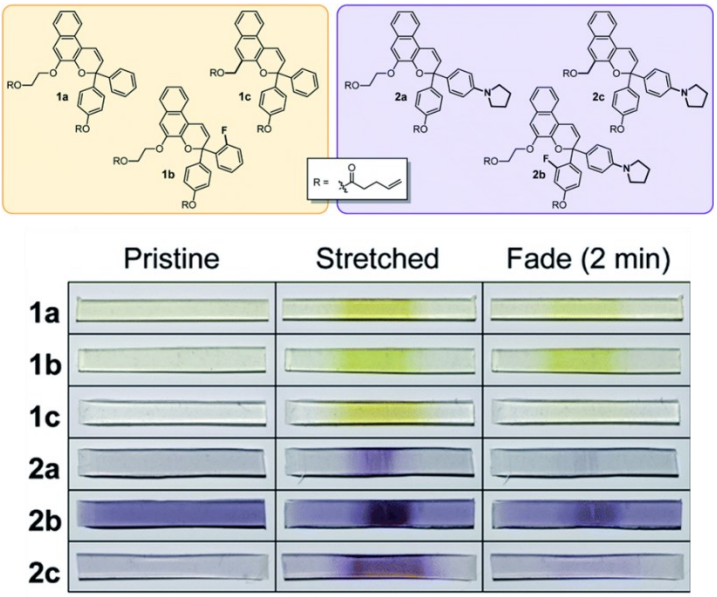

Figure 13. Schematic representation of different synthesized naphthopyran-based crosslinkers, their mechanochromic behaviour upon mechanical solicitation and their colour fading after 2 minutes from the stress application.[22]

All synthesized naphthopyran-based cross-linkers exhibited the characteristic colour change upon subjecting the material to tensile stress. However, cross-linkers 1a-c displayed a yellow-orange coloration, while cross-linkers 2a-c, characterized by pyrrolidine substituents, exhibited a purple coloration. Moreover, images captured two minutes after mechanophore activation revealed distinct thermal reversion kinetics among different naphthopyran-based cross-linkers. Materials containing mechanophores 1b and 2b, featuring ortho-positioned substituents, exhibited slower merocyanine decay. Conversely, materials incorporating mechanophores 1c and 2c, characterized by the presence of alkyl tether groups in the 5-position, demonstrated nearly complete colour decay within two minutes of force application.

Self-diagnostic materials utilizing mechanochromophores have garnered considerable scientific interest due to their capacity for detecting minor damage through a straightforward and immediate detection system. However, the widespread adoption of these materials in real-world applications necessitates addressing several challenges. Key issues include the development of cost-effective processes for large-scale mechanophore production and, more critically, the ability of these systems to function effectively in applications demanding high-performance durability and, consequently, long-term probe stability.

2. References

[1] *Global plastic waste management methods 2019, by select country:* http://www.statista.com/statistics/1358416/global-plastic-waste-management-share-by-region-country/

[2] *Thermoplastics vs. Thermosets*. https://www.protolabs.com/it-it/risorse/suggerimenti-di-progettazione/materiale-termoplastico-vs-materiale-termoindurente.

[3] Chen, X.; Dam, M. A.; Ono, K.; Mal, A.; Shen, H.; Nutt, S. R.; Sheran, K.; Wudl, F. A, *Science* **2002**, 295, 1698–1702.

[4] Scott, T. F.; Schneider, A. D.; Cook, W. D.; Bowman, C. N. *Science* **2005**, 308, 1615–1617.

[5] Scheutz, G. M.; Lessard, J. J.; Sims, M. B.; Sumerlin, B. S., *J. Am. Chem. Soc.* **2019**, 141, 16181–16196.

[6] Montarnal, D.; Capelot, M.; Tournilhac, F.; Leibler, L., *Science* **2011**, 334, 965–968.

[7] Fortman, D. J.; Brutman, J. P.; Cramer, C. J.; Hillmyer, M. A.; Dichtel, W., *J. Am. Chem. Soc.* **2015**, 137, 14019–14022.

[8] Denissen, W.; Winne, J. M.; Du Prez, F. E., *Chem. Sci.* **2016**, 7, 30–38.

[9] Tellers, J.; Pinalli, R.; Soliman, M.; Vachon, J.; Dalcanale, E., *Polym. Chem.* **2019**, 10, 5534–5542.

[10] Zych, A.; Pinalli, R.; Soliman, M.; Vachon, J.; Dalcanale, E., *Polymer* **2020**, 199, 122567.

[11] Calvino, C.; Neumann, L.; Weder, C.; Schrettl, S., *J. Polym. Sci. Part Polym. Chem.* **2017**, 55, 640–652.

[12] Traeger, H.; Kiebala, D. J.; Weder, C.; Schrettl, S., *Macromol. Rapid Commun.* **2021**, 42, 2000573.

[13] Black, A. L.; Lenhardt, J. M.; Craig, S. L., *J Mater Chem,* **2011**, 21, 1655–1663.

[14] Früh, A. E.; Artoni, F.; Brighenti, R.; Dalcanale, E., *Chem. Mater.* **2017**, 29, 7450–7457.

[15] Das, A. D.; Mannoni, G.; Früh, A. E.; Orsi, D.; Pinalli, R.; Dalcanale, E., *ACS Appl. Polym. Mater.* **2019**, 1, 2990–2997.

[16] Sagara, Y.; Karman, M.; Seki, A.; Pannipara, M.; Tamaoki, N.; Weder, C., *ACS Cent. Sci.* **2019**, 5, 874–881.

[17] Calvino C., Guha A., Weder C. and Schrettl S., *Adv. Mater.*, **2018**, 30, 1704603.

[18] Davis, D. A.; Hamilton, A.; Yang, J.; Cremar, L. D.; Van Gough, D.; Potisek, S. L.; Ong, M. T.; Braun, P. V.; Martínez, T. J.; White, S. R.; Moore, J. S.; Sottos, N. R., *Nature*, **2009**, 459, 68–72.

[19] Celestine, A.-D. N.; Beiermann, B. A.; May, P. A.; Moore, J. S.; Sottos, N. R., *Polymer*, **2014**, 55, 4164–4171.

[20] Chen, Y.; Mellot, G.; van Luijk, D.; Creton, C.; Sijbesma, R. P., *Chem. Soc. Rev.,* **2021**, 50, 4100–4140.

[21] Wang, T.; Zhang, N.; Dai, J.; Li, Z.; Bai, W.; Bai, R., *ACS Appl. Mater. Interfaces*,

2017, 9, 11874–11881.
[22] Varsaw B. A., McFadden M. E., Husic C. C. and Robb M. J., *Chem. Sci.*, **2020**, 11, 4525.

Chapter 2

Self-diagnostic and Self-Healing Epoxy-based Covalent Adaptable Network

Abstract

Self-diagnostic materials are polymers functionalized with mechanochromic dye able to change colour upon mechanical solicitations. These probes enable the early detection of crack formation inside a polymer matrix. So far, most of the activity has been concentrated on mechanochromic thermoplastics realized by directly linking dyes into the polymer chains of elastomeric or on glassy cross-linked polymers. More recently a different damage-reporting strategy has been introduced, using aggregation-induced emission of fluorophores confined in core-shell microcapsules.

Here, we present the preparation of self-diagnostic covalent adaptable network designed with the aim to detect in a non-destructive way early-stage damage introducing inside the polymer matrix a suitable probe encapsulated inside microcapsules.

TOC: Material design for stress detection.

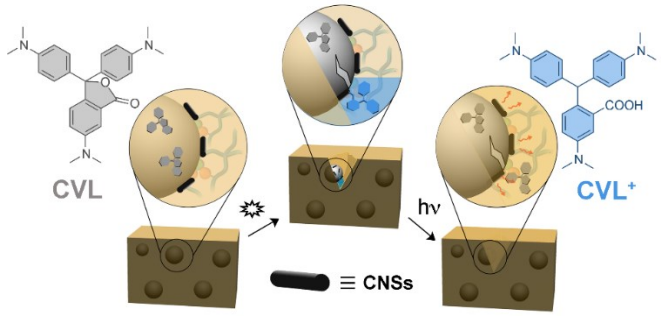

This project is in collaboration with Professor Mauricio Rodriguez, Professor Ivana Aguiar and Professor Marìa Eugenia Pérez from Universidad de la República de Uruguay (UDELAR)

1. Introduction

Thermochromic molecules, which can change colour in response to changes in temperature, are a unique class of compounds. Crystal Violet Lactone (CVL) (Figure 1) is a prominent example exhibiting a pronounced thermochromic transition from deep blue to colourless upon lactam ring closure.[1][2]

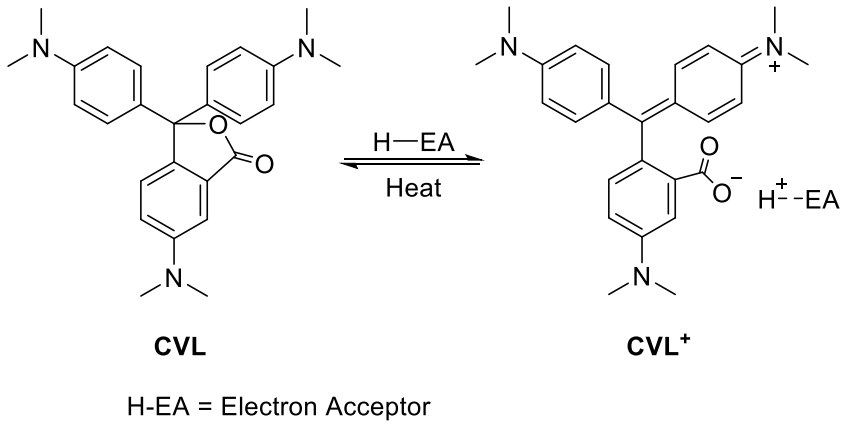

Figure 1. Opening of CVL lactam ring by addition of a proton and its thermal reversibility back to the closed form.[1]

Proton transfer between an acidic moiety and the amino-phthalein dye (CVL) initiates lactam ring opening, forming a resonance structure characterized by a positive charge on one nitrogen atom and a negative charge on the carboxylate (CVL^+). Thermal treatment can reverse this process, restoring the colourless closed form.

The reversible colour change associated with ring opening and closing makes CVL a promising candidate for stress detection. Hu et al. developed a three-component nanocapsular system comprising core-shell polymethylmethacrylate (PMMA) nanocapsules encapsulating CVL and a colour developer coating.[3] Upon capsule rupture, the colourless CVL is released, reacts with the colour developer (silica), and transforms into the blue-coloured open structure (CVL^+) (Figure 2).

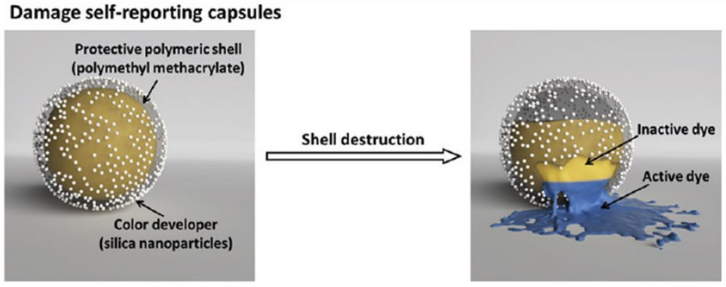

Figure 2. Working principle of the three-components polymer shell capsules containing CVL and coated with silica nanoparticles as colour developer.[3]

A one-step miniemulsion solvent-evaporation process utilizing silica nanoparticles as a Pickering stabilizer was employed for system preparation. During the emulsification phase, CVL and PMMA were dispersed in a chloroform-phenylacetate mixture. Subsequent chloroform evaporation rendered PMMA insoluble, leading to phase separation and the formation of the polymer shell. CVL remained solubilized in phenylacetate, constituting the liquid core within the polymer shell. The silica nanoparticles used for emulsion stabilization completely encapsulated the polymer shell, serving as the colour developer.[3]

The three-component system was then dispersed within a polyvinyl alcohol coating, demonstrating self-reporting properties of the coating upon cutting with a razor blade. Upon damage detection, a healing agent capable of forming strong hydrogen bonds between silica and CVL^+ was applied to simultaneously repair the coating fracture and quench CVL^+. As widely recognized, in addition to thermal stimuli, the reversion process from CVL^+ to CVL can be triggered by the introduction of a hydrogen bond acceptor group, such as an alcohol, capable of positioning itself between the dye and the acidic group responsible for ring opening.[3]

While the aforementioned systems demonstrate functionality, they necessitate the use of external healing agents for both fluorescence quenching and damage repair, leading to material modifications post-repair. It would be beneficial to develop a dynamic polymer matrix that can self-heal without the need for external agents, or by incorporating a healing agent directly into the base material to enable damage repair without having to reprocess the entire material.
Yan et al. demonstrated the creation of a composite material composed by a dynamic polyurethane-based covalent adaptable network polymer matrix integrated with carbon nanotubes, which enabled a shape memory effect triggered by near-infrared (NIR) radiation (Figure 3).[4] Initially set in shape “1”, the material can be reshaped into permanent shape “2” through NIR irradiation, which is irreversible. This phenomenon is attributed to the photothermal effect of carbon nanotubes, wherein irradiation induces a temperature exceeding the matrix's T_v, facilitating the dynamic exchange of cross-linking bonds. Subsequently, shape “2” can be modified into temporary shape “3” through a low-temperature treatment, followed by a return to shape “2” upon further NIR irradiation.

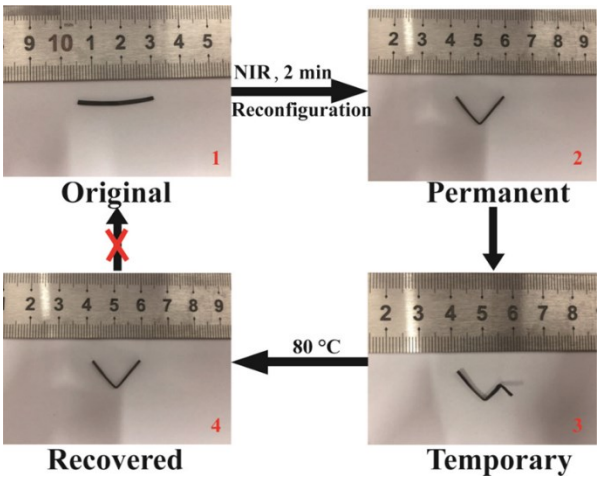

Figure 3. NIR-induced reshaping and recovery: (1) Original shape; (2) permanent reshaped material by NIR irradiation; (3) Temporary shape induced by therma treatment; (4) shape recovered by NIR irradiation.[4]

Yang et al. demonstrated the potential of incorporating carbon nanotubes (CNTs) into a dynamic polymer matrix as an integrated healing agent.[5] When irradiated by light, carbon nanotubes exhibit a significant photothermal effect, generating substantial heat capable of reaching temperatures exceeding 230°C.[6] By irradiating the material with NIR radiation, the material can be heated above its topological freezing temperature (T_v), enabling the exchange of dynamic cross-linking bonds and facilitating self-healing.

In the following sections, the application of CVL as a fluorescent probe for the development of a self-diagnostic material will be demonstrated. The dye will be encapsulated within core-shell morphology polymeric nanocapsules to facilitate controlled release of the fluorophore upon mechanical stress. The transition from CVL to CVL^+ will be catalyzed by an acidic group on a carbon nanostructure, while thermal treatment will be utilized to catalyze the reverse process, closing the dye.

2. Aim of the work

The aim of this work is to develop a self-diagnostic system using a covalent adaptable network polymer matrix that incorporates aggregation-induced emission fluorophores (CVL) confined within core-shell microcapsules for damage detection. Acidic moiety-functionalized carbon nanostructures will be employed to trigger the opening of crystal violet lactone (Figure 4).

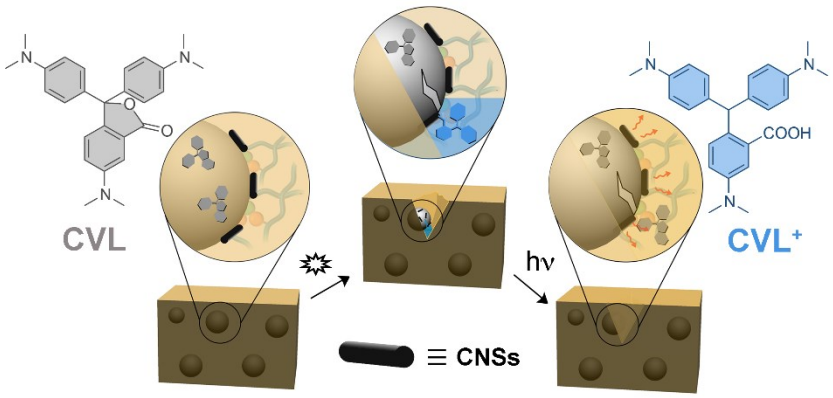

Figure 4. Schematic representation of the material design

The designed material consists of a reversible thermoset embedding polymethylmethacrylate (PMMA) core-shell nanocapsules containing CVL as a reversible stress detection probe, and acidic carbon nanostructures. The idea is that when exposed to mechanical stress, microcracks form within the material. These cracks can propagate toward the weaker polymer-nanoparticle interface, leading to the rupture of the nanoparticle shell and the subsequent release of the dye in its non-colored form. Upon diffusing outside the shell, the dye will interact statistically with the acid-functionalized carbon nanostructure, resulting in the opening of the lactam ring. This reaction will produce a blue color, indicating the presence of microdamage. By utilizing the carbon nanostructures' ability to absorb near-infrared (NIR) radiation and generate heat, the damaged area can be irradiated to induce localized heating. This process will revert the dye to its closed form and promote fracture healing through the inherent properties of the polymer matrix.

3. Results and discussion

3.1 Determination of Carbon Nanostructure (CNS)

Given the design of the detection system, the first step involved the identification of the carbon nanostructure that would yield the most effective reaction with crystal violet lactone (CVL). Specifically, the greater is the amount of fluorophore able to interact with the acidic groups on the carbon nanostructure, the more pronounced is the colour change, and, consequently, the more effective is the microfracture detection. Three different carbon nanostructures were tested: i) oxidized multi-walled carbon nanotubes (MWCNTs), ii) oxidized single-walled carbon nanotubes (SWCNTs), and iii) graphene-oxide (GO).

To assess the reaction performance between the acidic groups on the nanostructures and CVL, each nanostructure was dispersed into a dichloromethane (DCM) solution containing CVL. The mixtures were sonicated for 10 minutes, after which the solid phase was allowed to settle, and the colour intensity of the liquid phases was compared. In its closed lactone form, the fluorophore does not absorb in the visible range and, when dissolved in DCM,

produces a clear and colourless solution. Upon reaction with an acidic group, crystal violet transitions from its lactone form to its open form results in a blue-coloured solution. By visually comparing the colour changes in the three samples, it was possible to determine which nanostructure exhibited the greatest reactivity with the fluorophore (Figure 5).

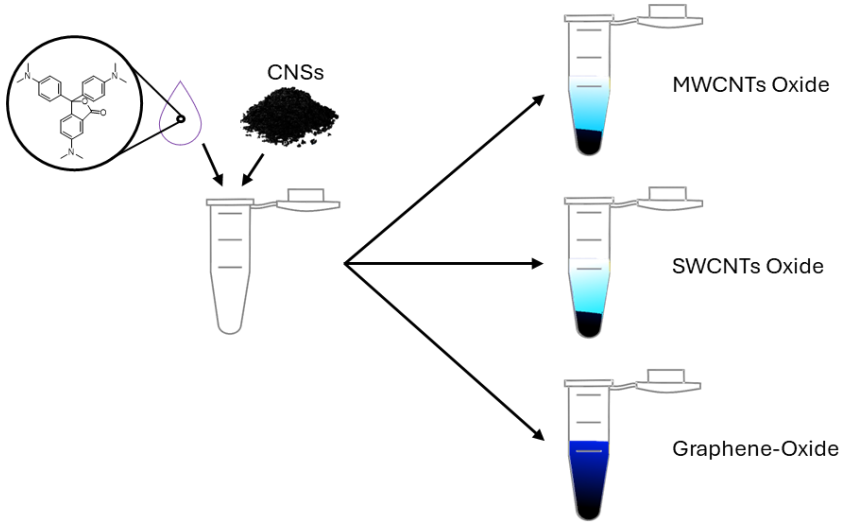

Figure 5. Schematic representation of different carbon nanostructures tested for the reaction with crystal violet lactone (CVL).

The results indicated that both multi-walled and single-walled nanotubes exhibited limited reactivity with the fluorophore, producing pale blue supernatants. In contrast, graphene oxide demonstrated significantly higher reactivity towards crystal violet, resulting in an intensely blue-coloured supernatant. Given the comparable pKa values of carboxylic acid groups present on carbon nanotubes and graphene oxide, the observed disparity in the reactivity of these nanostructures toward CVL can be attributed to the differential accessibility of the carboxylic acid groups. The tubular morphology of carbon nanotubes allows for functionalization both inside and outside the nanotube; however, the internal acidic functionalities are less accessible to the fluorophore due to the material's structure. In contrast, the planar structure of graphene sheets facilitates greater accessibility of the acidic functionalities for interaction with the fluorophore, resulting in enhanced reactivity of graphene oxide towards CVL.

3.2 Synthesis of core-shell nanoparticles

After identifying graphene oxide as the most reactive carbon nanostructure, the next step involved the synthesis of polymethyl methacrylate (PMMA) nanocapsules designed to encapsulate a solution of crystal violet lactone. To function effectively, the capsules must possess a core-shell structure: the shell must be robust enough to maintain stability within a solid matrix, yet fragile enough to rupture when a microfracture occurs in the material. Moreover, the core of the nanoparticle must remain liquid to ensure efficient flow of the

fluorophore upon capsule rupture and to facilitate its interaction with the carbon nanostructure.

The approach started with the synthesis and characterization of PMMA-based nanocapsules containing crystal violet lactone (CVL) as reporting unit dissolved in an organic phase made of phenyl-acetate. Control nanocapsules containing only the organic phase were also synthesized for comparison.

Two synthetic methods were employed to prepare PMMA nanocapsules, differing mainly in the order of sonication and chloroform evaporation steps (Figure 6): specifically, in the first method (A), after manually mixing the biphasic mixture, the chloroform is evaporated, and the resulting suspension, once evaporation is complete, is sonicated using an immersive sonicator. In the second method (B), on the other hand, the initial biphasic mixture is sonicated using the immersive sonicator, and only afterwards chloroform is evaporated.

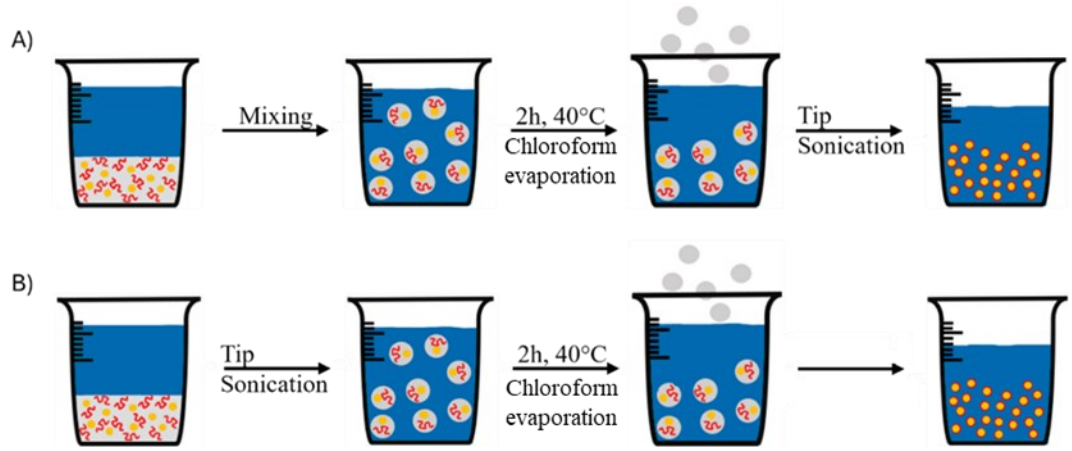

Figure 6. Methods A) and B) for PMMA nanoparticles preparation

The efficiency of droplet formation during synthesis was crucial for obtaining nanoscale particles. Characterization of the nanocapsules revealed significant differences between the two methods. Method A led to variations in particle size between batches, indicating lower reproducibility, while method B resulted in more consistent particle sizes, as highlighted by dynamic light scattering (DLS), scanning electron microscopy (SEM) and transmission electron microscopy (TEM) analyses.
The DLS measurement on nancapsules containing CVL made with method B gave an average diameter of the nanoparticles of 834 $\pm$ 22 nm, confirmed by the value calculated from the images acquired with SEM (Figure 7).

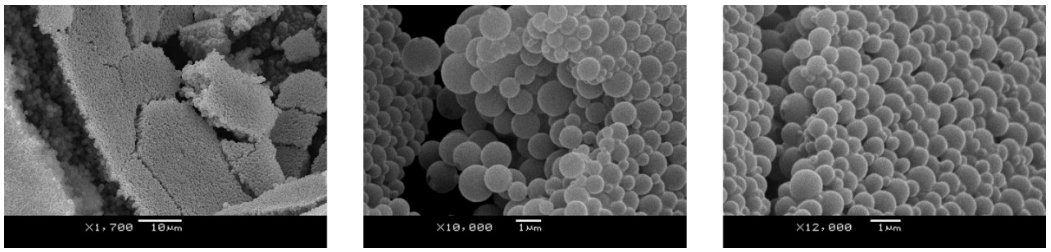

Figure 7. PMMA nanocapsules images acquired with scanning electron microscope (SEM) with increasing zoom magnitudes.

SEM images confirm the spherical shape of the nanoparticles and show a narrow distribution of the average dimension.
TEM images have been acquired to further investigate the morphology of the obtained nanocapsules (Figure 8).

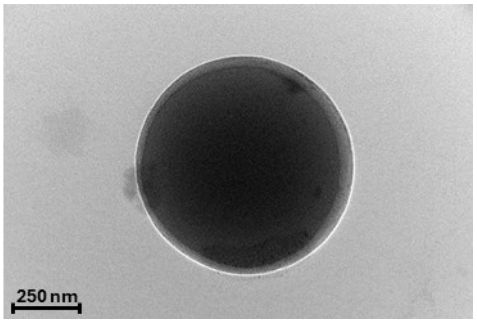

Figure 8. Transmission electron microscope (TEM) image of a PMMA nanoparticle.

TEM analysis (Figure 8) revealed the characteristic core-shell morphology of the nanoparticles, with a darker central region indicative of the liquid core and a lighter gray border corresponding to the polymeric PMMA shell.

Once fabricated, the rupture upon mechanical stress of the of the coreshell nanoparticles containing the CVL was evaluated. The nanocapsules and the graphene oxide were placed in a mortar and subjected to mechanical grinding. Chloroform was subsequently added to dissolve the released fluorophore. The suspension was then microfiltered to isolate the liquid phase from the solid residue. Under a fluorescence lamp, the liquid extract exhibited fluorescence compared to fresh solvent, confirming the interaction between the fluorophore and graphene oxide. A control experiment, in which the capsules were not subjected to mechanical stress, produced an extract that remained non-fluorescent under fluorescent lamp, demonstrating the capsules' integrity in the absence of mechanical solicitation (Figure 9). This result indicates that the color change is due to the release of the fluorophore from the capsule rather than interactions between the capsule and the graphene oxide (GO).

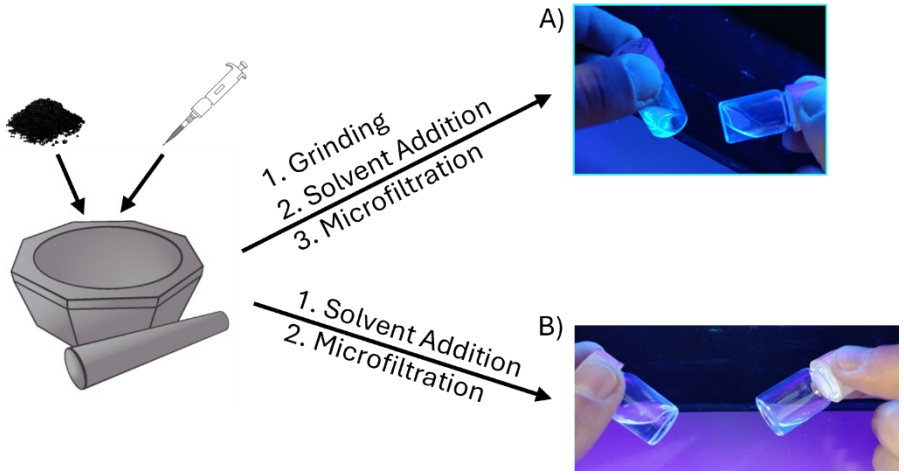

Figure 9. Schematic representation of mortar experiments: A) nanoparticles subjected to mechanical stress; B) nanoparticles not subjected to mechanical stress.

3.3 Three component system preparation and mechanical stress tests

After confirming that the rupture of the capsules in the presence of graphene oxide (GO) leads to the opening of the CVL and the subsequent appearance of color, the next step involved preparing a sample that incorporated nanocapsules and graphene oxide as standard additives within a polymer matrix. An epoxy resin, known for its high rigidity and low elasticity, was selected as model matrix due to its transparency in the emission window of CVL and due to the possibility of preparing samples without the necessity of organic solvents, which could compromise capsule integrity. This epoxy resin matrix lacks any covalent reversible bonds, however, it was selected to demonstrate the compatibility between the nanocapsules and the polymer preparation process.

To prepare the samples, nanocapsules containing CVL (0.8% in weight) and graphene oxide (0.3% in weight) were uniformly dispersed into bisphenol A diglycidyl ether (DGEBA), the epoxy component through vigorous mixing. The hardener (3,6-dioxaoctamethylenediamine) was then added and mixed thoroughly to ensure uniform cross-linking. The resulting mixture was poured into a dogbone mould and placed under high vacuum to eliminate any air bubbles introduced during the mixing process. Finally, the mould was transferred to an oven and cured at 40°C for 18 hours to allow complete resin hardening (Figure 10).

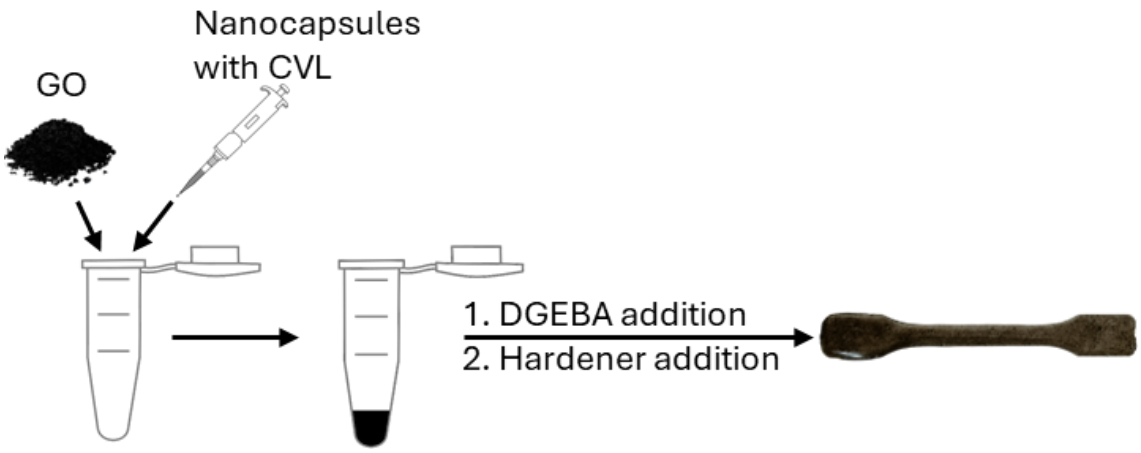

Figure 10. Preparation of epoxy resin specimen (10 x 3 x 0.3 cm) containing GO and nanocapsules.

After the resin had fully cured, the sample was removed from the mold and analyzed under a fluorescent lamp to assess the integrity of the nanocapsules. No fluorescent signal was detected, indicating that the nanocapsules remained intact throughout the epoxy resin formation process.

Subsequently, the sample was subjected to two distinct mechanical stresses—scratching and impact—at both ends. This approach allowed for simultaneous evaluation of the system's self-reporting ability and the relative effectiveness of different mechanical stresses in triggering a material response. In this case, both impact and scratch stresses produced a positive response, evidenced by the appearance of small fluorescent zones (Figure 11).

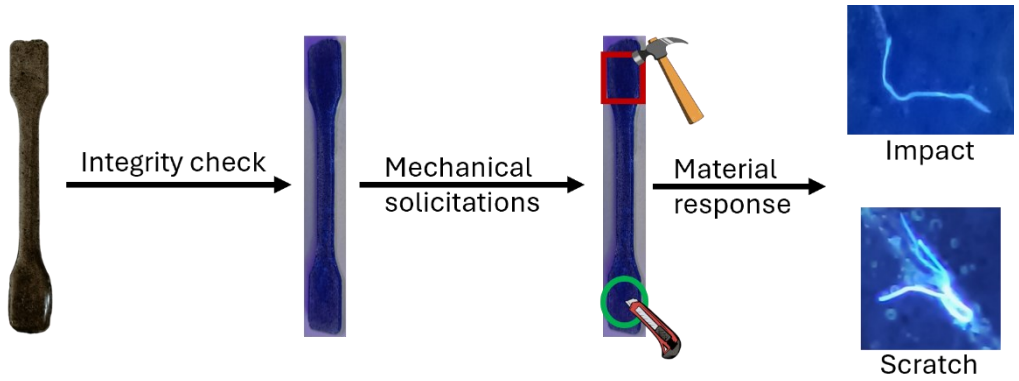

Figure11. Dogbone integrity check under fluorescent lamp, mechanical solicitation through mechanical stresses as impact and scratching, material response with self-reporting properties.

For enhanced visualization, the material was analysed using a two-photon microscope.

The acquired images showed that, in the case of impact stress (Figure 12 A), a microfracture formed, realising the fluorophore at the fracture site. In the case of scratch-induced stress (Figure 12 B), the images revealed the profile of the cut and fluorophore activation along the edges of the scratched area.

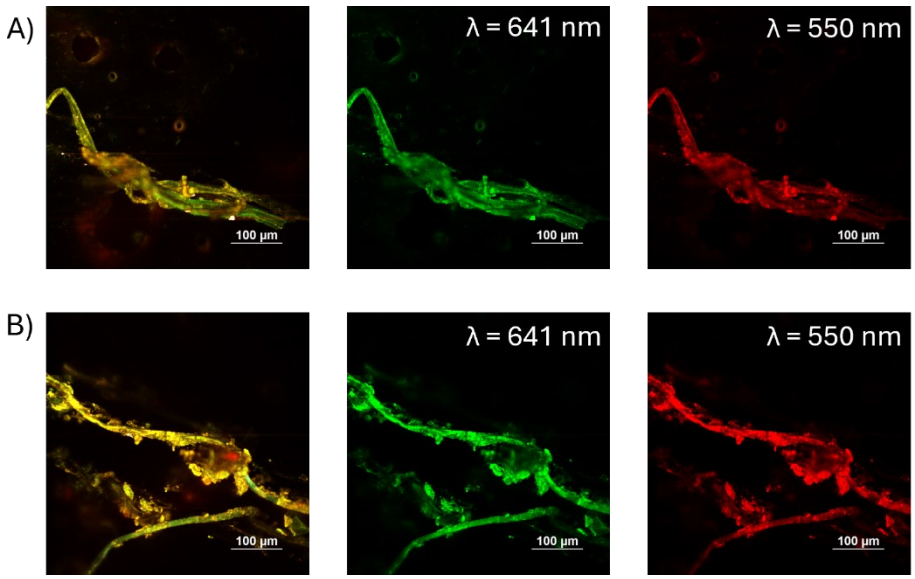

Figure 12. Two-photon microscope images of the specimen damaged by A) impact and B) scratching are presented. The images on the left side were collected overlapping 4 detectors (λ = 732, 641, 550 and 450 nm); central images were acquired with the detector set to λ = 641 nm; images on the right were acquired with the detector at λ = 550 nm.

To confirm that the fluorescence observed with the two-photon microscope originated from CVL released from ruptured nanocapsules rather than other material components, control images were acquired of the epoxy resin alone, the material containing only nanocapsules, a specimen containing only graphene oxide, and the full system prior to mechanical solicitation (Figure S1-4). By comparing the images acquired after mechanical stress with the control images, it is possible to confirm that the observed fluorescence, both in the case of impact stress and scratch stress, is due to the formation of CVL^+ when the capsule is broken, the CVL is released, and it reacts with the graphene oxide.

Employing the same technique, an aging test was conducted to assess the duration of fluorophore emission persistence following damage detection. This information is crucial for estimating the timeframe available for fracture identification. For the aging test, the sample was fractured by impact stress, and images were collected using the two-photon microscope immediately after fracture formation (t = 0), after 24 hours, and after 144 hours (6 days) (Figure 13). The images revealed a significant reduction in fluorophore emission intensity within 24 hours and nearly complete quenching after 6 days. This indicates that the

fluorophore effectively marks the damage for approximately 24 hours following capsule rupture and fracture formation.

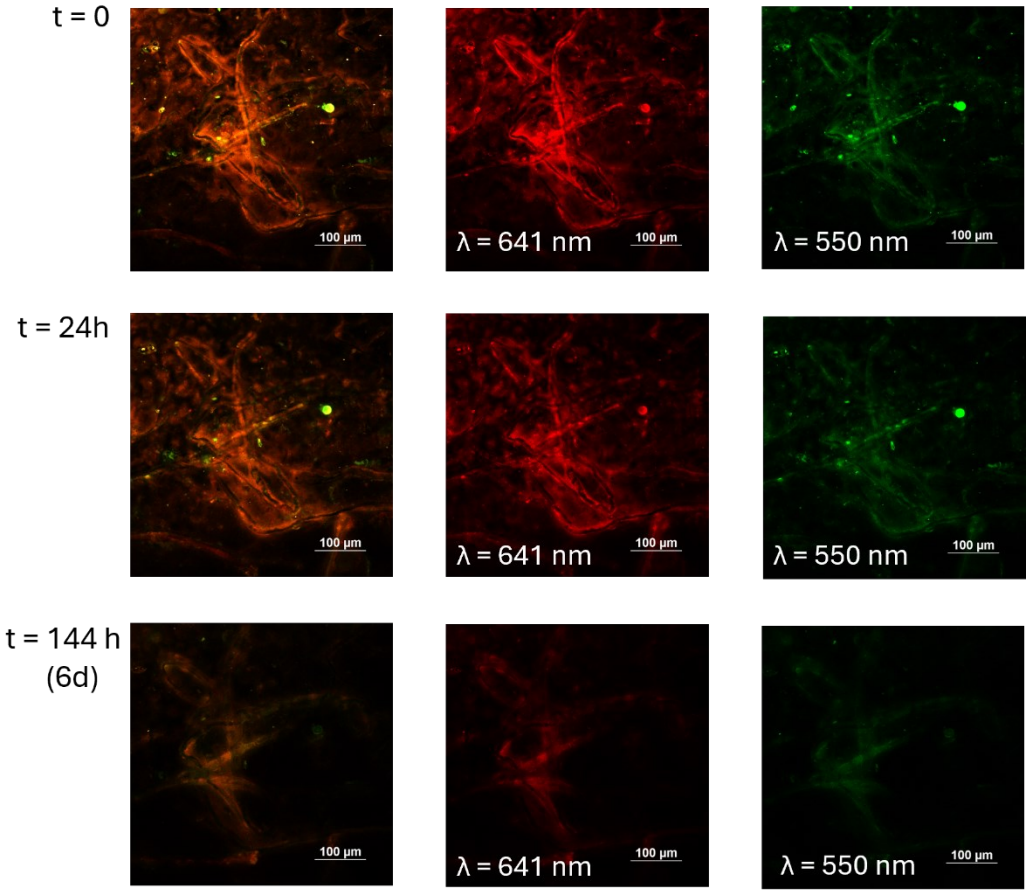

Figure 13. Aging test performed by two-photon microscope at time zero (t = 0), after 24 hours (t = 24 h) and after 144 hours (t = 144 h). The image on the left is the overlapping of 4 detectors (λ = 732, 641, 550 and 450 nm), central images was acquired with the detector at λ = 641 nm, image on the right was acquired with the λ = 550 nm detector.

Having established the system's self-reporting capabilities, the effective quenching of the fluorophore's emission through local thermal treatment was explored. This step is crucial because, in the final envisioned application, it not only deactivates the dye but also facilitates material reprocessing within a covalent adaptable network matrix. The localized thermal quenching of the fluorophore enables the same trigger to be used for the self-healing of the epoxy-based covalent adaptable network. Unfortunately, localized heating by NIR radiation exposure failed to achieve the desired quenching effect, despite varying exposure times and laser power levels. This is probably due to a non-perfect distance between the GO and the fluorophore or a non-efficient irradiation of the GO inside the polymeric matrix to allow the quenching of the fluorophore via local heating. However, complete fluorophore quenching

was successfully accomplished through thermal treatment. Specifically, placing the material in an oven at 80°C overnight resulted in the complete deactivation of the dye (Figure 14). As expected, the thermal treatment did not lead to the healing of the fracture due to the non-dynamic nature of the epoxy resin matrix.

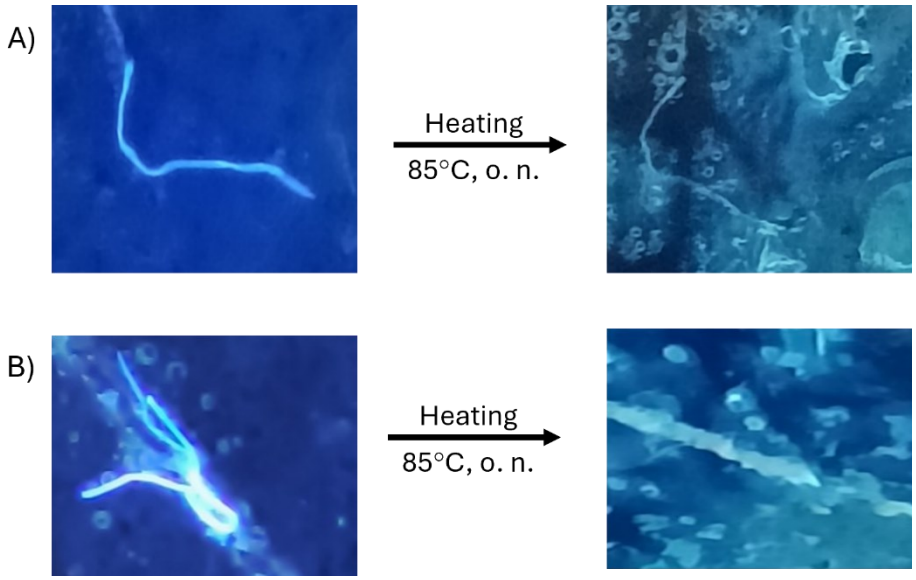

Figure 14. Fluorophore quenching by thermal treatment on damages provoked by A) impact and B) scratching.

While the developed system demonstrated satisfactory self-diagnostic properties, modifications to the nanocapsules were explored to enhance the efficiency of the response to mechanical stress and investigate the feasibility of quenching CVL^+ through localized heating induced by NIR radiation of the damaged area. In both scenarios, the spatial proximity between nanocapsules and graphene oxide plays a pivotal role. A closer proximity between the ruptured capsule and graphene oxide would facilitate the diffusion of CVL from the capsule to react with the GO. Moreover, spatial proximity would enhance heat transfer from the carbon nanostructure to CVL^+, improving the efficiency of fluorescence quenching through local heating. More flexible materials facilitate liquid diffusion, whereas rigid polymer matrices, such as epoxy resins, limit diffusion. Consequently, if a ruptured capsule is not in close proximity to the graphene oxide, the hindered diffusion of the liquid from the capsule can impede fluorophore-graphene contact, thereby reducing the quantity of activated dye. For this reason, further modifications were made to the PMMA nanocapsules to enhance interaction with graphene oxide (GO), aiming to maximize proximity between the two components. To this aim, pyrene moieties were inserted into the polymer shell, promoting supramolecular π-π interactions with GO.[7]

3.4 PMMA nanocapsules modification

Two co-monomers (S and L) were synthesized for copolymerization with methyl methacrylate to introduce pyrene moieties into the PMMA shell (Scheme 1). Following capsule formation, pyrene units are anticipated to be oriented both inwardly and outwardly from the capsule. Outward-facing units are expected to engage in supramolecular π-π interactions with graphene planes. Moreover, modifying the distance between the pyrene residue and the polymer chain can influence the molecular mobility of the system, affecting the material's ability to rearrange and form the capsule's polymeric shell. Specifically, when the pyrene is closer to the polymer chain, the steric hindrance from the pyrene moiety may restrict chain mobility but can favor a closer spatial proximity between the capsule and the graphene plane. Conversely, when the pyrene is located further from the main polymer chain, a greater distance between the capsule and graphene should observed, but with the advantage of an increased conformational freedom of the polymer, which could promote chain rearrangement and shell formation.

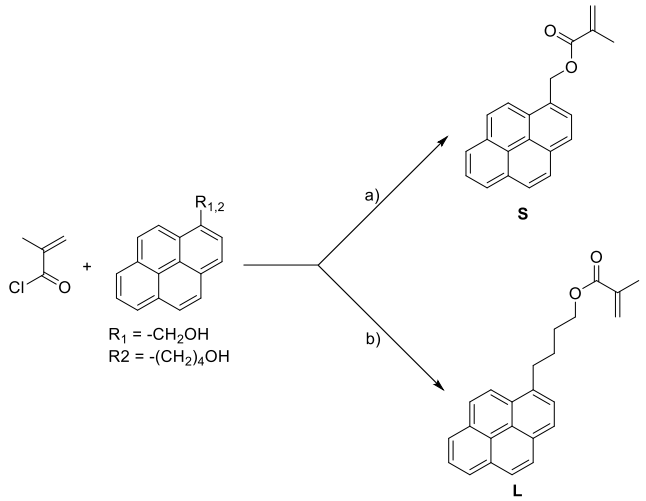

Scheme 1. a) *Et_3N, dry THF, 1-pyrene methanol, 16 h, 25°C, 98% yield; b) Et_3N, dry THF, 1-pyrene butanol, 16 h, 25°C, 98% yield.*

In this synthetic strategy, methacryloyl chloride is reacted with 1-pyrene methanol (for compound **S**) or buthanol (for compound **L**) in a basic solution of THF and triethylamine (Et_3N) to form the corresponding ester functionality. Changing the distance between the pyrene moiety and the methacrylic moiety allows for modulate the distance between the pyrene and the nanocapsule shell. For both reactions, the products were purified via liquid chromatography, to obtain **S** or **L** in 98% yield.

The two monomers have been characterized by ^{1}H-NMR spectroscopy (Figure 15).

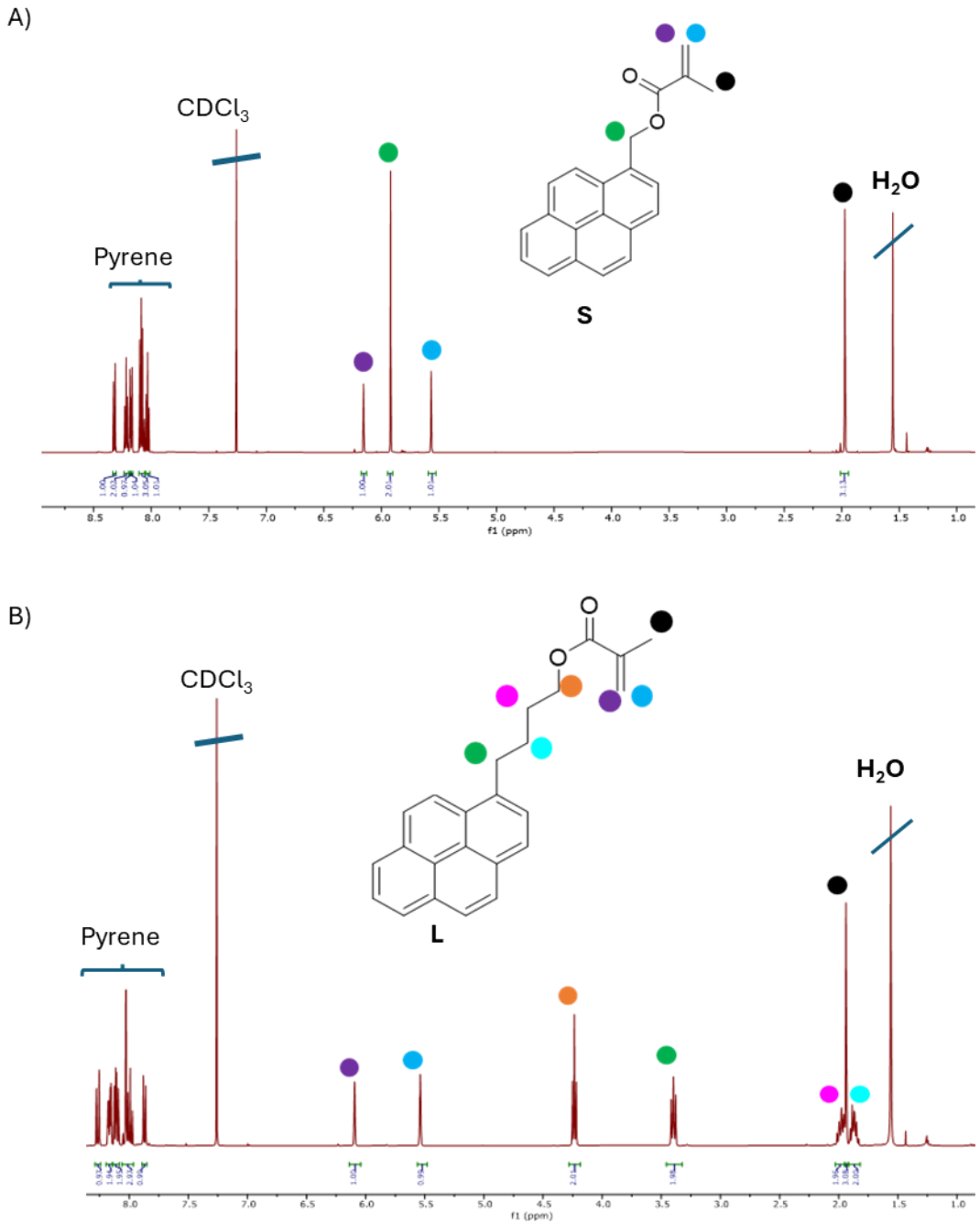

Figure 15. ^{1}H-NMR spectra ($CDCl_3$, 25°C, 400MHz) of A) comonomer **S** and B) comonomer **L**.

The two ^{1}H NMR spectra show all the diagnostic signals belonging to the target molecules, especially the signals of the methacrylate functionality (purple, blue and black spots).
Once obtained the two comonomers, four different copolymers have been synthesized, using different ratios between methyl-methacrylate (MM) and pyrene-comonomer.
The synthesized materials are summarized in Table 1:

Entry[a]	**Comonomer**	**Comonomer mol%**[b]
S4	S	4
S2	S	2
L4	L	4
L2	L	2

Table 1. [a]List of synthesized pyrene-modified poly-methyl methacrylate copolymers; [b] Molar percentage of pyrene-comonomer in the final material calculated by ^{1}H-NMR spectroscopy.

The synthesized polymers were characterized using ^{1}H-NMR spectroscopy (Figure S5 and S8) to determine the ratio (in mol%) between methyl methacrylate and the pyrene-functionalized comonomer. Additionally, the ability of all materials to form nanocapsules encapsulating CVL was verified. All materials demonstrated the capacity to form nanocapsules, which were further characterized using dynamic light scattering (DLS) (Table 2), scanning electron microscopy (SEM) (Figure 16), and transmission electron microscopy (TEM) (Figure 17).

Polymer	**PMMA**	**S4**	**S2**	**L4**	**L2**
Average diam. (nm)	833.64	334.45	824.00	829.41	984.82
Stand. Dev.	22.21	14.85	15.20	28.93	73.45

Table 2. Average diameter calculated by DLS analysis of nanoparticles made with different polymer shells.

The DLS analysis confirms that in all cases the average dimension of the nanoparticles is in the range of the nanoscale, even though in some cases (as for **L2** particles) the dimension is at the edge between the nano and the micro-scale.

For further characterization, SEM images have been acquired to gain information regarding the nanoparticles' morphology (Figure 16).

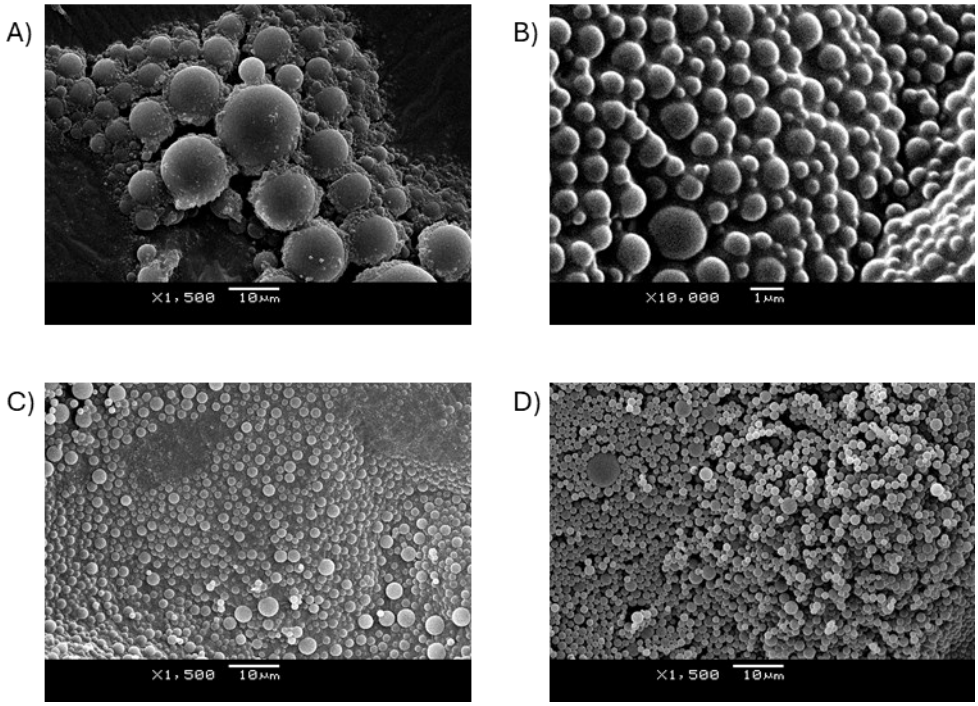

Figure 16. Scanning electron microscope (SEM) images of A) **S4**; B) **S2**; C) **L4** and D) **L2** nanoparticles.

SEM analysis confirmed the spherical shape of the nanoparticles and a wider size distribution of the nanoparticles for **S4**, **S2** and **L4** nanoparticles. **L2** turned out to be the best material for the preparation of modified nanoparticles due to the efficiency in the preparation and the narrowest dimensional distribution of the spheres.
The core-shell morphology of the nanoparticles was then confirmed by the images acquired with the transmission electron microscope (TEM) (Figure 17).

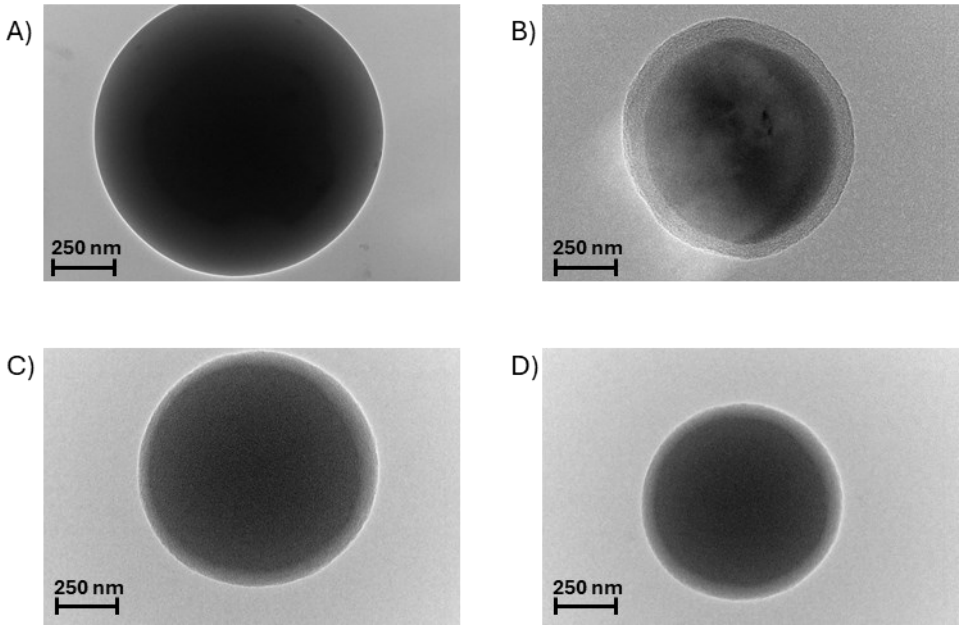

Figure 17. Transmission electron microscope (TEM) images of A) **S4**; B) **S2**; C) **L4** and D) **L2** nanoparticles.

Once confirmed the possibility of preparing core-shell nanoparticles with pyrene-modified PMMA, the following step focused on the investigation of the interaction between nanocapsules and graphene-oxide. To do so, different mixtures of nanoparticles and graphene-oxide have been prepared and analyzed by scanning electron microscopy (SEM) (Figure 18).

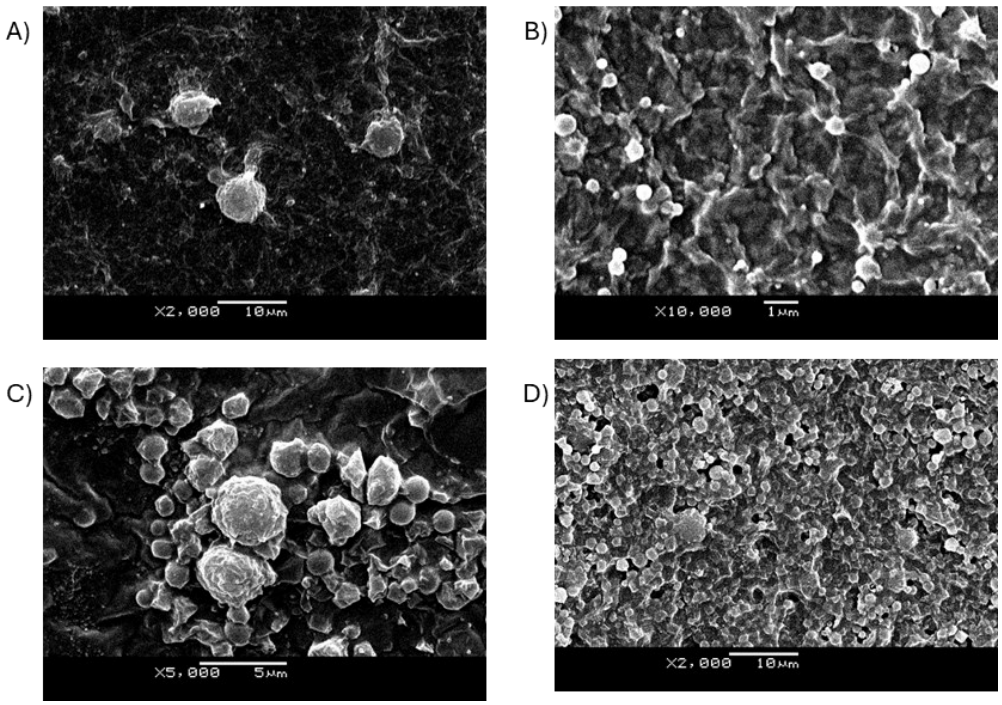

Figure 18. SEM images showing interaction between graphene-oxide and A) **S4**; B) **S2**; C) **L4** and D) **L2** pyrene-modified nanoparticles.

The acquired images unequivocally demonstrated the interaction between nanocapsules and graphene oxide, revealing the nanoparticles completely enveloped by graphene oxide sheets. This phenomenon is particularly evident when comparing the SEM images of the pristine nanocapsules (Figure 16) with those of the nanocapsule-graphene oxide mixture (Figure 18). Figures 18a and 18c reveal that, following the preparation of the nanocapsule-graphene mixture, the particle surface appears less smooth and loses some of its spherical regularity, exhibiting a seemingly rougher texture. This can be attributed to the interaction of the particles with the graphene oxide sheets, which, through interactions with the outwardly oriented pyrene units on the capsule, anchor onto the nanocapsule, resulting in a less regular surface.

Having confirmed the nanoparticle-graphene oxide interaction, modified nanocapsules and GO were dispersed within the polymer matrix to assess whether increased proximity could enhance self-reporting properties.

A new specimen was prepared following the previously reported method, involving the initial preparation of a mixture containing this time pyrene-modified nanocapsules and graphene oxide, to which the two components of the epoxy resin (DGEBA and hardener) were subsequently added. The material was then allowed to crosslink and cure for 18 hours at 40°C. Upon completion of the preparation process, the material was subjected to both impact and scratch mechanical stress. Theoretically, if the desired spatial proximity between the nanocapsules and graphene oxide within the solid state has been achieved, a more

pronounced activation of CVL should be observed following mechanical stress, as the interaction between the fluorophore and the acidic groups of the graphene would be favored. Despite the material's continued self-reporting capabilities, no significant improvements in CVL activation were observed. This suggests that the interaction may be insufficiently robust to persist during specimen preparation.

3.5 Three component system in dynamic polymer matrix

Having demonstrated the possibility of creating a three-component self-diagnostic system within an epoxy resin-based model matrix, it is particularly intriguing to explore the adaptation of this system to a polymeric matrix exhibiting similar mechanical properties, in terms of elasticity and rigidity, but incorporating a dynamic covalent crosslinking network. This approach would enable localized fracture repair after damage detection, extending the material's useful lifespan. While a reprocessable matrix offers the advantage of a longer material lifecycle, it is important to note that damage detection by individual nanocapsules is a one-time event, as the fluorescent probe function is compromised upon capsule rupture. CVL encapsulated in unmodified PMMA nanocapsules and GO were incorporated as an additive within a covalent adaptable network epoxy-based matrix. As in the previous case, the epoxy component consisted of DGEBA, while the primary diamine used as a hardener was 4,4'-dithionaline, featuring a reversible covalent disulfide bond connecting the two aromatic rings. This reversible disulfide bond is known for its ability to undergo reversible cleavage and reformation, enabling material reprocessability (Figure 19).[8]

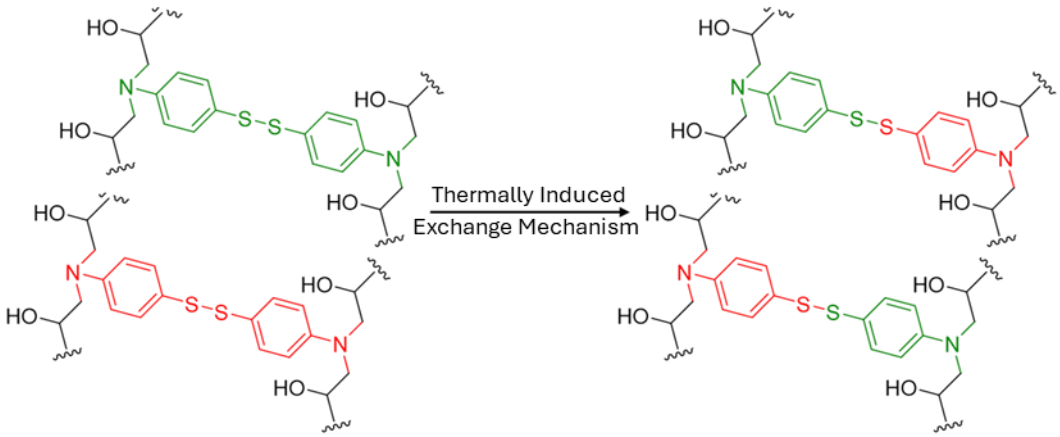

Figure 19. Exchange mechanism of the covalent adaptable network based on break up and reformation of a disulfide bond.[7]

As in the case of the epoxy-based polymetric matrix used model, also here the crosslinking reaction can be conducted without the use of solvents, that could potentially compromise the integrity of the nanocapsules' shell, as both DGEBA and the dianiline hardener are miscible liquids when heated at 80°C.

To prepare the specimen, PMMA nanocapsules containing CVL and graphene oxide were homogeneously dispersed into DGEBA, and then the hardener was added. The mixture was heated to 80°C under vacuum to ensure a homogeneous distribution of the components and to remove air bubbles introduced during mixing. The hot mixture was then poured into a dogbone Teflon mould and cured at 150°C for 120 minutes, followed by an additional curing cycle at 120°C for 150 minutes. After the resin had fully cured, the specimen was removed from the mould, and the integrity of the nanocapsules within the polymer matrix was assessed under a fluorescence lamp. No activation of CVL was observed, indicating the nanocapsules maintained their integrity throughout the material preparation process.

To evaluate the self-reporting properties of the material, the sample was subjected to mechanical stress via scratching testing, and the activation of the dye within the new matrix was verified under a fluorescence lamp. The specimen revealed different fluorescent zones in correspondence of the scratching sites, indicating the breakage of the nanocapsules and the consequent release and activation of the dye by the GO. Upon detecting the mechanical damage, thermal treatment of the specimen at 150°C for 10 minutes resulted in the complete quenching of the dye (Figure 20).

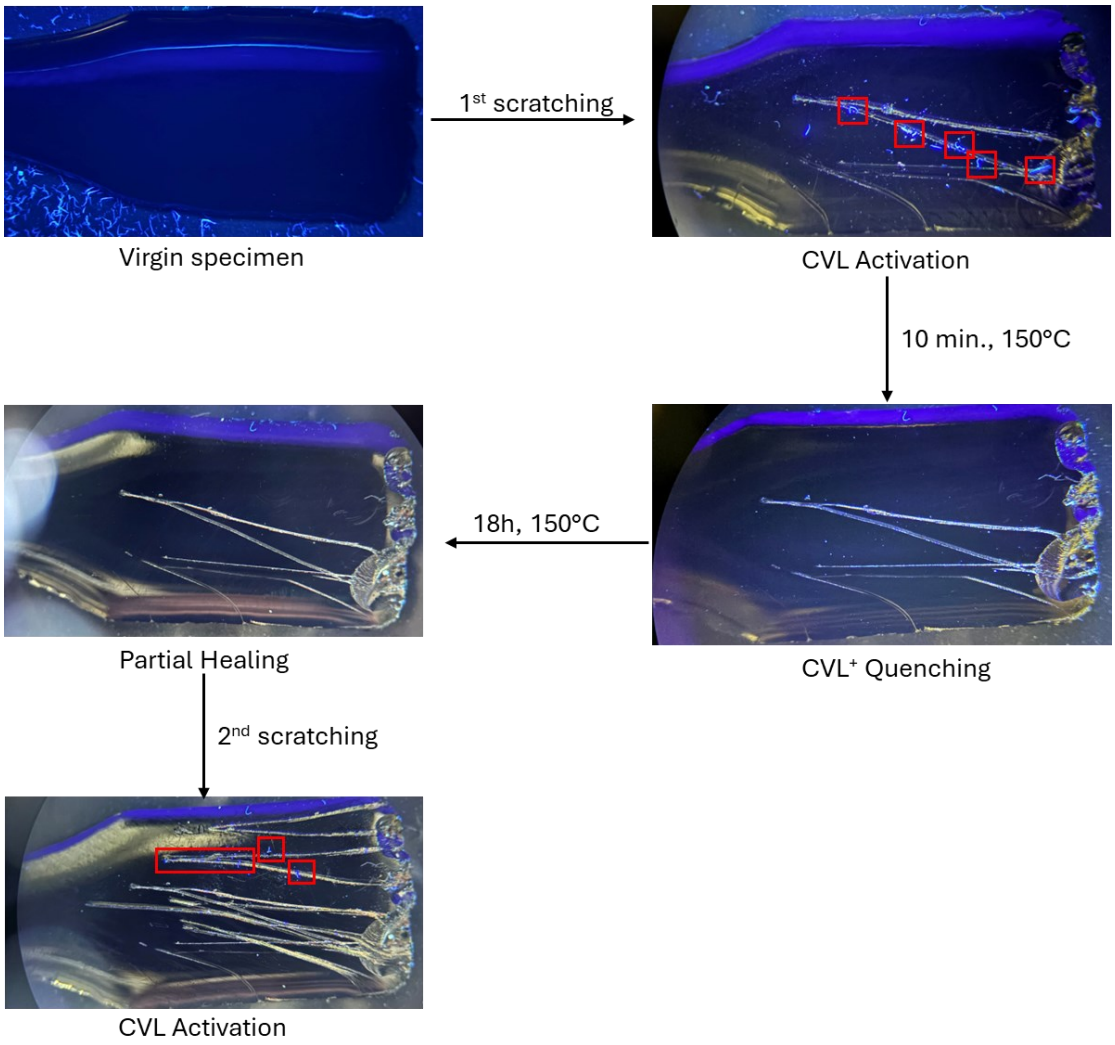

Figure 20. CVL activation (highlighted in red squares), CVL quenching, partial material healing and CVL reactivation process in a covalent adaptable network matrix.

Following CVL quenching, the material underwent a thermal treatment at 150°C for 18 hours to initiate the healing process. However, the material exhibited partial repair, as the initial scratches remained visible.

To assess the material retained self-diagnostic properties, an undamaged area of the healed material was subjected to mechanical stress. After the scratching, small fluorescent areas, caused by the activation of the CVL, were observed. This demonstrates that, although with lower performances with respect of the virgin specimen, the material was still able to retain its self-diagnostic properties even after undergoing healing.

In the future, further studies will be conducted to optimize the healing conditions to enable full damage repair and achieve stress detection performance comparable to that of the virgin material.

4. Conclusion

A three-component self-diagnostic system was developed utilizing core-shell nanoparticles containing CVL as a thermochromic dye. Various fabrication methods for the core-shell nanoparticles were investigated, and the most reproducible approach was selected. Graphene oxide was identified as the carbon nanostructure exhibiting the most effective interaction with CVL and was subsequently incorporated into the three-component system using an epoxy resin matrix as model. The nanocapsules demonstrated their ability to withstand the conditions required for epoxy resin production while maintaining the desired self-diagnostic properties in response to both scratching and impact mechanical stresses.

The self-reporting capability of the material was confirmed using both a fluorescence lamp and a two-photon microscope. The two-photon microscopy also estimated the timeframe available for damage identification before spontaneous fluorophore emission quenching occurred. Control experiments involving the epoxy-matrix without the self-reporting additive, individual components, and the three-component system prior to mechanical stress further validated the system's effectiveness, as none exhibited the fluorophore emission observed post-stress.

While NIR radiation-induced quenching was unsuccessful, thermal treatment effectively reverted CVL^+ to its closed, non-coloured form. To enhance the spatial proximity between nanoparticles and graphene oxide within the sample for fluorophore quenching via local heating, various core-shell nanoparticles were prepared using different synthetic copolymers functionalized with pyrene pendants to facilitate supramolecular interaction with graphene oxide. This interaction was further confirmed through SEM imaging, which revealed that the nanocapsules were completely covered by the carbon nanostructure.

Self-diagnostic systems were successfully constructed using the modified nanoparticles; however no significant improvement in fluorophore activation was observed. Finally, the functionality of the three-component system within a dynamic covalent network matrix was demonstrated. The material also showed partial self-healing capabilities, retaining some of its self-diagnostic properties

Future research will focus on optimizing the material's self-reporting properties.

5. Experimental

Nanocapsules synthetic method 1

Three different solutions are prepared:

1. 33mg of CVL into 310µL of phenylacetate
2. 102.1mg of PMMA into 1.1mL of $CHCl_3$
3. 88mg of Tween-80 in 6.7mL of distilled water.

Solutions **1** and **2** were poured into solution **3** and the obtained mixture was vigorously mixed with the vortex for 30 seconds, then the obtained mixture was poured into a 25mL beaker and heated to 40°C for 2 hours under mechanical stirring to evaporate the chloroform. Then, the white-milky mixture was sonicated with the immersive sonicator for 3 minutes (pulse 30/10; amplitude 30%) and then the mixture was centrifuged 2 times (9000 rpm, t = 10min).

Nanocapsules synthetic method 2

Three different solutions are prepared:

1. 33mg of CVL into 310µL of phenylacetate
2. 102.1mg of PMMA into 1.1mL of $CHCl_3$
3. 88mg of Tween-80 in 6.7mL of distilled water.

Solutions **1** and **2** were poured into solution **3** and the system was sonicated with the immersive sonicator for 3 minutes (pulse 30/10, amplitude 30%), then the white-milky suspension obtained was poured into a 25mL beaker and heated to 40°C under mechanical stirring for 2 hours to evaporate the chloroform. Then the capsules have been separated by centrifuge (2 times, t = 10min, 9000 rpm). The obtained nanocapsules have been characterized by DLS, scanning electron microscopy (SEM) (Figure 7) and transmission electron microscope (TEM) (Figure 8).

General procedure for epoxy resin sample preparation

For the preparation of the epoxy resin sample, 1.33g of bisphenol A diglycidyl ether (DGEBA), the epoxy component, were mixed with 260 mg of hardener (3,6-dioxaoctamethylenediamine). The resulting mixture was poured into a dogbone mould and placed under high vacuum to eliminate any air bubbles introduced during the mixing process. Finally, the mould was transferred to an oven and cured at 40°C for 18 hours to allow complete resin hardening.

In the preparation of the other samples containing GO (0.3% in weight) or PMMA nanocapsules (0.8% in weight), or both, the preparation method and the quantities are maintained, but in those cases, the fillers are previously mixed with the epoxy component and only after the hardener is added.

Two-photon Microscope images of Epoxy Resin

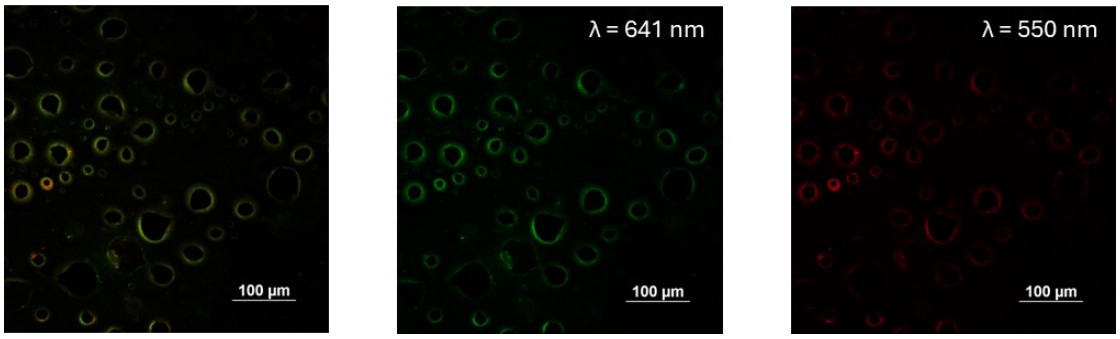

Figure S1. Two-photon microscope images of the epoxy resin matrix. The image on the left is the overlapping of 4 detectors (λ = 732, 641, 550 and 450 nm), central image was acquired with the detector set at λ = 641 nm, image on the right was acquired with the λ = 550 nm detector.

The images acquired of the blank epoxy resin demonstrated that the matrix is transparent in the spectral window for CVL detection.

Two-photon Microscope images of Epoxy Resin and Graphene-oxide

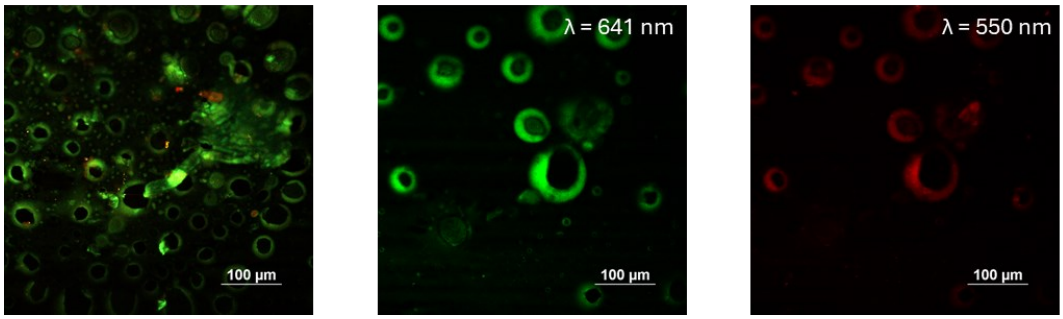

Figure S2. Two-photon microscope images of the epoxy resin matrix containing dispersed graphene-oxide. Image on the left is the overlapping of 4 detectors (λ = 732, 641, 550 and 450 nm), central image was acquired with the detector set at λ = 641 nm, image on the right was acquired with the λ = 550 nm detector.

The images acquired with the microscope demonstrate that the graphene-oxide is not responsible of the emission seen in the active sample broken by impact and by scratching.

Two-photon Microscope images of three-component system before mechanical solicitation

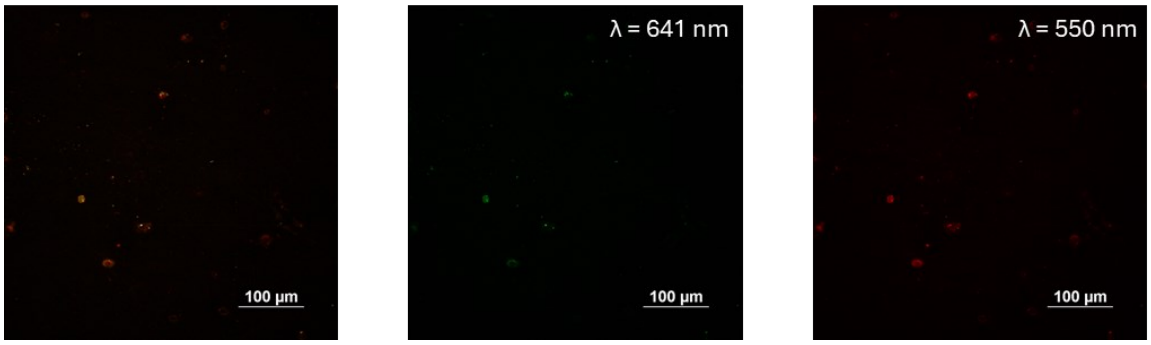

Figure S3. Two-photon microscope images of the epoxy resin matrix containing dispersed PMMA nanocapsules incorporating CVL. The image on the left is the overlapping of 4 detectors (λ = 732, 641, 550 and 450 nm), central image was acquired with the detector set at λ = 641 nm, image on the right was acquired with the λ = 550 nm detector.

The images acquired with the two-photon microscope of the epoxy resin containing dispersed PMMA nanoparticles incorporating CVL show a complete absence of emission traces. This indicates that, although some of the capsules may break during the specimen preparation, the content remains as colourless CVL, which does not emit. Additionally, the absence of graphene-oxide prevents the conversion of CVL to CVL^{+}.

Two-photon Microscope images of three-component system before mechanical solicitation

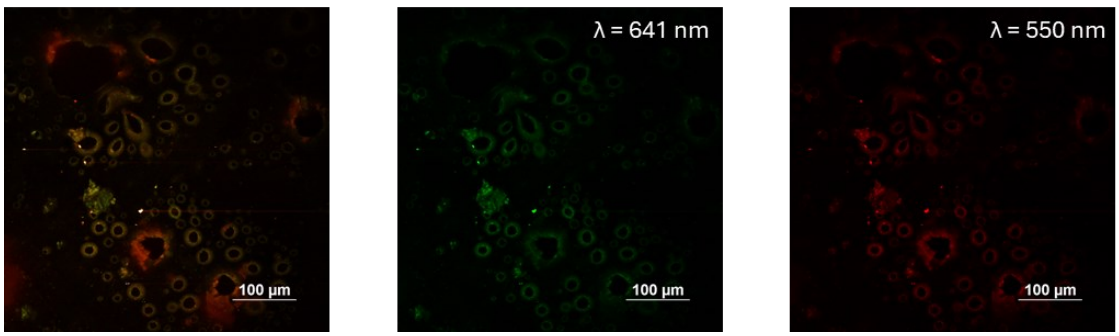

Figure S4. Two-photon microscope images of the epoxy resin matrix containing dispersed graphene-oxide and nanocapsules containing CVL. The image on the left is the overlapping of 4 detectors (λ = 732, 641, 550 and 450 nm), central image was acquired with the detector set at λ = 641 nm, image on the right was acquired with the λ = 550 nm detector.

The acquired images of the three-component specimen before mechanical solicitations demonstrated that nanocapsules resist the sample preparation. Thus, the emission observed

upon the application of a mechanical stress belongs to the CVL diffusing outside the capsules converted to CVL^+ by the graphene-oxide see main text (Figures 12-13).

Synthesis of monomer S

The preparation of monomer **S** was performed adapting a literature procedure.[9]
Methacryloyl chloride (117mg, 1.12 mmol, 1.3 eq.) is slowly added to a solution of 1-pyrene methanol (200 mg, 0.861 mmol, 1 eq.) and triethylamine (174 mg, 1.72 mmol, 2 eq.) in dry THF (10mL) at 0 °C. The reaction is then stirred at room temperature for 16 hours and monitored by TLC. When the complete disappearance of the limiting reagent was observed, the solvent was removed under vacuum, then the crude was dissolved in dichloromethane and washed with water (3x50mL). The crude product was purified by flash chromatography using hexane/ethyl acetate (98:2) as eluent, affording 253 mg of the desired product as white solid, in 98% yield. The product was carachterized by ^{1}H-NMR spectroscopy in $CDCl_3$.
^{1}H-NMR ($CDCl_3$, 400 MHz): δ (ppm) = 8.32 (d, 1H, J = 8Hz, Ar**H**), 8.22 (t, 2H, J = 4Hz, Ar**H**), 8.18 (d, 2H, J = 1.4Hz, Ar**H**), 8.17 (d, 2H, J = 1.4 Hz, Ar**H**), 8.09 (m, 3H, Ar**H**), 8.03 (m, 1H, Ar**H**), 6.15 (m, 1H, C=C**H**), 5.92 (s, 2H, OCOC**H$_2$**), 5.57 (m, 1H, C=C**H**), 1.97 (s, 3H, C**H$_3$**).

ESI-MS: m/z calculated for $C_{21}H_{16}NaO_2$ $[M+Na]^+$ = 323.10, experimental for $C_{21}H_{16}NaO_2$ $[M+Na]^+$ = 323.23.

Synthesis of monomer L

For the preparation of monomer L, a synthetic procedure was adapted from literature.[10]
Methacryloyl chloride (83.2 mg, 0.80 mmol, 1.1 eq.) is slowly added to a solution of 1-pyrene butanol (200 mg, 0.72 mmol, 1 eq.) and triethylamine (147 mg, 1.46 mmol, 2 eq.) in dry THF (10mL) at 0 °C. The reaction was stirred at room temperature for 16 hours and monitored by TLC. When the complete disappearance of the limiting reagent was observed, the solvent was removed under vacuum. The crude was dissolved in dichloromethane and washed with water (3x50mL). Purification by flash chromatography using hexane/ethyl acetate (98:2) as eluent, afforded 245 mg of the desired product as white solid, in 98% yield. The product was characterized by ^{1}H-NMR spectroscopy in $CDCl_3$.
^{1}H-NMR ($CDCl_3$, 400 MHz): δ (ppm) = 8.26 (d, 1H, J = 8Hz, Ar**H**), 8.216 (dd, 2H, J1 = 4Hz, J2 = 8Hz, Ar**H**), 8.11 (m, 2H, Ar**H**), 8.00 (m, 3H, Ar**H**), 6.08 (s, 1H, C=C**H**), 5.54 (t, 1H, C=C**H**), 4.24 (t, 2H, J = 8Hz, (C=O)OC**H$_2$**), 3.40 (t, 2H, J = 8Hz, Ar-C**H$_2$**), 1.99 (m, 2H, (C=O)OCH$_2$C**H$_2$**), 1.94 (s, 3H, C**H$_3$**), 1.86 (m, 2H, Ar-CH$_2$C**H$_2$**)

ESI-MS: m/z calculated for $C_{24}H_{22}NaO_2$ $[M+Na]^+$ = 365.15, experimental for $C_{24}H_{22}NaO_2$ $[M+Na]^+$ = 365.28.

Synthesis of S4 copolymer

Methyl methacrylate (633mg, 6.33 mmol, 19 eq.) and compound S (100mg, 0.33 mmol, 1 eq.) were dissolved in dry toluene (5mL) under nitrogen atmosphere, and the mixture was subjected to 3 freeze-pump-thaw cycles to ensure the complete oxygen removal from the reaction environment. Then., 2,2'-azobisisobutyronitrile (AIBN) (1 mol%) was added to the mixture as radical initiator, and the reaction was magnetically stirred at 80°C for 48 hours. The hot mixture was then poured into cold hexane and the obtained precipitate was filtered, washed with fresh hexane and dried under vacuum. The identity of the obtained polymer was confirmed by ^{1}H-NMR in $CDCl_3$ and the ratio between the two monomers was calculated from the integration of the signals belonging to the benzyl C**H**$_2$ of monomer S and the methyl ester O-C**H**$_3$ of methyl methacrylate. The molar ration between methyl methacrylate and monomer **S** in the final copolymer resulted to be 96:4, respectively.

^{1}H-NMR:

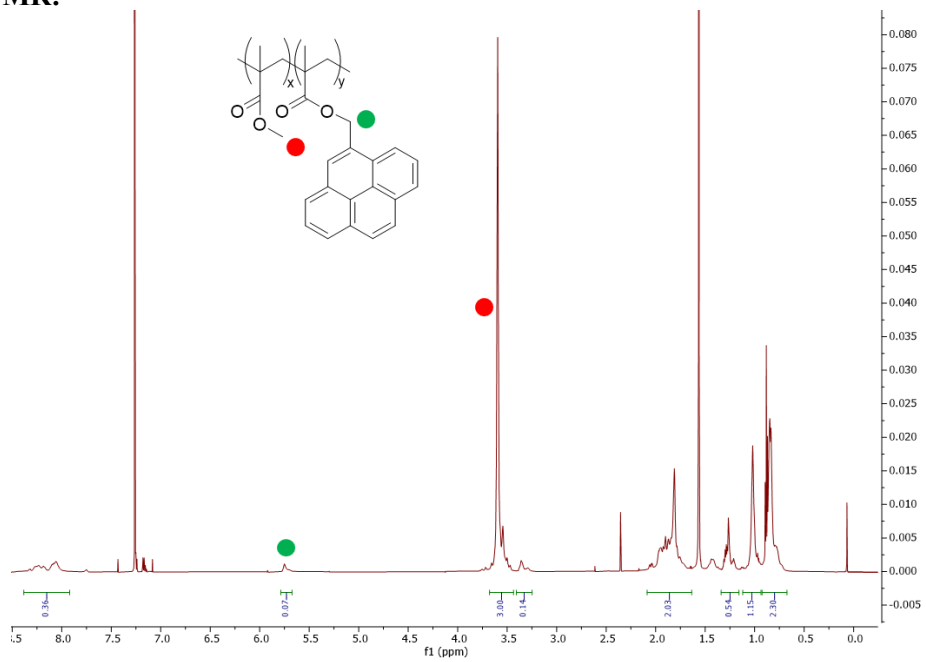

Figure S5. ^{1}H-NMR ($CDCl_3$, 25°C, 400MHz) of **S4** copolymer

The material was then analyzed using TGA to verify its thermal stability both at the operating temperature and at the thermal treatment temperatures used to quench the CVL^{+} after the damage detection (figure S).

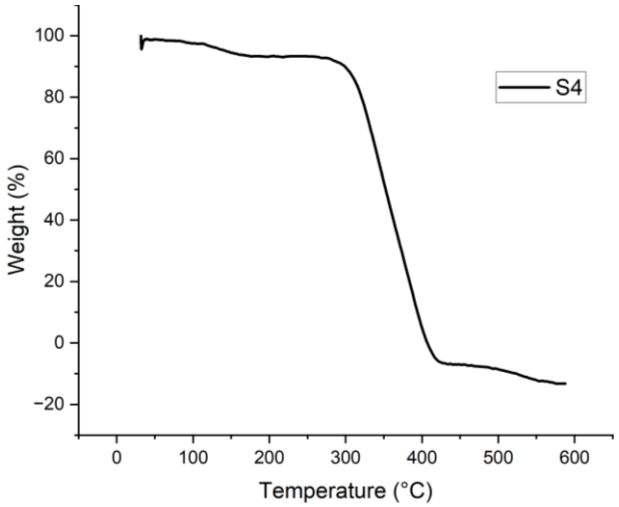

Figure S6. TGA analysis on polymer **S4**

Synthesis of S2 copolymer

A solution of methyl methacrylate (1.63 g, 16.3 mmol, 49 eq.) and compound **S** (100mg, 0.33 mmol, 1 eq.) in dry toluene (5mL) was subjected to 3 freeze-pump-thaw cycles to ensure the complete oxygen removal from the reaction environment. Then., AIBN (1 mol%) was added to the mixture as radical initiator, and the reaction was magnetically stirred at 80°C for 48 hours. The target copolymer was obtained by precipitating the hot rection mixture in cold hexane. The identity of the obtained polymer and the ration between the two monomer was checked by ^{1}H-NMR in $CDCl_3$.

The molar ratio between the two monomers was calculated from the integration of the signals belonging to the benzyl C**H₂** of monomer S and the methyl ester O-C**H₃** of methyl methacrylate.

The molar ration between methyl methacrylate and monomer **S** in the final copolymer resulted to be 98:2, respectively.

The material was then subjected to TGA analysis to verify its thermal stability both at the operating temperature and at the thermal treatment temperature (Figure S7).

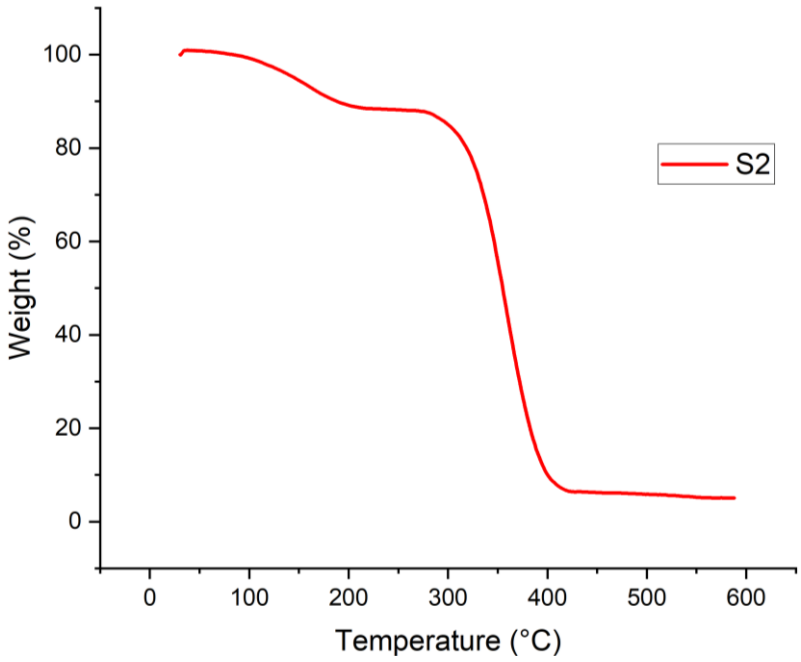

Figure S7. TGA analysis on polymer **S2**

Synthesis of L4 copolymer

Compound **L** (100mg, 0.29 mmol, 1 eq.) and methyl methacrylate (556mg, 5.55 mmol, 19 eq.) were dissolved in dry toluene (5mL) under nitrogen, and the mixture was subjected to 3 freeze-pump-thaw cycles to ensure the complete oxygen removal from the reaction environment. Once completed the third cycle, AIBN (1 mol%) was added as radical initiator. The reaction mixture was stirred at 80°C for 48 hours and then poured into cold hexane to precipitate the target polymer. The identity of the obtained polymer and the ration between the two monomer was checked by ^{1}H-NMR in $CDCl_3$.

The molar ratio between the two monomers was calculated from the integration of the signals belonging to the benzyl C**H$_2$** of monomer **L** and the methyl ester O-C**H$_3$** of methyl methacrylate.

The molar ration between methyl methacrylate and monomer **L** in the final copolymer resulted to be 96:4, respectively.

^{1}H-NMR:

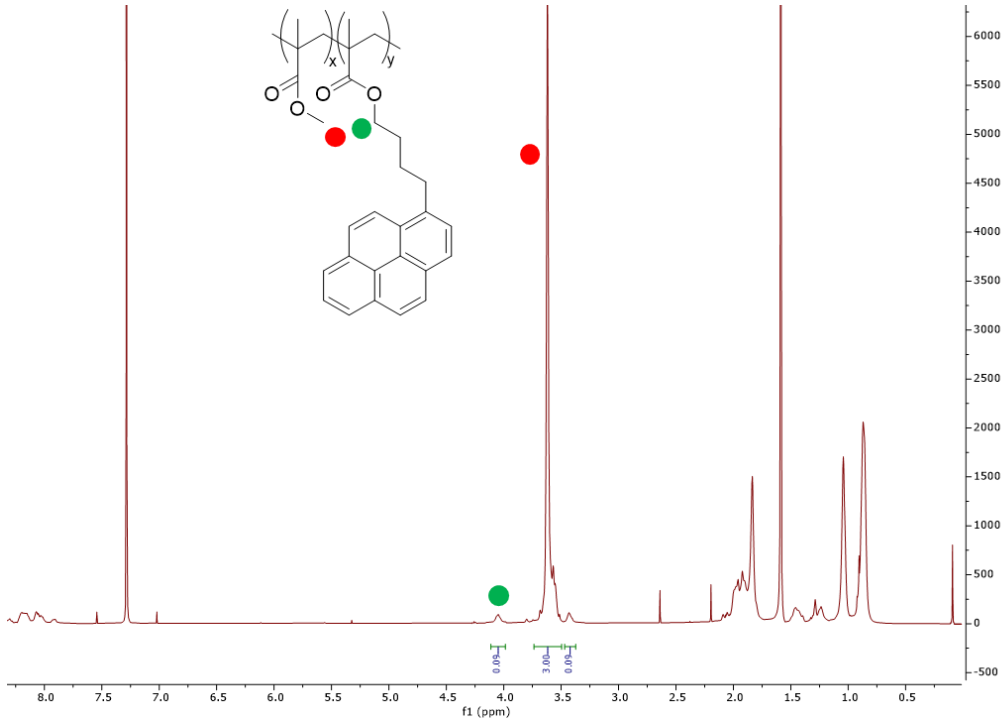

Figure S8. ^{1}H-NMR ($CDCl_3$, 25°C, 400MHz) of **L4** copolymer

The material was then analyzed using TGA to verify the thermal stability at the operating temperature and at the thermal treatment temperatures used to quench the CVL^+ after the damage detection (Figure S9).

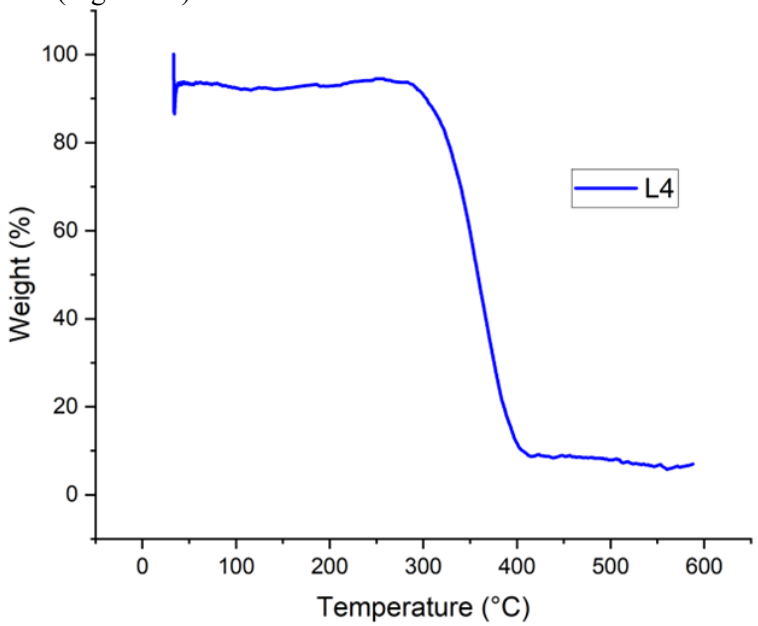

Figure S9. TGA analysis on polymer **L4**

Synthesis of L2 copolymer

A solution of methyl methacrylate (1.43 g, 14.3 mmol, 49 eq.) and compound **L** (100mg, 0.29 mmol, 1 eq.) in dry toluene (5mL) was subjected to 3 freeze-pump-thaw cycles to ensure the complete oxygen removal from the reaction environment. Then., AIBN (1 mol%) was added to the mixture as radical initiator, and the reaction was magnetically stirred at 80°C for 48 hours. The target copolymer was obtained by precipitating the hot rection mixture in cold hexane. The identity of the obtained polymer and the ration between the two monomer was checked by ^{1}H-NMR in $CDCl_3$.

The molar ratio between the two monomers was calculated from the integration of the signals belonging to the benzyl C**H$_2$** of monomer S and the methyl ester O-C**H$_3$** of methyl methacrylate.

The molar ration between methyl methacrylate and monomer **L** in the final copolymer resulted to be 98:2, respectively.

The thermal stability of the polymer was verified *via* TGA analysis (Figure S10).

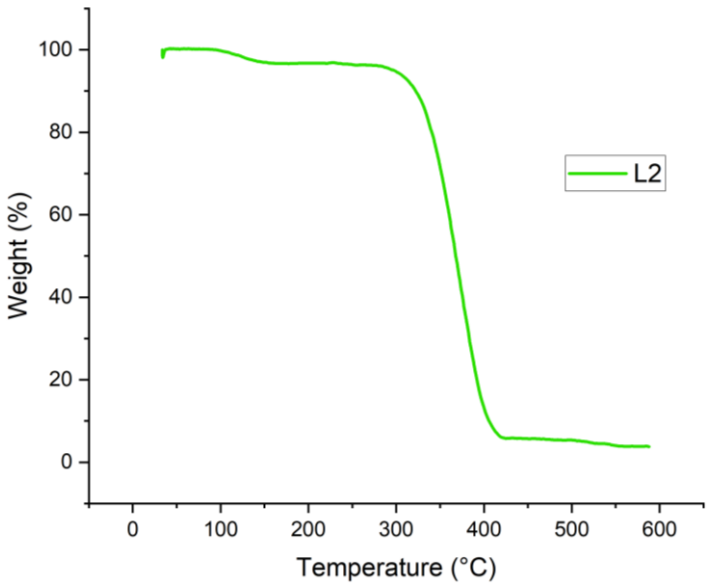

Figure S10. TGA analysis on polymer **L2**

General procedure for epoxy-based covalent adaptable network sample preparation

For the preparation of the epoxy-like covalent adaptable network matrix, 1.0 g of bisphenol A diglycidyl ether (DGEBA) was mixed at 80° with 400 mg of hardener (4,4'-ditioaniline) at 80°C. The mixture was kept at 80°C under vacuum for 10 minutes to ensure a homogeneous distribution of the components and to remove air bubbles introduced during

mixing. The hot mixture was then poured into a dogbone Teflon mould and cured at 150°C for 120 minutes, followed by an additional curing cycle at 120°C for 150 minutes.
In the preparation of the other samples containing GO (0.3% in weight) or PMMA nanocapsules (0.8% in weight), or both, the preparation method and the quantities are maintained, but in those cases, the fillers are previously mixed with the epoxy component and only after the hardener is added.

6. References

[1] C.F. Zhu, A.B. Wu, *Thermochimica Acta*, **2005**, 425, 7-12.
[2] S. M. Burkinshaw, J. Griffiths and A. D. Towns, *J. Mater. Chem.*, **1998**, 8, 2677–2683
[3] M Hu. et al., *Mater. Horiz.*, **2018**, 5, 51-58.
[4] P. Yan, W. Zhao, L. J. Jiang, B. Wu, K. Hu, Y. Yuan, J. Lei, *J. Appl. Polym. Sci.*, **2018**, 45748.
[5] Y. Yang, Z. Pei, X. Zhang, L. Tao, Y. Wei and Y. Ji, *Chem. Sci.*, **2014**, 5, 3486-3492.
[6] R. R. Kohlmeyer, M. Lor and J. Chen, *Nano Lett.*, **2012**, 12, 2757-2762.
[7] V. Georgakilas et al., Chem. Rev., **2016**, 116, 5464-5519.
[8] I. Azcune, A. Huegun, A.R. de Luzuriaga, E. Saiz, A. Rekondo, *Eur. Pol. Jour.*, **2021**, 148, 110362.
[9] Y. Jungmok, K. Eunkyoung, *J. of Nanosc. and Nanotech.*, **2016**, 16, 10927-10934.
[10] R. D. Martinez-Serrano, F. Cuétara-Guadarrama, M. Vonlanthen, J. Illescas, X. X. Zhu, E. Rivera, Polymers, **2023**, 15, 1687-1700.

Chapter 3

Dynamically cross-linked polyethylene with reversible self-reporting properties

Abstract

A powerful new strategy to produce reprocessable cross-linked polymers is the functionalization of the polymer matrix with cross-links able to reverse or exchange at elevated temperatures. These covalent adaptable networks (CANs) are able to shuffle chemical bonds through exchange reactions at high temperature, allowing for material reprocessing. Here, we present the preparation of self-diagnostic covalent adaptable network designed with the aim to detect in a non-destructive way early-stage damage introducing inside the polymer matrix a suitable probe. The probe has been used as cross-linker: the activation of the mechanophore off/on process allows for the identification of the microfracture, while dynamic nature of the vitrimers allows for the repairing of the damage by local heating.

TOC: Mechanophore activation upon mechanical solicitation and its reversibility by thermal treatment.

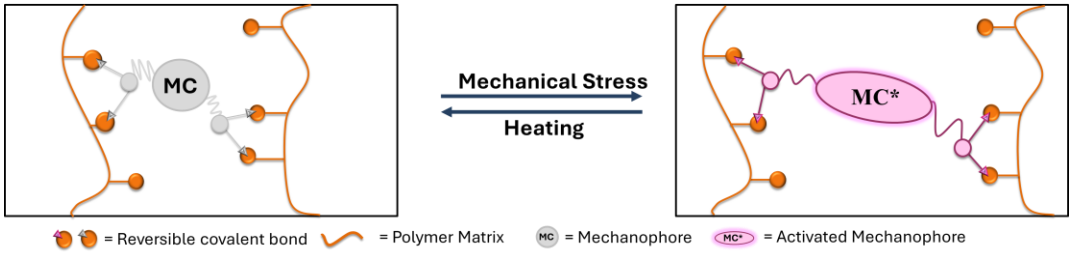

The content of this chapter was partially adapted from: Alessandro Torri, Chiara Paravidino, Gabriele Giovanardi, Francesco Rispoli, Fabrizio Moroni, Alessandro Pedrini, Alberto Fina, Enrico Dalcanale, and Roberta Pinalli*. *Submitted Manuscript*.

1. Introduction

As described by the Ellen MacArthur Foundation, the second principle of the circular economy emphasizes the importance of circulating products and materials at their highest value, ensuring that nothing becomes waste, and retaining the intrinsic value of materials throughout their lifecycle.[1] This principle advocates for the continual use of materials, either as products or, when no longer usable, as components or raw materials, with the most effective strategy being the maintenance and reuse of products. Thermosetting materials present unique challenges in this context. Traditional recycling methods for thermosets involve either mechanical recycling[2, 3] resulting in fillers or denser materials, thermal recycling[2, 4], or chemical recycling into other compounds.[2, 5-10] These methods, however, have significant drawbacks, including poor quality of mechanically recycled products, high energy consumption thus high CO_2 footprint, and complexity of purification required for chemical recycling. In response to these limitations, the concept of covalent adaptable networks (CANs) was introduced in 2010.[11] Unlike conventional thermosets, CANs can be reshaped or repaired under external stimuli such as heat and light due to the presence of reversible or exchangeable bonds.[12, 13] CANs are categorized into associative and dissociative types based on their dynamic chemistry.[14] Associative CANs maintain a constant cross-link density over varying processing temperatures through simultaneous bond-breaking and bond- reforming processes. In contrast, dissociative CANs, which include dynamic chemistries like Diels-Alder reactions, undergo these processes consecutively. Considering the associative CANs, the implementation of various dynamic chemistries, including transesterification[15-17], disulfides[18-21], silylethers[22-24] and vinylogous urethanes[25-27], offers promising solutions for sustainable material lifecycles.

In line with the circular economy principles, it is crucial not only to recycle thermosets, but also to maintain them in service for as long as possible to maximize their value and sustainability. Therefore, effective methods for detecting fractures and other forms of damage are required to extend the lifetime of polymeric materials.

Mechanochromic probes change their UV-vis absorption spectrum upon mechanical activation. Typically, this change in absorption is due to the change of conjugation in the molecule structure, resulting in a red shift of the absorption maximum. This color change provides a visible signal for localized stress, strain, or damage in polymeric materials. A wide range of mechanochromic moieties has been used as mechanophores in polymeric materials[28], with the first example reported by Moore and Sottos in 2009[29], when they proposed the use of a spiropyrane as reporting unit in both elastomeric and glassy polymers. The suitability of each mechanophore as a force reporter in various polymer materials is determined by their chemical stability, synthetic accessibility, mechanical activation parameters, and changes in absorption spectrum.

Rhodamine is a well-known fluorescent dye used extensively in biochemistry thanks to its excellent optical properties, including good stability, high absorption coefficient, and quantum efficiency, as well as long-wavelength absorption and emission. A unique feature

of rhodamine derivatives is their isomerization-induced color switch from a twisted structure to a planarized zwitterion, which significantly red-shifts the absorption band and activates fluorescence emission. The reversibility of the isomerization is favoured by UV light or heat. Despite these promising characteristics, the application of rhodamine as mechanophores for creating functional materials is limited. The first example was reported in 2015[30], when a spirorhodamine derivative was incorporated into an elastomeric polyurethane matrix, exhibiting reversible mechanochromism and photochromism. More recently, a spirorhodamine derivative was embedded in a polymer matrix as cross-linking unit: the resulting acrylate elastomer displayed reversible fluorescent emission upon mechanical activation.[31]

In this work, we introduced a new class of polyethylene (PE)-based CAN featuring both reversible self-reporting and reprocessability properties. Both features have been obtained by reacting polyethylene co-polymerized with hydroxyethyl methacrylate (PE-HEMA) with rhodamine derivative 3 which acts at the same time as fluorescent damage reporter and as dynamic crosslinker (Figure 1) via silylether exchange reactions.[24] Both reprocessability and restoration of the fluorescence damage detection are thermally triggered. In this way both features are fully restored with a single thermal annealing of the reprocessed polymer. Integrating such damage detection technologies into thermosetting materials not only extends their lifespan but also reduces the overall environmental impact, aligning with the principles of the circular economy.

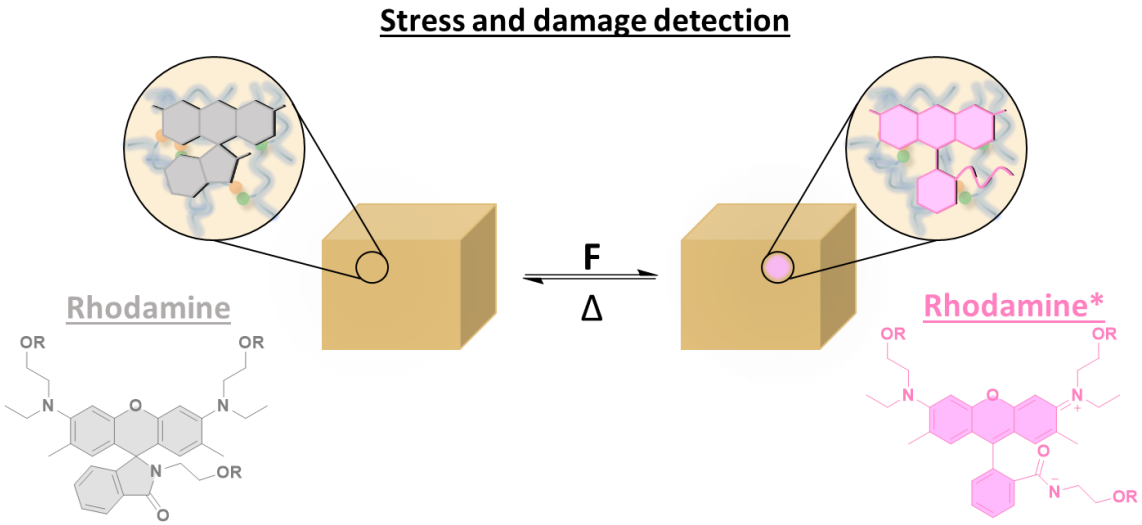

Figure 1. Schematic representation of rhodamine probe for stress detection and its reversibility

2. Results and Discussion

2.1 Synthesis of rhodamine 3

Rhodamine **3** was decorated with three -Si(OMe)$_3$ moieties suitable to act as reactive group in the crosslinking reaction with a hydroxyl functionality present on the linear polymer. An alkyl spacer was introduced between the reactive -Si(OMe)$_3$ moieties and the rhodamine core in order to reduce steric hindrance on the reactive functionalities during the crosslinking reaction, thus increasing the reactivity of the crosslinker. Rhodamine **3** was synthesised following a linear synthetic pathway (**Scheme 1**), which comprises: i) lactamization of commercial rhodamine **6G** (**Rh-6G**); ii) alkylation of the secondary amines on the xanthene scaffold to introduce tertiary amines (**2**); iii) functionalization of the three hydroxyl functionalities of rhodamine **2** to graft the desired -Si(OMe)$_3$ functionalities. The lactamization reaction was performed by refluxing commercially available rhodamine **6G** with an excess of ethanolamine in acetonitrile, following a literature procedure.[31] The subsequent alkylation of compound **1** to introduce an ethyl chain as spacer was carried out using 2-bromoethanol as both the alkylating agent and the solvent. K_2CO_3 was included as scavenger for HBr, which is formed during the alkylation process.[31] Finally, the desired silyl ether groups were introduced through an addition reaction between compound **2** and commercially available (3-isocyanatopropyl)trimethoxysilane, using dibutyltin dilaurate (DBTL) as catalyst. The final rhodamine **3** was recovered in quantitative yield upon washing the crude product with hexane. Rhodamine **3** was characterized by ^{1}H and ^{13}C-NMR spectroscopy (**Figures S3-S7**) and by high resolution ESI-Mass spectrometry (**Figure S8**).

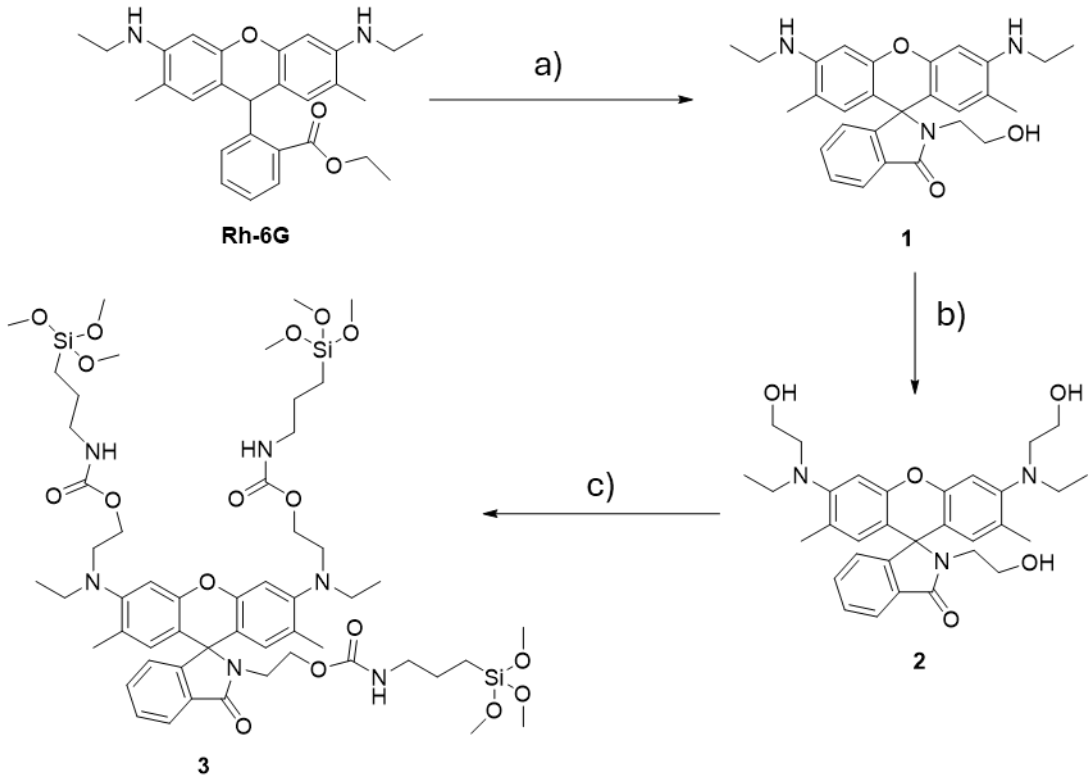

Scheme 1. Synthesis of rhodamine **3**: *a) ethanolamine, dry ACN, 80°C, 24h, 87% yield; b) 2-bromoethanol, K_2CO_3, KI, 110°C, 36h, 65% yield; c) (3-Isocyanatopropyl)trimethoxysilane, DBTL, dry DCM, 40°C, 24h, quantitative yield.*

2.2 Crosslinking of PE-HEMA with rhodamine 3

The crosslinking reaction between PE-HEMA and commercial N,N'-Bis(3-(trimethoxysilyl)propyl)ethylenediamine (TMSPEDA) (**Scheme 2a**) or rhodamine **3** (**Scheme 2b**) was conducted in solution using 1,2-dichlorobenzene as the solvent at 100°C for 24 hours. Once the viscosity of the reaction became too high to allow proper stirring, the reaction was quenched with hexane. A precipitate formed, which was filtered, washed, and dried under high vacuum at 80°C. Using this procedure, three different materials were prepared using rhodamine **3** or TMSPEDA as crosslinker to compare the mechanical properties.

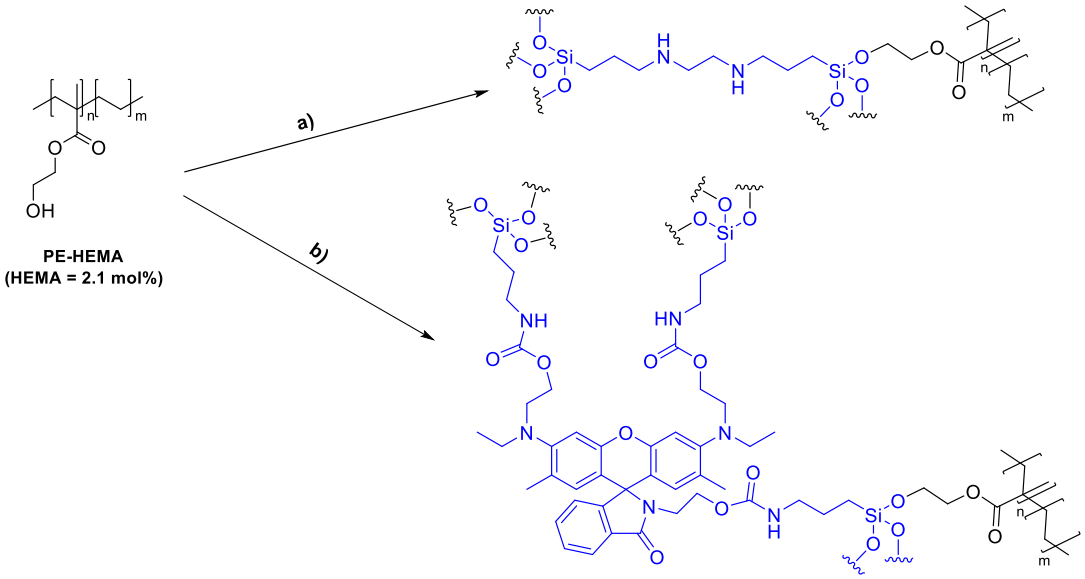

Scheme 2. Crosslinking reaction between PE-HEMA and: a) TMSPEDA; b) rhodamine **3**.

For the preparation of the self-reporting materials, all the methoxy groups present on the crosslinker were assumed to be involved in the dynamic bonds formation. This assumption, albeit unlikely, accounts for the maximum number of cross-linking connections theoretically possible. Thus, a functionality equal to 9 and 6 was considered for rhodamine **3** and TMSPEDA, respectively. The remaining free hydroxyls will enable associative dynamic exchange with the silyl ether linkages to achieve the desired dynamic function. **Table 1** summarizes the three produced materials, indicating the type of crosslinker and the corresponding percentage. XLPE**Rh-CAN** was prepared using rhodamine **3** as crosslinker. The control samples XLPE**TMSPEDA-Rhdisp** and XLPE**TMSPEDA**, were prepared using TMSPEDA as the crosslinker. In XLPE**TMSPEDA-Rhdisp**, rhodamine **1**, which lacks silyl ether exchangeable groups, was dispersed within the matrix. Since rhodamine **1** is dispersed rather than covalently attached to the polymer chain, its mechanical activation is not possible. The other control material, XLPETMSPEDA, does not contain any rhodamine. These control materials are essential for comparing the mechanical properties resulting from the use of two different crosslinkers and for demonstrating that rhodamine must be used as a crosslinker to effectively function as a self-reporting unit.

2.3 Polymers characterization

The nitrogen content in the resulting materials is diagnostic of the presence of the rhodamine and TMSPEDA respectively. Therefore, elemental analyses were performed to determine the presence of the probe and of TMSPEDA, as reported in Table 1.

Differential Scanning Calorimetry (DSC) was performed to gain further insight into the microstructure of the synthesized materials and to assess their thermal properties. Second

heating scan thermograms of all materials feature a slightly difference in the crystallinity degree respect to pristine PE-HEMA and a peak melting temperature T_m = 103 to 106-108 °C, slightly higher than reference PE-HEMA (Table 1 and Figure S9). The slight changes in the thermal properties of PE-HEMA after crosslinking suggests that both rhodamine and TMSPEDA are excluded from PE crystalline phase.

Entry	Polymer	PE-HEMA [g]	**3** [mg]	TMSPEDA [mg]	**1** [mg]	Experimental N%	G. F [%][a]	T_m[b] [°C]	X_{cr}[c] [%]
1	XLPE**Rh-CAN**	10	893	-	-	0.30	64	106.2	37
2	XLPE**TMSPEDA-Rhdisp**	10	-	444	400	0.62	72	105.2	30
3	XLPE**TMSPEDA**	10	-	444	-	0.29	69	108.3	38
4	PE-HEMA	10	-	-	-	-		102.9	34

Table 1. The amount of rhodamine **3** and TMSPEDA and the percentage of nitrogen are calculated assuming all the methoxy groups of the crosslinker can undergo to reaction with PE-HEMA hydroxyl groups. [a] Gel Fractions performed in xylene at 100°C for 18 hours. [b] Melting temperatures (T_m) were determined by DSC from the second heating scan. [c] Degrees of crystallinity and X_{cr} were calculated with respect to the melting enthalpy of 100% crystalline PE (286.2 J/g). The melting enthalpy of each formulation was determined from the DSC second heating scan.

The successful crosslinking reaction was assessed both by gel fraction calculation and dynamic mechanical thermal analysis (DMTA) measurements. To assess whether cross-linking of polymers resulted in insoluble networks, the samples were incubated in xylene for 18 hours at 100°C. This treatment led to the complete dissolution of pristine PE-HEMA polymer, while XLPE**Rh-CAN**, XLPE**TMSPEDA-Rhdisp** and XLPE**TMSPEDA** retained significant masses (Table 1), accompanied by considerable swelling rate (see SI).
DMTA was carried out to evaluate the dynamo-mechanical behaviour as a function of temperature. In particular, DMTA is used to evaluate the elastic modulus above the melting temperature, which has been previously reported for PEHEMA-TMSPEDA systems[24] as a consequence of crosslinking between the polymer chains. Storage modulus for XLPE**Rh-CAN** (Figure 2) at room temperature is at 415 MPa, which progressively decreases with increasing temperature. Across the melting, the modulus obviously drops, but the molten polymer retains a storage modulus at ca. 0.7 MPa, which is stable in temperature up to at least 180°C, confirming the covalent crosslinking of XLPE**Rh-CAN**.

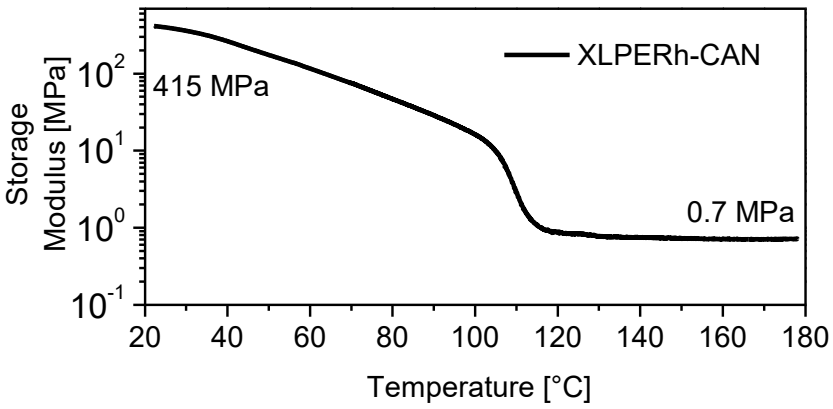

Figure 2. A) Storage Modulus vs Temperature of XLPE**Rh-CAN.**

To further investigate the viscoelastic properties at high temperature, small angle oscillary shear tests were carried out at temperature above the melting point of PE-HEMA. In particular, XLPE**Rh-CAN** was studied in comparison with the reference PE-HEMA crosslinked with TMSPEDA (XLPE**TMSPEDA**). For both XLPE**Rh-CAN** and XLPE**TMSPEDA** the elastic moduli dominate over the dissipative moduli over the whole range of frequency explored. Furthermore, G' shows a plateau at low frequency range while no Newtonian plateau is observed in viscosity, overall evidencing for a solid-like behaviour, in agreement with the crosslinked nature of these materials.

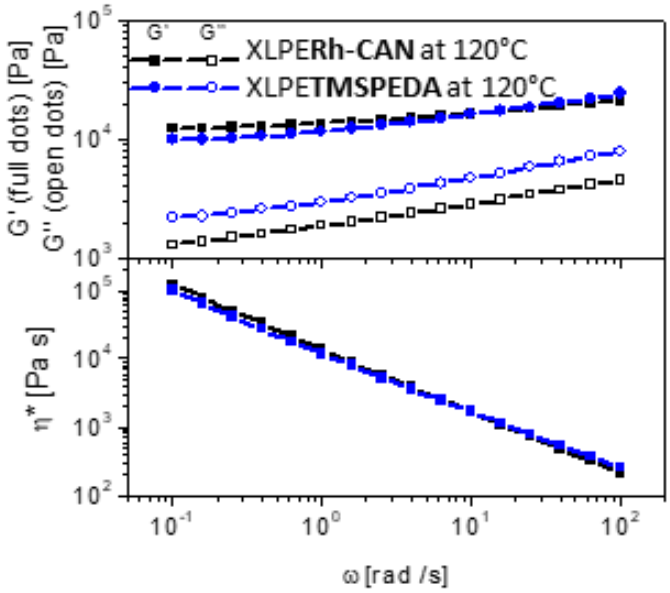

Figure 3. Small angle oscillary shear tests of XLPE**Rh-CAN** (black trace) and XLPE**TMSPEDA** (blue trace) at 120°C.

Stress-strain analyses were conducted on samples XLPE**Rh-CAN** and XLPE**TMSPEDA**, and their mechanical properties and reprocessability were analysed and compared (Figure 4). In the case of XLPE**Rh-CAN**, tests not only assessed the materials reprocessability but also evaluated its ability to maintain self-reporting properties (Figure 5). The stress-strain measurements have been performed with three replicates with a strain-rate of 250 mm/min. XLPE**Rh-CAN** was tested as synthesized (V), and reprocessed, thus it was subjected to compression moulding. Three cycles of compression moulding were performed, and the material was tested after each cycle (Reprocessing 1 (R1), 2 (R2) and 3 (R3)). The graph in figure 4B shows that as synthesized XLPE**Rh-CAN** (V, dark green bar) has a Young Modulus of 69.4 MPa, comparable to XLPE**TMSPEDA**, which remains approximately constant during the reprocessing, as well as the ultimate strength. This is consistent with the behaviour of PE-HEMA-based CANs, containing silyl-ether exchange chemistry.[24] After the reprocessing, a decrease of strain at break was instead recorded.

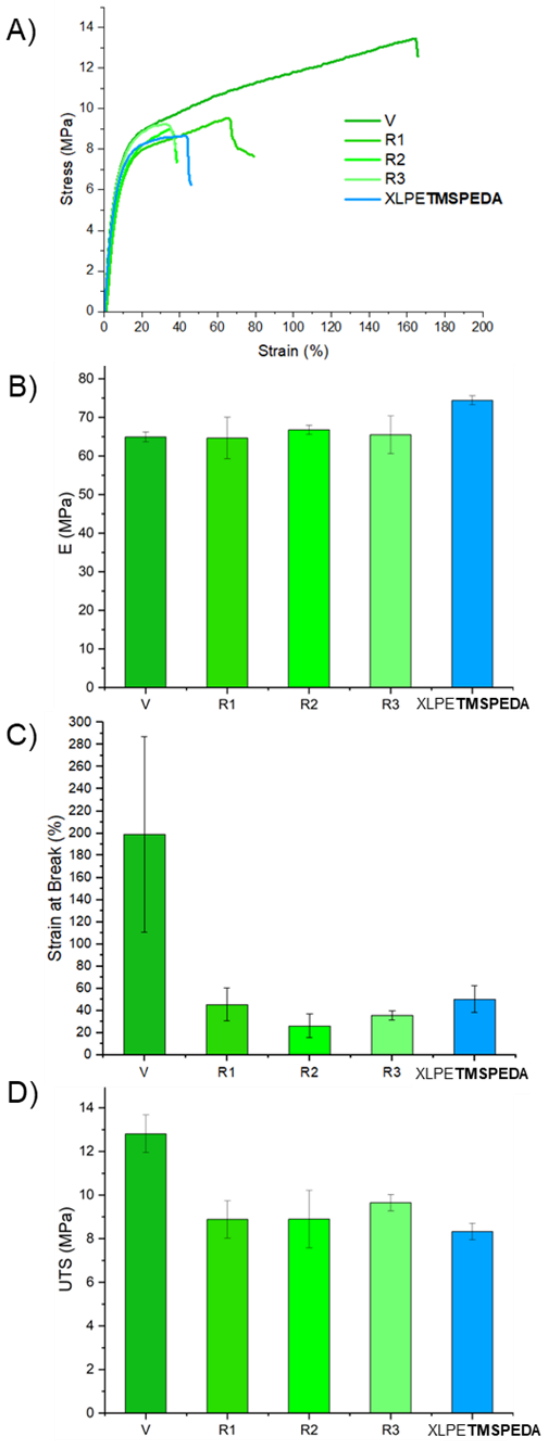

Figure 4. A) Representative stress-strain curves**,** B) Young Modulus, C) Strain at break and D) Ultimate tensile Strength of as synthesized XLPE**Rh-CAN** (V), subsequent recycling steps (R1 – R3) and XLPE**TMSPEDA**. Average of n = 3.

2.4 Self-Reporting Properties

Once the reprocessability of XLPE**Rh-CAN** was demonstrated, the self-reporting properties and their reversibility were investigated through scratching tests on a polymer film.

After the first scratch, a strong pink coloration appeared at the site (Figure 5A). When the material was heated, the mechanophore was completely quenched, and the polymer film healed. Upon re-scratching, the self-reporting properties were displayed again. This cycle of mechanophore activation, healing and quenching could be repeated several times. A control experiment was performed using XLPE**TMSPEDA-Rhdisp**, the TMSPEDA crosslinked polymer with rhodamine **1** dispersed in the polymer matrix. The scratching test revealed no traces of activation (Figure 5B). This demonstrates that the rhodamine must not only be present in the polymer matrix but also covalently linked to the polymer backbone to detect damage.

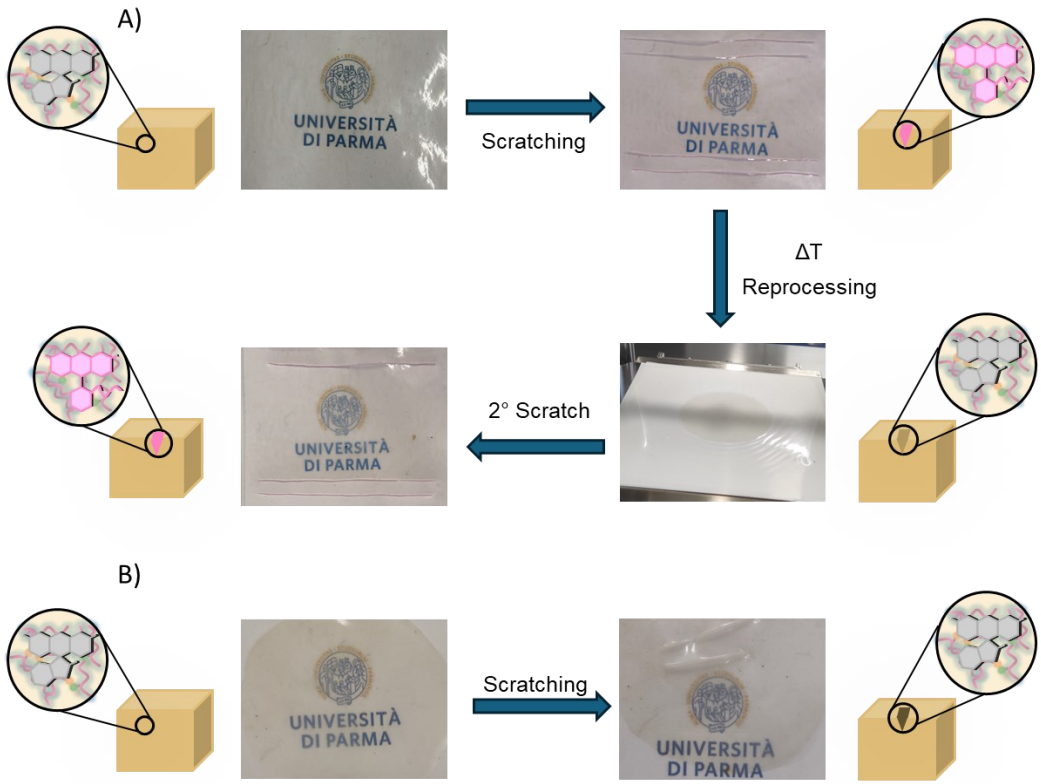

Figure 5. A) XLPE**Rh-CAN** scratching and quenching test, B) control experiment on XLPE**TMSPEDA-Rhdisp**.

The self-reporting property was also observed upon mechanical stretching and was fully restored after the thermal annealing. When virgin XLPE**Rh-CAN** was stretched, rhodamine **3** activation was observed at the necking zone, where local strains are large, becoming more evident as the specimen began to break (figure 6A). After the first reprocessing, as shown by the strain-at-break graph (Figure 4C), the material's elasticity decreased significantly. This reduction in elasticity decreased the efficiency of the self-diagnostic properties, making the mechanophore activation visible only when the specimen began to break, rather than during the stress while still intact (Figure 6B).

As before, XLPE**TMSPEDA-RHdisp** was used as reference sample. Also in this case, when the specimen was subjected to tensile stress, no color change was observed in the material (Figure 6C), demonstrating once again that the self-reporting features are present only when rhodamine is used as crosslinker in the polymer.

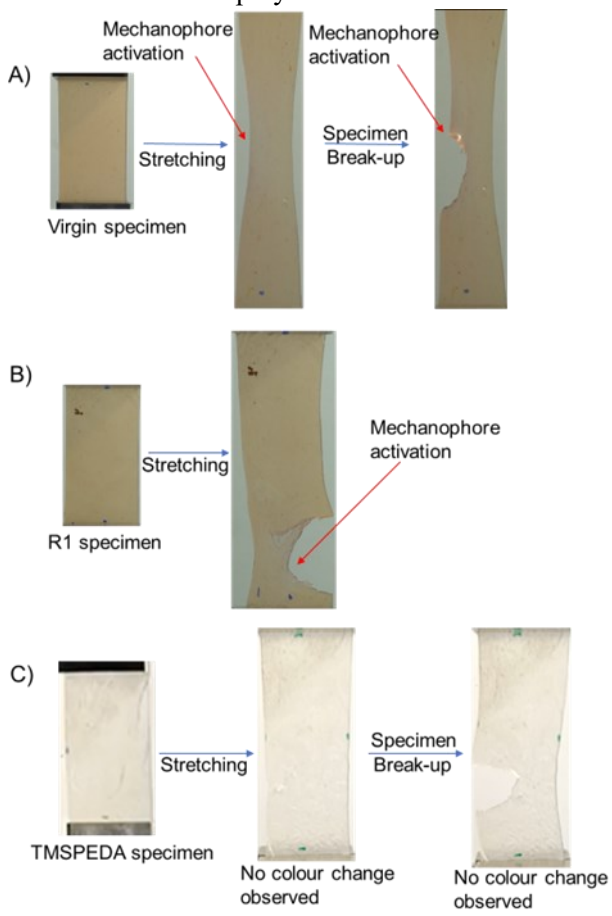

Figure 6. Self-reporting properties of A) virgin XLPE**Rh-CAN** (V), B) reprocessed XLPE**Rh-CAN** during stress-strain measurement; C) Control experiment with XLPE**TMSPEDA-Rhdisp** as reference.

3. Conclusions

In summary, we have successfully developed a novel self-reporting and self-healing thermoset that aligns with the principles of the circular economy by extending the functional lifespan of the polymer. By integrating dynamic chemistries and mechanochromic features, this thermoset demonstrates both reversible self-reporting and self-healing properties, achieved through the incorporation of a rhodamine-based crosslinker, as well as reprocessability. The self-reporting feature is particularly pronounced in the more elastic virgin polymer, where localized stress and damage are visibly indicated by a color change. This capability allows for real-time damage detection and facilitates prompt maintenance or repair, significantly reducing waste and improving material sustainability. Importantly, both the self-reporting and self-healing functionalities can be fully restored through a simple thermal treatment of the damaged zone, demonstrating the robustness and reusability of the material. The development of such advanced materials not only enhances the safety and durability of polymeric systems but also paves the way for innovative applications in sustainable material management, design and usage.

4. Experimental

4.1 Chemicals

Unless stated otherwise, all reactions were conducted in flame-dried glassware under an atmosphere of nitrogen using anhydrous solvents (either freshly distilled or passed through activated alumina columns). All reagents and solvents were purchased from certified commercial sources and used as received, without further purification. For synthesis, all anhydrous solvents (either freshly distilled or passed through activated alumina columns) have been used. Rhodamine **6G** was purchased from TCI Chemicals (product number R0039). TMSPEDA was purchased from ABCR (product number AB131042). Pristine PE-HEMA was provided by Saudi Basic Industries Corporation (Sabic) with 2.1 mol% of HEMA content calculated by NMR spectroscopy. Silica Gel for chromatographic separation was purchased from Sigma-Aldrich in technical grade, pore size 60 Å, 230-400 mesh particle size, 43-60 μm particle size. Thin layer chromatography was performed using TLC Analytical Chromatography F254®, Merck.

Nuclear Magnetic Resonance. ^{1}H and ^{13}C spectra were recorded on Bruker 400 MHz AVANCE, using $CDCl_3$ as solvent. All chemical shifts (δ) were reported in parts for million (ppm) relative to proton resonances resulting from incomplete deuteration of NMR solvents. The abbreviations: s, d, t, m and bs indicated the spectrum peaks referred to: singlet, doublet,

triplet, multiplet and broad singlet, respectively. The coupling constant (J) are expressed in Hz.

MS Spectrometry. ESI-MS characterization experiments were performed on a Waters ACQUITY Ultra Performance LC HO6UPS-823M with ESI source ionization (electrospray ionization) in positive modality. ***HR-MS.*** High-Resolution ESI-MS characterization experiments were performed on a LTQ ORBITRAP XL Thermo with ESI source ionization (electrospray ionization) in positive modality and new generation Ion Trap FT Orbitrap as analyser.

Thermal Gravimetric Analysis (TGA). TGA analyses have been achieved using a Perkin Elmer TGA 8000 with gas controller GC10 (pure air/nitrogen), Mettler Toledo. Samples were heated at 800 °C at a heating rate of 10 °C/min.

Dynamic Mechanical Analysis (DMTA). DMTA analyses were carried out on bars with nominal dimensions 6x1x30 mm^3, cut from plates obtained by compression moulding. Specimens were tested in tensile mode on a Q800 equipment (TA Instruments) at 2 °C/min heating rate (RT to 180 °C) and 1Hz frequency in strain-controlled mode, deformation amplitude at 0.05% and 0.01N preload. Specimens were conditioned at 23 °C and 50%RH for at least 48h before analyses.

Rheological analysis. Small angle oscillatory shear test were carried out on an ARES rheometer (TA Instruments) operated with a 25 mm parallel plate geometry and 1 mm thickness samples. Dynamic frequency sweep tests were carried out to determine G', G'' and complex viscosity (η*) between 0.1 and 100 rad/s at 1% strain (linear viscoelasticity) at temperatures between 120 °C and 200 °C.

Compression Moulding. Polymer films for scratching tests and stress strain measurements were printed by compression moulding using a *Gibitre Laboratory Press Drive* at 150 °C applying 15000 kg for 3 minutes. Specimens for DMTA and rheology were compression moulded on a Collins P200T press at 150 °C, 100 bar hydraulic pressure for 4 minutes, followed by water cooling to 50°C before extraction.

Stress-strain. Mechanical tests were carried out at room temperature on bars with nominal dimensions 25x0.7x80 mm^3 cut from plates obtained by compression moulding to have a free length of 40 mm for the measurements. Specimens were tested using an Instron 4400, electromechanical testing machine, equipped with a 30 kN load cell. Test speed was set to 250 mm/min.

Synthesis of functionalized rhodamine 1

Rhodamine **1** was synthesized according to a procedure adapted from literature.[25]

Ethanolamine (383 mg, 0.38 mL, 6.28 mmol, 6 eq) was added to a solution of rhodamine **6G** (500 mg, 1.05 mmol, 1 eq) in dry acetonitrile ACN (10 mL), and the reaction was refluxed overnight under mechanical stirring. As the reaction progressed, a pink precipitate formed. The reaction progress was monitored by TLC using ethyl acetate (EtOAc) as eluent. Once the complete disappearance of rhodamine **6G** was observed, the precipitate was filtered and washed with water. The obtained solid was purified by liquid chromatography on silica gel using 100% EtOAc as the eluent. The product was obtained as a white solid (418 mg, yield = 87%) and characterized by ^{1}H-NMR spectroscopy in $CDCl_3$.

^{1}H NMR ($CDCl_3$, 25 °C, 400 MHz) δ (ppm) = 7.92 (dd, J=8 Hz, 1H, Hi), 7.45 (m, 2H, Hg, Hh), 7.04 (d, J=8 Hz, 1H, Hf), 6.35(s, 2H, He), 6.28 (s, 2H, Hc), 4.16 (bs, 1H, Hm), 3.53 (bs, 1H, Hl), 3.44 (t, 2H, Hk), 3.25 (t, 2H, Hj), 3.21 (q, 4H, Hb), 1.92 (s, 6H, Hd), 1.32 (t, 6H, Ha).
ESI-MS: m\z = calculated for $C_{28}H_{30}N_3O_3$ $[M-H]^-$ 456.23, experimental value for $[M-H]^-$ 456.30

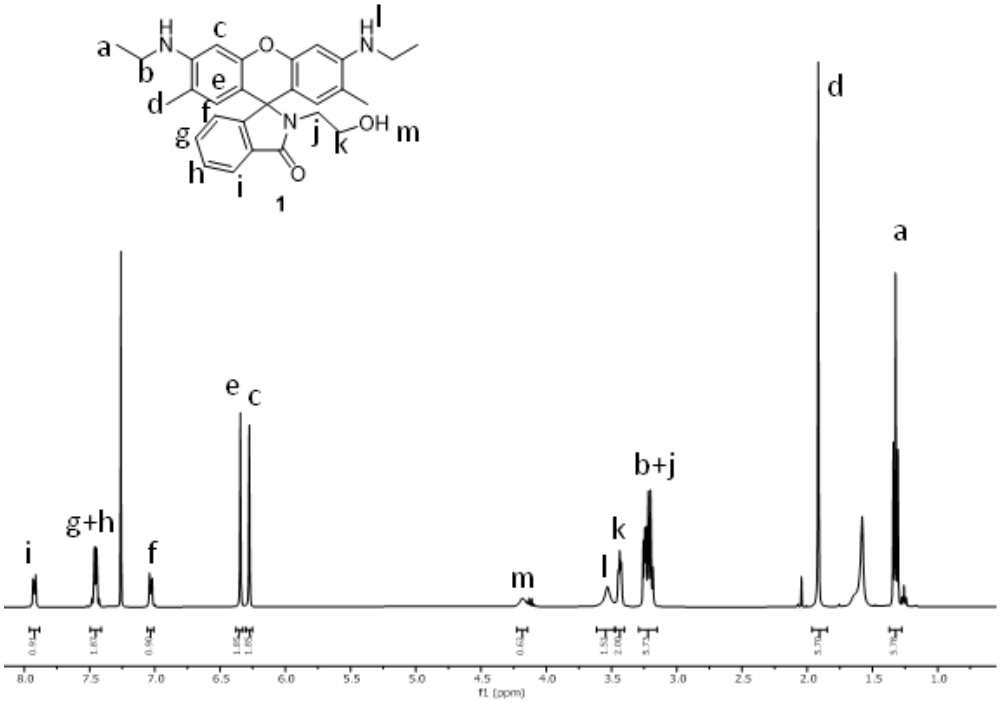

Figure S1. ^{1}H-NMR ($CDCl_3$, 25°C, 400MHz) spectrum of Rhodamine **1**

Synthesis of functionalized rhodamine 2

Rhodamine **2** was synthesized according to a procedure adapted from literature.[31]
Rhodamine **1** (500mg, 1.09 mmol, 1eq.) was added to a suspension of K_2CO_3 (906 mg, 6.56 mmol, 6 eq) and KI (4 mg, 0.02 mmol, 0.02 eq) in 2-bromoethanol (4 g, 2.3 mL, 30 mmol, 30 eq). The resulting red suspension was stirred mechanically at 110°C for 24 hours. The solvent was than evaporated under high vacuum, and the crude solid was dissolved in 250 mL of dichloromethane (DCM) and washed with water (3 x 50 mL). The organic phase was dried over Na_2SO_4, and the solvent evaporated under high vacuum. The crude was purified by liquid chromatography on silica gel using a mixture of DCM : EtOH (97:3) as the eluent. Rhodamine **2** was obtained as a white solid with a yield of 65% (387 mg).

^{1}H NMR ($CDCl_3$, 25 °C, 400 MHz) δ (ppm) = 7.99 (dd, J=8 Hz, 1H, H**i**), 7.53 (m, 2H, H**g**, H**h**), 7.07 (m, 1H, H**f**), 6.93(s, 2H, H**e**), 6.52 (s, 2H, H**c**), 4.25 (bs, 1H, H**m**), 3.94 (br, 1H, H**o**), 3.65 (m, 4H, H**n**), 3.48 (t, J=4 Hz, 2H, H**k**), 3.26 (m, 6H, H**j**, H**l**), 3.05 (q, 4H, H**b**), 2.13 (s, 6H, H**d**), 1.05 (s, 6H, H**a**).

ESI-MS: m\z = calculated for $C_{32}H_{49}N_3O_5$ $[M+H]^+$ 546.30, experimental value for $[M+H]^+$ 546.35.

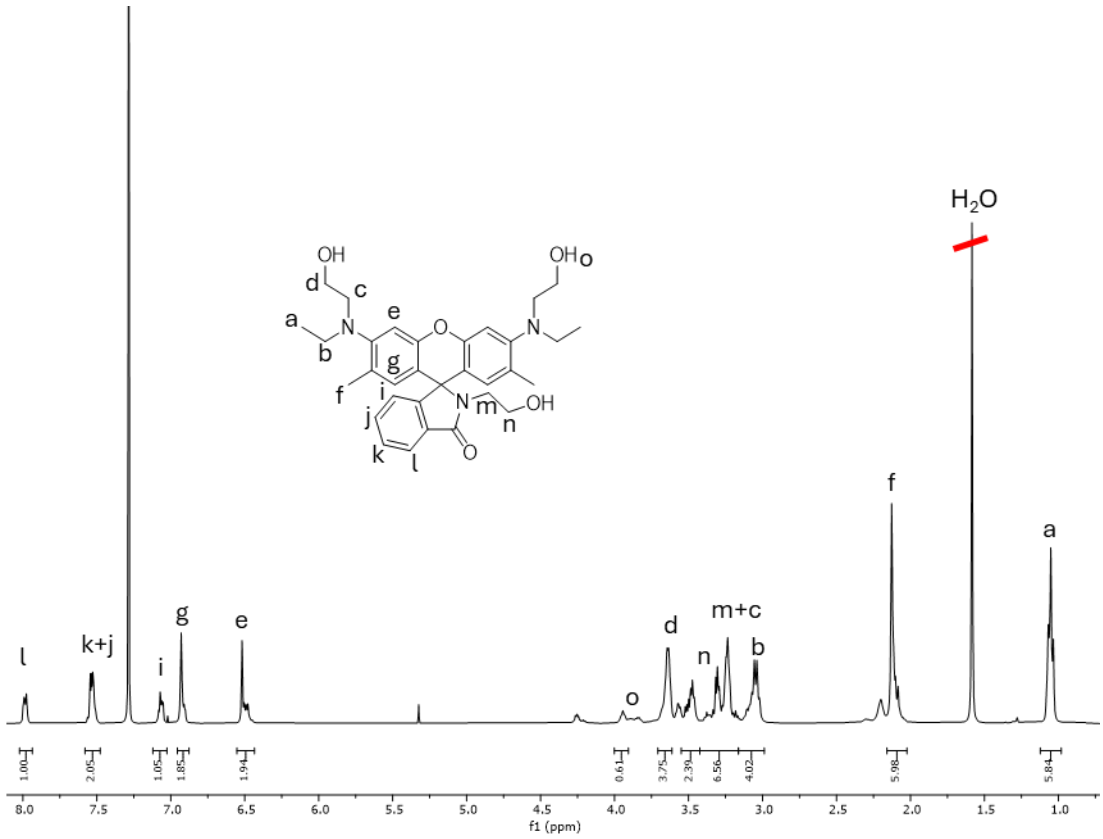

Figure S2. ^{1}H-NMR ($CDCl_3$, 25°C, 400MHz) spectrum of Rhodamine **2**

Synthesis of functionalized rhodamine 3

3-Isocyanatopropyltrimethoxysilane (167.5 mg, 154 µL, 0.81 mmol, 3.5 eq) was slowly added to a solution of rhodamine **2** (127.2 mg, 0.23 mmol, 1 eq) and dibutyltin dilaurate (DBTL, catalytic amount) in dry DCM (1.5 mL). The reaction was stirred mechanically at 40 °C in a dark environment for 16 hours. The solvent was then evaporated under high vacuum, and the resulting yellow oil was triturated in hexane (3 x 10 mL) and filtered. The target rhodamine **3** was obtained as a yellow solid in quantitative yield (270 mg) and fully characterized by NMR spectroscopy and HR ESI-MS.

^{1}H NMR ($CDCl_3$, 25 °C, 400 MHz) δ (ppm) = 7.96 (m, 1H, Hg), 7.50 (m, 2H, Hf, He), 7.06 (m, 1H, Hd), 6.89(s, 2H, Hb), 6.42 (s, 2H, Ha), 4.14 (m, 4H, Hj), 3.57 (m, 28H, Ho, Hq), 3.24 (m, 4H, Hp, Hk), 3.16 (m, 6H, Hl), 3.08 (m, 4H, Hh), 2.06 (s, 6H, Hc), 1.64 (m, 6H, Hm), 1.04 (t, 6H, Hi), 0.65 (m, 6H, Hn).

^{13}C NMR ($CDCl_3$, 25 °C, 100 MHz) δ (ppm) = 168.80, 168.59, 156.94, 156.58, 156.05, 153.80, 151.48, 151.22, 150.29, 147.26, 132.81, 130.51, 129.96, 129.73, 128.46, 123.93, 123.10, 118.63, 113.30, 109.80, 96.42, 70.60, 69.78, 69.48, 69.20, 67.87, 64.84, 64.65, 63.92, 63.07, 62.35, 61.93, 51.97, 51.42, 50.83, 50.66, 47.83, 43.98, 43.49, 39.57, 23.27, 17.83, 16.79, 12.37, 6.40.
HR ESI-MS: m/z = calculated for ($C_{53}H_{85}N_6O_{17}Si_3$) $[M+H]^+$ 1161.5291, experimental value for $[M+H]^+$ 1161.5279.

^{1}H-NMR:

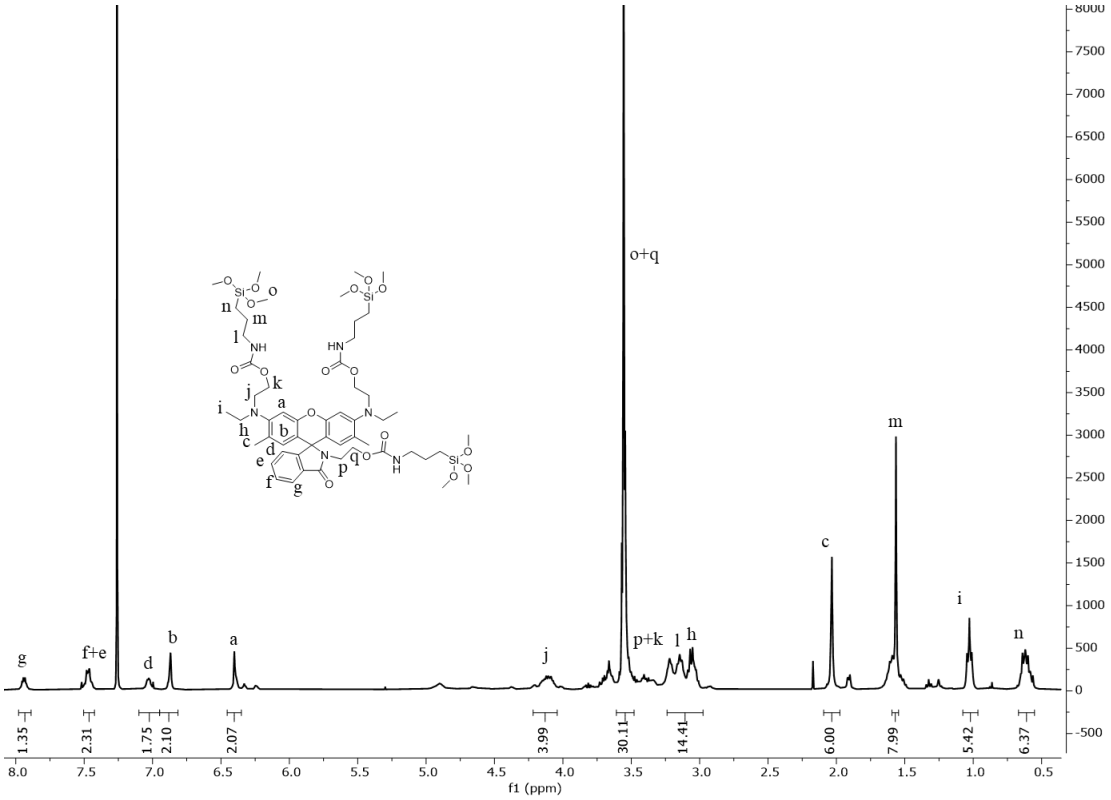

Figure S3. ^{1}H-NMR ($CDCl_3$, 25°C, 400MHz) spectrum of Rhodamine **3**

COSY-NMR:

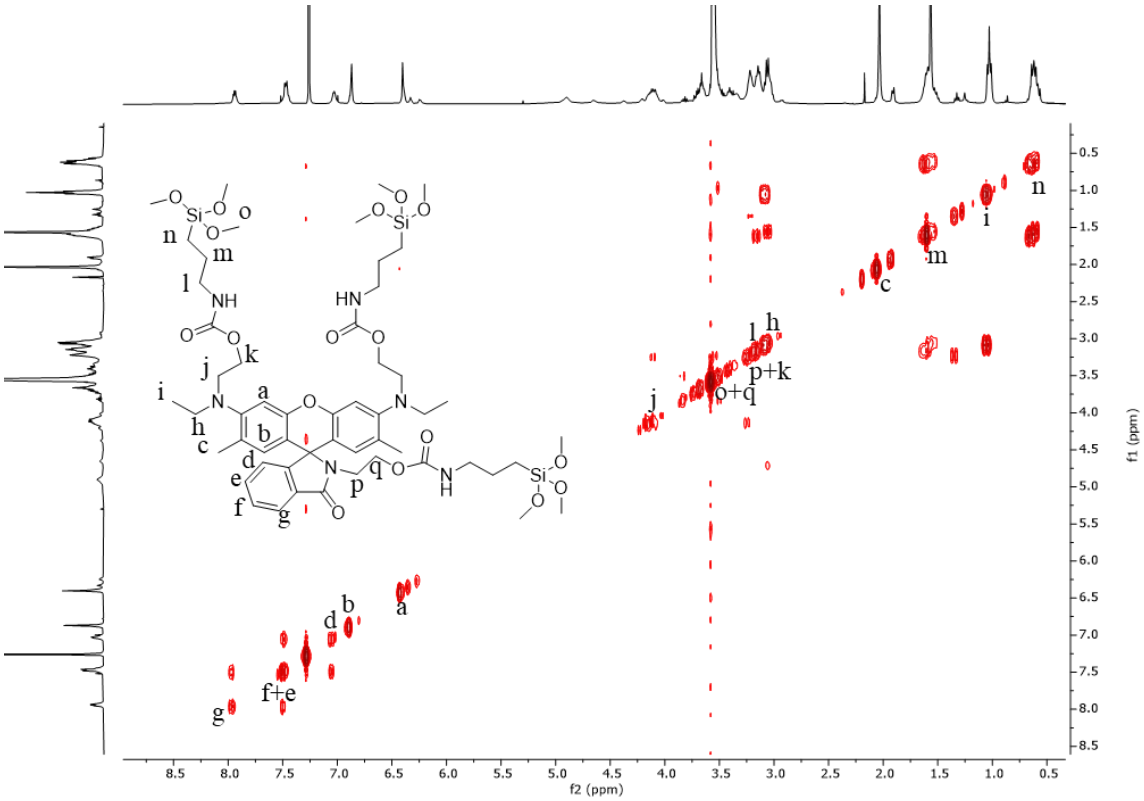

Figure S4. COSY-NMR ($CDCl_3$, 25°C, 400MHz) Spectrum of Rhodamine **3**

HSQC-NMR:

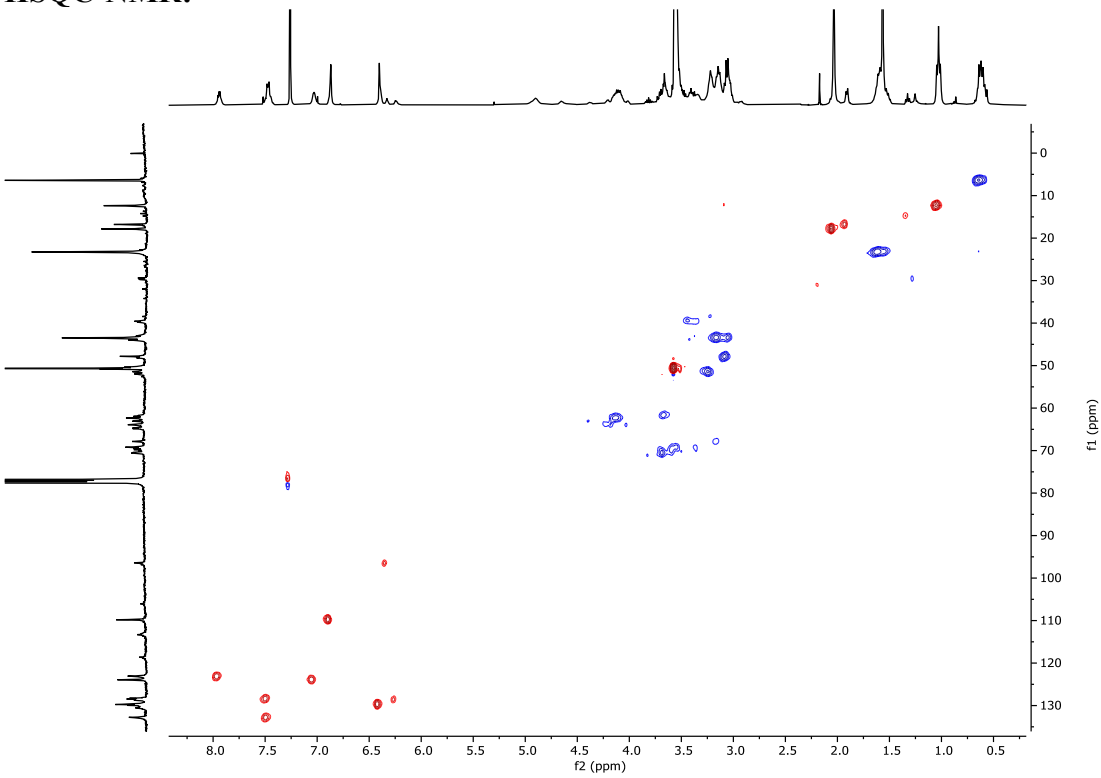

Figure S5. HSQC-NMR ($CDCl_3$, 25°C, 400MHz) Spectrum of Rhodamine **3**

DEPT-135:

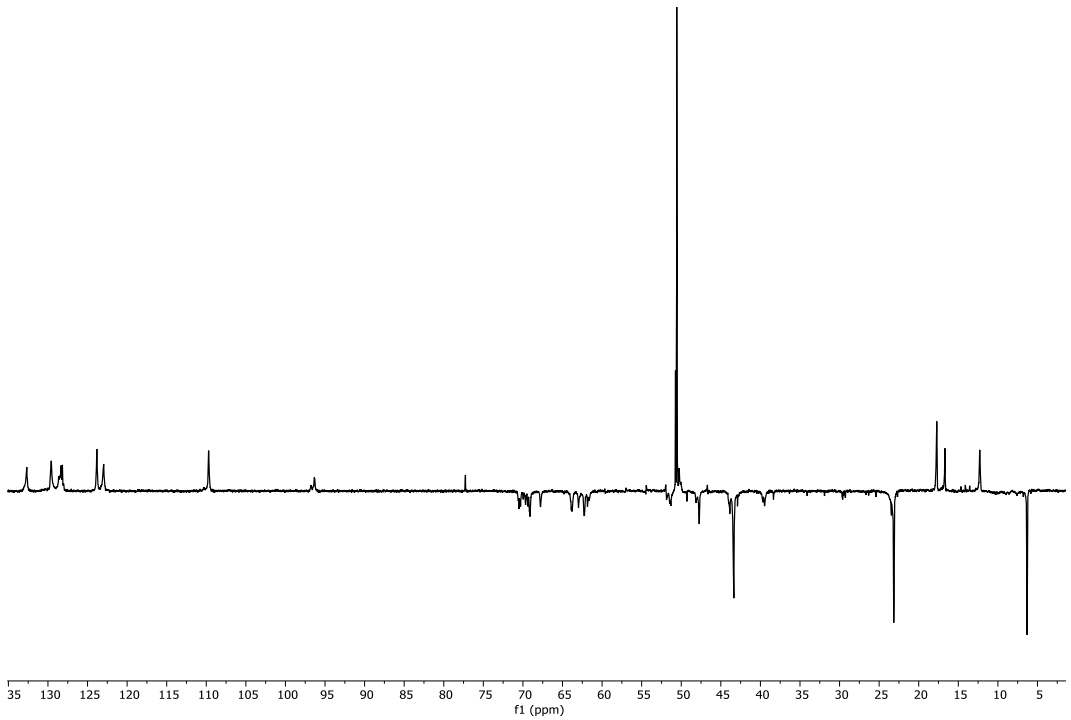

Figure S6. DEPT135-NMR ($CDCl_3$, 25°C, 100MHz) Spectrum of Rhodamine **3**

^{13}C-NMR:

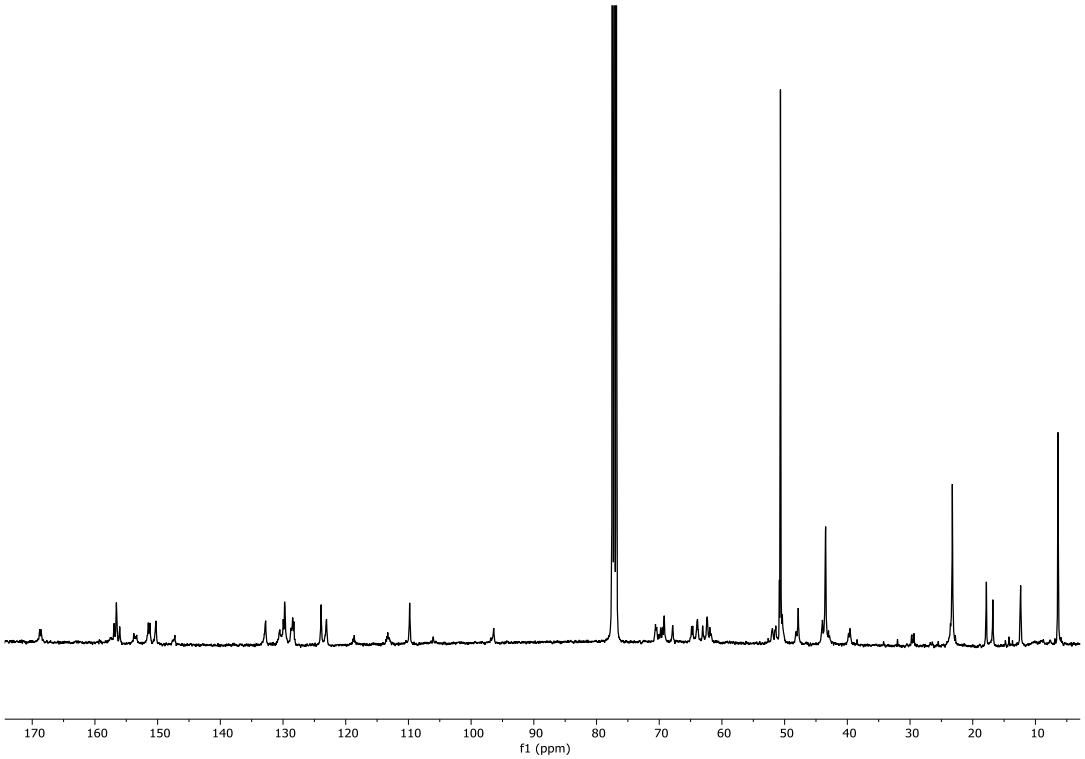

Figure S7. ^{13}C-NMR ($CDCl_3$, 25°C, 100MHz) Spectrum of Rhodamine **3**

High-Resolution MS:

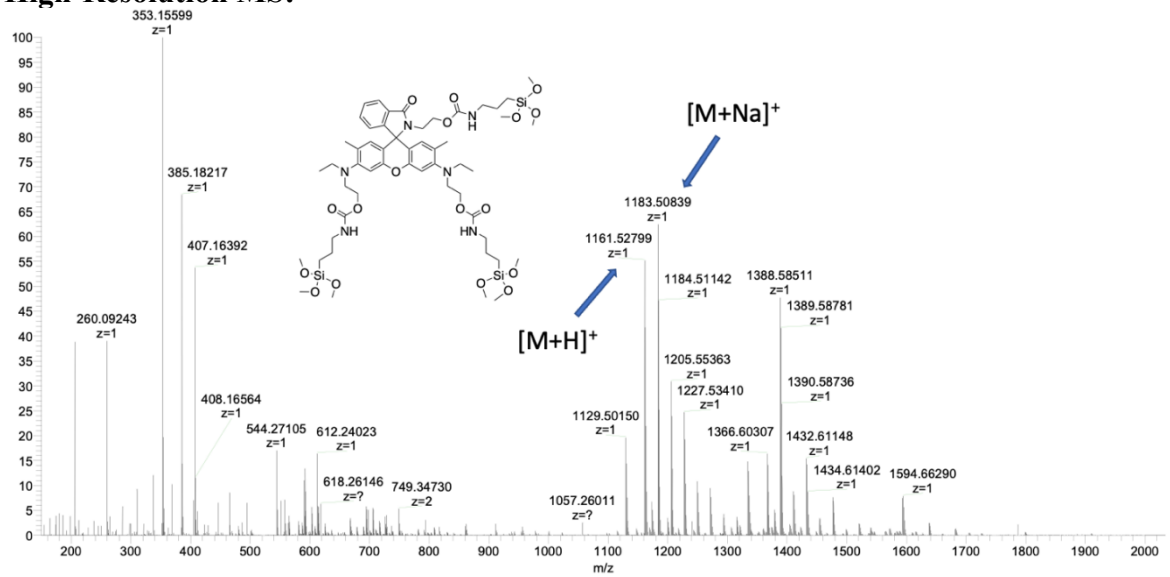

Figure S8. HR-MS of Rhodamine **3**

DSC Analyses

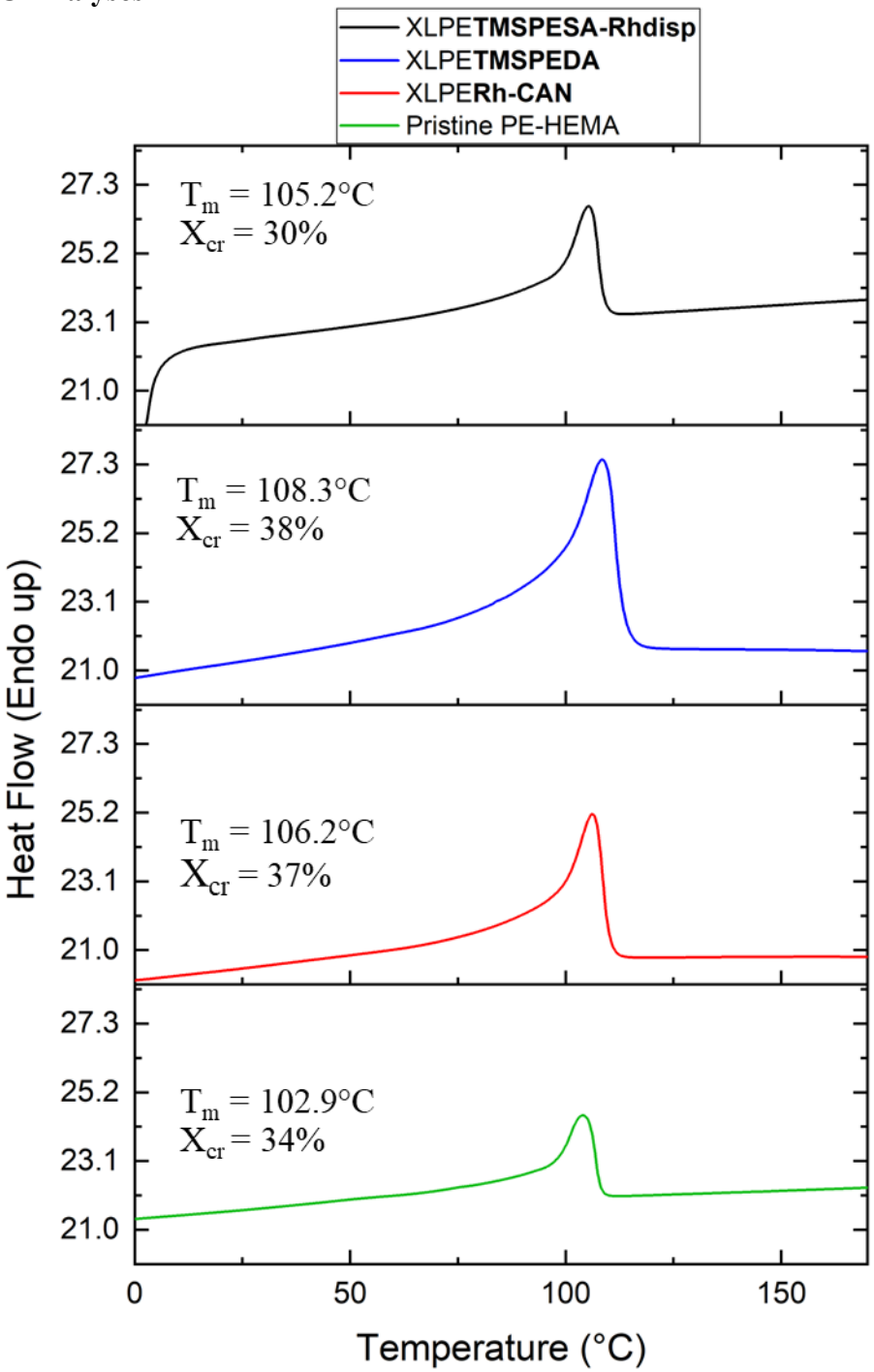

Figure S9. DSC second heating ramp of pristine PE-HEMA (green trace), XLPE**Rh-CAN** (red trace), XLPE**TMSPEDA** (blue trace), XLPE**TMSPEDA-Rhdisp** (black trace).

Gel-Fraction Measurements:

Gel-fraction measurements have been performed on 100 mg of crosslinked material heating the polymer in xylene at 100 °C for 18 hours. The samples have been then dried in high vacuum at 100 °C until the weight of the insoluble fraction remained constant.

All the crosslinked samples have shown a considerable amount of insoluble fraction as reported in **table S1**:

Material	Initial Mass [mg]	Final Mass [mg]	Gel-Fraction [%]	Swelling [%]
XLPE**Rh-CAN**	100	64	64	258
XLPE**TMSPEDA-Rhdisp**	100	72	72	330
XLPE**TMSPEDA**	100	69	69	307
PE-HEMA	100	-	-	-

Table S1: Gel-fraction of pristine PE-HEMA and crosslinked polyethylene XLPE**Rh-CAN**, XLPE**TMSPDEA-Rhdisp**, XLPE**TMSPEDA**.

TGA Measurements

Rhodamine 1

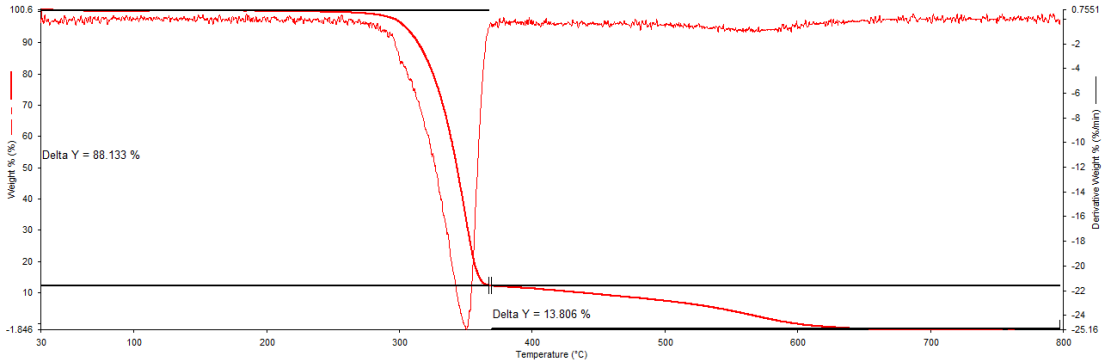

Figure S10. TGA measurement on Rhodamine **1**

Rhodamine 2

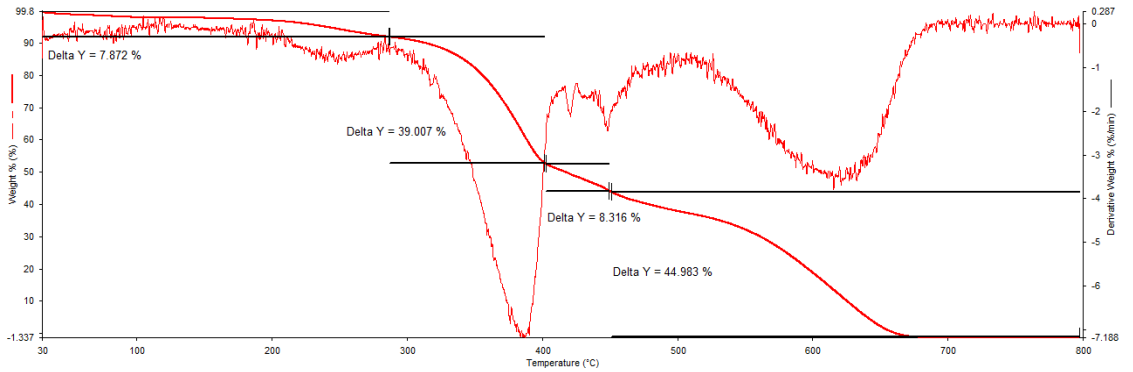

Figure S11. TGA measurement on Rhodamine **2**

Rhodamine 3

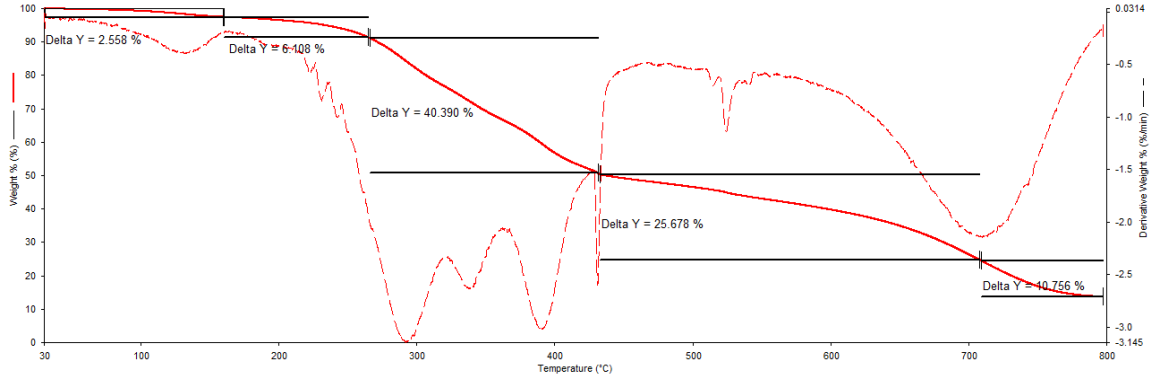

Figure S12. TGA measurement on Rhodamine **3**

Film Preparation

Polymer films for self-reporting tests were prepared by compression moulding 2g of XLPE**Rh-CAN**.

The material was firstly heated at 150 °C for 1 minute and then hot pressed at constant temperature with a 15000 kg pressure for 3 minutes. After 3 minutes, keeping the material pressed, the hot plates have been cooled down to 25 °C with a cooling rate of 50 °C/min.

Additional self-reporting, quenching and reversibility tests

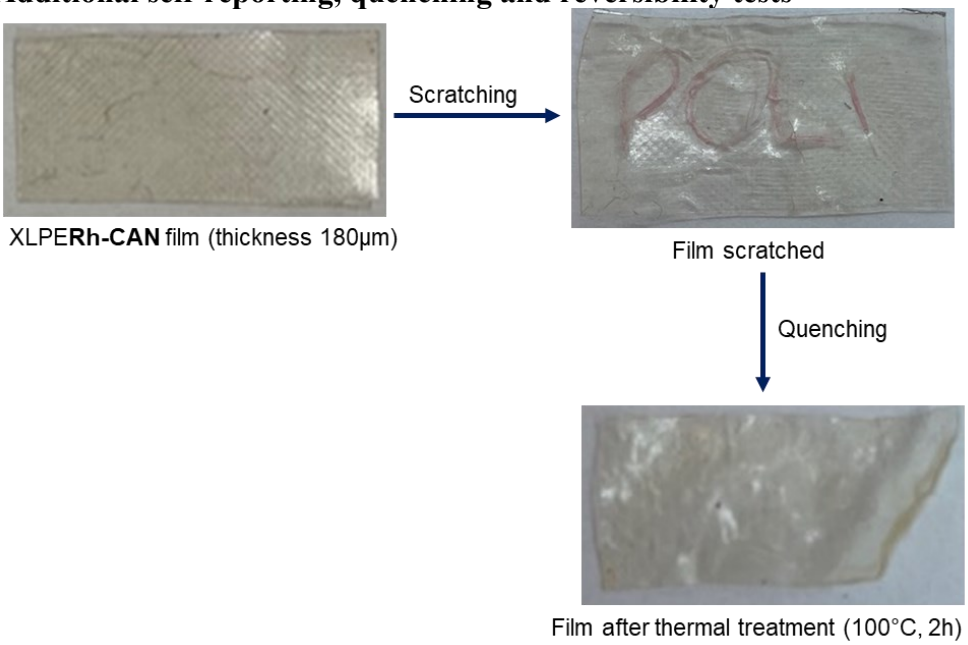

Figure S13. XLPE**Rh-CAN** scratching and quenching test.

It was observed that after the printing process the polymer film is completely transparent, when the polymer is scratched a clear pink coloration appears in correspondence of the mechanical damage. After a thermal treatment at 100°C for 2 hours, the material is completely healed and the mechanophore is completely quenched.

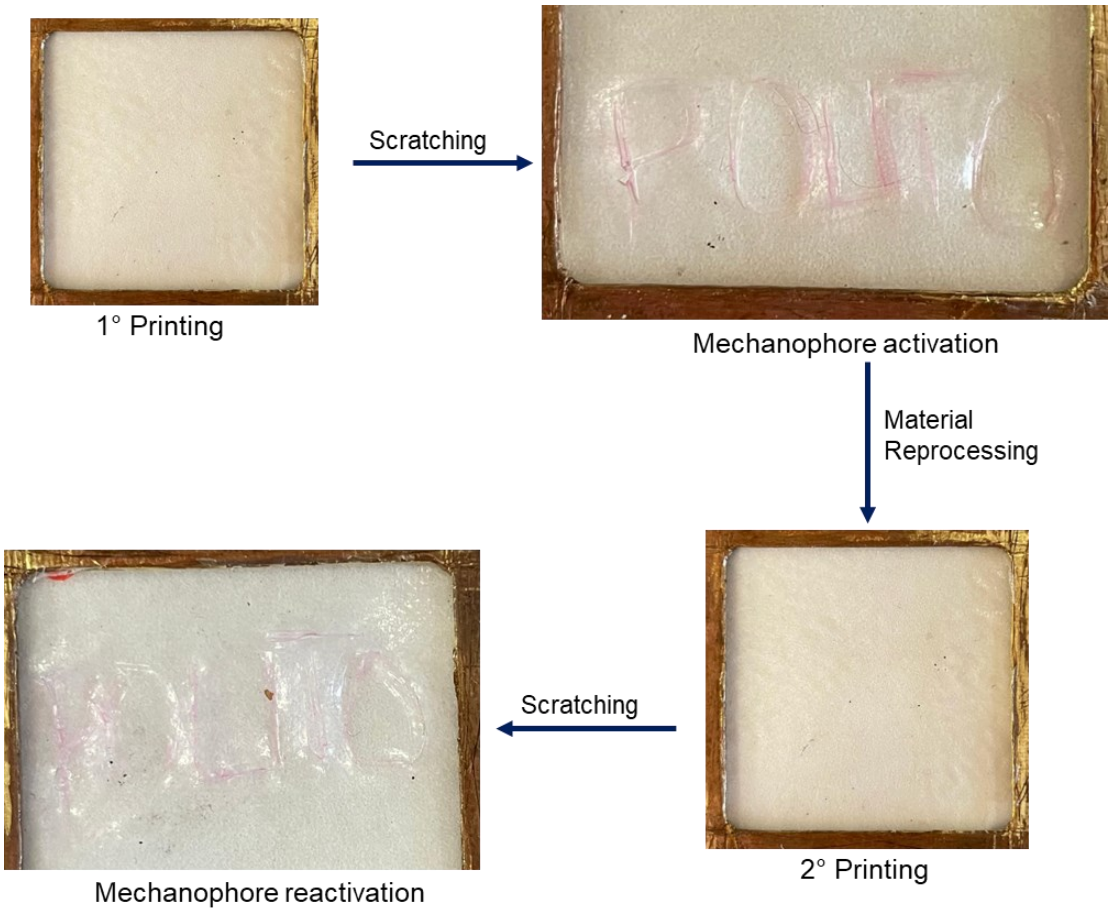

Figure S14. XLPE**Rh-CAN** printing, activation, reprinting and reactivation test.

5. References

[1] “What is a circular economy? | Ellen MacArthur Foundation.” Accessed: Jun. 11, 2024. [Online]. Available: https://www.ellenmacarthurfoundation.org/topics/circular-economy-introduction/overview

[2] Morici E. and Dintcheva N. T., *Polymers*, **2022**, 14, 4153.

[3] Yang Y., Boom R., Irion B., Van Heerden D. J., Kuiper P., de Wit H., *Chem. Eng. Process.: Process Intensif.*, **2012**, 51, 53–68.

[4] Pickering S. J., *Compos. Part A Appl. Sci. Manuf.*, **2006**, 37, 1206–1215.

[5] Kemona A., Piotrowska M., *Polymers*, **2020**, 12, 1752.

[6] Zia K. M., Bhatti H. N., Ahmad Bhatti, *React. Funct. Polym.*, **2007**, 67, 675−692.

[7] Beran R., Zarybnicka L., Machova, D., *J. Appl. Polym. Sci.,* **2020**, 137, 49095.

[8] Grdadolnik M., Drinčić, A., Oreški A., Onder O. C., Pahovnik D., Žagar E., *ACS Sustain. Chem. Eng.*, **2022**, 10, 1323−1332.

[9] Sheel A., Pant D., Chemical Depolymerization of Polyurethane Foams via Glycolysis and Hydrolysis. *Recycling of Polyurethane Foams*; **2018**; pp 67−75, Elsevier

[10] Deng Y., Dewil R., Appels L., Ansart R., Baeyens J., Kang, Q., *J. Environ. Manage.*, **2021**, 278, 111527.

[11] Kloxin C. J., Scott T. F., Adzima B. J., Bowman C. N., *Macromolecules*, **2010**, 43, 2643–2653.

[12] Maes S., Scholiers V., Du Prez F. E., *Macromol. Chem. Phys.*, **2023**, 224, 2100445.

[13] Winne J. M., Leibler L., Du Prez F. E., *Polym. Chem.*, **2019**, **10**, 45, 6091–6108.

[14] Scheutz G. M., Lessard J. J., Sims M. B., Sumerlin B. S., *J. Am. Chem. Soc.*, **2019**, 141, 16181–16196.

[15] Capelot M., Montarnal D., Tournilhac F., Leibler L., *J. Am. Chem. Soc.*, **2012**, 134, 7664–7667.

[16] Self J. L., Dolinski N. D., Zayas M. S., Read De Alaniz J., Bates C. M., *ACS Macro Lett.*, **2018**, 7, 817–821.

[17] Snyder R. L., Fortman D. J., De Hoe G. X., Hillmyer M. A., Dichtel W. R., *Macromolecules*, **2018**, 51, 389–397.

[18] Fortman D. J., Snyder R. L., Sheppard D. T., Dichtel W. R., *ACS Macro Lett.*, **2018**, 7, 1226–1231.

[19] Gyarmati B., Némethy Á., A. Szilágyi, *Eur. Polym. J.*, **2013**, 49, 1268–1286.

[20] Otsuka H., Nagano S., Kobashi Y., Maeda T., Takahara A., *Chem. Commun.*, **2010**, 46, 1150–1152.

[21] Canadell J., Goossens H., Klumperman B., *Macromolecules*, **2011**, 44, 2536–2541.

[22] Nishimura Y., Chung J., Muradyan H., Guan Z., *J. Am. Chem. Soc.*, **2017**, 139,14881–14884.

[23] Tretbar C. A., Neal J. A., Guan Z., *J. Am. Chem. Soc.*, **2019**, 141, 16595–16599.

[24] Zych A., Pinalli R., Soliman M., Vachon J., Dalcanale E., *Polymer*, **2020**, 199, 122567.

[25] Denissen W., Rivero G., Nicolaÿ R., Leibler L., Winne J. M., Du Prez F. E., *Adv. Funct. Mater.*, **2015**, 25, 2451–2457.
[26] Denissen W., Droesbeke M., Nicola R., Leibler L., Winne J. M., Du Prez F. E., *Nat. Commun.*, **2017**, 8**, 14857**
[27] Tellers J., Pinalli R., Soliman M., Vachon J., Dalcanale E., *Polym. Chem.*, **2019**, 10, 5534–5542.
[28] Chen Y., Mellot G., Van Luijk D., Creton C., Sijbesma R. P., *Chem. Soc. Rev.*, **2021**, 50, 4100–4140.
[29] Davis D. A., Hamilton A., Yang J., Cremar L. D., Gough D. V., Potisek S. L., Ong M. T., Braun P. V., Martı´nez T. J., White S. R., Moore J. S., Sottos N. R., *Nature*, **2009**, 459, 68–72.
[30] Wang Z., Ma Z., Wang Y., Xu Z., Luo Y., Wei Y., Jia X., *Adv. Mater.*, **2015**, 27, 6469–6474.
[31] Wang T., Zhang N., Dai J., Li Z., Bai W., Bai R., *ACS Appl. Mater. Interf.*, **2017**, 9, 11874–11881.
[32] Wunderlich B., Cormier C. M., *J.Polym. Sci. Part A-2: Polym. Phys.* **1967**, 5, 987–988.

Chapter 4

Supramolecular reprocessable liquid crystal elastomers

Abstract

Hydrogen bonding motifs represent a precious tool for the realization of adaptable crosslinking networks which combine the high mechanical performances of thermosets with the reprocessability of thermoplastics. This work presents various approaches to synthesize and characterize photoactive liquid crystal elastomers fabricated via electrospinning. These materials incorporate reversible supramolecular crosslinks *via* hydrogen bonds, which is expected to block in the orientation of mesogens post-fabrication, promoting the formation of highly ordered liquid crystalline domains while maintaining material reprocessability.

TOC: Electrospinning of liquid crystal elastomers containing azo-benzene derivatives as photo-actuators.

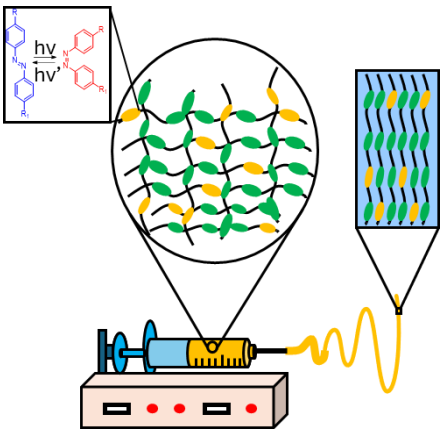

1. Introduction

1.1 Liquid Crystal and Liquid Crystal Elastomer

Liquid crystals represent an intermediate state of matter, exhibiting properties characteristic of both liquids and crystalline solids. This behavior is attributed to the presence of rigid, anisotropic molecules known as mesogens, which tend to align collectively along specific directions, forming mesophases.

To function as mesogens, molecules must possess pronounced anisotropy in shape and polarizability. Consequently, mesogens are typically rigid, elongated rod-like molecules incorporating an aromatic core or a conjugated π system, which enhances their polarizability along the long axis (Figure 1).[1]

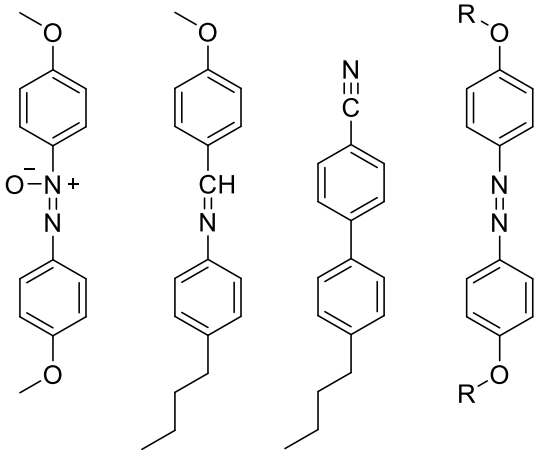

Figure 1. Typical chemical structure of mesogens.[1]

Mesogen alignment is governed by two mechanisms: an entropic mechanism dependent on mesogen concentration and an enthalpic mechanism influenced by both mesogen concentration and temperature.

In lyotropic liquid crystals, mesogens align through an entropic effect. By adopting a parallel arrangement, mesogens can flow more freely without overlapping, maximizing translational entropy.

In thermotropic liquid crystals, mesogens align due to an enthalpic effect. For molecules with anisotropic polarizability, Van der Waals interactions are stronger when molecules are oriented parallel. An instantaneous dipole moment created along the long axis of a mesogen, the direction of greater polarizability, induces a larger dipole moment in nearby molecules if they expose their most polarizable parts. This interaction favors the parallel alignment of mesogens. Generally, both alignment mechanisms operate concurrently.[1]

The concentration of mesogens directly influences liquid-crystalline order, with higher concentrations leading to more numerous alignment-promoting interactions. The influence of temperature is attributed to thermal motions, which oppose the formation of long-range order. As a result, liquid crystals possess a specific temperature, known as the isotropic

transition temperature (Ti), above which the liquid-crystalline order dissipates, and the material behaves as an isotropic liquid.[2]
Three distinct types of liquid-crystalline phases exist: nematic, cholesteric, and smectic (Figure 2).[3] The nematic phase exhibits the lowest degree of order, resembling an anisotropic liquid with long-range order in one direction and free flow in the other two. The nematic phase can be described using a single parameter, the nematic director $\vec{n}$, which represents the average direction of mesogen alignment.

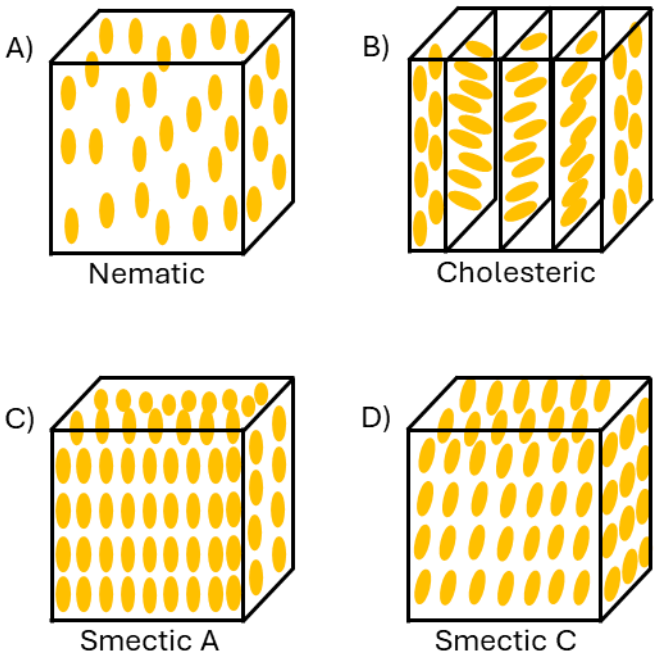

Figure 2. Molecular order in LC phases, A) nematic; B) cholesteric; C) smectic A and D) smectic C.[3]

In the cholesteric phase, molecules are locally oriented as in the nematic phase, but the average mesogen direction rotates periodically around an axis perpendicular to the nematic director.[3]

Smectic phases, characterized by the highest degree of order, involve mesogens aligned parallel to each other and organized into equidistant parallel planes. The smectic A phase occurs when the nematic director is parallel to the plane normal, while the smectic C phase arises when the two form an angle θ.
A single material can transition through different liquid-crystalline phases depending on temperature, with smectic phases typically occurring at lower temperatures than the nematic phase due to the decreasing degree of order with increasing temperature.[3]

Mesogens retain their ability to autonomously orient themselves even when covalently bonded to a polymer chain, capitalizing on the ample conformational freedom afforded by the free volume within the polymer chains above the glass transition temperature (T_g).[4]
The presence of mesogens can confer liquid-crystal properties to a polymer. When mesogens are incorporated into the main backbone of the polymer chain, the material is classified as a main-chain liquid crystal. Conversely, when mesogens are present as side substituents on the main chain, the material is referred to as a side-chain liquid crystal (Figure 3).[4]

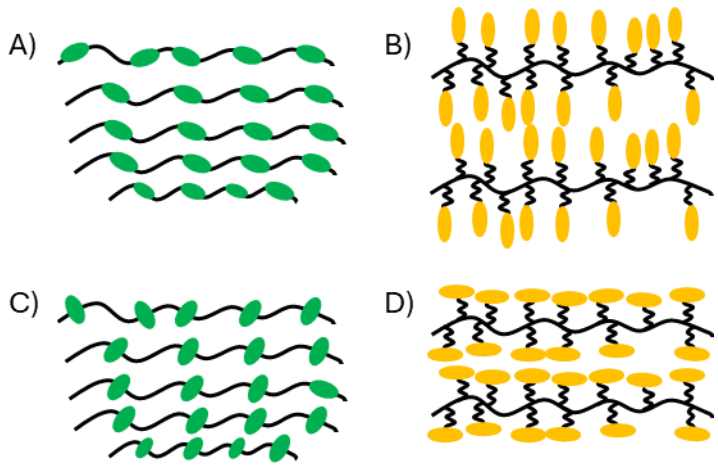

Figure 3. Schematic representation of possible covalent bond geometries of mesogen molecules in a liquid crystal polymers: A) main-chain *end on*; B) side-chain *end on*; C) main-chain *side on*; D) side-chain *side on*.[4]

Elastomeric liquid crystals (LCE) are liquid crystals containing a small percentage of crosslinking between polymer chains. These materials exhibit the optical and mechanical anisotropy characteristic of liquid crystals, combined with the mechanical energy dissipation, reversible deformability, and elasticity typical of elastomers. The interplay of these properties results in unique features such as *shape memory* and reversible mechanical actuation, enabling the performance of mechanical work when subjected to appropriate stimuli.

A prerequisite for a polymer to exhibit these properties is the coherent orientation of all liquid-crystal domains within the material. Liquid crystals lacking such order, known as polydomain, display isotropic properties resembling common polycrystalline materials due to the random orientation of mesogens, which averages properties across all directions.

Macroscopic anisotropic behavior is observed in monodomain liquid crystals, also known as liquid single crystal elastomers, where liquid-crystal domains are aligned in a single direction. To achieve a high degree of mesogen orientation, an anisotropic force must be

applied to the system during polymer synthesis or crosslink formation. This force can be a unidirectional or bidirectional mechanical stress, an electric or magnetic field, or irradiation with polarized light.[2]

To enable actuation, controlling the conditions under which the liquid-crystal phase is established is essential. This can be achieved by understanding phase transition temperatures or utilizing a photoactivatable mesogen that facilitates entry into and exit from the liquid-crystal phase through light irradiation.
Compared to thermal actuation, light-driven actuation offers the advantage of precise modulation through controlled incident radiation parameters and remote operation.[5] Moreover, the wide spectrum of frequencies enables selective control of actuation in composite materials, producing complex mechanical movements. However, efficient light-driven actuation requires uniform irradiation of the entire sample, currently limiting its applications to thin films and fibers with negligible thickness compared to the surface area.
Azobenzene is a commonly used mesogen for this purpose due to its ability to undergo trans-cis isomerization when exposed to ultraviolet radiation (Figure 4).[5] [6]

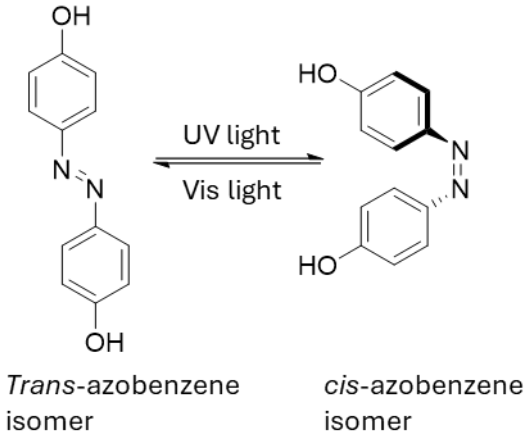

Figure 4. Light-driven trans-cis isomerization process of azobenzene.

The trans isomer possesses a structure suitable for mesogenic function, while the cis isomer, with its bent bonding geometry and shorter molecular length, cannot support liquid-crystal order and induces the decay of the liquid-crystal phase.[7]

In elastomeric liquid crystals containing azobenzene, irradiation acts similarly to an increase in temperature, reducing nematic order. This allows for the control of the liquid-crystal phase through the manipulation of azobenzene trans-cis isomerism, consequently transforming a light stimulus into mechanical work. Macroscopically, this results in material deformation, causing it to bend either towards or away from the light source, depending on the orientation of mesogens within the material (Figure 5).[8]

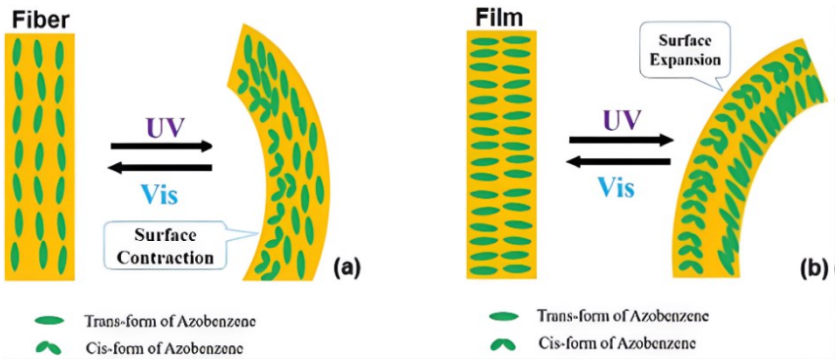

Figure 5. Light-induced activation of a (a) fiber and (b) film liquid crystal elastomer containing azobenzene moieties.[8]

1.2 Electrospinning as printing technique

Electrospinning is a printing technique involving an electrodynamic process in which a liquid droplet is electrified to generate a jet that undergoes stretching and elongation, ultimately forming a fiber. The apparatus consists of a high-voltage power supply, a syringe pump, a spinneret (typically a hypodermic needle), and a conductive collector. The power supply can operate in either alternating current (AC) or direct current (DC) mode.[9]

The electrospinning process comprises four primary phases: (i) the liquid stored in the syringe is slowly expelled from the needle, forming a pendant droplet due to surface tension; (ii) the electrified needle induces electrostatic repulsion between charges of the same sign, deforming the droplet into a Taylor cone from which a charged jet is ejected; (iii) initially extending as a straight line, the jet subsequently undergoes a vigorous whipping motion due to bending instabilities, leading to stretching and thinning; (iv) the jet rapidly solidifies, resulting in the deposition of a solid fiber onto the grounded collector (Figure 6).[10]

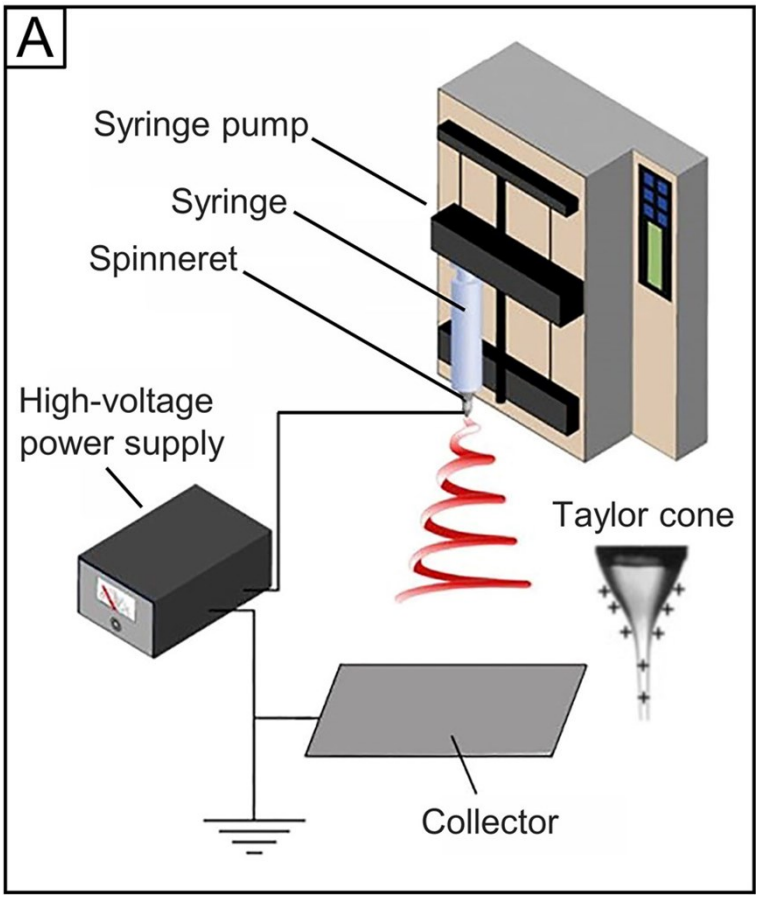

Figure 6. Schematic representation of electrospinning technique working principle.[9]

The formation of electrospun fibers and the control of their diameter can be precisely adjusted by modifying process parameters. Key parameters include the distance between the needle tip and the collector, flow rate, and applied voltage.[9] The applied voltage directly influences the magnitude of positive or negative charges carried by the jet, affecting electrostatic repulsion among charges and the strength of interactions between the jet and the external electric field. Generally, higher voltages favor the formation of thinner fibers.[11] Additionally, the flow rate of the liquid significantly influences fiber diameter, with increased flow rates typically resulting in larger fibers. The distance between the spinneret end and the collector determines the level of instability at which the jet is deposited. To ensure the formation of solid fibers, complete extension and solidification of the jet are necessary, requiring an adequate distance between the spinneret and the collector. In general, increasing this distance tends to result in thinner fibers.[9] Electrospun fibers are characterized by a high degree of polymer chain orientation, which significantly influences material properties.[12] Electrospinning liquid crystalline materials enables the creation of fibers with a remarkably high level of mesogen orientation within the polymer chains,

facilitating the production of materials with enhanced photoactuation properties, faster response times, and the capability to execute complex movements.

Electrospinning is a technique suitable for processing several types of materials among which the most commonly used are organic polymer in form of solutions or melt.[9] The solution electrospinning is the most commonly used and the most studied as many organic polymers can be dissolved in appropriate solvents to obtain solutions. When a polymer solution is ejected from the spinet, due to the processes of stretching, elongation and spinning, the solvents quickly evaporate allowing the solidification and the deposition of the nanofiber on the collector.[13] Many examples of both natural and synthetic polymer have been successfully printed by electrospinning in solution mode to form nanofibers. Synthetic polystyrene (PS) and poly(vinyl chloride) (PVC) nanofibers produced by electrospinning have been used for commercial applications in the environmental protection field. Biocompatible and biodegradable polymer as polylactic acid (PLA), poly(lactic-co-glycolic acid) (PLGA) has shown the capability of forming nanofibers through electrospinning suitable for biomedical applications.[9]

Successful electrospinning of a polymer solution requires careful consideration of several parameters, including the nature of the polymer, solvent, polymer solution, process parameters, and ambient conditions.[14] Two primary requirements for a successful process are (i) high molecular weight polymers and (ii) a suitable solvent. The molecular weight of the polymer significantly influences the rheological behavior and electrical properties of the solution. Polymers with excessively low molecular weights exhibit poor chain entanglement, leading to droplet formation rather than fibers.

Regarding the solvent, a necessary but not sufficient condition for effective electrospinning is determined by the solubility parameter and volatility. Volatility influences the evaporation rate and jet solidification rate. Excessively volatile solvents can result in premature jet solidification upon exiting the spinneret, while low volatility can lead to wet fibers upon collection. Additionally, the solvent's dielectric constant determines the strength of electrostatic forces.[15] A higher dielectric constant requires a higher applied voltage to stabilize the jet. For these reasons, solvents such as DMF, THF, DMSO, HFIP (hexafluoroisopropanol), and alcohols are commonly used for electrospinning polymer solutions, while water is generally not preferred due to its high dielectric constant.

Another crucial factor for successful electrospinning is the concentration of the polymer solution.[16] Concentrations below the critical entanglement concentration can result in weak interactions between polymer chains, leading to droplet formation at the needle exit due to jet breakup. Conversely, excessively high concentrations can lead to the dominance of viscoelastic forces, preventing jet formation.

To obtain a liquid-crystalline elastomer, the introduction of a small percentage of crosslinking is necessary. However, traditional covalent crosslinking commonly found in elastomeric materials can compromise material solubility and hinder electrospinning processability. A strategy for preserving both processability via electrospinning and covalent crosslinking in elastomeric materials involves utilizing linear polymers incorporating reactive functional groups capable of undergoing crosslinking reactions. The material is initially electrospun in its linear polymer form, with a crosslinking agent added to the polymer solution. An external stimulus, such as UV radiation or thermal treatment, subsequently initiates the crosslinking reaction forming the network immediately after the formation of the fiber. However, it is essential to consider that this approach may compromise the orientation of mesogens within the fibers following the crosslinking reaction.[18]

Another promising approach to preserve both properties involves incorporating a reversible supramolecular crosslinking network. This network can be formed during material preparation, broken during solution preparation for electrospinning, and reformed upon solvent removal following the molding process. Hydrogen bonds, being weak interactions, offer an effective strategy for establishing such a dynamic reversible crosslinking network.

1.3 Hydrogen Bonding as reversible supramolecular crosslinking

Hydrogen bonding, a specific type of dipole-dipole interaction, is widely utilized in supramolecular chemistry. It involves an electrostatic attraction between the partial positive charge (δ^+) on a hydrogen atom covalently bonded to an electronegative atom (donor, D) and the partial negative charge (δ^-) on another electronegative atom on a different molecule or adjacent functional group (acceptor, A). Nitrogen and oxygen are the most common hydrogen donor and acceptor atoms.

The strength of a single hydrogen bond is influenced by the nature of the donor and acceptor but is significantly affected by the solvent. Consequently, hydrogen bond strengths can vary between 4 and 60 kJ/mol.

Hydrogen bonding involves two types of interactions: primary interactions, representing the direct interaction between D and A, and secondary interactions, occurring when the molecules involved in the hydrogen bond possess multiple donor or acceptor groups. Certain heteroaromatic compounds, featuring multiple arrays of hydrogen bonds with a favourable D-A arrangement, can self-assemble to form dimers with high association constants.[16] A notable example of such molecules capable of forming multiple hydrogen bonds are the complementary DNA bases, which assemble into the characteristic double-helix structure.[19]

Among the extensively studied heteroaromatic compounds are derivatives of 2-ureido-4-pyrimidone (UPy). These compounds self-dimerize through hydrogen bonding with a high dimerization constant ($K_a > 10^6$ M^{-1} in $CHCl_3$), forming a quadruple DDAA array.[20][21] Another molecule capable of forming stable dimers is 7-acylamino-[1H]-2-oxo-1,8-naphthyridine (NAPY).[22] It dimerizes with an association constant of approximately 10^3 M^-

[1] in $CHCl_3$, exhibiting an ADAD arrangement. Another particularly noteworthy example of a hydrogen bond array is 1-(7-oxo-7,8-dihydro-1,8-naphthyridin-2-yl)urea (ODIN), which exhibits a 5-point array and an association constant in $CHCl_3$ of $4*10^4$ M^{-1}, positioning it between UPy and NAPY (Figure 7).[23]

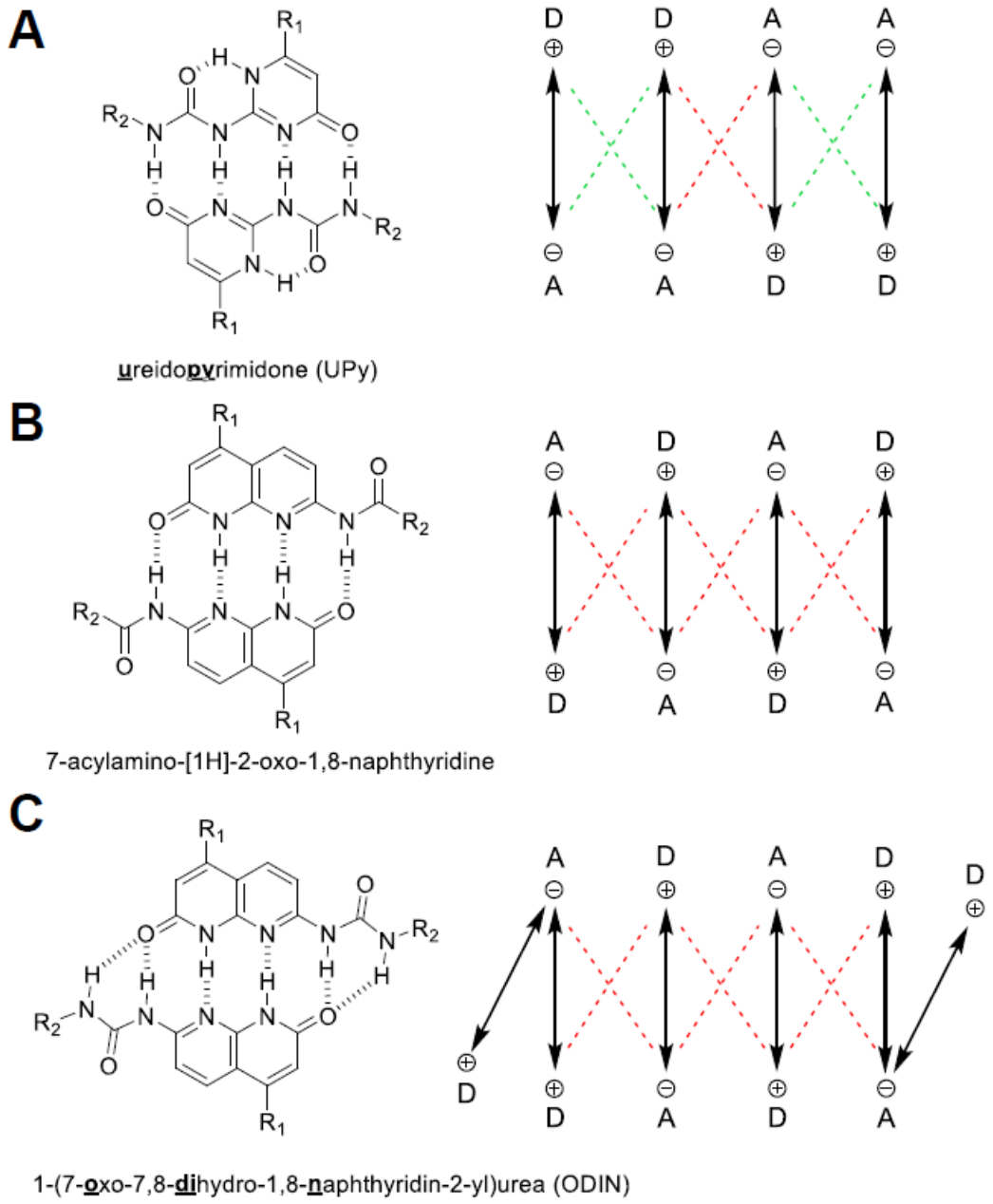

Figure 7. Chemical structures and hydrogen bonding arrays of A) UPy[21]; B) NAPY[22] and C) ODIN[23].

2. Aim of the work

The objective of this research is to synthesize liquid-crystalline reversible elastomeric materials, featuring either side-chain or main-chain geometry, that are reprocessable and photo-activatable. These materials will incorporate an azobenzene-based comonomer, which, through the reversible trans-cis isomerization process, will induce molecular-level movement. Leveraging the collective behaviour of liquid crystals, this molecular response will be translated into a macroscopic response within the material. Moreover, the liquid-crystalline nature of the material should facilitate its recovery to the original shape following the reverse isomerization process from cis to trans, enabling a high number of activation and recovery cycles. By incorporating non-covalent supramolecular crosslinking through hydrogen bonds, the material's mechanical properties can be enhanced while maintaining its reprocessability. Hydrogen bonds can be readily broken at elevated temperatures and reformed at lower temperatures, offering improved mechanical properties compared to standard thermoplastics while preserving full reprocessability.

3. Results and discussion

3.1 Side-Chain Liquid Crystal Elastomers

The first approach used for the synthesis of side chain liquid crystal elastomers involved the separate synthesis of the azobenzene derivative, which would serve both as a photo-actuator and a liquid crystal mesogenic unit, as well as the synthesis of a reversible H-bonding crosslinker (Scheme 1).

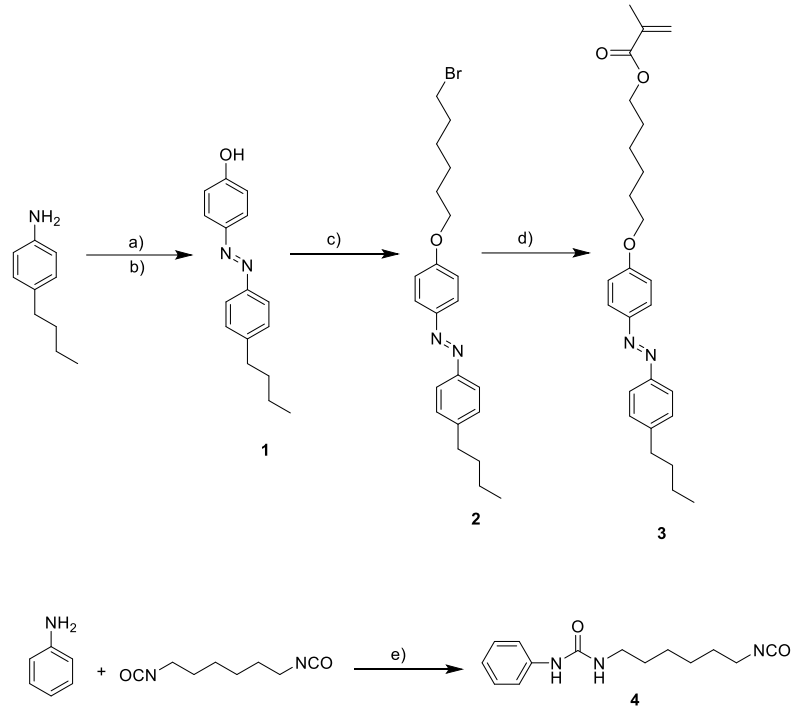

Scheme 1. *a) HCl, $NaNO_2$, water:acetone (1:1), -10 °C, 30 min; b) NaOH, Na_2CO_3, Phenol, -10 °C, 90 min, 63% yield; c) K_2CO_3, 1,6-dibromohexane, dry acetone, 60 °C, 20 h, 69% yield; d) K_2CO_3, methacrylic acid, dry DMF, 100 °C, 18 h, 95% yield; e) R.T, 5 h, 82% yield.*

The first step involved a standard aromatic electrophilic substitution using a diazonium salt as the electrophile. In step a), 4-butylaniline reacts with sodium nitrite ($NaNO_2$) and hydrochloric acid to form the diazonium salt, which is then directly reacted with phenol in step b) to form the corresponding azobenzene moiety. The purification by precipitation in dichloromethane/hexane afforded the target compound **1** as an orange solid in 63% yield. In the second step the phenol hydroxyl group was alkylated using dry acetone as solvent and 1,6-dibromohexane as electrophile in a basic environment of K_2CO_3. The purification by precipitation in dichloromethane/ethanol afforded the target product **2** as a yellow solid in 69% yield. The final step for the synthesis of monomer **3** is the SN_2 reaction between the sodium methacrylate and the brominated alkyl chain of the azo derivative. The reaction was carried out in dry DMF at 100°C for 18 hours to maximise the conversion. The target azobenzene derivative (compound **3**) was obtained as yellow solid in 95% yield by precipitation of the hot mixture into deionized water, and subsequent filtration. All the obtained compounds were fully characterized.

Separately, the synthesis of compound **4**, which will act as reversible crosslinker *via* hydrogen bonding, was achieved through a solvent-free reaction of aniline with hexamethylene diisocyanate (HMDI). Purification by recrystallization in cyclohexane yielded the target derivative **4** as white solid in 82% yield.

Once the azobenzene monomer was obtained, the chosen synthetic strategy for the final material involved the initial random radical polymerization of the three comonomers, followed by post-functionalization of the hydroxyethyl methacrylate group with compound **4** (Scheme 2). This approach allows for finer tuning of the crosslinking percentage due to the post-functionalization reaction.

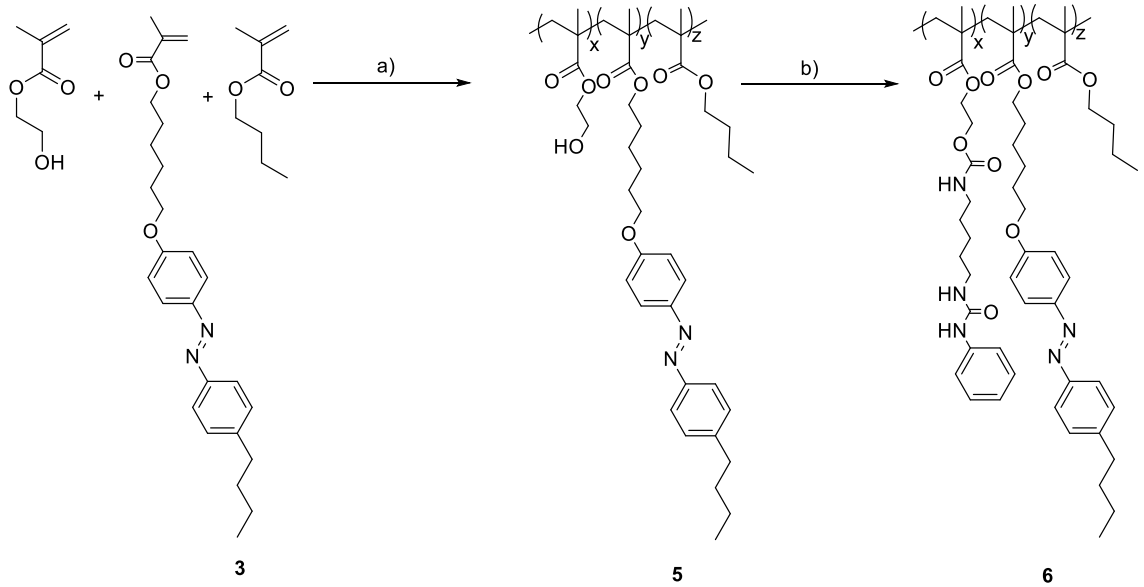

Scheme 2. *a) benzoyl peroxide, dry toluene, 80 °C, 48 h; b) DBTL, **4**, dry acetone, 80 °C, 20 h.*

The free radical polymerization involved the copolymerization between the azobenzene monomer **3** with 2-hydroxyethyl methacrylate (HEMA) and butyl methacrylate in a 4:1:3 molar ratio, respectively. HEMA was chosen as comonomer to take advantage of the OH groups for the introduction of the H-bonding motifs, while butyl methacrylate was chosen as diluent. Benzoyl peroxide (BPO) was used as radical initiator and dry toluene as solvent. The purification by precipitation in dichloromethane/methanol afforded the target prepolymer as a yellowish solid. The obtained polymer **5** was characterized by ^{1}H-NMR spectroscopy in $CDCl_3$ (Figure 8) and its liquid crystalline properties were investigated by DSC (Figure S1) and by polarized optical microscope (Figure 9).

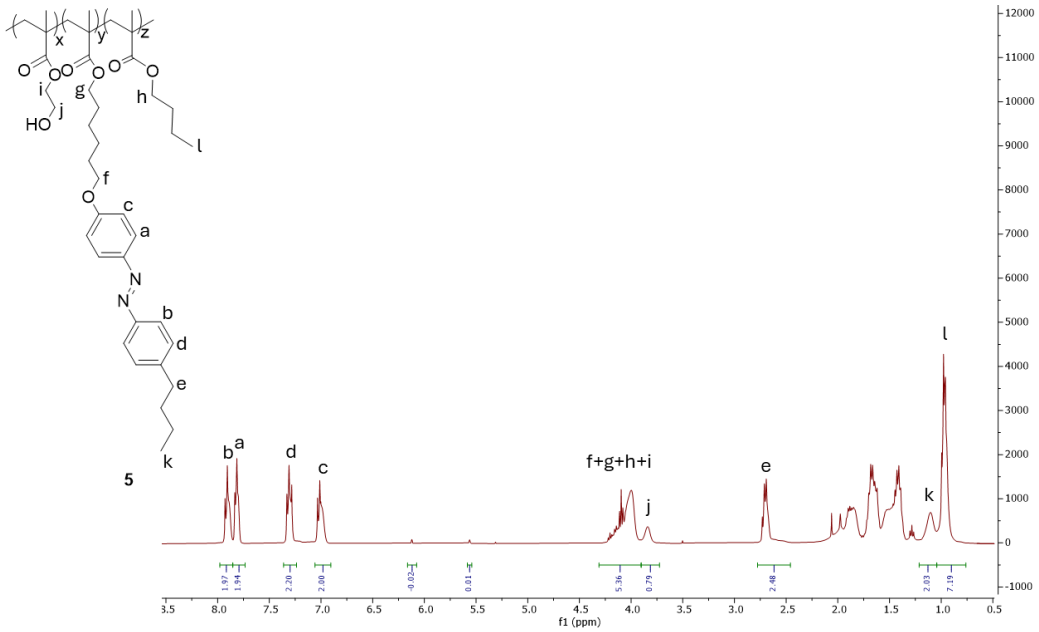

Figure 8. ^{1}H-NMR spectrum ($CDCl_3$, 25 °C; 400 MHz) of polymer **5**.

The ^{1}H-NMR spectrum shows the diagnostic signals belonging to the target polymer, including the aromatic protons *a*, *b*, *c*, and *d* belonging to the azobenzene moiety, the signal of protons *l* of to the butyl methacrylate alkyl chain, and the signal *j* belonging to the hydroxyethyl methacrylate. Furthermore, integration of the NMR spectrum enabled the determination of the molar ratio of the three comonomers resulting: 59% of monomer **3**, 16% butyl methacrylate, and 25% of hydroxyethyl methacrylate.

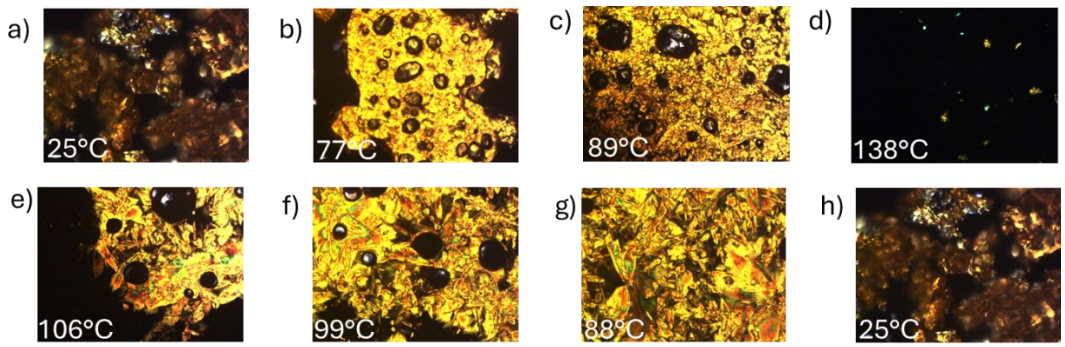

Figure 9. Polarized Optical Microscope (POM) images of polymer **5**. Heating ramp: a) 25 °C, b) 77 °C; c) 89 °C; d) 138 °C. Cooling ramp: e) 106 °C; f) 99 °C; g) 88 °C; h) 25 °C.

The images acquired with the polarized optical microscope (POM) show the birefringence typical of a liquid crystal elastomer. In agreement with the values obtained from the DSC analysis, heating the material from room temperature to 77 °C (Figure 9b) the appearance of the birefringence phenomenon is observed, which lasts until the transition to the isotropic

above 135 °C (Figure 9d). Consistently with the behaviour of a liquid crystal elastomer, once the material is cooled down, it shows again the phenomenon of birefringence confirming the reversibility liquid crystalline phase (Figures 9 e-h).
While the material exhibited the desired liquid crystalline properties, challenges arose during the synthesis of polymer **5**. When polymerizing the three monomers in pairs, the azo-containing monomer exhibited an inhibition effect on the reactivity of the other two comonomers. Hydroxyethyl methacrylate and butyl methacrylate reacted quantitatively when copolymerized together, but their conversion rates significantly decreased when copolymerized with the azo-comonomer. This significant challenge hindered the possibility of scaling up production and compromised batch-to-batch reproducibility in polymerization reactions.
Nevertheless, it was decided to test whether it was possible to graft the H-bonding moieties, present on compound **4**, onto the free OHs of the HEMA moieties and still maintaining the liquid crystalline properties. This provided the material with reversible supramolecular crosslinking *via* hydrogen bonding. Compounds **5** and **4** were reacted in dry acetone at 80 °C for 20 hours, using dibutylthin dilaurate (DBTL). Upon purification by precipitation in cold methanol, polymer **6** was recovered as dark orange solid and characterized by ^{1}H-NMR in chloroform-d ($CDCl_3$) (Figure 10), by DSC, and by POM.

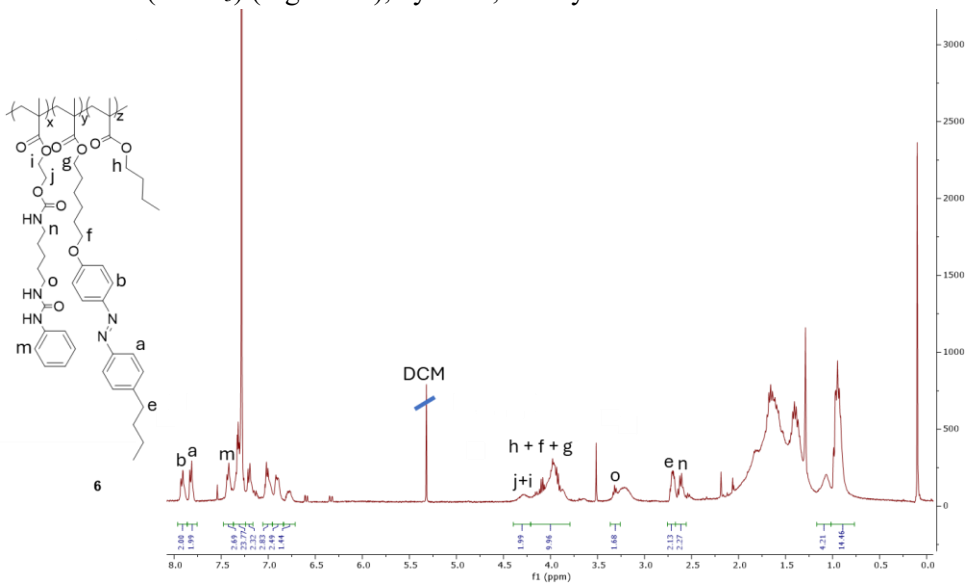

Figure 10. ^{1}H-NMR ($CDCl_3$, 70 °C, 400 MHz) of polymer **6**.

The proton NMR confirms the successful functionalization of polymer **5**; indeed, the spectrum shows the diagnostic signals of the grafted phenylurea, as the protons *m* of the aromatic ring and the signal *n* of the CH_2 next to the urethane group. The spectrum also highlights the complete functionalization of the HEMA groups with compound **4**, as evidenced by the integral of thew signal given by *i* and *j* protons of the functionalized HEMA at 4.27 ppm, which are now respectively in beta and alpha position from the urethane group.

Once determined the success of the grafting reaction, the material was analysed by DSC (Figure 11) and POM to assess the liquid crystalline behaviour (Figure 12).

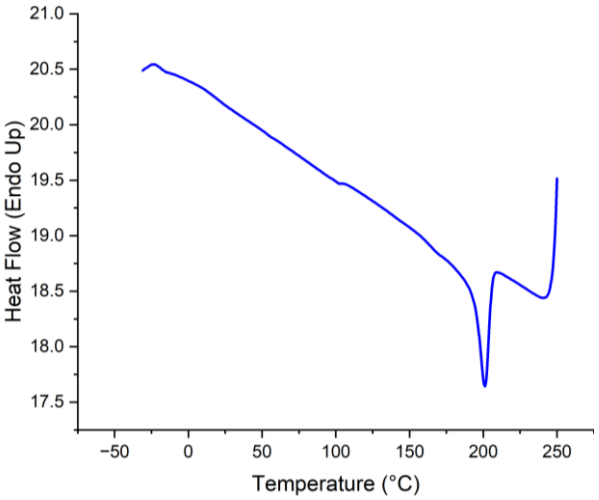

Figure 11. DSC analysis (second cooling ramp) of copolymer **6**.

DSC analysis revealed a single peak during the second cooling ramp. In a liquid crystalline material, two distinct peaks would be expected: one corresponding to the transition from the isotropic liquid to the mesophase, and another marking the end of the mesophase range. The absence of these characteristic peaks suggests that the material may not exhibit liquid crystalline behaviour. To further investigate, polarized optical microscopy (POM) was employed.

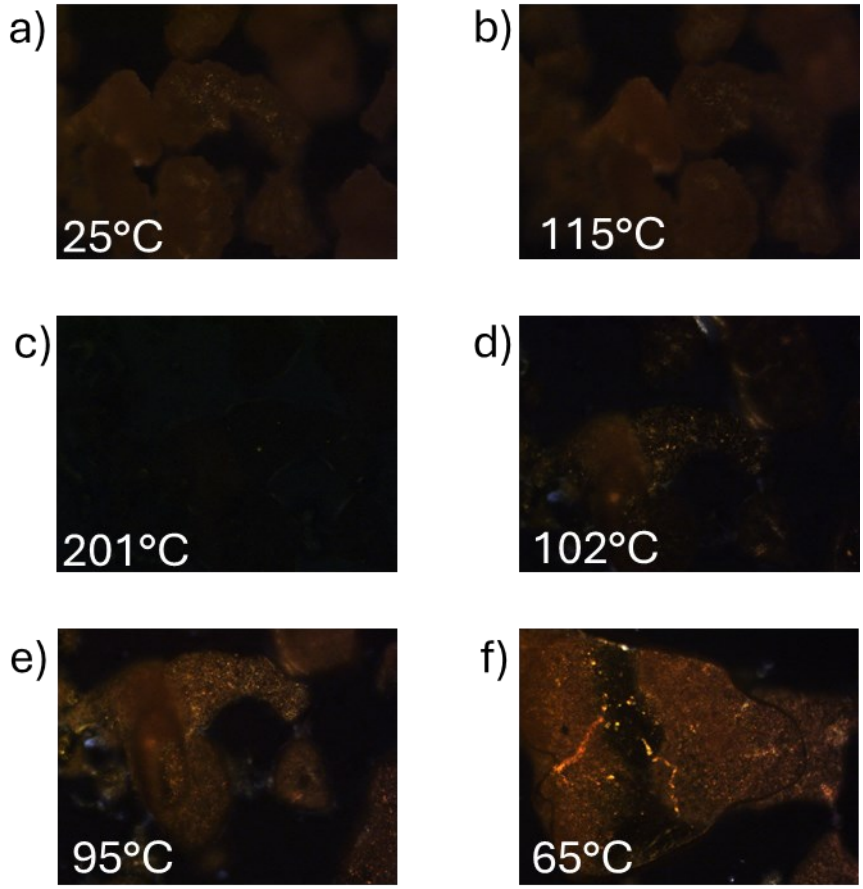

Figure 12. Polarized Optical Microscope (POM) images of polymer **6** acquired at: a) 25 °C before the heating ramp; b) 115 °C during the heating ramp; c) 201 °C at the end of the heating ramp; d) 102 °C during the cooling ramp; e) 95 °C during the cooling ramp; f) 65 °C during the cooling ramp.

Images acquired with the polarized optical microscope (POM) revealed a barely visible birefringence phenomenon, making it challenging to definitively confirm the liquid crystalline properties of polymer **6**. However, a transition, potentially attributable to the shift from the liquid crystalline mesophase to an isotropic liquid during heating (Figure 12b-c) and its reverse transition during cooling (Figure 12d-e), was observed. Nevertheless, as previously mentioned, the phenomenon was not pronounced enough to conclusively demonstrate the liquid crystalline nature of the material. Probably, the high number of hydrogen bonds decreases a lot the average molecular mobility even at high temperatures.
Given the challenges encountered in synthesizing polymer **6** due to the reactivity of the monomers and the difficulties in demonstrating its liquid crystalline nature, an alternative strategy was adopted involving the selection of a different mesogen to impart liquid crystalline properties.

As new mesogen, we selected the biphenyl ester derivative **10** (Scheme 3). Biphenyl derivatives are popular mesogens in liquid crystal research due to their high thermal stability and strong molecular ordering, making them ideal for thermotropic liquid crystals.[24] In this new approach, the mesogen will be employed as a comonomer alongside HEMA in the polymerization reaction, while azobenzene will act as a photoactuator but not as a comonomer. Azobenzene will be incorporated through a post-functionalization reaction, as compound **3** has probably an inhibitory effect on the reactivity of other comonomers, hindering the production of high-molecular-weight materials with high monomer conversion levels.

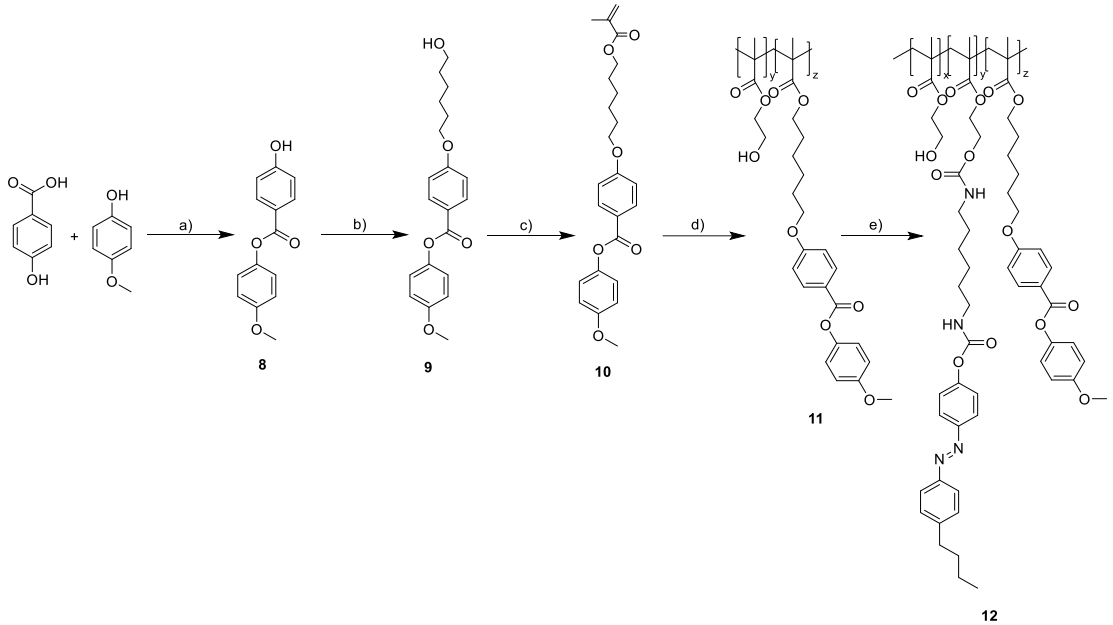

Scheme 3. *a) $B(OH)_3$, H_2SO_4, Toluene:xylene (3:1), 110°C, 24h, 50% yield; b) K_2CO_3, 6-bromo-1-hexanol, dry acetonitrile, 80°C, 48h, 55% yield; c) methacryloyl chloride, Et_3N, dry DCM, RT, 16h, 75% yield; d) 2-hydroxyethyl methacrylate, AIBN, dry toluene, 80°C, 24h; e) 7, DBTL, dry MEK, 70°C, 24h.*

The initial step involved the synthesis of compound **10** and the characterization of its liquid-crystalline properties. An esterification reaction between 4-methoxyphenol and 4-hydroxybenzoic acid was conducted to construct the rigid core of the mesogen. This reaction also preserved a free phenolic hydroxyl group for subsequent alkylation. The core synthesis reaction was carried out in a toluene:xylene (3:1) solvent mixture, using dual catalysis from boric acid and sulfuric acid. The progress of the reaction was monitored by observing the formation of a gray precipitate, which was filtered and washed with a ethanol:water (1:1) mixture, yielding the target product **8** as a light grey solid with a 50% yield.

The second step entailed the alkylation of the free phenolic hydroxyl group in a basic environment using potassium carbonate in dry acetonitrile, with 6-bromo-1-hexanol serving

as the alkylating agent. Purification of the crude reaction product through column chromatography on silica gel resulted in the target product **9** with a 55% yield.
The final step was an esterification reaction between derivative **9** and methacryloyl chloride. The reaction was performed in dry dichloromethane using triethylamine as an acidity scavenger. Purification of the crude product by column chromatography yielded the target compound **10** as a white solid with a 75% yield.
Derivative **10** was characterized by NMR spectroscopy (Figure 13), and by DSC and POM to confirm its liquid-crystalline properties.

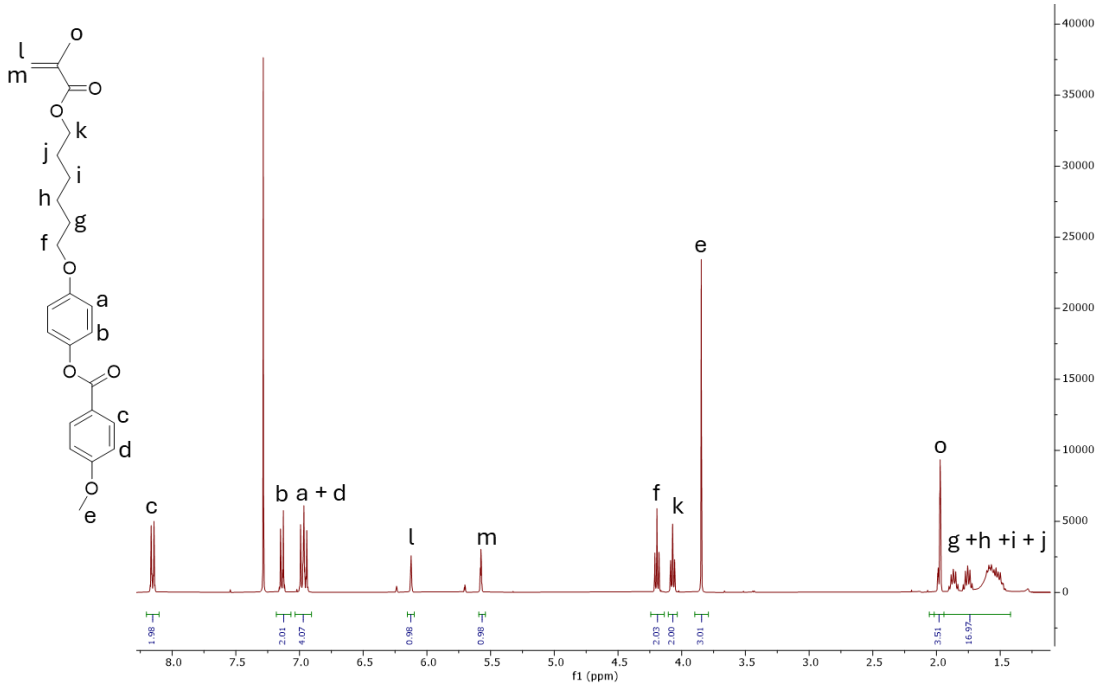

Figure 13. ^{1}H-NMR ($CDCl_3$, 25 °C, 400 MHz) of liquid crystal **10**.

The ^{1}H-NMR spectrum exhibited all signals corresponding to the target molecule, in particular the diagnostic signals of the olefin protons *l* and *m* of the methacrylate unit and the alpha-methyl group adjacent to the double bond *o*.
DSC analyses (Figure 14) and polarized optical microscope images (Figure 15) confirmed the liquid-crystalline nature of the molecule.

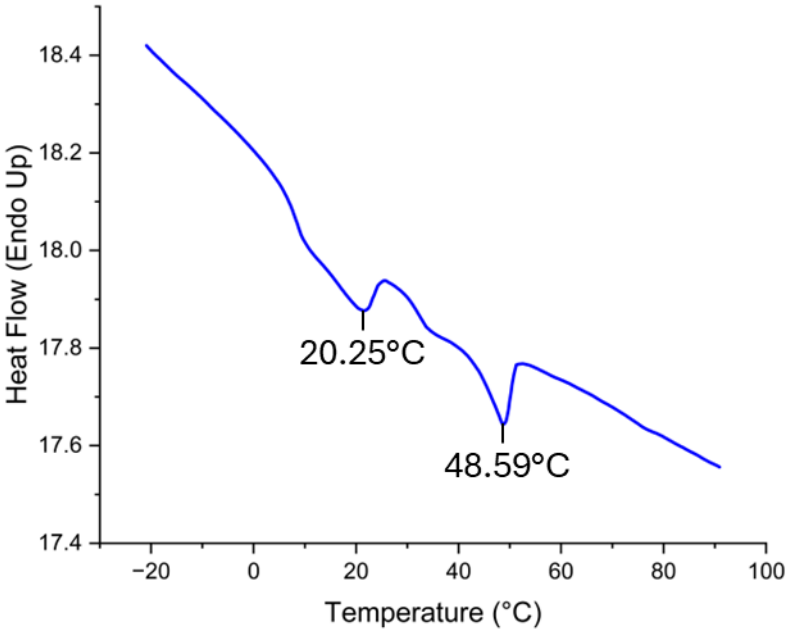

Figure 14. DSC analysis (second cooling ramp) of derivative **10**.

The cooling curve of the DSC analysis revealed two transitions: one at 48.59 °C corresponding to the transition from isotropic liquid to the mesophase, and the second at 20.25 °C corresponding to the transition of the mesophase to the solid phase. Additionally, polarized optical microscopy images (Figure 15) showed the phenomenon of birefringence, which appeared upon heating from 25 °C to 36 °C (Figures 15a and b), and disappeared at 50 °C, marking the transition from the mesophase to the isotropic liquid. Upon cooling, the birefringence phenomenon reappeared after the transition from isotropic liquid to mesophase (Figure 15d).

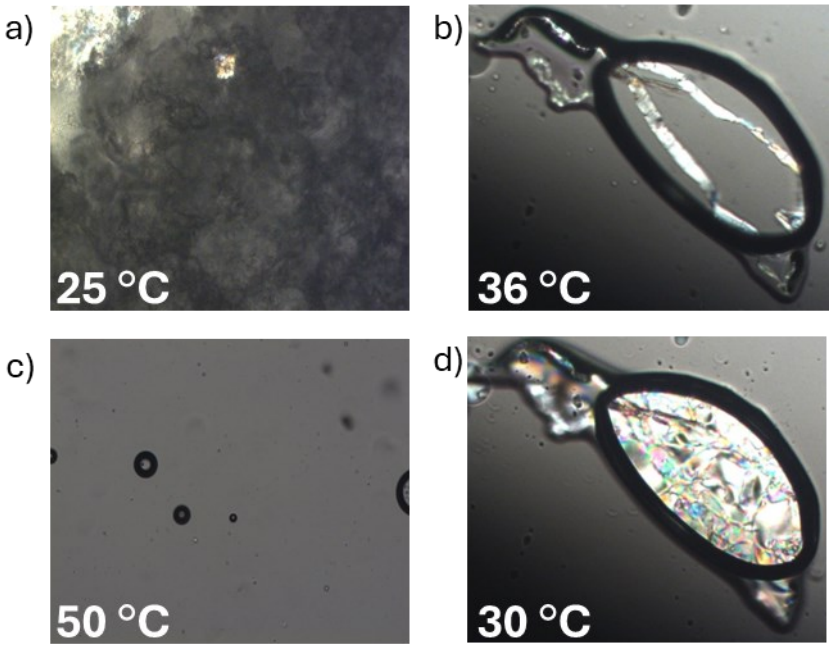

Figure 15. Polarized optical microscope images of liquid crystal **12** taken at: a) 25 °C before starting the heating ramp; b) 36 °C during heating ramp; c) 50 °C at the end of the heating ramp; d) 30 °C during the cooling cycle.

Monomer **10** was then co-reacted with HEMA through a random radical copolymerization to obtain polymer **11** (Scheme 3), which was characterized through ^{1}H-NMR spectroscopy and DSC analysis (Figures S3-4). Last step involved grafting of the azobenzene derivative onto polymer **12** by reacting the OH groups of the HEMA with the isocyanate moieties of the azobenzene unit (Scheme 3). This introduced photo-actuation properties. Compound **12** was characterized by ^{1}H-NMR spectroscopy (Figure 16) in deuterated chloroform, and by DSC (Figure 17) and POM analyses (Figure 18) to confirm its liquid-crystalline nature.

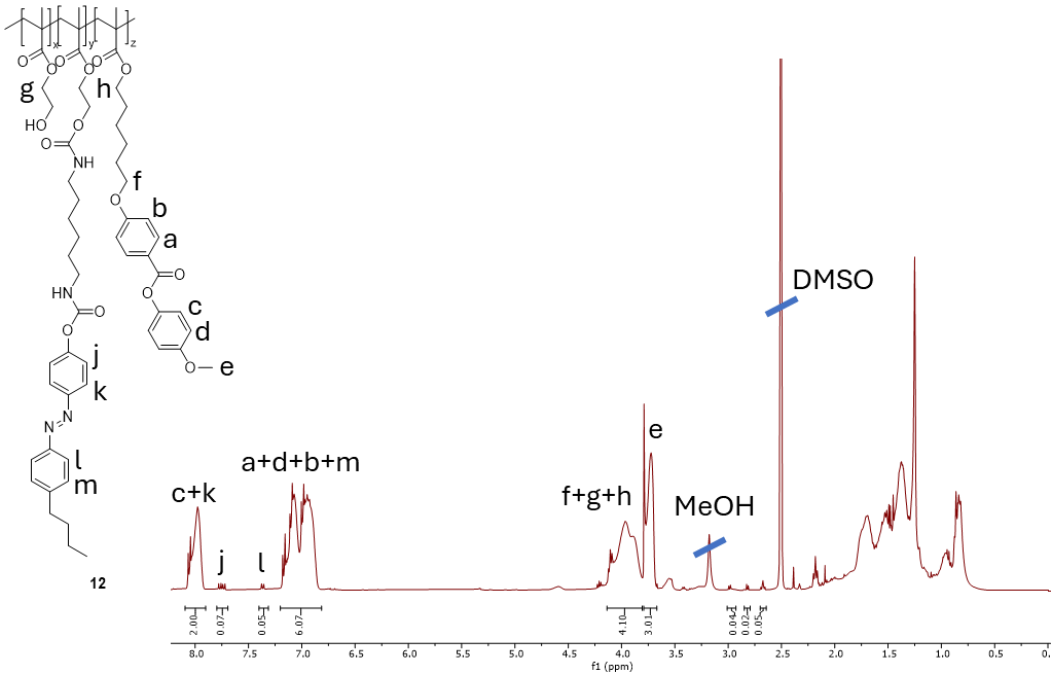

Figure 16. ^{1}H-NMR (DMSO-d_6, 60 °C, 400MHz) of polymer **12**.

The NMR spectrum displayed all diagnostic signals of the material, including the protons of the azobenzene aromatic rings (*j* and *l*), and the mesogen aromatic rings (*c, a, d and b)*. DSC analysis (Figure 17) did not reveal distinct peaks indicative of a liquid crystalline phase, only highlighting a prominent peak at 41°C.

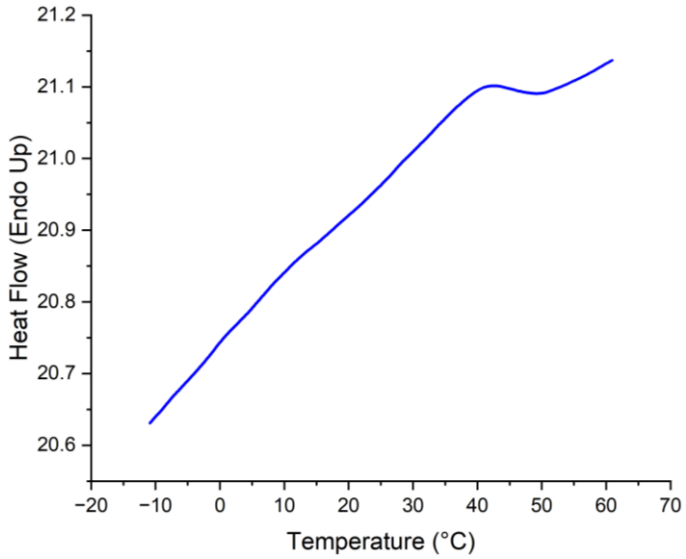

Figure 17. DSC analysis (second heating ramp) of copolymer **12.**

To gain further insights into the possible liquid crystalline nature of the material, the polymer was observed under polarized optical microscopy (POM) to detect the birefringence phenomenon typical of liquid crystalline materials and the transition from a liquid crystal to an isotropic liquid as the temperature increases.

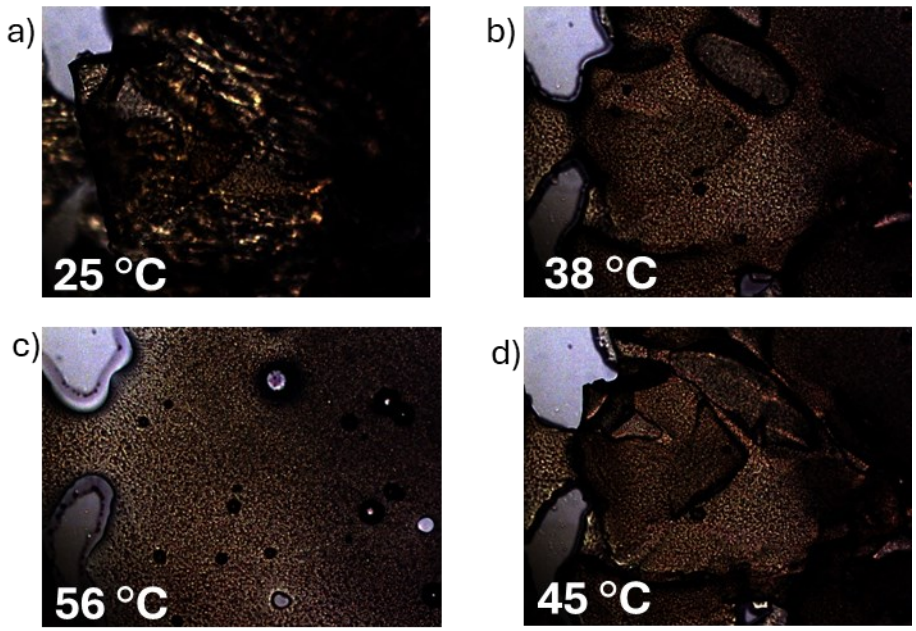

Figure 18. Polarized optical microscope images of polymer **12**: a) image taken at room temperature before starting the heating ramp; b) image acquired at 38 °C during the heating ramp; c) image acquired at 56 °C at the end of the heating ramp; d) image taken at 45 °C during the cooling ramp.

Similar to the previous case, polarized optical microscopy (POM) images of copolymer **12** did not exhibit significant birefringence phenomena, making it challenging to attribute liquid crystalline properties to the material. The incorporation of the azobenzene unit likely disrupted the liquid crystalline domains, hindering the mesogen ability to impart liquid crystalline properties to the final material.
Furthermore, attempts to electrospin the synthesized materials resulted in inefficient fiber formation, producing a mixture of thin fibers and electrospray droplets. This is likely attributed to the low molecular weight of the materials, which hindered adequate polymer chain entanglement.

3.2 Main-chain liquid crystal elastomers

Since it is not possible to synthesize a side-chain liquid crystalline elastomer functionalized with an azobenzene derivative to be used as a photoactuator, a strategic shift was made to focus on synthesizing main-chain liquid crystals incorporating azobenzene units as photo-

actuators to achieve macroscopic material responses to external stimuli. Once more, a biphenyl ester derivative was chosen as the mesogen, valued for its robust thermal stability and excellent molecular ordering. For the polymer matrix, a polyurethane was selected due to its proven capacity to form fibers efficiently in the electrospinning process.
The synthesis of the mesogen, outlined in scheme 4, involved a linear approach, starting from an esterification reaction between p-hydroquinone and 4-hydroxybenzoic acid to construct the aromatic core. The two phenolic units can then be alkylated with an alkyl chain, introducing a flexible component to balance the rigidity of the aromatic core and forming the liquid crystalline mesogen. The alkylating chain, terminated with a hydroxyl group, provides the necessary functionality for subsequent polymerization with an isocyanate to yield a polyurethane-based matrix. The urethane groups formed during the polymerization reaction, acting as excellent hydrogen bond donors and acceptors, are expected to establish numerous supramolecular interactions between polymer chains, thereby providing a highly oriented liquid crystalline domain.

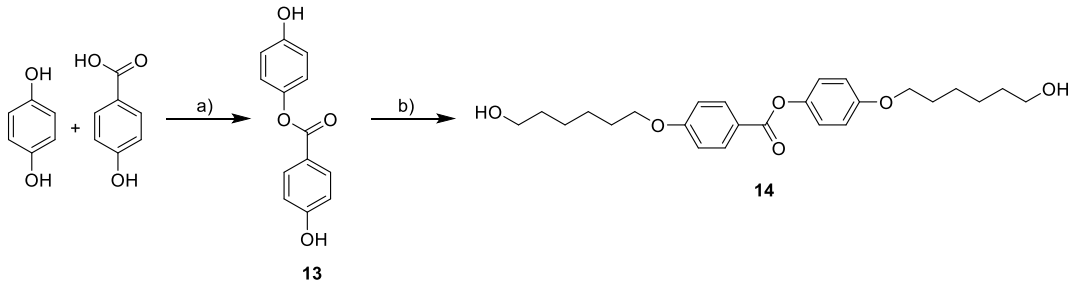

Scheme 4. *a) $B(OH)_3$, H_2SO_4, toluene:xylene (3:1), 110°C, 24h, 40% yield; b) 6-bromo-1-hexanol, K_2CO_3, dry acetonitrile, 80°C, 48h, 70% yield.*

The reaction was conducted under reflux in a toluene-xylene (3:1) mixture, employing dual catalysis from boric acid and sulfuric acid. The precipitate formed during the reaction was filtered and thoroughly washed with deionized water to remove excess hydroquinone, resulting in a 40% yield of the target compound **13**.
Once compound **13** was obtained, alkylation of the phenolic units was performed using 6-bromo-1-hexanol as the alkylating agent in a basic solution of K_2CO_3, in dry acetonitirile. Purification through silica gel chromatography yielded the target liquid crystal **14** with a 70% yield. The product was characterized by ^{1}H-NMR spectroscopy (Figure 19) in $CDCl_3$, and its liquid-crystalline nature was investigated using DSC and POM analyses.

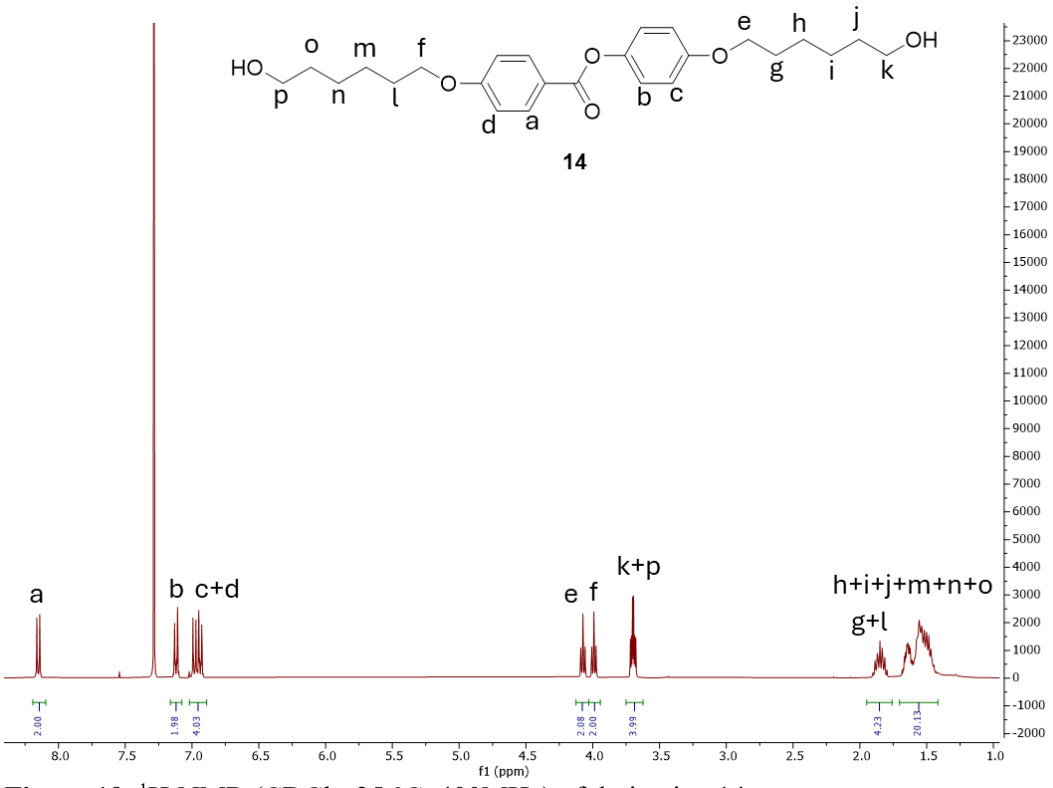

Figure 19. ^{1}H-NMR ($CDCl_3$, 25 °C, 400MHz) of derivative **14**.

The spectrum displayed all expected signals for the target molecule, including the diagnostic signals of the aromatic core (*a*, *b*, *c*, *d*), and the CH_2 in the alpha position relative to the phenolic oxygen (*e*, *f*) and the terminal hydroxyl groups (*k*, *p*). DSC analysis (Figure 20) confirmed the liquid-crystalline nature, revealing typical phase transition peaks, one at 106 °C related to the transition from isotropic liquid to mesophase, the second at 87 °C related to the end of the mesophase range.

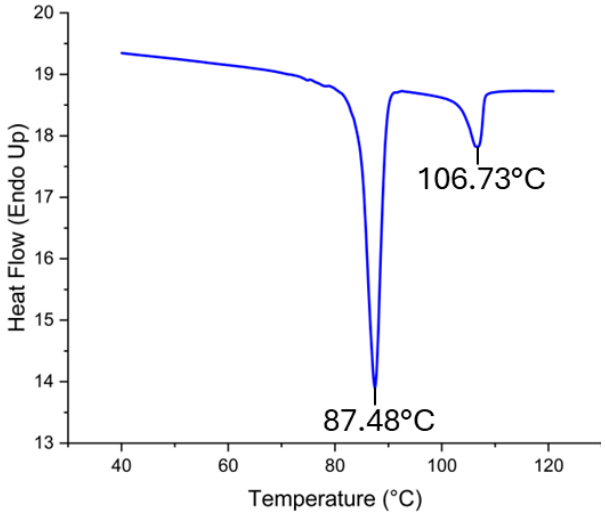

Figure 20. DSC analysis (second cooling ramp) of derivative **14**.

Polarized light microscopy images (Figure 21) further supported the liquid crystalline behaviour of compound **14**, showing birefringence. In particular, upon heating the material from room temperature to 87 °C (Figures 21a and b), the emergence of birefringence was observed, indicating entry into the mesophase range. This mesophase persisted at 100 °C and 103 °C (Figures 21c and d) before transitioning to an isotropic liquid at 106 °C (Figure 21e). The birefringence reappeared upon cooling the sample to a temperature within the mesophase range (Figure 21f).

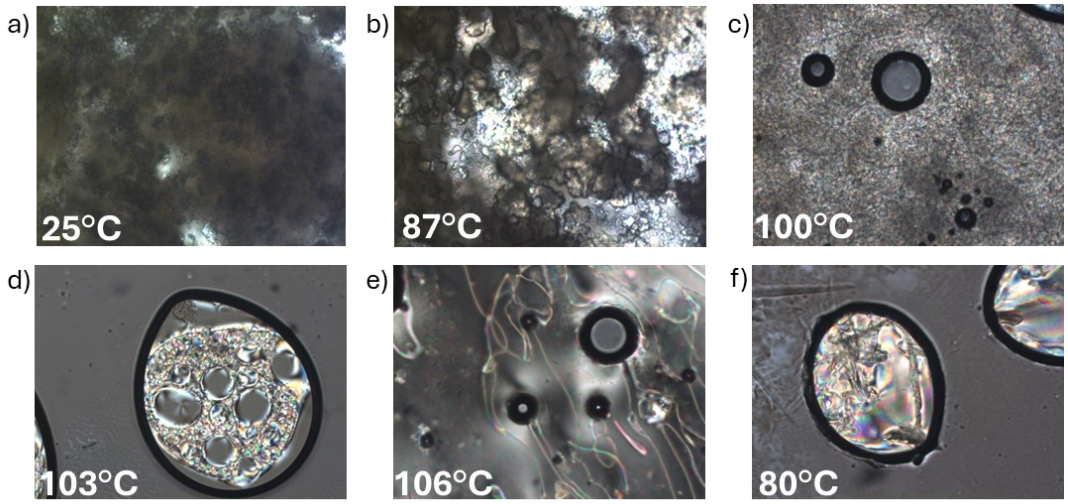

Figure 21. Polarized optical microscope images of liquid crystal monomer **14**: a) image acquired at 25 °C; b) image acquired at 87 °C during the heating ramp; c) image acquired at 100 °C during the heating ramp; d) image acquired at 103 °C during the heating ramp; e) image acquired at 106 °C at the end of the heating ramp; f) image acquired at 80 °C during the cooling ramp.

Having confirmed the liquid-crystalline nature of derivative **14**, the subsequent step involved formulating a polyurethane-based material exhibiting the desired liquid-crystalline properties. An initial attempt entailed direct polymerization of derivative **14** with hexamethylene diisocyanate. However, the resulting material did not display liquid-crystalline characteristics, likely due to the excessive rigidity of the matrix, which hampers the efficient mobility of the mesogens.

To enhance the material flexibility, tetraethylene glycol was added as comonomer with chain extender function.

To impart desired photoactuation properties to the material, an azobenzene comonomer was synthesized (scheme 5). The synthesis involved alkylating the two phenolic units of azobenzene with six-carbon alkyl chains terminating in hydroxyl groups. This approach aimed to ensure similar reactivity between the alkyl OH groups of the azo, mesogen, and chain extender, maximizing conversion of all three polyols in the polymerization reaction. Additionally, the incorporation of two sufficiently long alkyl chains onto azobenzene was expected to minimize changes to material rigidity, preserving good mesogen mobility.

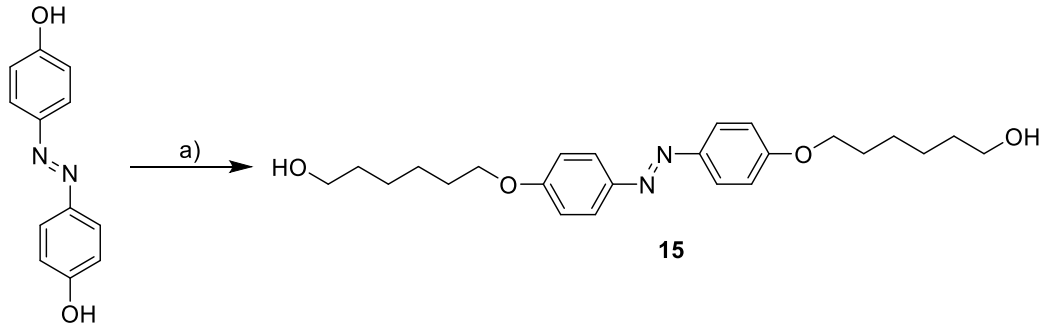

Scheme 5. *a) K_2CO_3, 6-bromo-1-hexanol, dry acetonitrile, 80°C, 48h, 80% yield.*

The alkylation reaction of the phenolic OH groups of azobenzene was carried out using potassium carbonate as a base for deprotonation, 6-bromo-1-hexanol as the alkylating agent, and dry acetonitrile as the solvent. Purification of the crude reaction product through precipitation from dichloromethane/hexane resulted in a yield of 80% for the target comonomer **15**.

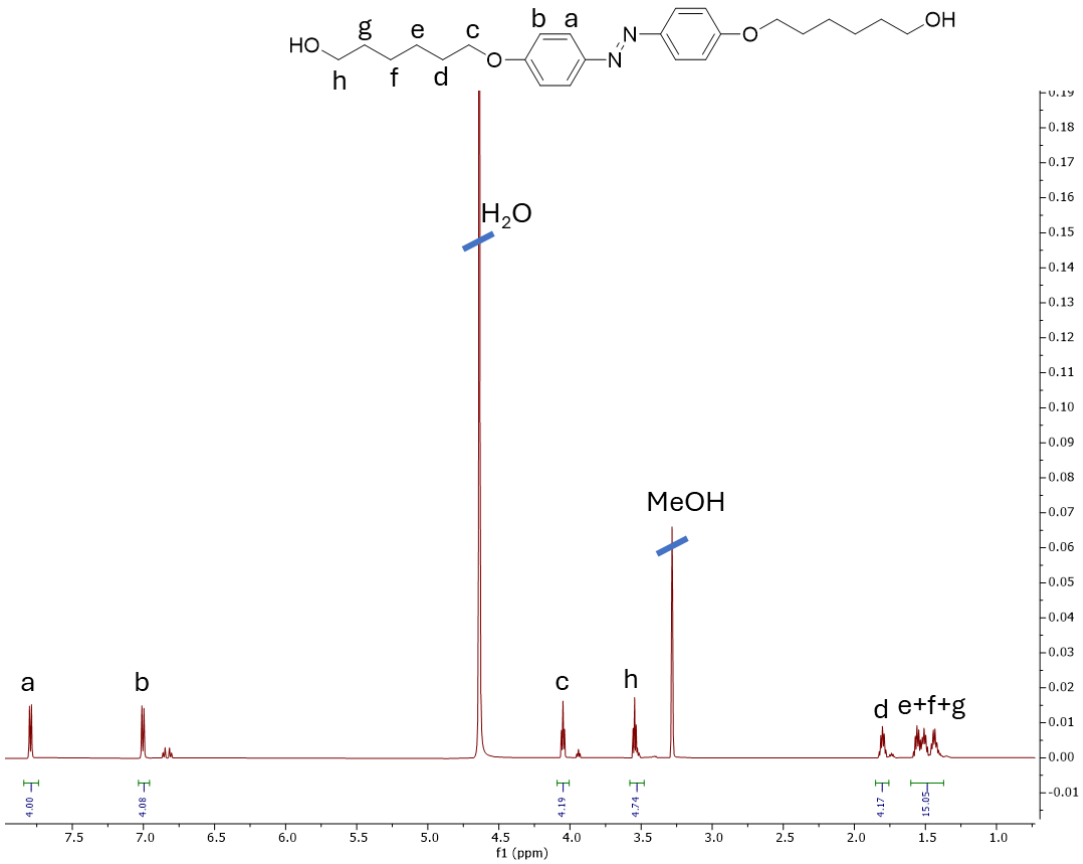

Figure 22. ^{1}H-NMR (MeOD-d$_4$, 25 °C, 400 MHz) of derivative **15**.

The monomer was characterized by ^{1}H-NMR spectroscopy in MeOD-d$_4$, (Figure 22) revealing all diagnostic signals corresponding to the target molecule, including the aromatic signals of azobenzene (*a* and *b*), and the CH_2 signals of the alkyl chain in the alpha position with respect to both the terminal hydroxyl groups *h* and the phenol moieties *c*. Azobenzene derivative **15** was then polymerized together with mesogen **14**, hexamethylene diisocyanate and tetraethylene glycole to obtain a polyurethane-based liquid crystal. The tetraethylene glycol was added as chain extender to enhance the mobility of the polymer chain in order to favour the mobility of the mesogen units.

A 2:1 molar ratio of mesogen to chain extender was selected for the formulation, with 15% azobenzene actuator used as a comonomer, while the isocyanate was added to stoichiometrically match all the -OH functionalities coming from the three polyols (3.15 eq. in total) (Scheme 6).

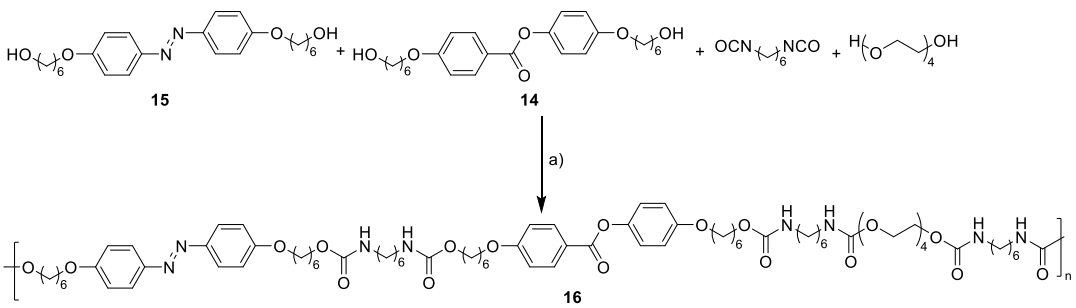

Scheme 6. *a) Dry DMF, DBTL, 25°C, 48h.*

The reaction was carried out in dry DMF to ensure polymer solubility during the reaction, employing DBTL as a catalyst. The target polymer was recovered by precipitating the reaction mixture in cold methanol. ^{1}H-NMR spectroscopy in DMSO-d_6 (Figure 23) was used to characterize the obtained material, confirming the presence of all diagnostic signals of the target polymer.

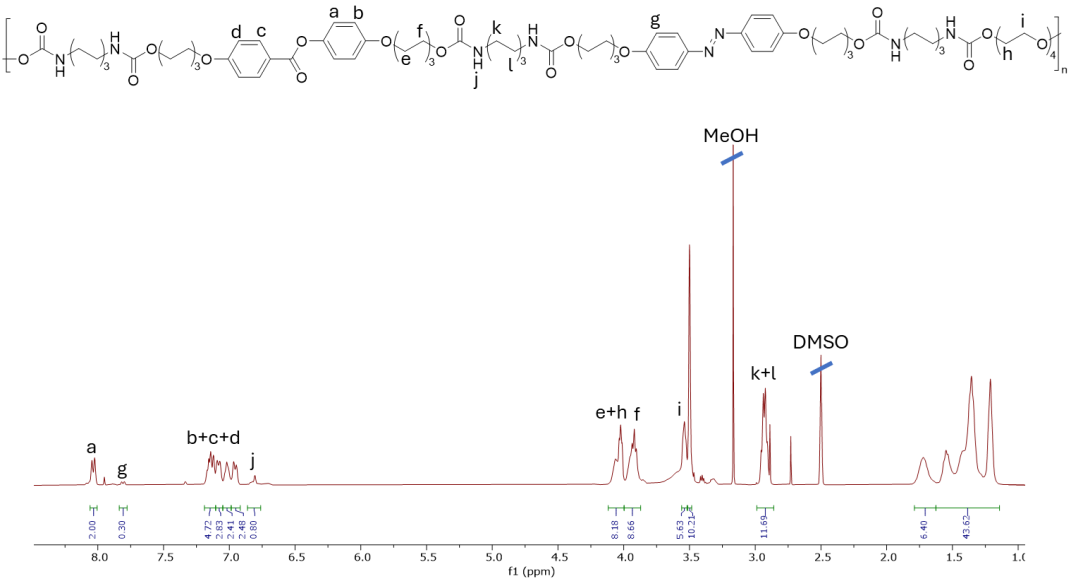

Figure 23. ^{1}H-NMR spectrum (DMSO-d_6, 25 °C, 400MHz) of copolymer **16**.

Notably, the incorporation of all three polyols into the final material was evidenced by the presence of aromatic ring signals corresponding to the azo and mesogen units (*g* and *a* respectively), as well as the CH_2 signals of tetraethylene glycol (*h* and *i*). Furthermore, integration of the NMR spectrum confirmed that the molar ratio of the three monomers in the resulting polymer closely matched the stoichiometric ratio employed in the polymerization reaction.

In collaboration with the group of Professor Chiara Gualandi in Bologna, the material was subsequently processed via electrospinning, and its photo-actuation properties and liquid-crystalline nature were investigated. During electrospinning, the material exhibited excellent fiber formation as it exited the needle, with fibers collected initially on a static support and subsequently on a rotating drum. Scanning electron microscopy (SEM) analysis (Figure 24) of the fibers collected on both static (Figure 24a-b) and dynamic supports (Figure 24c-d) confirmed the material high fiber-forming capacity and demonstrated that the use of a dynamic support (rotating drum) for fiber collection enabled the formation of a highly ordered material with aligned fibers in the same direction.

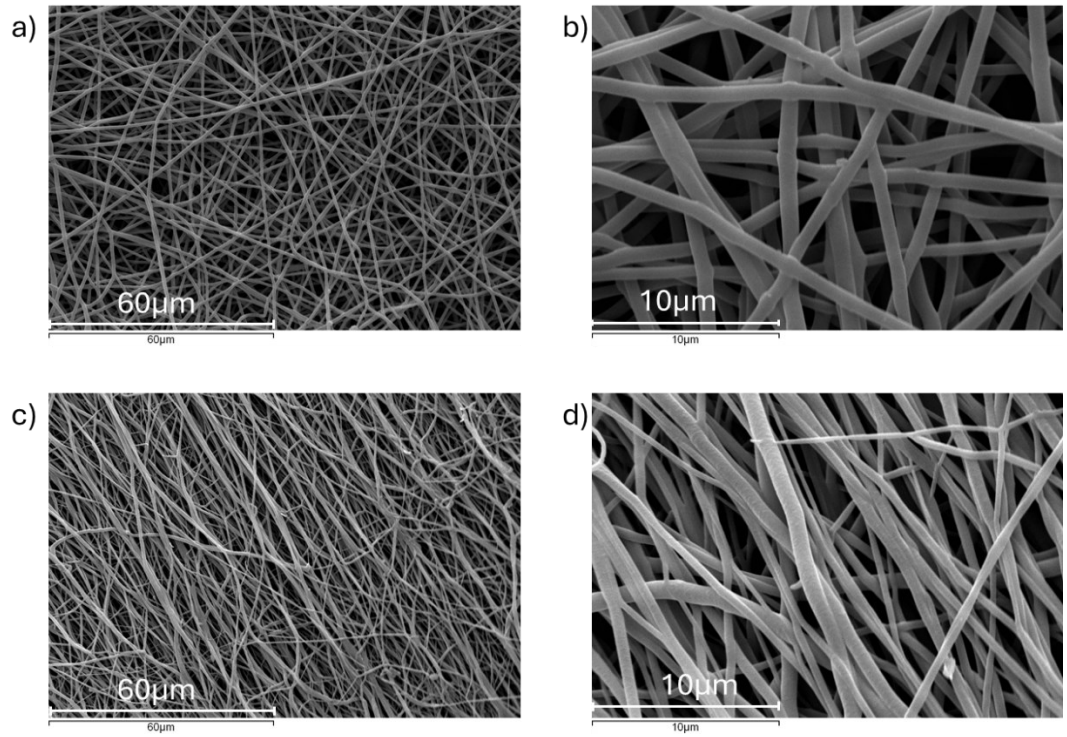

Figure 24. Scanning electron microscope (SEM) images at different magnifications of electrospun copolymer **16**: a) and b) fibers collected onto static support; c) and d): electrospun oriented fibers collected onto rotating drum.

Having successfully electrospun the material into oriented fibers, the liquid crystalline nature of the material was investigated through DSC analysis. However, the analysis failed to reveal characteristic peaks indicative of mesophase transitions. The loss of liquid crystalline properties following the polymerization reaction may be attributed to the mesogen lacking a sufficiently rigid aromatic core; thus, the macroscopic movement generated by azobenzene actuation may be due to the high flexibility of the material rather than the collective behavior of the mesogens. To confirm this theory, the material response to UV light stimulus and potential movement reversibility were tested. The cis-trans isomerization of azobenzene,

coupled with the collective behavior of mesogens, was anticipated to induce a macroscopic response. A strip of the material was clamped, irradiated with UV light to initiate azobenzene isomerization, and subsequently observed to undergo a macroscopic response, bending spontaneously in the direction of the light source (Figure 25).

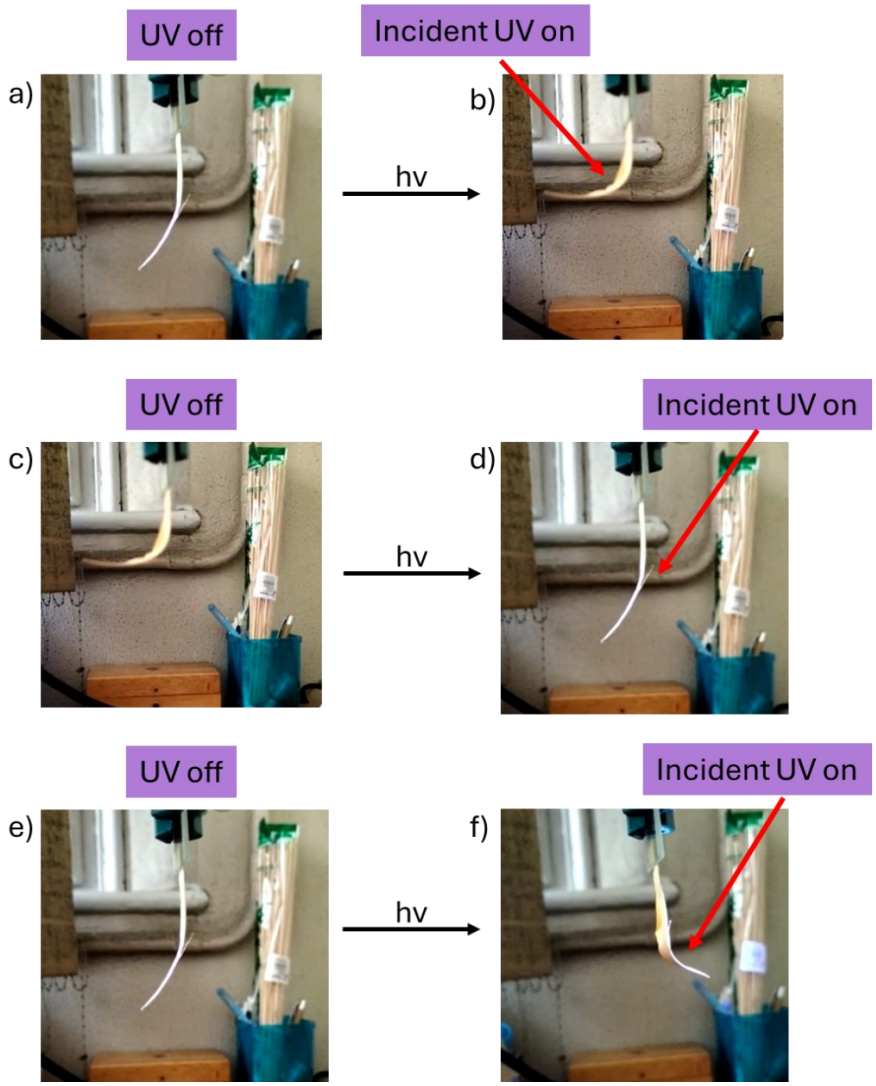

Figure 25. Light-triggered activation of the electrospun copolymer **16** in the direction of the incident UV light source (direction of incident UV light indicated by the red harrow): a) original shape of the specimen; b) shape acquired when the polymer is irradiated with UV light coming from the left side; c) shape maintained also when the UV light is remove; d) original shape recovered only when UV irradiation is applied on the other side of the specimen (right side) to trigger the opposite movement; e) original shape maintained when the UV source is removed; f)shape acquired when the polymer is irradiated with UV light coming from the right side.

While the material exhibited a single instance of light-induced response, it failed to demonstrate reversibility, remaining fixed in the shape imparted by azobenzene activation. A strip of the material was suspended from a support (Figure 25a) and prior to UV light irradiation, the material exhibited a specific, unbent shape. Upon irradiation with ultraviolet light from the left side (Figure 25b), the material bent towards the light source. However, after removing the UV light, the material retained its bent shape (Figure 25c). To revert the material to its original shape, a second UV light stimulus was applied from the opposite side (right side) (Figure 25d). Once the UV light was removed, the material maintained its shape, as induced by the second light stimulus (Figure 25e). Continuous UV light irradiation from the right side resulted in further bending of the material (Figure 25f), with the bent shape persisting even after the removal of the light source. In a liquid-crystalline material, the collective behavior of mesogens would facilitate a return to the original shape upon removal of the light stimulus (due to reversible cis-trans isomerization of azobenzene), enabling multiple activation and recovery cycles. However, in this case, despite exhibiting desired photoactuation capabilities, the material lacked the necessary liquid-crystalline properties.
At the light of the obtained results, we decided to change the mesogen and we turned our attention to a mesogen featuring a core composed of three aromatic rings linked by two ester bonds. This modification aimed to preserve the mesogen rigidity post-polymerization, thereby maintaining liquid-crystalline properties in the final material. The additional aromatic ring increases the overall rigidity of the mesogen, which can enhance the stability of the liquid crystalline phase. This rigidity helps maintain the ordered arrangement of molecules necessary for liquid crystallinity. Moreover, more aromatic rings can provide greater π-π stacking interactions and other intermolecular forces, which can lead to stronger and more stable liquid crystalline phases. This improved interaction can enhance the temperature range over which the mesogen remains in a liquid crystalline state. Summarizing, the addition of a third aromatic ring can significantly enhance the structural and functional properties of mesogens, leading to better liquid crystalline behavior.[25,26]
The chosen mesogen was synthesized following the outlined Scheme 7.

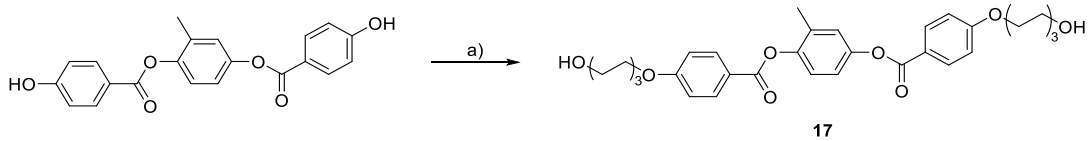

Scheme 7. *a) 6-Bromohexan-1-ol, K_2CO_3, dry Acetonitrile, 80°C, 48h, 75% yield.*

Similarly to the previous mesogen, the two phenolic functionalities at the ends of the aromatic core were alkylated via an SN_2 bimolecular nucleophilic substitution reaction using 6-bromohexan-1-ol as the alkylating agent, in a basic potassium carbonate environment, using acetonitrile as the solvent. Purification through silica gel column chromatography resulted in a 75% yield of the target mesogen **17**. Compound **17** was characterized by ^{1}H-NMR spectroscopy in Acetone-d_6 (Figure 26).

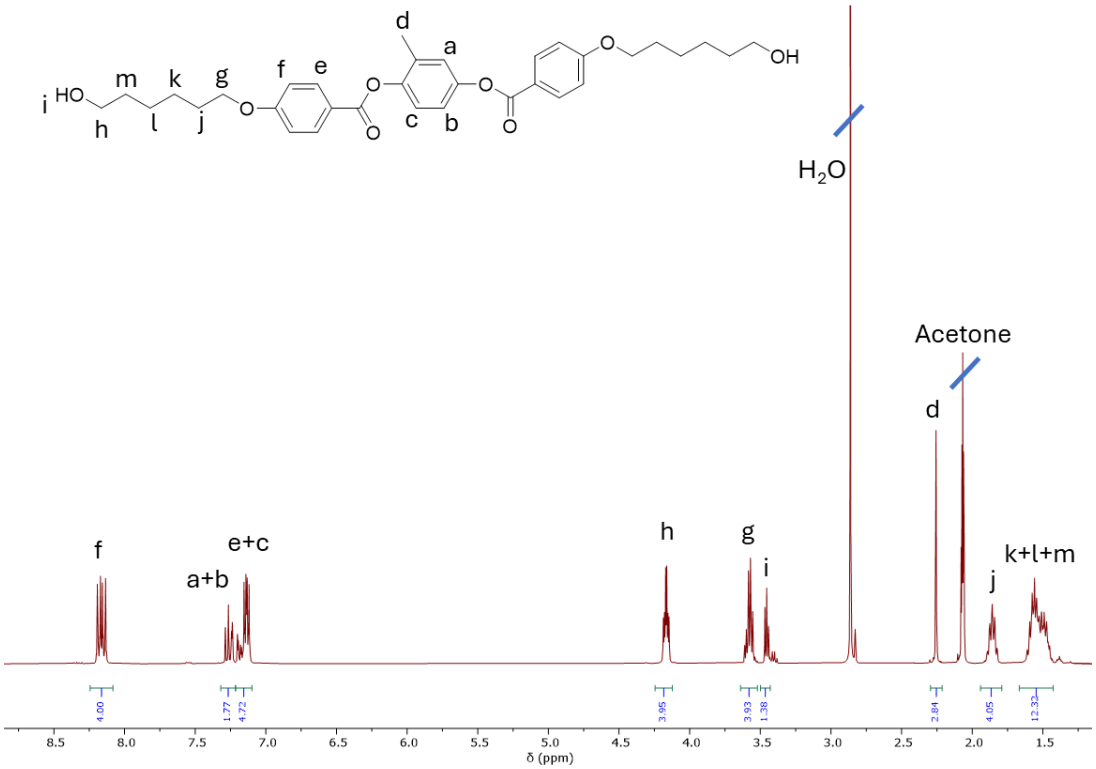

Figure 26. ^{1}H-NMR spectrum (Acetone-d_6, 25°C, 400 MHz) of compound **17**.

The spectrum exhibited all the signals corresponding to the target molecule, including the aromatic core signals (*a*, *b*, *c*, *e*, *f*), the methyl group signal *d* of the central ring within the aromatic core, and the alkyl chain signals. To confirm the liquid-crystalline behaviour of the target molecule, DSC analysis (Figure S7) and polarized light optical microscopy (POM) (Figure 22) were employed.

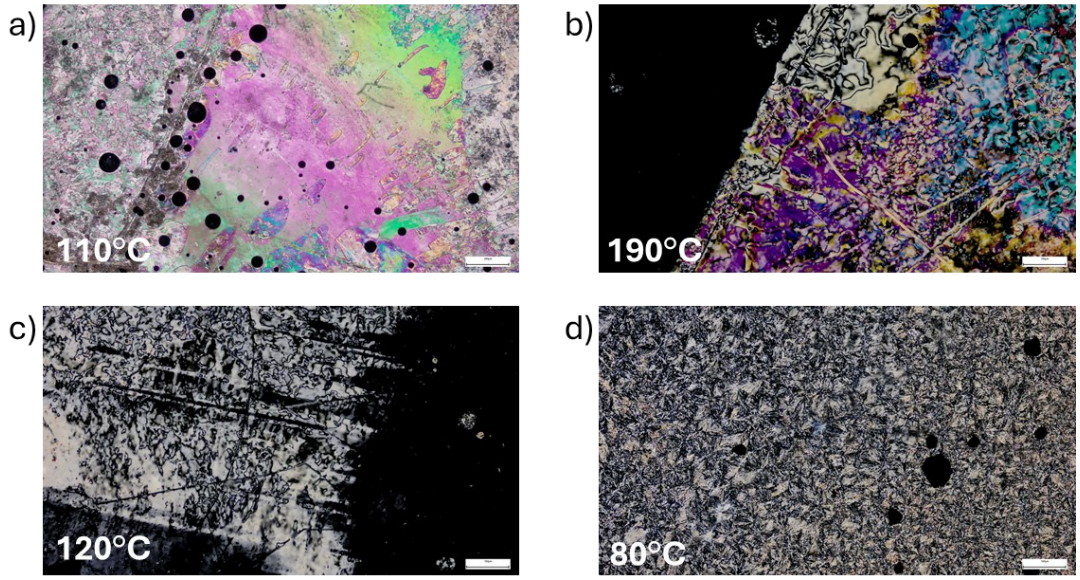

Figure 27. Polarized optical microscope images of liquid crystal monomer **17**: a) image at 110 °C during the heating ramp; b) image taken at 190 °C at the end of the heating ramp before starting the cooling cycle; images c) and d) were taken at 120 and 80 °C, respectively, during the cooling ramp from 190 °C to room temperature.

The images acquired through polarized light optical microscopy confirmed the liquid crystalline nature of monomer **17**, showing the typical birefringence of mesogens in the liquid crystalline phase at 110 °C (Figure 27a) and the progressive disappearance of the phenomenon following the onset of the transition from mesophase to isotropic liquid (Figure 27b). Consistently with the behaviour of a liquid crystalline material, the birefringence reappears during the cooling process (Figure 27c-d).
Once confirmed the liquid crystalline behaviour of monomer **17**, a first polymerization attempt was performed by reacting monomer **17**, 1**5** and hexamethylene-diisocyanate (HMDI) (Scheme 8) in 1:0.05:1.05 ratio respectively. The initial polymerization attempt, conducted without a chain extender, aimed to assess the mesogen ability to retain its liquid crystalline properties post-polymerization.

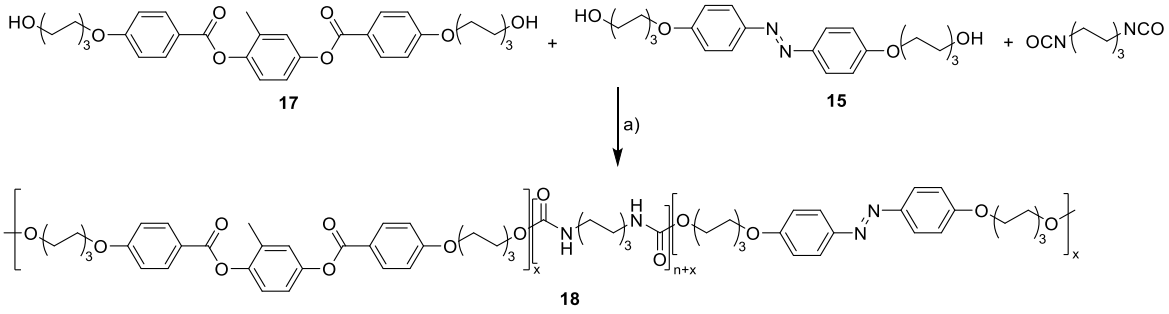

Scheme 8. *a) DBTL, dry DMF, 25°C, 48h.*

The reaction was performed by dissolving 1 eq. of monomer **17**, 0.05 eq. of monomer **15** and 1.05 eq. of HMDI in dry DMF. Then, 1% of DBTL was added as catalyst and the reaction was stirred at room temperature for 48 hours. Purification by precipitation of the reaction mixture into cold methanol afforded the target polymer as yellow solid, which was characterized by ^{1}H-NMR spectroscopy in DMSO-d$_6$ (Figure 28).

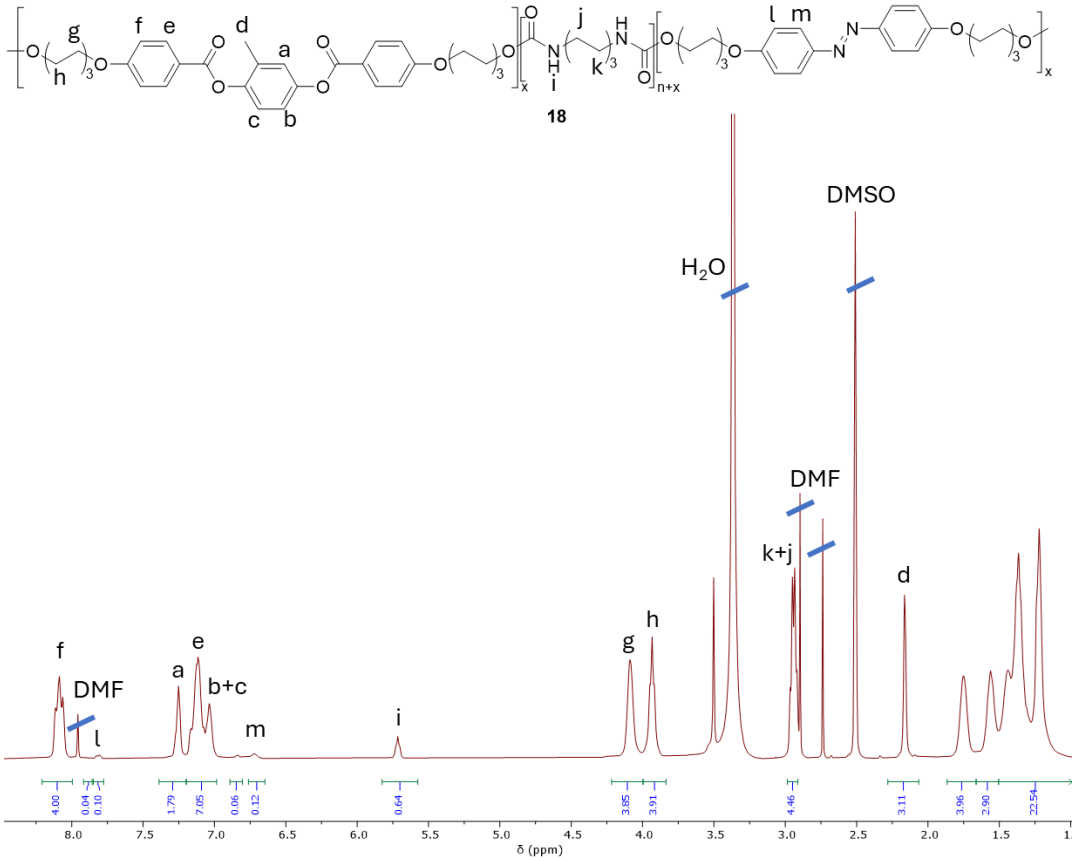

Figure 28. ^{1}H-NMR spectrum (DMSO-d$_6$, 25 °C, 400MHz) of copolymer **18**.

The spectrum shows all the diagnostic signals belonging to the target polymer **18**, like the signals of the aromatic core of the mesogen (*a*, *b*, *c*, *f*), the signal of the methyl group the in the central aromatic ring of the mesogenic core *d*, and the signals of the aromatic rings of the azobenzene comonomers (*m* and *l*). Furthermore, integration of the aromatic signals in the NMR spectrum confirmed that the molar ratio of the two comonomers, **17** and **15**, in the resulting polymer closely matched the stoichiometric ratio employed in the polymerization reaction.

The polymer was then subjected to DSC analysis to investigate its liquid crystalline behaviour (Figure 29).

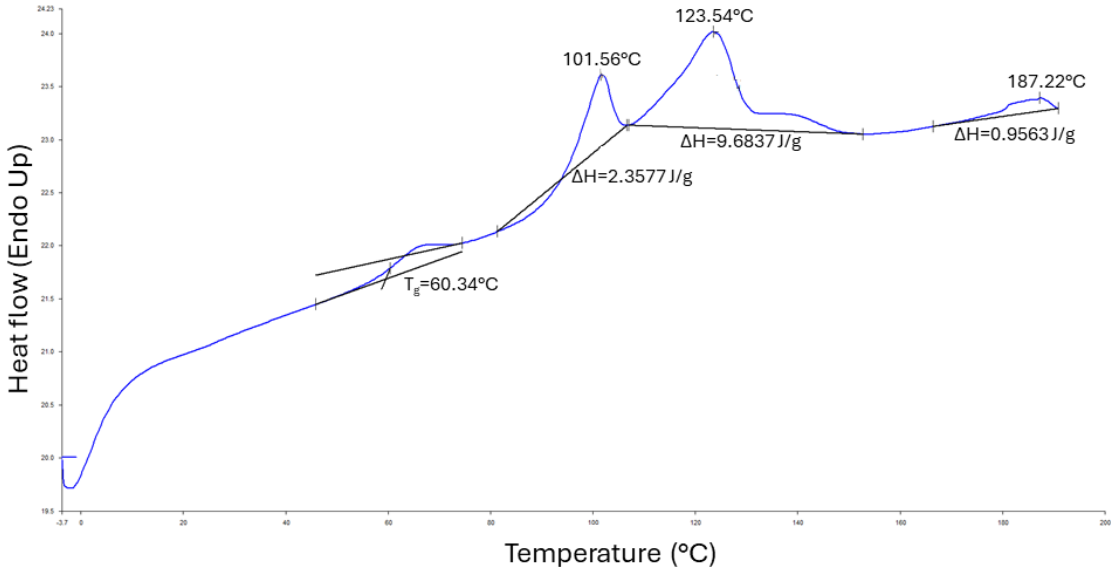

Figure 29. 1st heating DSC curve of polymer **18**.

The DSC measurement revealed a polymer T_g around 60°C and a huge crystallization peak from 100 to 123°C. To obtain a proper liquid crystalline phase, it was necessary to decrease the degree of crystallinity of the material, so the polymerization reaction was repeated adding another polyol to enhance the flexible component of the resulting polyurethane. At first, tetraethylene glycol (TEG) was tested as chain extender (scheme 9):

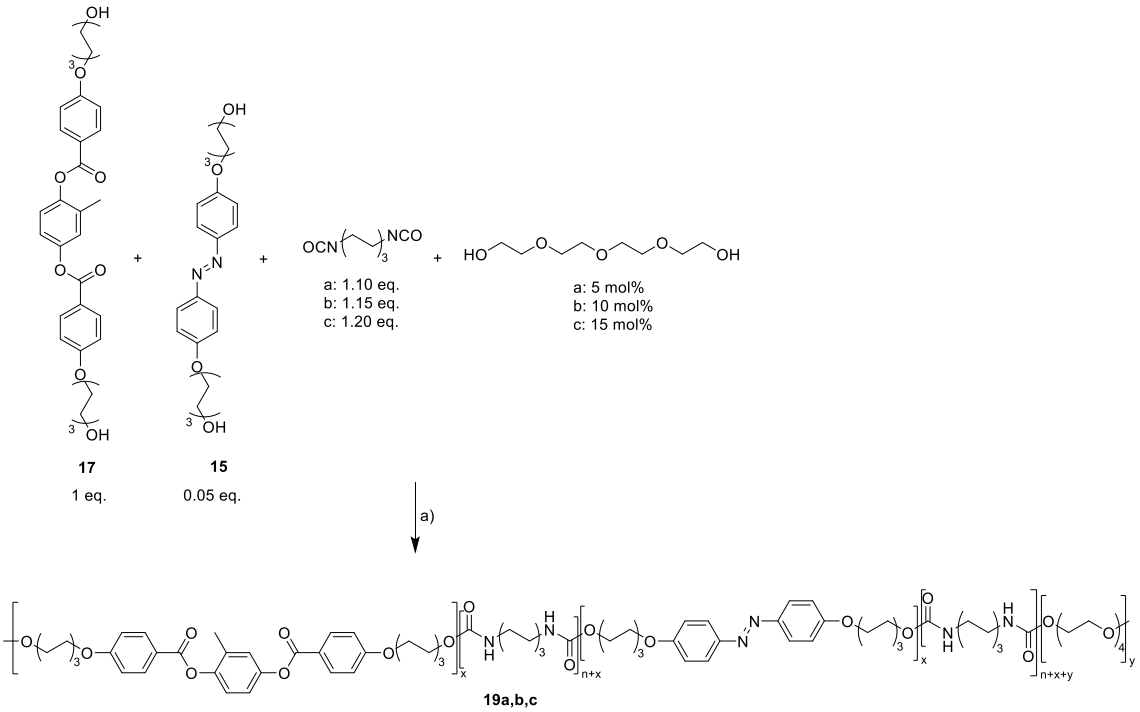

Scheme 9. *a) DBTL, dry DMF, 25 °C, 48h.*

Three different materials have been prepared by changing the amount of chain extender comonomer, and results are summarized in table 1:

Entry	Polymer Name	Chain extender	Mol% of Chain extender
1	**19a**	TEG	5 mol%
2	**19b**	TEG	10 mol%
3	**19c**	TEG	15 mol%

Table 1. Summary of prepared material.

In all the prepared materials, the reaction procedure is the same followed for the synthesis of **18**, thus DBTL as catalyst and DMF as solvent. All the synthesised polymers have been characterized by ^{1}H-NMR spectroscopy to confirm the successful incorporation of all the monomers, and by DSC analysis to investigate their liquid crystalline behaviour. In Figure 30 the ^{1}H-NMR spectrum of polymer **19a** is reported.

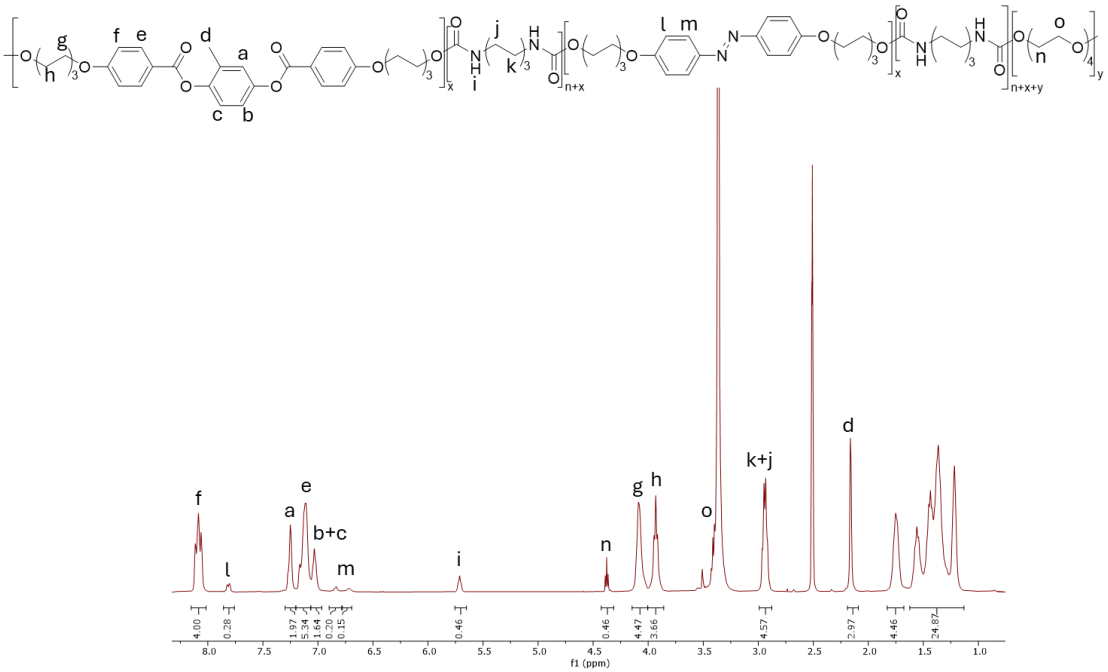

Figure 30. ^{1}H-NMR spectrum (DMSO-d_6, 25 °C, 400 MHz) of copolymer **19a**.

The spectrum exhibits diagnostic signals corresponding to mesogen **17** (*a*, *b*, *c*, *d*, *e*, *f*), the azobenzene photoactuator **15** (*l*, *m*), the tetraethylene glycol chain extender (*n*, *o*), and the hexamethylene diisocyanate (*k*, *j*). Additionally, integration of the diagnostic signal integrals enables the determination of the relative comonomer ratio, which aligns with the stoichiometry employed in the polymerization reaction.

The three materials have been compared by DSC analysis to determine the effect of the amount of chain extender in the crystalline phase (Figure 31)

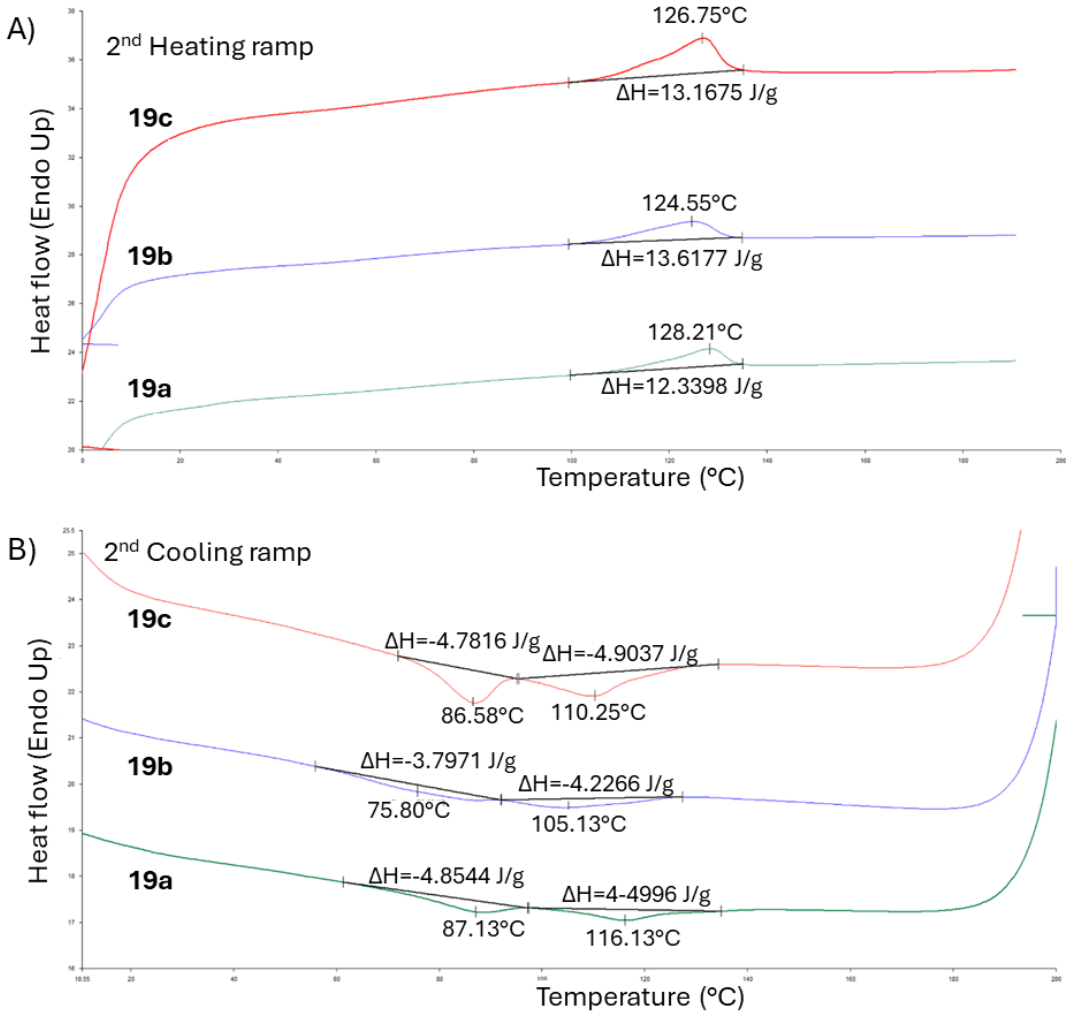

Figure 31. DSC analyses A) 2nd heating ramp and B) 2nd cooling ramp of polymers: **19a** (green trace), **19b** (blue trace), and **19c** (red trace).

By comparing the results obtained from the DSC analyses, it is possible to notice that during the heating ramp (Figure 31A), polymer **19a** with a 5 mol% content of chain extender shows the lower crystallinity degree and during the cooling cycle (Figure 31B) shows the best separation between the peaks related to the nematic mesophase.
Polarized optical microscopy (POM) revealed similar behaviours for all three materials. As an example, the images acquired for sample **19a** are presented.

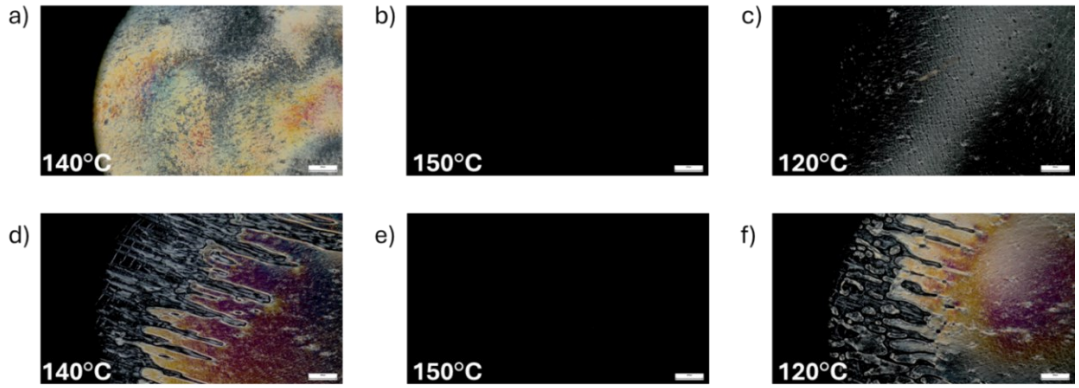

Figure 32. POM images of copolymer **19a** acquired at: a) 140 °C during the first heating scan; b) 150 °C during the first heating scan; c) 120 °C during the first cooling scan; d) 140 °C during the second heating scan; e) 150 °C during the second heating scan; f)120 °C during the second cooling scan.

Images revealed birefringence phenomena, characteristic feature of liquid crystalline materials, within the temperature range of 130-140 °C. Specifically, Figure 32a depicts birefringence observed upon heating the material to 140 °C. As the temperature increased to 150 °C, a transition from the liquid crystalline phase to the isotropic liquid phase occurred, accompanied by the loss of birefringence (Figure 32b). Upon cooling to 120 °C, a stable birefringent texture formed, persisting under mechanical stress (Figure 32c), indicating a crystallization process. Subsequent reheating to 140 °C resulted in the reappearance of birefringence (Figure 32d), which was again lost upon heating to 150 °C and transitioning to the isotropic liquid phase (Figure 32e). Cooling to 120 °C once more induced crystallization, with the material maintaining its texture under mechanical stress (Figure 32f).

To further reduce the crystallinity of the material while maintaining the liquid crystalline behaviour, a new formulation of the polymer was carried out by changing the length of the chain extender from the tetraethylene glycol (TEG) to a longer polyethylene glycol (PEG Mw = 400 g/mol) (Scheme 10).

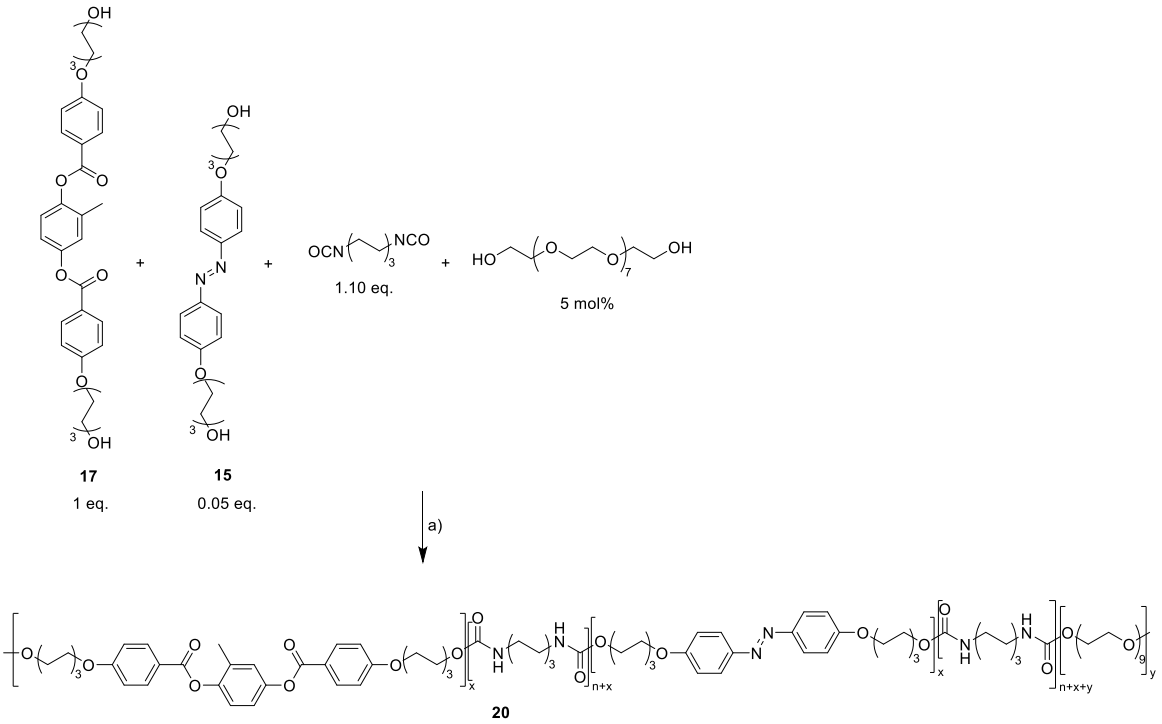

Scheme 10. *a) DBTL, Dry DMF, 25 °C, 48h.*

In this reaction, considering the thermal analyses of **19a, b** and **c**, only 5 mol% of chain extender have been used. The material was prepared following the same procedure previously reported and was characterized by ^{1}H-NMR spectroscopy in DMSO-d_6 (Figure 33), and by DSC to assess the material liquid crystalline properties.

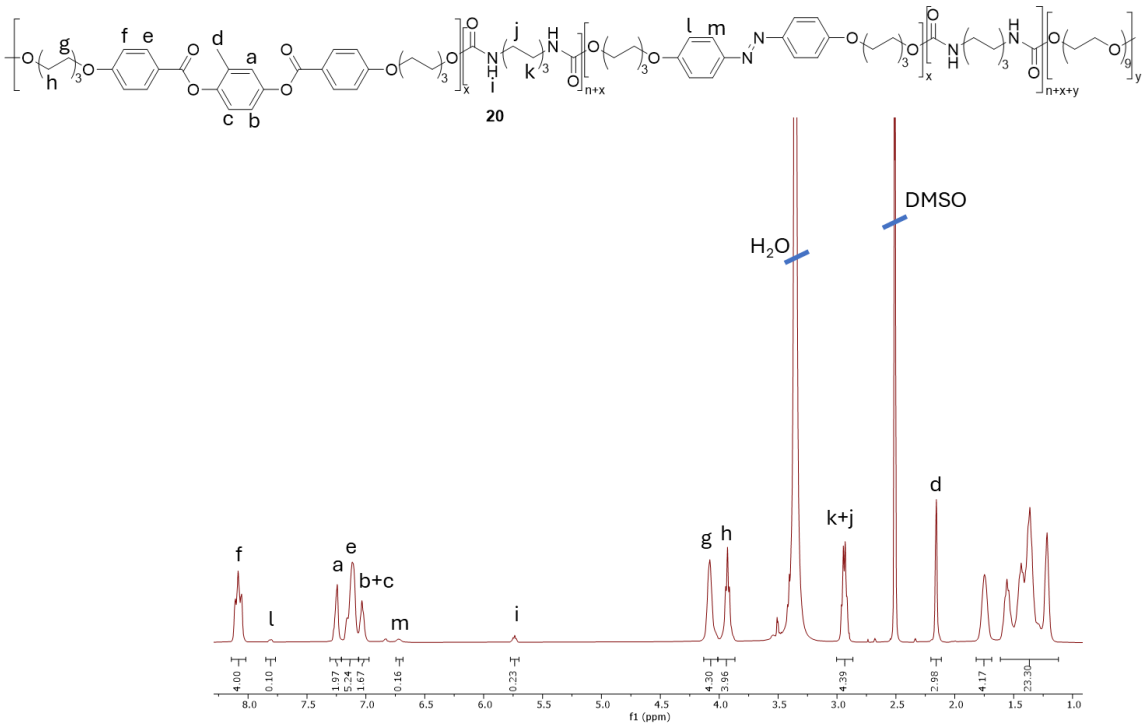

Figure 33. ^{1}H-NMR spectrum (DMSO-d$_6$, 25 °C, 400 MHz) of copolymer **20**.

The spectrum shows all the diagnostic signals belonging to both comonomers **17** and **15** as the protons of the aromatic rings (*a*, *b*, *e* and *f*) for monomer **17** and protons *l* and *m* for monomer **15**. As in previous cases, the relative ratios between the integrals show good agreement between the stoichiometry used in the polymerization reaction and the molar ratio of the monomers in the final material

The liquid crystalline behaviour of polymer **20** was further investigated by DSC analysis (Figure 34) which revealed a lower degree of crystallinity with respect to polymer **19a** together with less intense peaks belonging to the nematic phase transition.

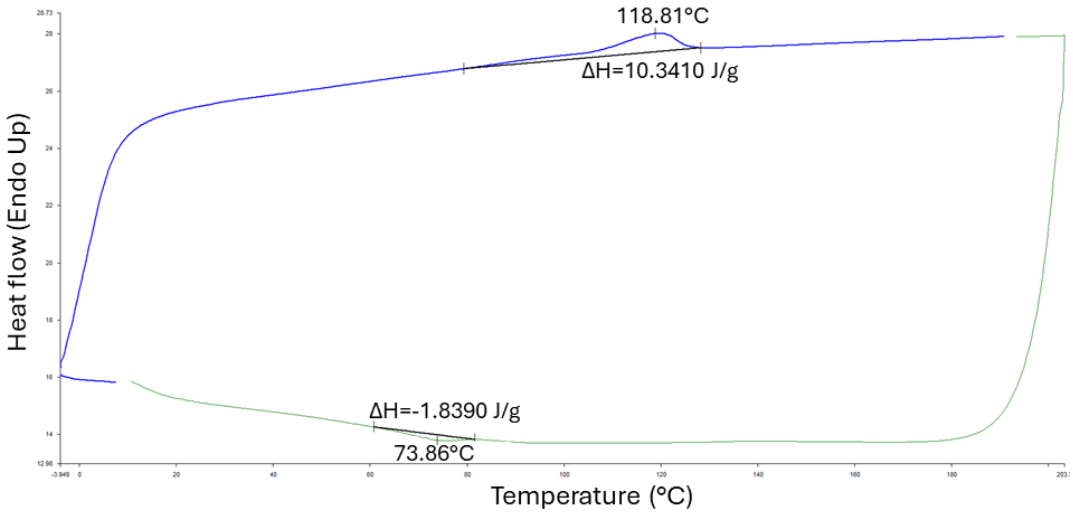

Figure 34. 2nd heating ramp (blue trace) and 2nd cooling ramp (green trace) from DSC analysis performed on copolymer **20**.

Polarized optical microscopy measurements are currently ongoing to confirm the liquid crystalline nature of material **20.** Subsequently, the ability of materials **19a,b,c** and **20** to form oriented fibers through electrospinning and their capacity to exhibit a reversible photoactuation response under UV irradiation will be investigated.

4. Conclusion

In conclusion, several materials were synthesized to obtain a photoactivated liquid crystal elastomers for electrospinning. Regarding the side-chain geometry materials, none of the synthesized materials exhibited the desired characteristics, either due to insufficient molecular mobility or a molecular weight that was too low, which did not ensure sufficient entanglement of the polymer chains during the electrospinning process. On the other hand, for the main-chain geometry materials, a polyurethane matrix material was initially developed and characterized, which showed excellent fiber-forming ability during electrospinning as well as good photoactuation ability following the application of an external UV irradiation stimulus. The polyurethane matrix was chosen for its capability, thanks to the hydrogen bonding donor and accepting groups, to form a high number of interactions between the chains, resulting in highly oriented polymer. However, since the material did not possess the desired liquid crystalline properties, its photoactuation was irreversible. A new liquid crystalline monomer was then successfully synthesized, characterized, and copolymerized with the photoactuator. Monomer **17** features a core composed of three aromatic rings interconnected by ester bonds, which enhance the structural and functional properties of the mesogen. Various materials were prepared to finely tune the material crystallinity percentage and its liquid crystalline mesophase range. Polymer **20** exhibited the best compromise between the degree of crystallinity and the width

of the liquid crystalline mesophase. In the future, polymer **20** ability to form oriented fibers through electrospinning and its capability to exhibit photoactuation responses following external UV irradiation will be further investigated.

5. Experimental

Synthesis of 4-((4-butylphenyl)diazinyl)phenol (1)

Compound **1** was prepared adapting a literature procedure.[27]

4-butylaniline (3.780 g, 25.33 mmol, 1 eq.) and HCl (9.22mL) were slowly dissolved in a mixture of acetone (8mL) and water (12mL). The mixture was cooled to -10°C and then a solution of sodium nitrite (1.748 g, 25.33 mmol, 1 eq.) in deionized water (DI) (8 mL) was added dropwise, keeping the temperature at -10°C. The obtained mixture was slowly added to a cold solution of phenol (2.370 g, 25.15 mmol, 0.99 eq.), Na_2CO_3 (2.685 g, 25.33 mmol, 1 eq.) and NaOH (1.013 g, 25.33 mmol, 1 eq.) in DI water (60mL). The reaction was magnetically stirred for 90 minutes keeping the temperature below 0°C, then the formed precipitate was filtered on büchner funnel, washed with DI water and dried under high vacuum. The purification by precipitation in dichloromethane/hexane (DCM/Hex) afforded the 3.97 g of target product **1** (63% yield) as orange solid. The product was characterized by ^{1}H-NMR spectroscopy in $CDCl_3$.

^{1}H-NMR ($CDCl_3$, 400 MHz): δ (ppm) = 7.89 (d, 2H, J = 8Hz, Ar**H**), 7.83 (d, 2H, J = 8Hz, Ar**H**), 7.32 (d, 2H, J = 8Hz, Ar**H**), 6.98 (d, 2H, J = 8Hz, Ar**H**), 2.70 (t, 2H, J = 8Hz, ArC**H$_2$**), 1.66 (qn, 2H, J = 8Hz, $ArCH_2C$**H$_2$**), 1.40 (sx, 2H, J = 8Hz, $ArCH_2CH_2C$**H$_2$**), 0.97 (t, 3H, J = 8Hz, -C**H$_3$**).

Synthesis of 1-(4-((6-bromohexyl)oxy)phenyl)-2-(4-butylphenyl)diazene (2)

For the preparation of compound **2**, a procedure adapted from literature was followed.[28]

A solution of compound **1** (3.98 g, 15.65 mmol, 1 eq.) in dry acetone (70mL) was added dropwise to a solution of 1,6-dibromohexane (11.42 g, 46.80 mmol, 3 eq.) and potassium carbonate (9.05 g, 65.50 mmol, 4 eq.), in dry acetone (100mL). The reaction mixture was refluxed under magnetic stirring for 24 hours and monitored by TLC in hexane : ethyl acetate (Hex/EtOAc) (9:1). Once the complete disappearance of limiting reagent was observed, the reaction was cooled to room temperature, and the solvent was evaporated under high vacuum. The crude was dissolved in DCM (200mL) and washed with water (3x75mL). The purification by precipitation in DCM/EtOH afforded 4.5 g of target compound **2** (69% yield) as yellowish solid. The product was characterized by ^{1}H-NMR spectroscopy in $CDCl_3$.

^{1}H-NMR ($CDCl_3$, 400 MHz,) δ ppm= 8.02 (d, 2H, J = 8.0Hz, Ar**H**), 7.90 (d, 2H, J = 8Hz, Ar**H**), 7.35 (d, 2H, J = 8Hz, Ar**H**), 7.05 (d, 2H, J = 8Hz, ArH), 4.11 (t, 2H, J = 6Hz, -OC**H$_2$**), 3.48 (t, 2H, J = 6Hz, C**H$_2$**Br), 2.73 (t, 2H, J = 8Hz, ArC**H$_2$**), 1.94 (m, 2H, -OCH_2C**H$_2$**), 1.87 (m, 2H, CH_2C**H$_2$**Br), 1.67 (m, 2H, $ArCH_2C$**H$_2$**), 1.56 (m, 4H, -OCH_2CH_2C**H$_2$C H$_2$**), 1.40 (m, 2H, $ArCH_2CH_2C$**H$_2$**), 0.97 (t, 3H, J = 7Hz, -C**H$_3$**).

Synthesis of 6-(4-((4-butylphenyl)diazenyl)phenoxy)hexyl methacrylate (3)

Compound **3** was prepared adapting a procedure reported in literature.[29]
Methacrylic acid (1.4 mL, 16.2 mmol, 1.5 eq.) was added to a solution of compound **2** (4.5 g, 10.8 mmol, 1 eq.) and potassium carbonate (4.5 g, 32.4 mmol, 3 eq.), in dry DMF (100mL). The reaction was magnetically stirred at 100°C for 36 hours and checked by TLC in Hex/EtOAc (9:1). When the complete disappearance of the limiting reagent was observed, the reaction mixture was poured into cold water and the obtained precipitate was filtered and dried under high vacuum. 4.3 g of target product **3** were obtained as pale-yellow solid in 95% yield.

^{1}H-NMR (DMSO-d6, 400 MHz) δ ppm= 7.87 (d, 2H, J = 8Hz, Ar**H**), 7.78 (d, 2H, J = 8Hz, Ar**H**), 7.40 (d, 2H, J = 8Hz, Ar**H**), 7.13 (d, 2H, J = 8Hz, Ar**H**), 6.02 (s, 1H, C=C**H**), 5.65 (s, 1H, C=C**H**), 4.13 (m, 4H, ArO-C**H$_2$** and COOC**H$_2$**), 2.68 (t, 2H, ArC**H$_2$**), 1.89 (s, 3H, C=CC**H$_3$**), 1.38-1.89 (m, 12H, $ArCH_2C$**H$_2$**+ $ArCH_2CH_2C$**H$_2$**+ ArO-CH_2C**H$_2$** + ArO-CH_2CH_2C**H$_2$**+ $COOCH_2C$**H$_2$**+ $COOCH_2CH_2C$**H$_2$**), 0.93 (t, 3H, J = 7Hz, $ArCH_2CH_2CH_2C$**H$_3$**).

Synthesis of 1-(6-isocyanatohexyl)-3-phenylurea (4)

Aniline (0.98mL, 10.73 mmol, 1 eq.) was added to hexamethylene diisocyanate (HMDI) (20 mL, 124.4 mmol, 11 eq.) under inert atmosphere. The reaction was kept under magnetic stirring at room temperature for 12 hours. After 12 hours, the formation of a white precipitate was observed so the reaction mixture was filtered on büchner funnel, and the precipitate was washed with cyclohexane to remove the excess of HMDI. The obtained white solid was dried under high vacuum affording 2.3 g of compound **4** in 82% yield. The product was characterized by ^{1}H-NMR spectroscopy in DMSO-d_6.

^{1}H-NMR (DMSO-d6, 600 MHz) δ ppm= 8.31 (s, 1H, ArN**H**), 7.33 (d, 2H, J = 7Hz, Ar**H**), 7.16 (m, 2H, Ar**H**), 6.83 (t 1H, J = 7Hz, Ar**H**), 6.05 (t, 1H, J = 6Hz, CON**H**CH_2), 3.31 (t, 2H, J = 7Hz, C**H$_2$**NCO), 3.03 (m, 2H, CONHC**H$_2$**), 1.52 (m, 2H, $CONHCH_2C$**H$_2$**), 1.39 (m, 2H, C**H$_2$**CH_2NCO), 1.28 (m, 4H, $CONHCH_2CH_2C$**H$_2$C H$_2$**).

Synthesis of Copolymer (5)

Compound **3** (1g, 2.36 mmol, 4 eq.), hydroxyethyl methacrylate (76.9 mg,0.59 mmol, 1 eq.), and butyl methacrylate (252 mg, 1.77 mmol, 3 eq.) were dissolved in dry toluene (20 mL)

under nitrogen atmosphere. The mixture underwent three freeze-pump-thaw cycles to remove oxygen from the reaction environment. Under inert atmosphere, benzoyl peroxide (3%) was added as radical initiator, and the reaction was magnetically stirred at 90°C for 72 hours. Afterward, the solvent was evaporated under high vacuum, and the target product (300 mg) was recovered by precipitation from acetone and cold methanol.

The polymer was characterized by ^{1}H-NMR in $CDCl_3$, and the ratio between the comonomers was calculated resulting in 59% of compound **3**, 16% of butyl methacrylate and 25% if hydroxyethyl methacrylate.

The calculations made by the ^{1}H-NMR spectrum have been confirmed by the results obtained from the elemental analysis:

Predicted: %C = 71.50; %H = 8.13; %N = 5.50

Experimental: %C = 70.5; %H = 8.05; %N = 5.12

The material was characterized by DSC analysis to asse the liquid crystalline properties (Figure S1)

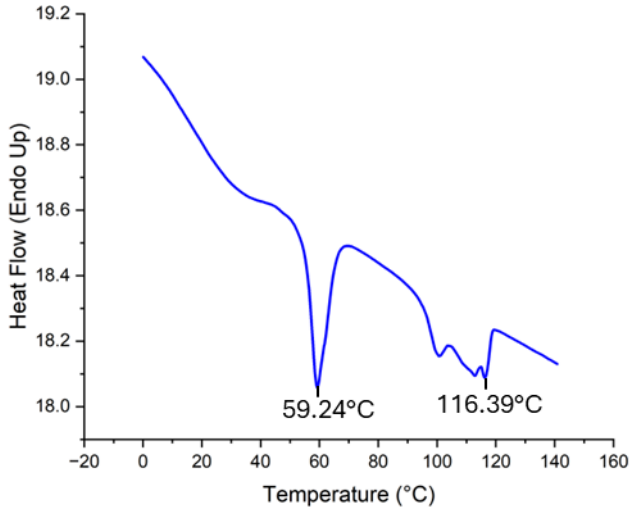

Figure S1. DSC Analysis (second cooling ramp) of polymer **5**

Synthesis of Copolymer (6)

Compound **4** (150 mg, 0.57 mmol, 10 eq.) was added to a solution of compound **5** (50 mg calculated on hydroxyethyl methacrylate), and DBTL (10 mol%) in dry acetone (5mL). The rection was magnetically stirred at 70°C for 24 hours. The hot mixture was then poured into cold methanol and the obtained precipitate was filtered and dried under high vacuum. The target polymer **6** was obtained as orange solid and characterized by ^{1}H-NMR in $CDCl_3$ (Figure S2), DSC analysis and POM images.

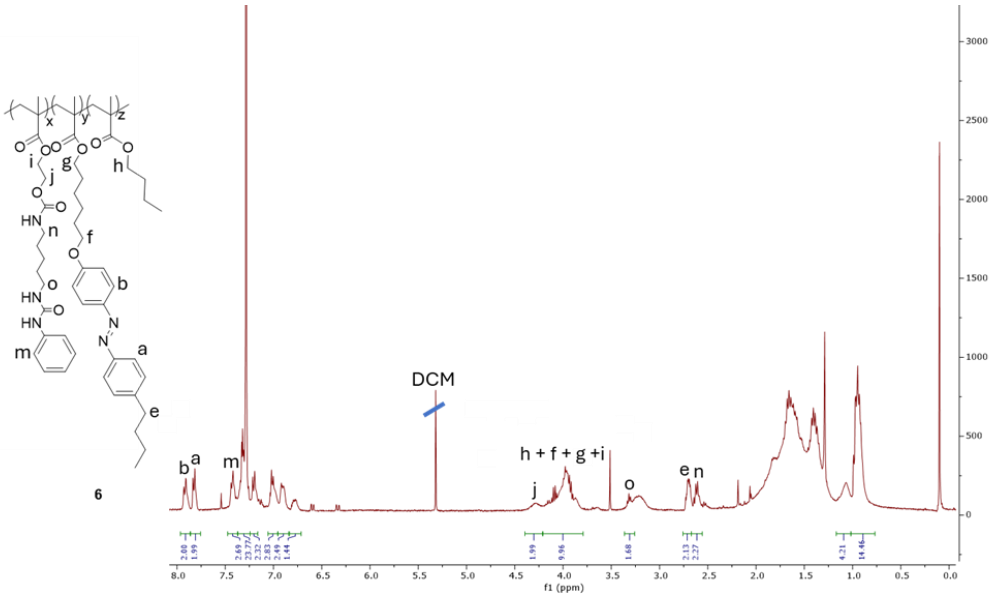

Figure S2. ^{1}H-NMR spectrum ($CDCl_3$, 70°C, 400MHz) of copolymer **6**.

Synthesis of 4-((4-butylphenyl)diazenyl)phenyl (6-isocyanatohexyl)carbamate (7)

A solution of compound **1** (250 mg, 0.983 mmol, 1 eq.) in dry toluene (10mL) was slowly added to a solution of 1,6-hexamethylene diisocyanate (HMDI) (165 mg, 0.983 mmol, 1 eq.), and DBTL (1%) in dry toluene (10mL). The reaction was magnetically stirred at room temperature for 14 hours. The reaction was monitored by TLC in Hex/EtOAc (9:1) and when the complete disappearance of the substrate was observed, the solvent was evaporated under high vacuum and the target product was purified by precipitation in DCM/Hex. 380 mg of target compound **7** were recovered as yellow solid in 90% yield, and characterized by ^{1}H-NMR in $CDCl_3$.

^{1}H-NMR ($CDCl_3$, 400 MHz) δ ppm= 7.91 (d, 2H, J = 8 Hz, Ar**H**), 7.82 (d, 2H, J = 8 Hz, Ar**H**), 7.29 (m, 4H, Ar**H**), 5.08 (t, 1H, J = 4 Hz, N**H**), 3.31 (m, 4H, NHC**H$_2$** and C**H$_2$**NCO), 2.69 (t, 2H, J = 8 Hz, ArC**H$_2$**), 1.64 (m, 6H, $ArCH_2C\mathbf{H_2}$ + $NHCH_2C\mathbf{H_2}$ + $C\mathbf{H_2}CH_2NCO$), 1.41 (m, 8H, $ArCH_2CH_2C\mathbf{H_2}$ + $NHCH_2CH_2C\mathbf{H_2}$ + $C\mathbf{H_2}CH_2CH_2NCO$), 0.94 (t, 3H, J = 4 Hz, $ArCH_2CH_2CH_2C\mathbf{H_3}$).

Synthesis of 4-methoxyphenyl 4-hydroxybenzoate (8)

Compound **8** was synthesized adapting a literature procedure.[30]

4-methoxyphenol (1 g, 9 mmol, 1.3 eq.) and 4-hydroxybenzoic acid (1 g, 7 mmol, 1 eq.) were dissolved in a mixture of dry toluene : xylene (10mL) in 4:1 ratio, respectively. Boric acid (40 mg, 0.6 mmol, 0.08 eq.) and sulfuric acid (90 mg, 0.9 mmol, 0.13 eq.) were added as catalysts, and the reaction was refluxed under magnetic stirring for 16 hours. The formed

precipitated was filtered and washed with deionized water. The target compound **8** was recovered in 40% yield (707 mg) as grey solid and characterized by ^{1}H-NMR spectroscopy in DMSO-d_6.

^{1}H-NMR (DMSO-d_6, 400 MHz) δ ppm= 10.48 (s, 1H, O**H**), 7.96 (d, 2H, J = 8 Hz, Ar**H**), 7.15 (d, 2H, J = 8Hz, Ar**H**), 6.98 (d, 2H, J = 8 Hz, Ar**H**), 6.91 (d, 2H, J = 8Hz, Ar**H**), 3.77 (s, 3H, C**H$_3$**).

Synthesis of 4-methoxyphenyl 4-((6-hydroxyhexyl)oxy)benzoate (9)

For the preparation of derivative **9**, a known literature procedure was followed.[31]
6-bromohexan-1-ol (556 mg, 3.07 mmol, 1.5 eq.) was added to a solution of compound **8** (500 mg, 2.05 mmol, 1eq.) and potassium carbonate (424 mg, 3.07 mmol, 1.5 eq.) in dry acetonitrile (15mL). _The mixture was refluxed under magnetic stirring for 24 hours. The reaction was monitored by TLC in Hex/EtOAc (6:4) and when the complete disappearance of limiting substrate was observed, the solvent was evaporated under vacuum. The crude was dissolved in DCM (200mL) and washed with aqueous HCl 1M (3x75mL). The purification by liquid chromatography on silica gel in Hex/EtOAc (6:4) afforded 500mg of target compound **11** as white solid (71 % yield). The compound was characterized by ^{1}H-NMR spectroscopy in $CDCl_3$.

^{1}H-NMR ($CDCl_3$, 400 MHz) δ ppm= 8.15 (d, 2H, J = 8 Hz, Ar**H**), 7.14 (d, 2H, J = 8Hz, Ar**H**), 6.96 (m, 4H, Ar**H**), 4.07 (t, 2H, J = 8Hz, ArOC**H$_2$**), 3.85 (s, 3H, C**H$_3$**), 3.70 (t, 2H, J = 8Hz, C**H$_2$**OH), 1.87 (qt, 2H, J = 4 Hz, ArOCH$_2$C**H$_2$**), 1.57 (m, 6H, ArOCH$_2$ C**H$_2$**C**H$_2$**C**H$_2$**).

Synthesis of 4-methoxyphenyl 4-((6-(methacryloyloxy)hexyl)oxy)benzoate (10)

For the preparation of liquid crystal **10**, a synthetic procedure was adapted from literature.[32]
Methacryloyl chloride (50 mg, 0.48 mmol, 1.5 eq.) was added to a cold solution of compound **9** (110 mg, 0.32 mmol, 1 eq.) and triethylamine (49 mg, 0.48 mmol, 1.5 eq.) in dry THF (8mL). The resulting mixture was magnetically stirred at room temperature for 16 hours. The reaction was monitored by TLC in Hex/EtOAc (6:4), and when the complete disappearance of the limiting reagent was observed, the solvent was evaporated under vacuum, the crude dissolved in ethyl acetate (100mL) ,and washed with water (3x40mL). The purification by liquid chromatography on silica gel in Hex/EtOAc (6:4) afforded the target compound **10** (118 mg) as white solid in 90% yield. Compound **12** was characterized by ^{1}H-NMR spectroscopy in $CDCl_3$, ESI-MS, DSC and POM images.

^{1}H-NMR ($CDCl_3$, 400 MHz) δ ppm= 8.13 (d, 2H, J = 8 Hz, Ar**H**), 7.11 (d, 2H, J = 8Hz, Ar**H**), 6.94 (m, 4H, Ar**H**), 6.10 (m, 1H, C=C**H**), 5.55 (qt, 1H, J = 4 Hz, C=C**H**), 4.17 (t, 2H, J = 8Hz, ArOC**H$_2$**), 4.05 (t, 2H, J = 4Hz, $COOCH_2$) 3.82 (s, 3H, OC**H$_3$**), 1.95 (t, 3H, J = 4Hz, C=CC**H$_3$**), 1.84 (m, 2H, J = 4 Hz, $ArOCH_2C$**H$_2$**), 1.73 (m, 2H, $COOCH_2C$**H$_2$**), 1.51 (m, 4H, $ArOCH_2CH_2C$**H$_2$C H$_2$**).

ESI-MS: m/z calculated for $C_{24}H_{28}O_6Na$ = 435.47 $[M+Na]^+$, experimental m/z = 435.40 $[M+Na]^+$

Synthesis of Copolymer (11)

Compound **11** (577 mg, 1.40 mmol, 9 eq.) and hydroxyethyl methacrylate (20.2 mg, 0.15 mmol, 1 eq.) were dissolved in dry methyl ethyl ketone (10mL) then the mixture underwent three freeze-pump-thaw cycles to ensure the complete oxygen removal from the reaction environment. After the third cycle, 2,2'azobisiiosobutyronitrile (AIBN) (2.55 mg, 0.015 mmol, 0.1 eq.) was added as radical initiator, and the reaction was magnetically stirred at 80°C for 24 hours. The target polymer was recovered upon precipitation of the cold mixture into cold hexane and solvent removal under high vacuum. The obtained polymer **11** was characterized by ^{1}H-NMR spectroscopy in $CDCl_3$ (Figure S3) and by DSC analysis (Figure S4).

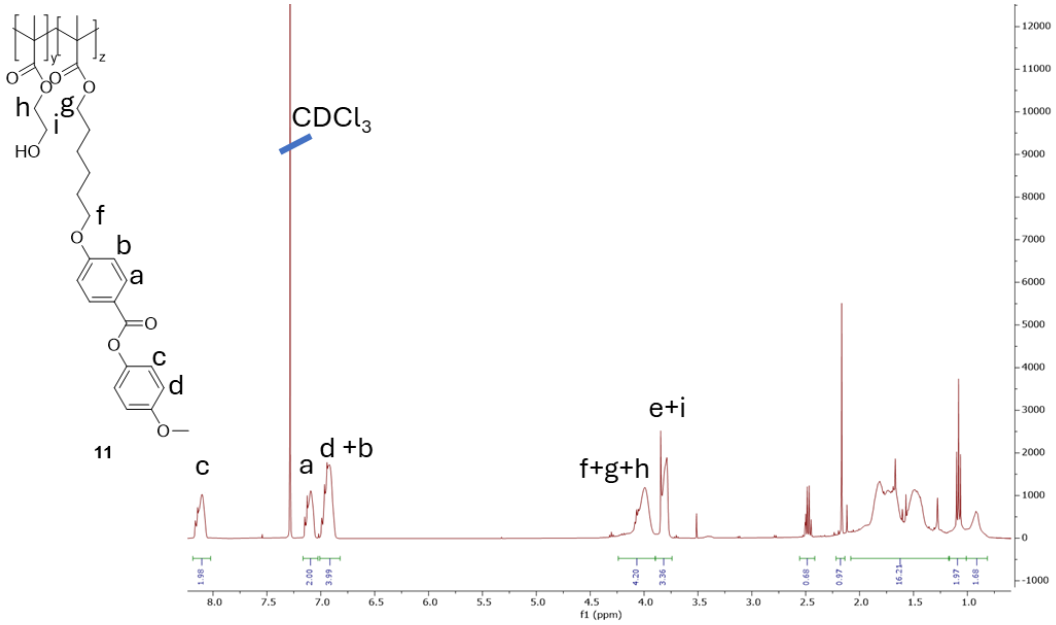

Figure S3. ^{1}H-NMR spectrum ($CDCl_3$, 25°C, 400MHz) of copolymer **11**.

DSC Analysis:

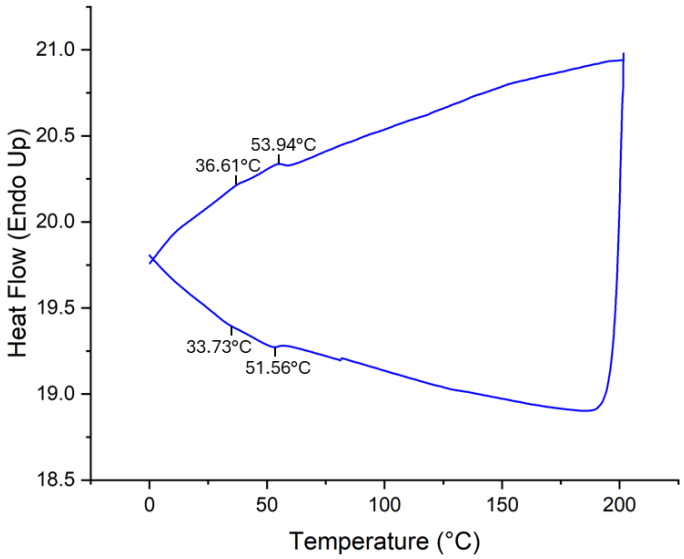

Figure S4. DSC analysis (second heating ramp and second cooling ramp) of polymer **11**.

Synthesis of Copolymer (12)

Copolymer **11** (131 mg, 0.23 mmol, 1 eq.) and compound **7** (96.7 mg, 0.23 mmol, 1 eq.) were dissolved in dry methyl ethyl ketone (5mL), then DBTL (2%) was added as catalyst, and the reaction was refluxed under magnetic stirring for 24 hours. The target copolymer **14** was isolated as yellow solid through precipitation of the hot reaction mixture in cold methanol. The target compound was characterized by ^{1}H-NMR spectroscopy in DMSO-d_6.

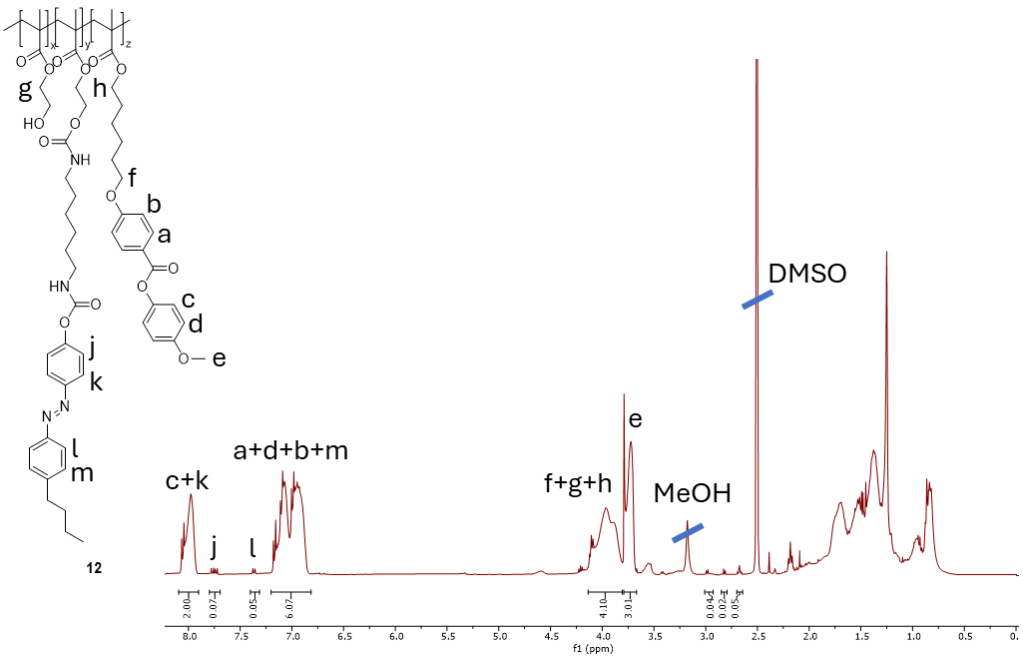

Figure S5. ^{1}H-NMR spectrum (DMSO-d$_6$, 60 °C, 400MHz) of copolymer **12**.

Synthesis of 4-hydroxyphenyl 4-hydroxybenzoate (13)

For the preparation of liquid crystalline core **15**, a synthetic procedure was adapted from literature.[29]

Hydroquinone (1 g, 9 mmol, 1.3 eq.) and 4-hydroxybenzoic acid (1 g, 7 mmol, 1 eq.) were dissolved in a mixture of dry toluene : xylene (10mL) in 4:1 ratio, respectively. Boric acid (40 mg, 0.6 mmol, 0.08 eq.) and sulfuric acid (90 mg, 0.9 mmol, 0.13 eq.) were added as catalysts, and the reaction was refluxed under magnetic stirring for 18 hours. The formation of a grey precipitate was observed which was filtered and washed with deionized water. Target compound **13** was obtained as grey solid in 45% yield and characterized by ^{1}H-NMR spectroscopy in DMSO-d$_6$.

^{1}H-NMR (DMSO-d$_6$, 400 MHz) δ ppm= 10.48 (s, 1H, O**H**), 9.46 (s, 1H, O**H**), 7.95 (d, 2H, J = 8 Hz, Ar**H**), 7.01 (d, 2H, J = 8Hz, Ar**H**), 6.91 (d, 2H, J = 8 Hz, Ar**H**), 6.79 (d, 2H, J = 8Hz, Ar**H**).

Synthesis of 4-((6-hydroxyhexyl)oxy)phenyl 4-((6-hydroxyhexyl)oxy)benzoate (14)

The preparation of liquid crystal monomer **14** was performed adapting a procedure known in literature.[32]

6-bromohexan-1-ol (2 g, 10 mmol, 3 eq.) was added to a solution of compound **13** (1g, 4 mmol, 1 eq.) and potassium carbonate (2 g, 4 mmol, 3 eq.) in dry acetonitrile (20mL). The mixture was magnetically stirred at 80°C for 36 hours The reaction was monitored by TLC

in Hex/EtOAc (6:4), and when the complete disappearance of the limiting substrate was observed the solvent was evaporated under vacuum and the crude was dissolved in dichloromethane (200 mL). The organic phase was washed with deionized water (3x75mL), and the crude was purified by liquid chromatography on silica gel in Hex/EtOAc (6:4). Compound **16** was recovered as white solid in 75% yield (1.40 g), and characterized by ^{1}H-NMR spectroscopy in $CDCl_3$, ESI-MS, DSC and polarized optical microscopy (POM).

^{1}H-NMR ($CDCl_3$, 400 MHz) δ ppm= 8.13 (d, 2H, J = 12 Hz, Ar**H**), 7.10 (d, 2H, J = 8Hz, Ar**H**), 6.94 (m, 4H, Ar**H**), 4.05 (t, 2H, J = 8 Hz, ArOC**H$_2$**), 3.97 (t, 2H, J = 8 Hz, ArOC**H$_2$**), 3.67 (m, 4H, C**H$_2$**OH), 1.82 (m, 4H, ArOCH$_2$C**H$_2$**) 1.61 (m, 4H, C**H$_2$**CH$_2$OH), 1.50 (m, 8H, C**H$_2$**CH$_2$CH$_2$OH + ArOCH$_2$CH$_2$C**H$_2$**).

ESI-MS: m/z calculated for $C_{25}H_{35}O_6$ = 431.24 $[M+H]^+$, experimental m/z = 431.42 $[M+H]^+$

Synthesis of 6,6'-((diazene-1,2-diylbis(4,1-phenylene))bis(oxy))bis(hexan-1-ol) (15)

6-Bromohexan-1-ol (211mg, 1.17 mmol, 2.5 eq.) was added to a solution of 4,4'-(diazene-1,2-diyl)diphenol (100 mg, 0.47 mmol, 1 eq.) and potassium carbonate (161 mg, 1.17 mmol, 2.5 eq.) in dry acetonitrile (6mL). The mixture was refluxed under magnetic stirring for 24 hours. The reaction was monitored by TLC in Hex/EtOAc (6:4), and when the complete disappearance of the limiting reagent was observed, the solvent was removed under vacuum, the crude dissolved in dichloromethane (100mL) and washed with deionized water (3x50mL). Purification by precipitation in DCM/Hex afforded the target compound **17** as yellow solid in 80% yield (155 mg). Derivative **15** was characterized by ^{1}H-NMR spectroscopy in MeOD-d_4.

^{1}H-NMR (MeOD-d_4, 400 MHz) δ ppm= 7.82 (d, 2H, J = 4 Hz, Ar**H**), 7.03(d, 2H, J = 4 Hz, Ar**H**), 4.08 (t, 4H, J = 4 Hz, ArOC**H$_2$**), 3.58 (t, 4H, J = 4 Hz, C**H$_2$**OH), 1.83 (m, 4H, ArOCH$_2$C**H$_2$**), 1.53 (m, 12H, ArOCH$_2$CH$_2$C**H$_2$**C**H$_2$**C**H$_2$**).

Synthesis of copolymer (16)

1,6-diisocyanatohexane (690 mg, 4.10 mmol, 3.15 eq.) was added to a solution of compound **16** (1.12 g, 2.60 mmol, 2 eq.), compound **17** (81 mg, 0.19 mmol, 0.15 eq.), tetraethylen glycol (TEG) (253 mg, 1.3o mmol, 1 eq.), and DBTL (1%) in dry DMF (20mL). The reaction mixture was kept under magnetic stirring for 48 hours. The target polymer was recovered as yellow solid by precipitation into cold methanol, filtration and solvent evaporation in high vacuum. The material was characterized by ^{1}H-NMR spectroscopy in DMSO-d_6 and by DSC analysis.

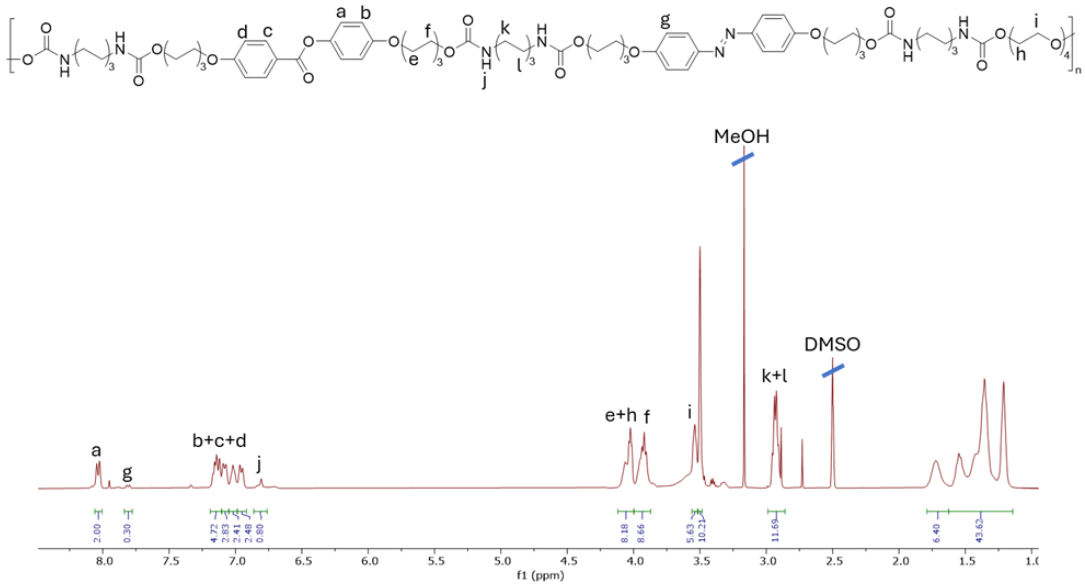

Figure S6. ^{1}H-NMR spectrum (DMSO-d_6, 25°C, 400MHz) of copolymer **16**.

Synthesis of 2-methyl-1,4-phenylene bis(4-((6-hydroxyhexyl)oxy)benzoate) (17)

For the preparation of liquid crystal monomer **17**, a procedure known in literature was followed.[33]

6-Bromohexan-1-ol (248 mg, 1.37 mmol, 2.5 eq.) was added to a solution of 2-methyl-1,4-phenylene bis(4-hydroxybenzoate) (200 mg, 0.55 mmol, 1 eq.), and potassium carbonate (228 mg, 1.65 mmol, 3 eq.) in dry acetonitrile (10mL). The mixture was refluxed under magnetic stirring for 48 hours. The reaction was monitored by TLC in Hex/EtOAc (6:4), and when the complete disappearance of the limiting substrate was observed, the solvent was evaporated under vacuum, the crude was dissolved in dichloromethane (100mL) and washed with water (3x50mL). Purification by liquid chromatography on silica gel in Hex/EtOAc (6:4) afforded the target compound **17** as a white solid in 75% yield (232 mg). Derivative **17** was characterized by ^{1}H-NMR spectroscopy in acetone-d_6, by DSC analysis and by polarized optical microscope (POM).

^{1}H-NMR (Acetone-d_6, 400 MHz) δ ppm= 8.15 (m, 4H, Ar**H**), 7.24 (m, 2H, Ar**H**), 7.12 (m, 5H, ArH), 4.15 (m, 4H, C**H$_2$**OH), 3.56 (m, 4H, ArOC**H$_2$**), 3.44 (t, 2H, J = 4 Hz, CH_2O**H**), 2.24 (s, 3H, ArC**H$_3$**), 1.83 (m, 4H, C**H$_2$**CH_2OH), 1.52 (m, 12H, ArOCH_2C**H$_2$**C**H$_2$**C**H$_2$**).

DSC analysis:

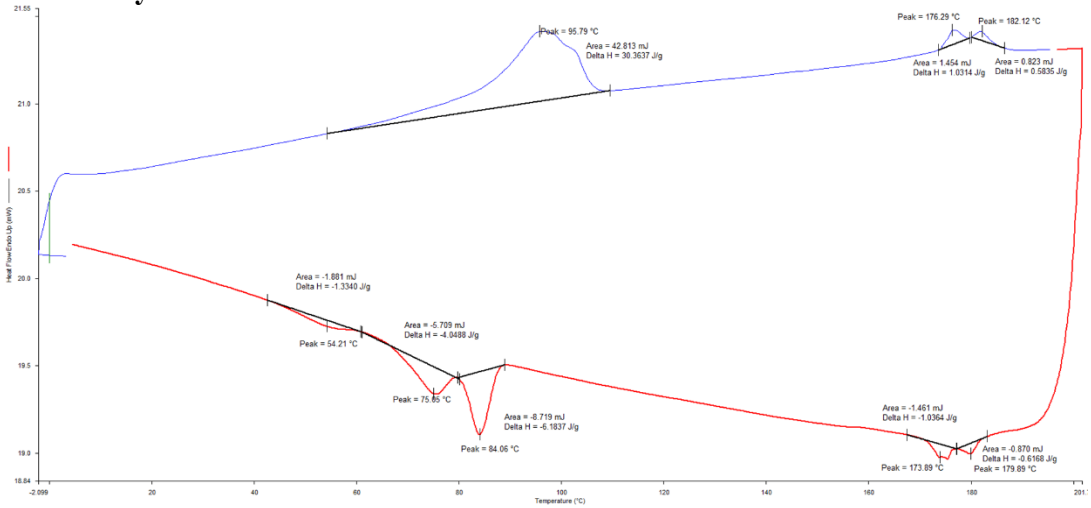

Figure S7. 2nd heating ramp (blue trace) and 2nd cooling ramp (red trace) DSC curve of compound **17**.

Synthesis of copolymer (18)

1,6-diisocyanatohexane (156 mg, 0.93 mmol, 1.05 eq.) was added to a solution of compound **17** (500 mg, 0.88 mmol, 1 eq.), compound **15** (18 mg, 0.04 mmol, 0.05 eq.), and DBTL (1%) in dry DMF (5mL). The reaction mixture was kept under magnetic stirring for 48 hours. The target polymer was recovered as yellow solid by precipitation of the reaction mixture into cold methanol, filtration and solvent evaporation in high vacuum. The material was characterized by ^{1}H-NMR spectroscopy in DMSO-d_6 and by DSC analysis.

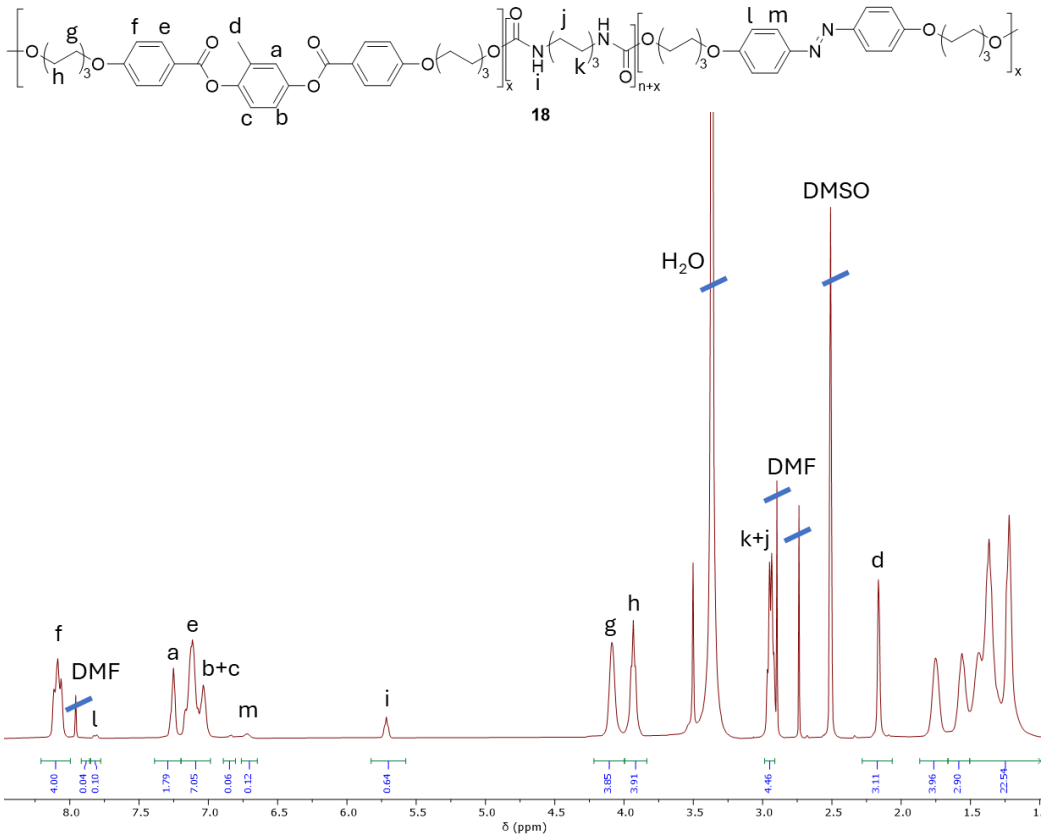

Figure S8. ^{1}H-NMR spectrum (DMSO-d$_6$, 25 °C, 400MHz) of copolymer **18**.

DSC analysis:

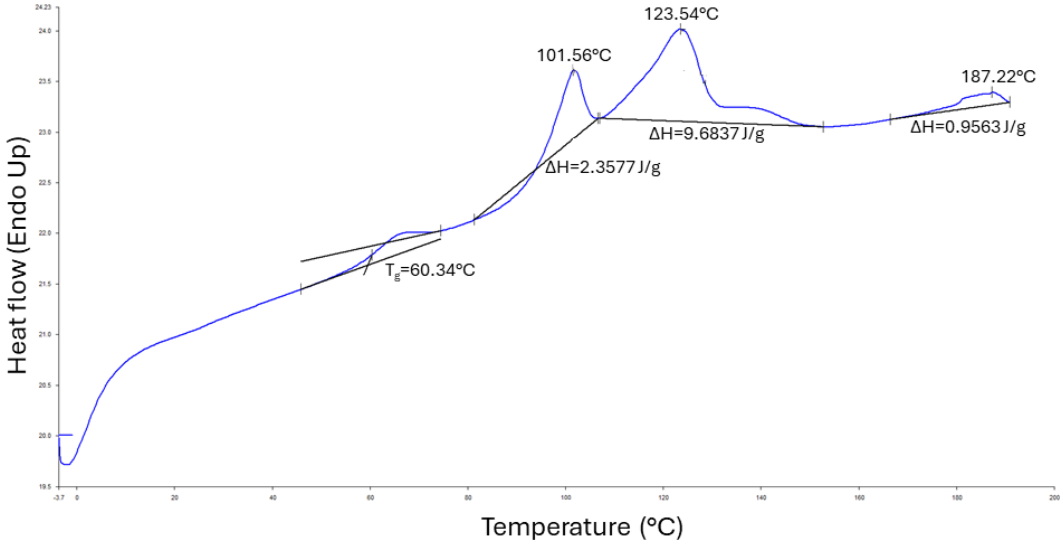

Figure S9. 1st heating DSC curve of polymer **18**.

Synthesis of copolymer 19: general procedure

1,6-diisocyanatohexane (1.1 eq.; 1.15 eq. or 1.2 eq.) was added to a solution of compound **17** (100 mg, 0.18 mmol, 1 eq.), compound **15** (3.67 mg, 0.009 mmol, 0.05 eq.), tetraethylene glycol (0.05 eq.; 0.10 eq.; 0.15 eq.), and DBTL (1%) in dry DMF. The resulting solution was magnetically stirred at room temperature for 48 hours, and the reaction mixture was poured into cold methanol. The obtained yellow precipitate was filtered and dried under high vacuum. The target material was recovered as yellow solid and characterized by ^{1}H-NMR spectroscopy in DMSO-d_6 and by DSC analysis.

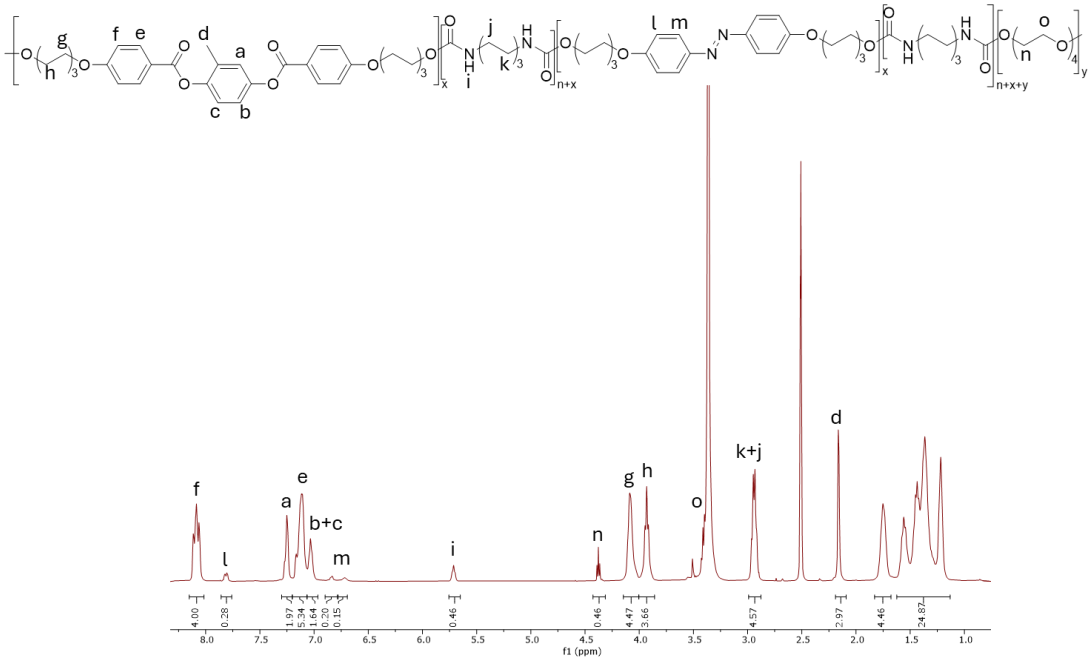

Figure S10. ^{1}H-NMR spectrum (DMSO-d_6, 25 °C, 400 MHz) of copolymer **19a**.

Synthesis of copolymer 20: general procedure

1,6-diisocyanatohexane (32.8 mg, 0.19 mmol, 1.1 eq.) was added to a solution of compound **19** (100 mg, 0.18 mmol, 1 eq.), compound **15** (3.67 mg, 0.009 mmol, 0.05 eq.), polyethylene glycol (PEG 400) (3.54 mg, 0.009 mmol, 0. 05 eq.), and DBTL (1%) in dry DMF. The resulting solution was magnetically stirred at room temperature for 48 hours, and the reaction mixture was poured into cold methanol. The obtained yellow precipitate was filtered and dried under high vacuum. The target material was recovered as yellow solid and characterized by ^{1}H-NMR spectroscopy in DMSO-d_6 and by DSC analysis.

6. References

[1] Warner M., Terentjev E. M., *Liquid Crystal Elastomers*, **2003**, p. 9-11, Oxford University Press

[2] Ula S. W., Traugutt N. A., Volpe R. H., Patel R. R., Yu K., Yakacki C. M., *Liq. Cryst. Rev.*, **2018**, 6, 78-107

[3] Tatsunosuke M., *Numerical Simulations of Physical and Engineering Processes*, **2011**, 207, IntechOpen

[4] Brömmel F., Kramer D., Finkelmann H., *Liquid Crystal Elastomers: Materials and Applications*, **2012**, p. 4, Springer

[5] White T. J., *Polymer Physics*, **2018**, 56, 695-705

[6] Warner M., Terentjev E. M., *Liquid Crystal Elastomers*, **2003**, p. 108, Oxford University Press

[7] Warner M., Terentjev E. M., *Liquid Crystal Elastomers*, **2003**, p. 109, Oxford University Press

[8] Ni B., Xie H., Tang J., Zhang H., Chen E., *Chem. Comm.*, **2016**, 52, 10257-10260

[9] Xue J., Wu T., Dai Y., Xia Y., *Chem. Rev.*, **2019**, 119, 5298-5415

[10] Sun B., Long Y. Z., Zhang H. D., Li M. M., Duvail J. L., Jiang X. Y., Yin H. L., *Prog. Polym. Sci.*, **2014**, 39, 862-890

[11] Hu J., Wang X., Ding B., Lin, J., Yu, J., Sun, G., *Macromol. Rapid Commun.*, **2011**, 32, 1729-1734

[12] Richard-Lacroix M., Pellerin C., *Macromolecules*, **2013**, 46, 9473-9493

[13] Liao Y., Loh C. H., Tian M., Wang R., Fane A. G., *Prog. Polym. Sci.*, **2018**, 77, 69-94

[14] Li D., Xia Y., *Adv. Mater.*, **2004**, 16, 1151-1170

[15] Luo C. J., Stride E., Edirisinghe M., *Macromolecules*, **2012**, 45, 4669-4680

[16] Husain O., Lau W., Edirisinghe M., Parhizkar M., *Mater. Sci. Eng. C*, **2016**, 65, 240-250

[17] Sijbesma R., and Meijer E., *Chem. Commun.*, **2022**, 5-16

[18] Pandini S., Agnelli S., Merlettini A., Chiellini F., Gualandi C., Paderni K., Focarete A. L., Messori M., Toselli M., *Macromol. Mater. Engineer.*, **2017**, 302, 1600519.

[19] Watson J. D., Crick F.H., *Nature*, **1953**, 171, 737–738.

[20] Sijbesma R., Beijer F., Brunsveld L., Folmer B., Hirschberg J., Lange R., Lowe J., and Meijer E., *Science*, **1997**, 278, 1601-1604

[21] Beijer F. H., Sijbesma R. P., Kooijman H., Spek A L., Meijer E. W., *J. Am. Chem. Soc.,* **1998**, 120, 6761–6769

[22] Osmialowski B., Kolehmainen E., Kalenius E., Behera B., Kauppinen R., Sievänen E., *Struct. Chem.,* **2011**, 22, 1143–1151

[23] Tellers J., Canossa S., Pinalli R., Soliman M., Vachon J., Dalcanale E., *Macromolecules,* **2018**, 51, 7680–7691

[24] Springer J., Weigelt F.W., *Recent Advances in Liquid Crystalline Polymers*, **1985**, 14, p. 233-243, Springer, Dordrecht.

[25] Kumar S., Singh R. K., *Liquid Crystals*, **2014**, 41, 1014-1032.
[26] Aizawa S., Yokoyama S., *Journal of Materials Chemistry C*, **2017**, 5, 7800-7809
[27] Fujita D., Murai M., Nishioka T., Miyoshi H., *Biochemistry*, **2006**, 45, 6581–6586
[28] Kamruzzaman M., Kuwahara Y., Ogata T., Ujiie S., Kurihara S., *Molecular Crystals and Liquid Crystals*, **2011**, 550, 134-148
[29] Z. Y. Kuang, Y. J. Fan, L. Tao, M. Li, N. Zhao, P. Wang, E. Q. Chen, F. Fan, H. L. Xie, *ACS Applied Materials & Interfaces,* **2018**, 10, 27269-27277
[30] A. Tomizawa, Y. Mori, N. Kasuya, *Journal of Macromolecular Science Part A*, **2017**, 54, 860-866
[31] L. Shi, Z. Zhao, L. Zong, J. Wang, *Polymers for Advanced Technologies*, **2023**, 34, 3125-3136
[32] S. Huang, Y. Shen, H. K. Bisoyi, Y. Tao, Z. Liu, M. Wang, H. Yang, Q. Li, *J. Am. Chem. Soc.*, **2021**, 143, 12543-12551
[33] Y. Watanabe, R. Kato, K. Fukushima, T. Kat o, *Macromolecules*, **2022**, 55, 10285-10293.

Chapter 5

Quinoxaline Cavitands for PFAS detection and removal

Abstract

Per- and polyfluoroalkyl substances (PFAS) are a class of emerging pollutants known for their environmental persistence and detrimental health effects. This work presents a supramolecular approach utilizing functionalized quinoxaline cavitands to develop sensors and membranes for PFAS detection and removal from aqueous matrices. Two new quinoxaline cavitands were synthesized presenting a novel upper rim functionalization with thiophene or pyrrole moieties to allow their incorporation into conductive polymers.

TOC: Structures of the two new synthesized quinoxaline cavitands.

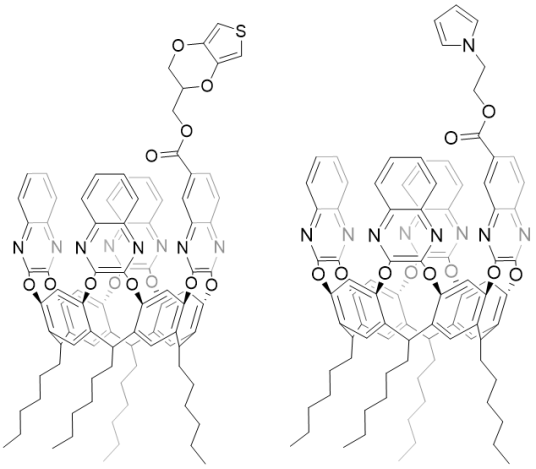

1. Introduction

1.1 Per and poly-fluoroalkyl substances (PFAS)

Per and poly-fluoroalkyl substances (PFAS) represent a large class of compounds composed of either fully or partially fluorinated alkyl chains. These substances have been in production for over 50 years and continue to be utilized across a broad spectrum of industrial products and processes.[1]

Because of their exceptional thermal and chemical resistance, along with their surface-active properties, PFAS are widely incorporated into various commercial products such as cleaning agents, paints, waxes, floor polishes, textile and carpets treatments, paper coatings, firefighting foams, fire retardant packaging formulations and insecticides.[1] Consequently, PFAS have become widely distributed in the environment and within human populations, raising significant concerns for public health. Animal studies linked PFAS exposure to various adverse health effects, including hepatotoxicity, neurobehavioral toxicity, immunotoxicity reproductive harm, pulmonary toxicity, endocrine disruption and a modest potential for genotoxicity and carcinogenicity.[1]

Due to the significant environmental impact of this class of pollutants, the scientific community has become increasingly active over the past decade in developing innovative methods for detecting or removing these substances from major natural sources, which represent a possible source of exposure for mankind. Among the most studied compounds are Pefluorooctanesulfonic acid (PFOS) and Perfluorooctanoic acid (PFOA) (Figure 1), whose removal through conventional treatments such as biological degradation, reduction, oxidation, and sedimentation has proven to be ineffective due to the high physicochemical stability of these compounds in the environment.[2]

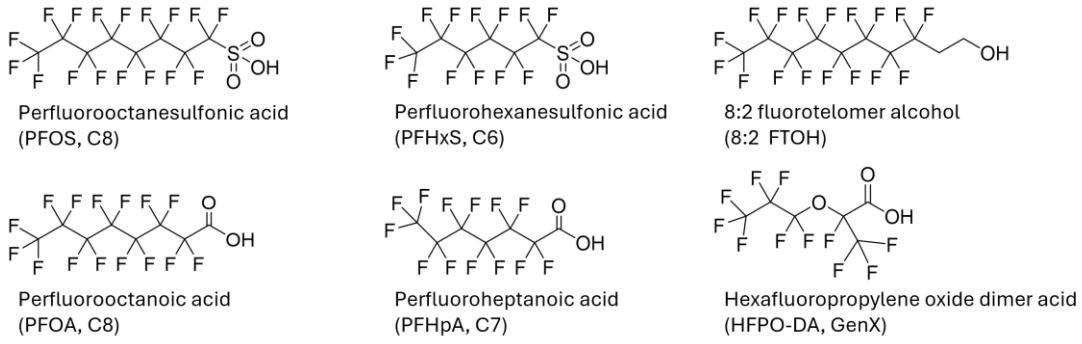

Figure 1. PFOS (top left), PFOA (bottom left) and other notable examples of common per and poly-fluoroalkyl substances (PFAS).

Their breakdown requires specific conditions, such as high temperatures, and generally involves processes with extremely high energy consumption.[3] As a result, more innovative methods have been developed, including photocatalytic processes, ion exchange resin

treatments, adsorption technologies, and membrane-based techniques.[4] However, these methods have demonstrated limited pollutant removal efficiency and often lack practicality on a large scale or involve high economic costs relative to their system efficiency.[5]

Regarding the detection of these substances, numerous methods based on traditional analytical techniques have initially been developed. [6-8] To date, EPA-approved methods 533, 537, and 537.1 involving an initial solid-phase extraction using a polystyrene-divinylbenzene matrix to concentrate the sample, followed by analysis via LC/MS.[9-10] These techniques offer good sensitivity, and low detection limits applicable to various analytes. Method 537.1 achieves LOD levels ranging from 0.71 to 2.8 ppt, with the capability to detect up to 18 different analytes, while method 533 reports a LOD of 1.4-1.6 ppt, enabling the detection of up to 25 different analytes.[10] However, these methods are limited to potable water matrices and cannot be applied to other important matrices such as soil, wastewater, sediments, or sludge.[11]
A desirable solution would be the development of a sensor capable of performing on-site, rapid detection of these substances, allowing for continuous monitoring of exposure levels. However, to achieve this goal, it is necessary to combine good performance in terms of sensitivity, selectivity, and ease of sample preparation within the same device, while also ensuring the sensor' portability.[12]

To achieve the goal of developing new sensors or materials capable of high-performance pollutant removal, an interesting approach could be drawn from supramolecular chemistry. This approach allows for the design of receptors with high selectivity for target analytes, while also enabling large-scale production and ensuring high batch-to-batch reproducibility. Among all the classes of organic receptors suitable for the purpose, a good option is represented by quinoxaline cavitands.

1.2 Quinoxaline Cavitands

Quinoxaline cavitands are a class of synthetic organic receptors characterized by a hydrophobic cavity that can be exploited for the complexation of ions and small lipophilic molecules through host-guest supramolecular interactions as π-π, CH- π, Van der Waals interactions and hydrophobic effect. The ability of these receptors to form complexes with small molecules has been exploited to selectively control the reactivity of two identical functional groups within the same molecule.[14] Rebeck and collaborators demonstrated that by preparing an aqueous solution containing a receptor and an alkyl chain functionalized with two azides in α-ω positions, a 1:1 host-guest complex forms, where one azide is located inside and the other outside the macrocycle cavity in dynamic exchange conditions. Upon adding 3 equivalents of triphenylphosphine (a reagent commonly used for the Staudinger reaction that quantitatively reduces azides to primary amines) to this solution, it was observed that after the reduction of the first azide group, a complex preferentially forms with the newly formed amine positioned outside the cavity, while the remaining azide at the

opposite end of the chain resides within the cavity. The formation of this complex, where the terminal groups of the chain exhibit a preferential orientation outward the macrocycle cavity, prevents further reduction of the remaining azide, effectively stopping the reaction at the mono-reduction product, even when additional equivalents of reducing agent are introduced.[14]

Furthermore, the experiment demonstrates that in an aqueous environment, the receptor can form a host-guest complex where the lipophilic portion of the guest resides within the cavity, while the hydrophilic portion interacts with the aqueous environment.

These hosts are synthesized from resorcin[4]arene scaffolds that can be functionalized at both the upper and lower rims to finely tune their solubility and selectivity for specific guests.[13] Moreover, this class of receptors has the ability of reversibly change their spatial conformation in response to external stimuli, such as variations in pH, mechanical forces, or redox events. These stimuli allow the cavitands to switch from a closed conformation, known as the *vase* form, where the quinoxaline walls are parallel to one another, to an open form called *kite*, in which the walls are splayed apart.[15] In the *vase* conformation, the quinoxaline walls create a hydrophobic cavity capable of encapsulating small lipophilic guests, while in the *kite* conformation, the hydrophobic cavity is lost, and the receptor can no longer act as a host, releasing any encapsulated guests. When solubilized in water, the quinoxaline cavitands adopt the *kite* conformation, forming dimers called velcrands. However, at the solid-water interface, whether in powder form or anchored to solid supports, these receptors retain their *vase* conformation.[16]

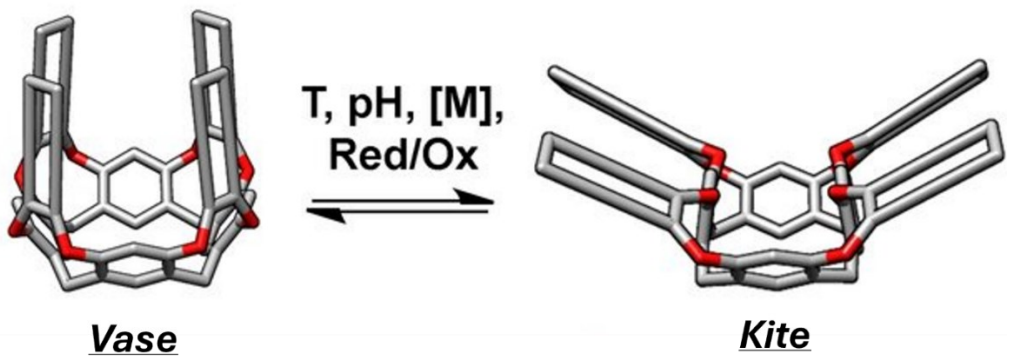

Figure 2. *Vase-kite* triggered conformational switch of quinoxaline cavitand.

As previously mentioned, the interconversion between the two conformations is influenced by experimental parameters such as temperature, pH, and the presence of divalent cations like zinc and lead in solution. The temperature dependence of the *vase-kite* equilibrium is governed by the free energy of solvation. In dichloromethane, the *vase* form is favoured at

temperatures of 25°C or higher, while the *kite* conformation, which exposes a larger surface area of the molecule to the solvent, is stable at -60°C, due to the fact that the TΔS term increases with rising temperature. Acidic solutions favour the *kite* conformation due to electrostatic repulsions resulting from the protonation of the heterocyclic nitrogen atoms in the quinoxaline walls.[17] The presence of zinc ions (Zn^{2+}) in solution stabilizes the *kite* form through coordination with the nitrogen atoms, forming a 2:1 Zn^{2+}-cavitand complex.[18]
This reversible interconversion mechanism, coupled with the known capability of quinoxaline cavitands to be used as absorbents of organic pollutants in water[19], has been utilized in the development of sensors for detecting small organic molecules[21] and in the fabrication of membranes designed for their removal.[20]

Amorini et al. developed electrospun polyacrylonitrile membranes incorporating dispersed benzoquinoxaline cavitands as additives. The benzoquinoxaline cavitands are characterized by a deeper hydrophobic cavity compared to the quinoxaline cavitands, and carry two aromatic rings on the quinoxaile moiety. These cavitands show the same *vase-kite* switch as the quinoxaline cavitands under the same stimuli. These membranes demonstrated the ability to remove polycyclic aromatic hydrocarbons from aqueous matrices, while also allowing for regeneration through acidic washing treatments.[20] This process induces the cavitands transition from the *vase* to the *kite* form, leading to pollutant decomplexation. Subsequently, an alkaline treatment regenerates the hydrophobic cavity by restoring the *vase* conformation (Figure 3).

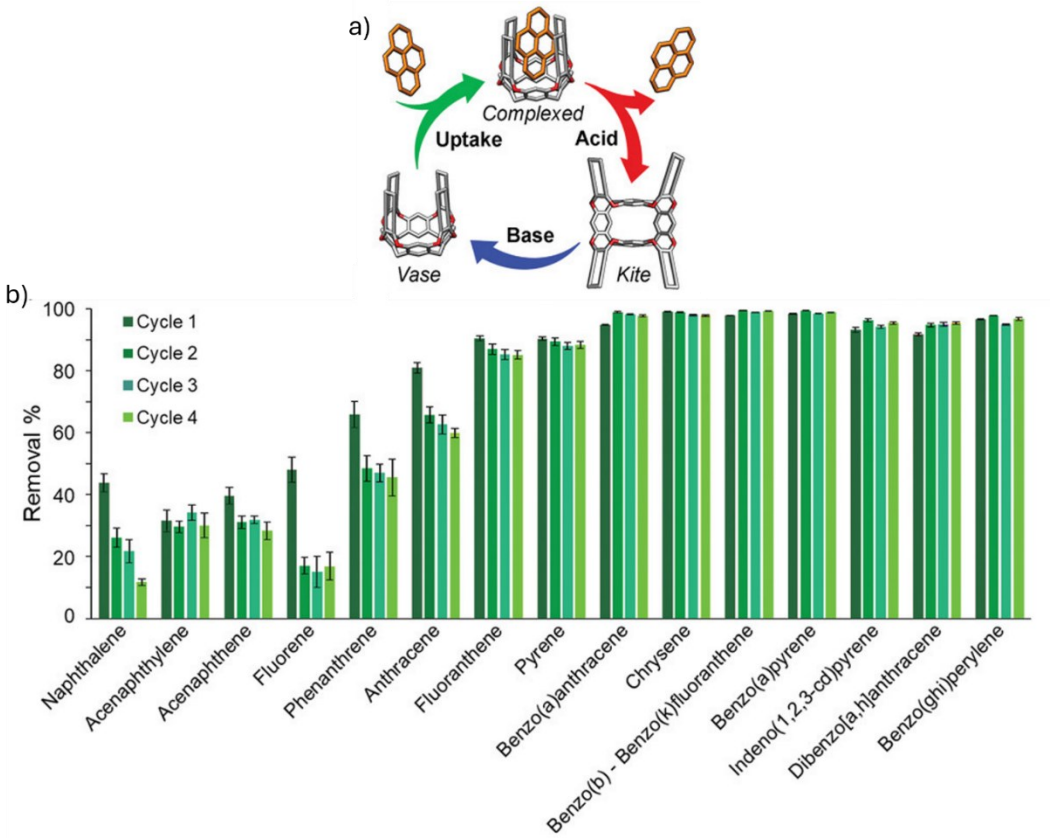

Figure 3. a) absorption and desorption cycle of quinoxaline cavitand; b) membrane removal performances of polycyclic aromatic hydrocarbons in water through 4 different cycles.[20]

In the context of sensor development, Giannetto et al. demonstrated that appropriate functionalization of a quinoxaline cavitand with a thiophene derivative allows the electro polymerization of the macrocycle onto an ITO surface. This approach enabled the creation of a piezoelectric sensor capable of detecting halogenated aromatic hydrocarbons in aqueous matrices (Figure 4).[21] This is particularly interesting because the use of a cavitand as a monomer in a polymerization reaction forming a conductive polymer backbone allows for the dual exploitation of the macrocycle's complexation capabilities and the inherent properties of the polymer matrix.

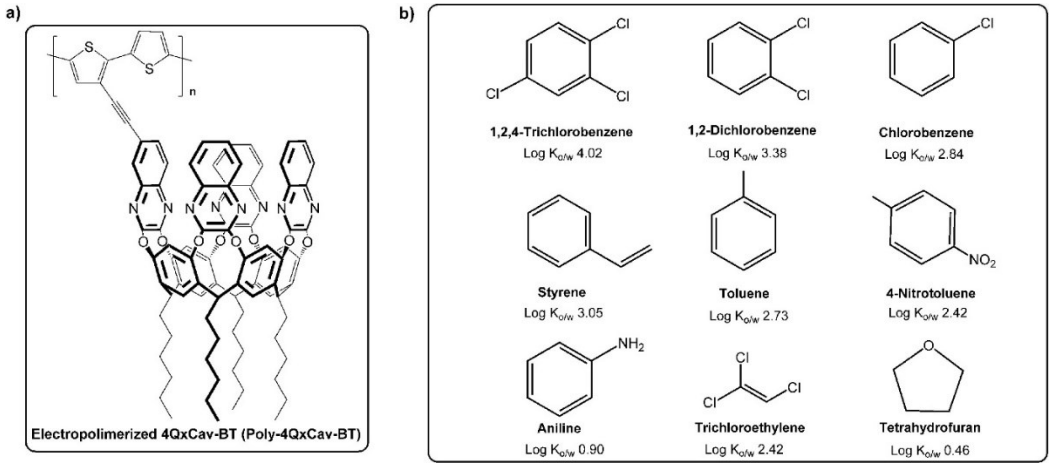

Figure 4. a) conductive polymer with quinoxaline cavitand as side-chain pendant; b) halogenated aromatic hydrocarbons and other guests used during the study.[21]

1.3 Conductive polymers

Similarly to metals and inorganic semiconductors, conductive polymers represent a class of materials characterized by unique optical and electrical properties. Moreover, they can be easily synthesized in large scale through cheap and versatile processes.[22]

Among all the different classes of conductive polymers, one of the most common and most studied is the class of conjugated π conductive polymers, characterized by electrons held in their backbone. These delocalized π electrons can freely move through the unsaturated backbone constructing an electrical pathway for mobile charge carries. The most common materials belonging to this class are polyacetylene (PA), polypyrrole (PPy), polythiophene (PT), poly[3,4-(ethyeledioxy)thiophene (PEDOT), and polyaniline (PANi) (Figure 5).[23]

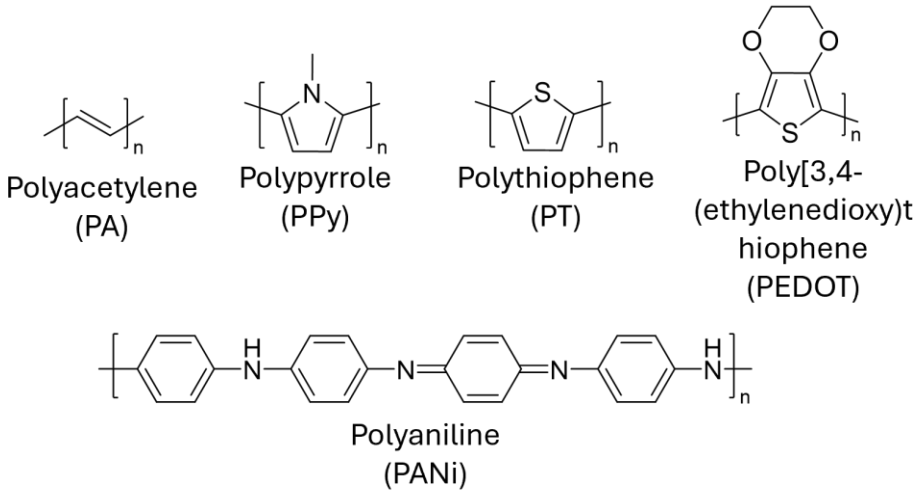

Figure 5. Some of the most common polymers belonging to conjugated π conductive polymers: Polyacetylene (PA), polypyrrole (PPy), polythiophene (PT), poly[3,4-(ethylenedioxy)thiophene (PEDOT) and polyaniline (PANi).

Nowadays, these polymers are used for a wide range of applications ranging from nerve regeneration[23] and biomedicine[24] to the realization of biosensors.[25]

Given the widespread use of conductive polymers for the development of sensors and biosensors, recent years have seen efforts to apply these materials to the creation of devices aimed at detecting pollutants, including PFAS. Park et al. developed an innovative method for PFAS detection utilizing polyaniline nanofibers as the conductive polymer, employing a detection strategy based on an electrically read lateral flow assay (e-LFA). In this approach, oxidized polyaniline nanofibers (PANI-ES) are reduced to their non-conductive form (PANI-EB). A dispersion of PANI-EB nanofibers combined with a perfluorinated surfactant is prepared, forming a viscous ink that is deposited onto a nitrocellulose membrane or a strip of filter paper. This solid support is then immersed in the aqueous solution to be analyzed, allowing the liquid to flow along the solid substrate and interact with the conductive polymer-surfactant ink. If the analyzed pollutant (in this case PFOA) contains a protonated acid group, it reacts with the non-conductive polyaniline during its passage, inducing a transition to its highly conductive PANI-ES form (Figure 6). By measuring the change in resistance across the polyaniline test line, the amount of pollutant present in the solution can be quantified, with detection limits (LOD) as low as 400 ppt.[26]

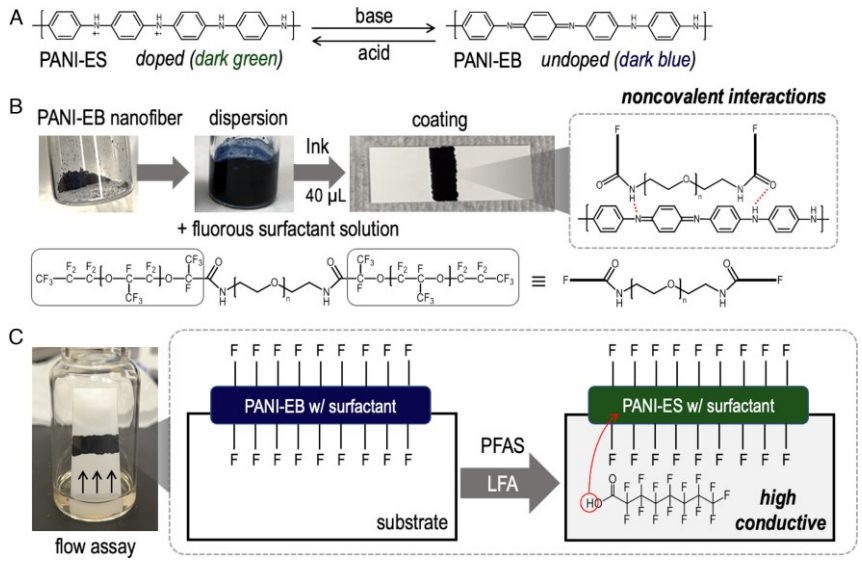

Figure 6. PFAS sensing platform based on polyaniline, A) doped (PANI-ES) and undoped (PANI-EB) forms of polyaniline, B) ink fabrication process and deposition on nitrocellulose stripe, C) lateral flow assay on nitrocellulose device.[26]

2. Aim of the Work

The aim of this study is to combine the ability of quinoxaline cavitands to reversibly complex specific classes of analytes with the features of conductive polymers for two different applications, i) the development of a sensor for PFAS detection and ii) the preparation of an adsorbent material for PFAS removal.

In sensor development, the objective is to harness the conductive polymer ability to generate a response upon a trigger, which in this case is represented by the formation of the host-guest complex.

For the absorbent material, the focus is to utilize the conductive polymer ability to be oxidized, inducing positive charges along the polymer backbone. This approach could optimize the cavitand complexation efficiency by simultaneously taking advantage of the interaction between the macrocyclic cavity and the lipophilic guest chain, as well as the formation of an ion pair between the positively charged polymer backbone and the negatively charged hydrophilic group of the pollutant. The establishment of the PFAS-polymer ion pair would enhance host-guest complex formation by increasing the proximity between the components and facilitating the dissociation of the ion pair between the PFAS anion and its alkaline counterion, crucial for the complexation.

3. Results and discussion

3.1 Synthetic strategies for lower rim functionalization of quinoxaline cavitands

The initial strategy for synthesizing a conductive polymer incorporating a tetraquinoxaline cavitand involves functionalizing the lower rim of the macrocycle with groups that can either be polymerized to form conductive polymers or be specifically designed for subsequent post-functionalization. Two notable approaches in this context are: 1) use of post-functionalization by incorporation of free thiol groups, as polypyrrole can be post-functionalized by reactions with thiol groups, or 2) functionalizing the lower rim with pyrrole units that can be polymerized to produce conductive polypyrrole.

To implement the first strategy, the synthetic pathway outlined in Scheme 1 was employed, utilizing intermediate **3** as a precursor:

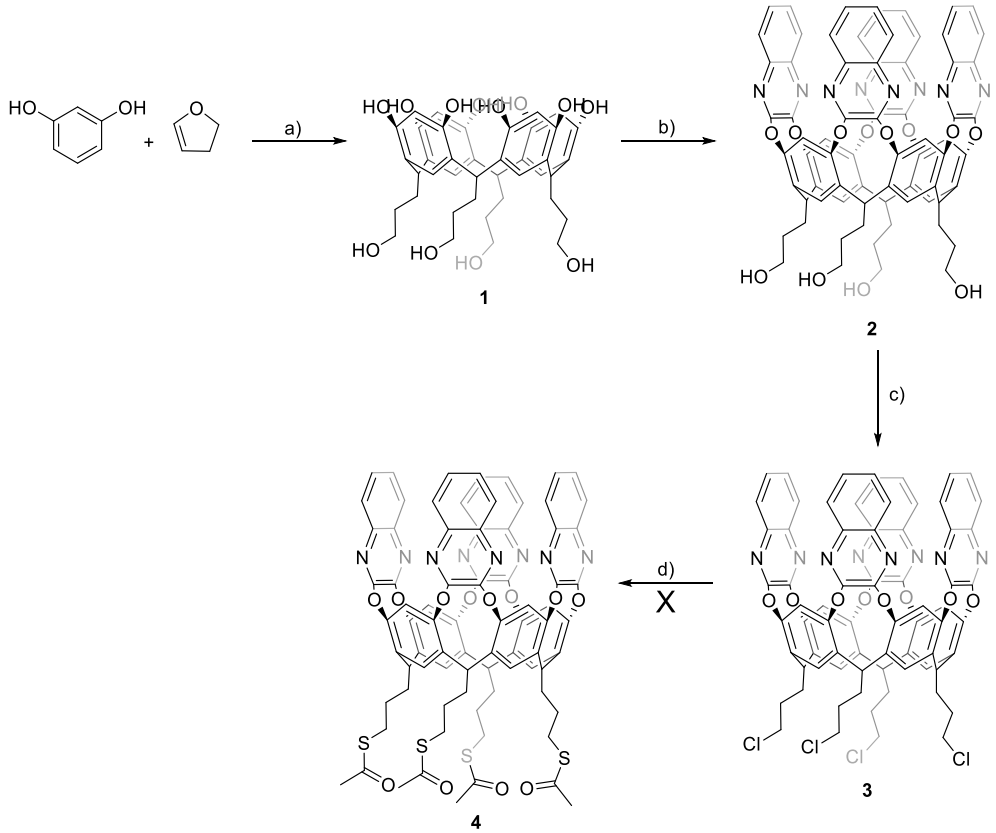

Scheme 1. *a) HCl 12M, MeOH, 55°C, 96h, 70% yield; b) K_2CO_3, 2,3-dichloroquinoxaline, dry DMF, 80°C, 16h, 70% yield; c) $SOCl_2$, dry DMF, 55°C, 18h, 80% yield; d) potassium thioacetate.*

In this strategy, the first step involves preparing the resorcinarene scaffold by reacting resorcinol and 2,3-dihydrofuran in acidic environment using 12M HCl. Quenching the reaction mixture and filtering the obtained precipitate allows for the recovery of the target scaffold in 70% yield. In the second step, four identical quinoxaline walls are bridged on the

resorcinarene scaffold by reacting the macrocycle with commercially available 2,3-dichloroquinoxaline in a basic environment using K_2CO_3 in dry DMF. Purification by recrystallization in methanol afforded the target tetraquinoxaline cavitand **2** as a white solid in 70% yield. Once the cavitand scaffold was obtained, the free hydroxyl functionalities at the lower rim were converted into good leaving groups by reacting a suspension of compound **2** in dry DMF with thionyl chloride, substituting the OH groups with four chlorine atoms. Precipitation and filtration of the precipitate obtained upon reaction quenching allowed for the recovery of the target tetrachloroquinoxaline cavitand **3** as a brown solid in 80% yield. At this point, macrocycle **3** represents a suitable substrate for a SN2 reaction to substitute the chlorine atoms with four thioacetate moieties, which then can be deprotected to obtain the free thiol groups. For this path, different temperatures, solvents, and reaction times have been explored but, unfortunately, any of them afforded the desired product, and the starting material was recovered each time. All the reaction conditions are reported in Table 1.

Pot. Thioacetate (eq.)	Solvent	Temperature	Reaction time	KI (eq.)
8	Dry Acetone	50°C	48h	0.1
16	Dry Acetone	50°C	72h	4
8	Dry DMF	RT	48h	0.1
16	Dry DMF	80°C	72h	4

Table 1. *Reaction conditions for the SN2 reaction between cavitand 3 and potassium thioacetate.*

Considering the impossibility of functionalizing the lower rim with the target thiol functionalities, the other valuable strategy can be using substrate **3** for another SN2 reaction to graft four pyrrole moieties (Scheme 2), which can act as monomers for a further polymerization reaction.

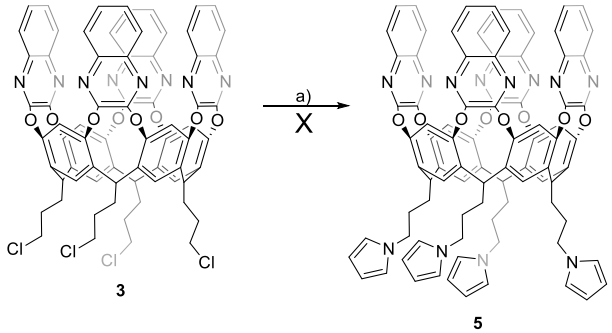

Scheme 2. *a) sodium pyrrol-1-ide, dry DMF, RT*

The reaction was carried out in dry DMF at room temperature using 5 equivalents of sodium pyrrol-1-ide as nucleophile. Unfortunately, the reaction did not afford the target compound. After purification, it was observed that the preferential reaction pathway was the SNAr

reaction, leading to cleavage of the quinoxaline wall and the formation the product reported in Figure 7.

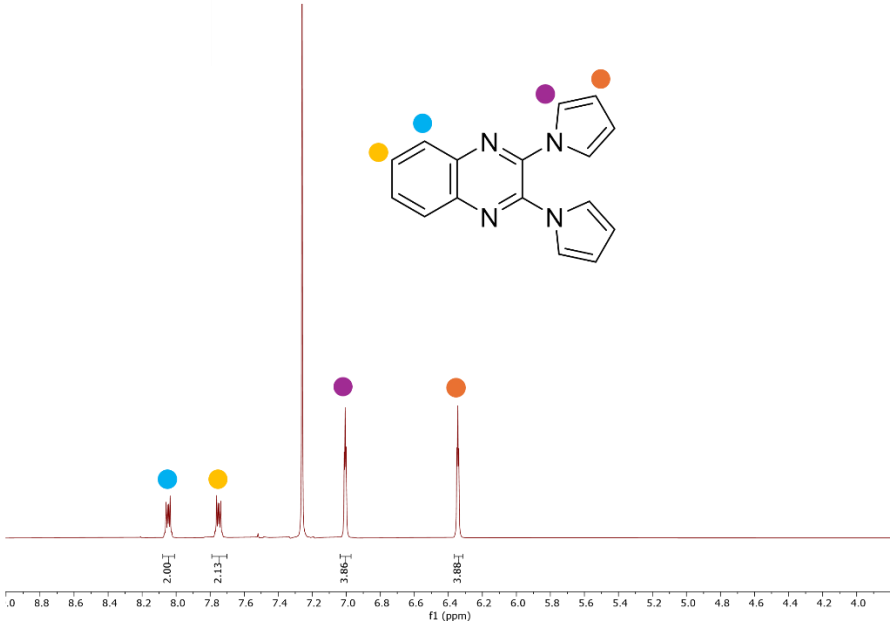

Figure 7. Structure and ^{1}H-NMR ($CDCl_3$, 25°C, 400MHz) of the side product.

This suggests that the aromatic carbon on the quinoxaline ring is a significantly stronger electrophile than the aliphatic carbon of the lower rim alkyl chain.
Due to the challenges faced in functionalizing the lower rim of the quinoxaline cavitand, the strategy was shifted to modifying the receptor's upper rim. This alternative approach involved modifying the macrocycle with a residue capable of undergoing polymerization to form a conductive polymer. Polythiophene and polypyrrole were selected as candidate polymer matrices for this strategy.

3.2 Synthesis of Thiophene-functionalized Quinoxaline Cavitand 14

To synthesize a polythiophene conductive polymer incorporating a tetraquinoxaline cavitand, an effective approach involves functionalizing the tetraquinoxaline cavitand at its upper rim with an appropriate thiophene moiety. This objective could be achieved through a convergent synthetic strategy, divided into two distinct pathways: (i) synthesis of a modified quinoxaline (Scheme 3) and (ii) preparation of the macrocyclic scaffold (Scheme 4).

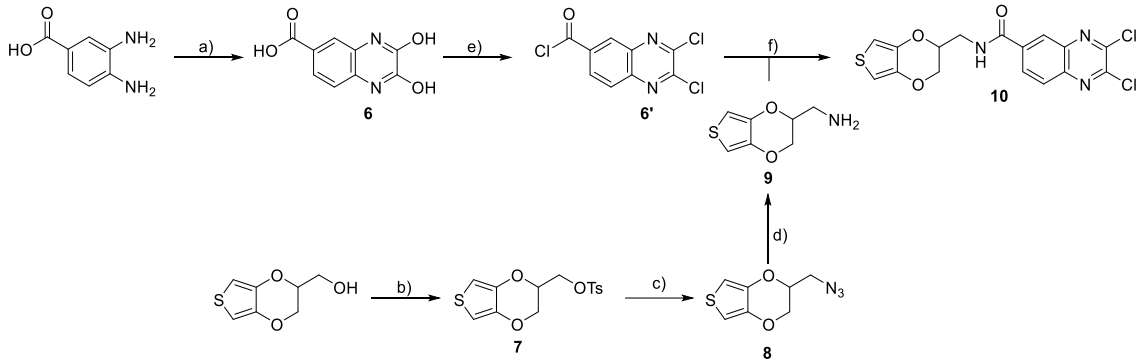

Scheme 3. *a) oxalic acid, HCl 4N, 100°C, 18h, 74% yield; b) p-toluenesulfonyl chloride, Et_3N, Dry DCM, RT, 24h, 87% yield; c) NaN_3, Dry DMF, RT, 5 days, 91% yield; d) 1. PPh_3, Dry THF, 30 min., 50°C. 2. NaOH aq. 2M, THF, 50°C, 4h, 99% yield; e) 1. $SOCl_2$, Dry DMF, 70°C, 5h; f) Dry DCM, Et_3N,* **9***, RT, 16h, 30% yield.*

For the modification of the quinoxaline wall, 2,3-dihydroquinoxaline-6-carboxylic acid **6** was selected due to its carboxylic acid functionality, which can undergo esterification or amidation reactions with suitable reactants[27] (Scheme 3). As thiophene moiety, (2,3-dihydrothieno[3,4-b][1,4]dioxin-2-yl)methanol was chosen (Scheme 3). A first attempt of direct esterification between the quinoxaline derivative **6** and (2,3-dihydrothieno[3,4-b][1,4]dioxin-2-yl)methanol was unsuccessful. Consequently, the hydroxyl group of the latter was converted into a primary amine to exploit its higher nucleophilicity in subsequent amidation reactions.

To introduce the amino group, the hydroxyl group was first converted into tosylate, via reaction with p-toluenesulfonyl chloride in a basic medium of triethylamine.[28] After purification by flash column chromatography, product **7** was obtained as a white solid in 87% yield. Compound **7** was then subjected to a nucleophilic substitution (SN2) reaction with sodium azide in dry DMF, replacing the tosylate with an azide moiety.[29] Purification by flash column chromatography, allowed to obtain compound **8** as a colorless liquid with a 91% yield.

Subsequently, the azide group was reduced to the corresponding primary amine using standard Staudinger reaction conditions.[30] Compound **8** was reacted with triphenylphosphine (PPh_3) in dry THF, followed by cleavage of the phosphorus-nitrogen bond using an aqueous solution of NaOH. The final primary amine (compound **9**) was isolated as a colourless liquid in quantitative yield after acid and alkaline washing.

In the last steps, compound **6** was chlorinated with thionyl chloride ($SOCl_2$) in dry DMF to form the corresponding acyl chloride **6'**. Because of its high moisture sensitivity, intermediate **6'** was not isolated but, after solvent evaporation, was recovered in a solution of dry DCM and Et_3N, and directly reacted with primary amine **9** to form the corresponding amide **10**. The desired thiophene-functionalized quinoxaline (compound **10**) was isolated as a yellow solid in 30% yield after purification by flash liquid chromatography. Derivative **10**

was then fully characterized by ^{1}H (Figure 8), ^{13}C, COSY, HSQC, and HMBC NMR spectroscopy (Figures S1-3).

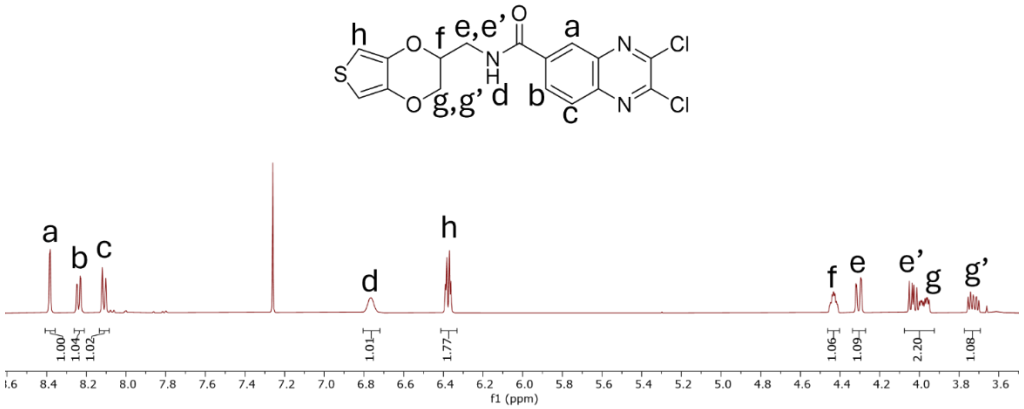

Figure 8. ^{1}H-NMR ($CDCl_3$, 25 °C, 500 MHz) spectrum of thiophene-modified quinoxaline **10**.

The ^{1}H-NMR spectrum shows all the signals belonging to the target product; among which the most diagnostic are the proton of the amide functional group (H**d**) at 6.77 ppm, the protons of the thiophene moiety (H**h**) at 6.34 ppm, and the three signals of the quinoxaline aromatic ring (H**a**, H**b**, and H**c**) at 8.38, 8.24, and 8.11 ppm, respectively.

As for the cavitand, the most efficient route for the synthesis of the triquinoxaline cavitand **13** (Scheme 4) involves the initial functionalization of resorcinarene (compound **11**) with four identical quinoxaline walls, leading to the formation of the tetraquinoxaline cavitand (compound **12**). This is followed by the selective excision of a single quinoxaline wall.

In the first synthetic step, hexyl-footed resorcinarene **11** was reacted with 2,3-dichloroquinoxaline to produce the tetraquinoxaline cavitand **12**. Purification by recrystallization in ethyl acetate (EtOAc) yielded the target compound with a 60% yield.

The selective cleavage of one quinoxaline wall was achieved by reacting **12** with pyrocatechol under basic conditions using cesium fluoride. The desired triquinoxaline cavitand **13** was obtained as a white solid with a 60% yield after purification by flash column chromatography.

The final step is the bridging reaction of triquinoxaline cavitand **13** with the modified quinoxaline wall **10** in a basic medium of K_2CO_3. Purification by flash liquid

chromatography afforded the target thiophene-functionalized quinoxaline cavitand **14** in a 40% yield.

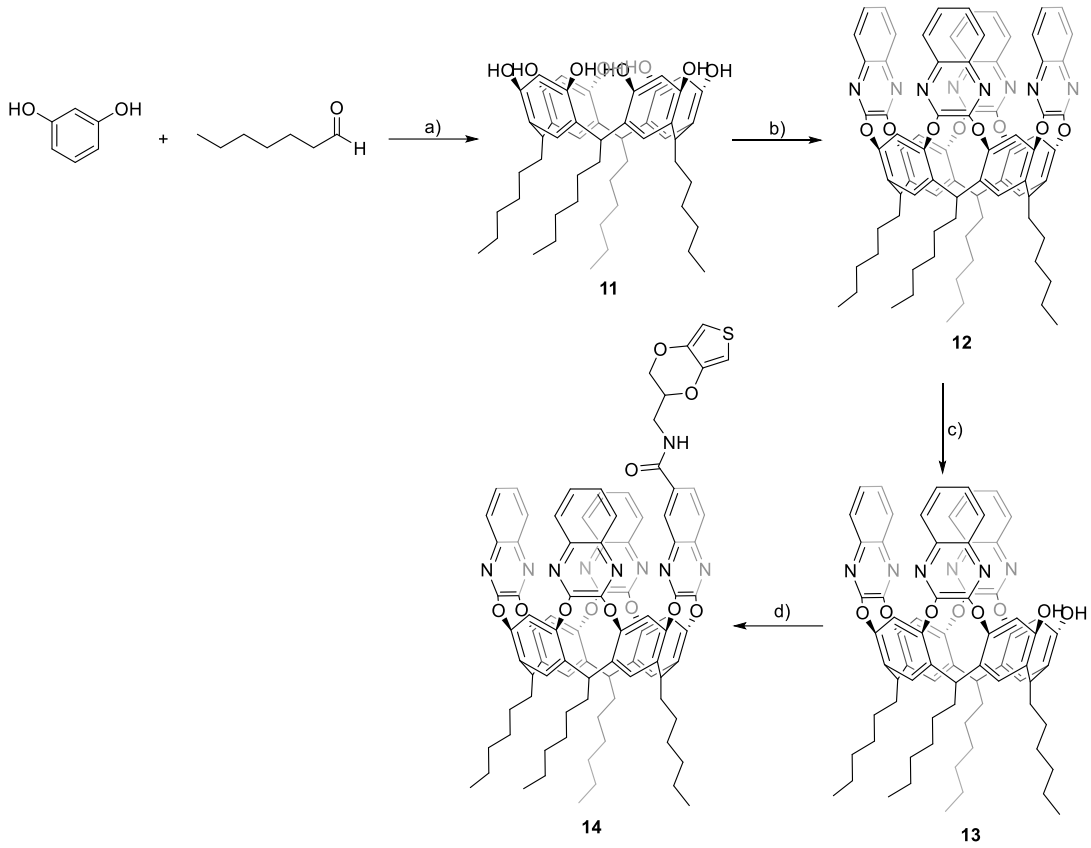

Scheme 4. *a) HCl 12M, MeOH, 55°C, 72h, 50% yield; b) K_2CO_3, 2,3-dichloroquinoxaline, Dry DMF, 80°C, 18h, 60% yield; c) CsF, pyrocatechol, 80°C, 30min, 60% yield; d) K_2CO_3, **10**, Dry DMF, 80°C, 18h, 40% yield.*

Compound **14** was fully characterized by ^{1}H (Figure 9), ^{13}C and bidimensional NMR spectroscopy (Figures S4-7).

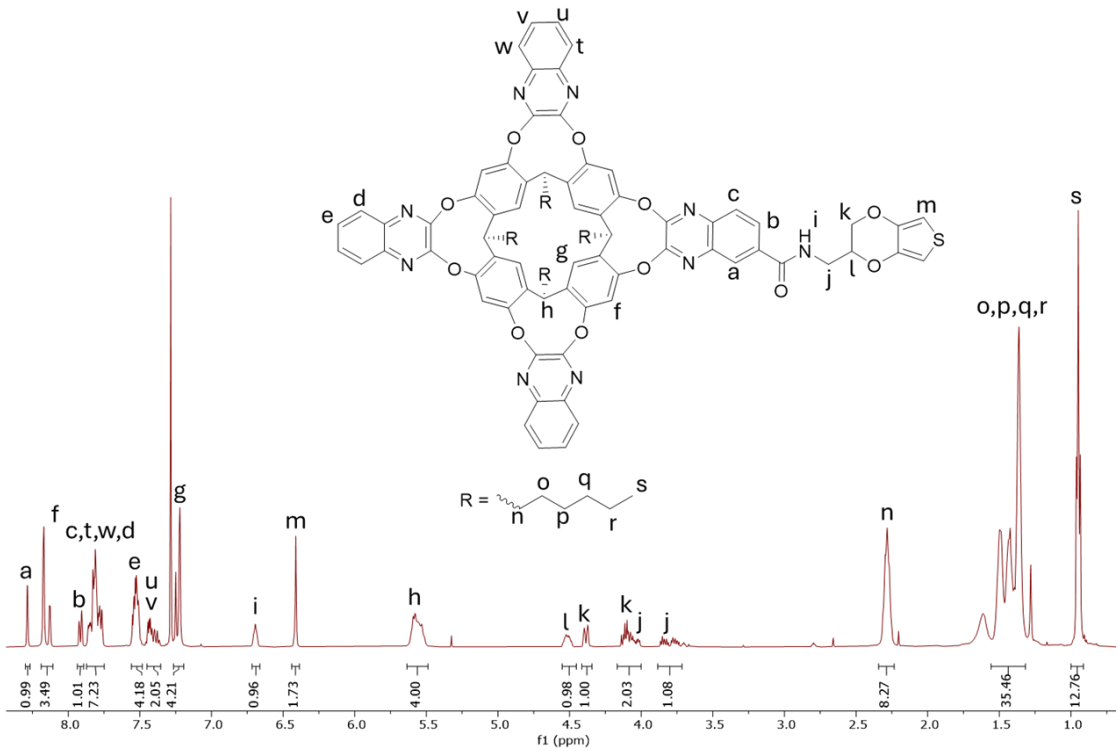

Figure 9. ^{1}H-NMR ($CDCl_3$, 25°C, 500MHz) spectrum of compound **14**

The ^{1}H-NMR spectrum reported in Figure 3 shows all the diagnostic peaks belonging to the target compound. The most significant are the aromatic signal (H**a**) of the modified quinoxaline's aromatic ring in the alpha position with respect to the amide at 8.29 ppm, the proton of the amide (H**i**), and the protons of the thiophene (H**m**) at 6.69 and 6.49 ppm, respectively. Moreover, the signals of the bridging protons (H**h**) at 5.56 ppm indicate that the macrocycle is in its vase conformation.

The identity of the target compound **14** was confirmed by the MALDI-TOF analysis (Figure 10), which shows the protonated adduct of the cavitand, in agreement with the simulated isotopic pattern, and the adduct with sodium.

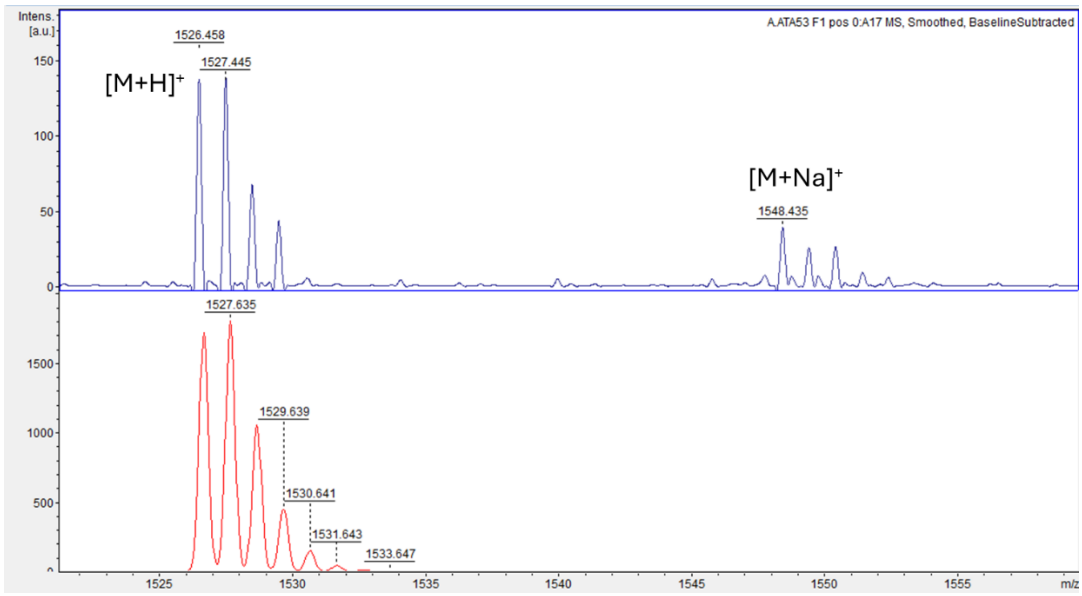

Figure 10. Stacking between experimental (blue trace) and simulated spectra (red trace) of the MALDI-TOF analysis on compound **14**.

3.3 Electrochemical copolymerization of Cavitand 14

Once a robust and reliable route for the synthesis of the quinoxaline cavitand **14** was established, it was decided to use it as a co-monomer in a polymerization reaction with (2,3-dihydrothieno[3,4-b][1,4]dioxin-2-yl)methanol. The co-polymerization approach was chosen due to the high steric hindrance of the macrocycle, which could prevent the formation of the corresponding homo-polymer. Additionally, electrochemistry was selected as an effective polymerization strategy because it minimizes material consumption and allows for mild, highly controlled reaction conditions.

First, the cyclic voltammetry (CV) of the individual monomers was measured to determine the oxidation potential necessary to oxidize the thiophene moiety and consequently perform the polymerization (Figure 11). As a reference, the reversible oxidation/reduction potential of ferrocene/ferrocenium (Fc/Fc^+) was measured, yielding a formal potential $E_{1/2}$ = +0.44 V calculated as the medium potential between the oxidation and reduction peaks.

The potential was scanned over a range from -2.0 to +1.8 V using a mixture of DCM/ACN (5:1) as the solvent, with a 0.1 M solution of tetrabutylammonium hexafluorophosphate (TBAHFP) as the supporting electrolyte. A glassy carbon (GC) electrode was used as the working electrode, Ag/AgCl as the reference electrode, and a platinum rod as the counter electrode (Figure 11). The two monomers exhibited a clear oxidation peak attributed to the oxidation of the thiophene moiety. The oxidation potentials, calculated from the corresponding maximum current values, were +1.62 V and +1.53 V for the quinoxaline cavitand **14** and the co-monomer EDOT, respectively.

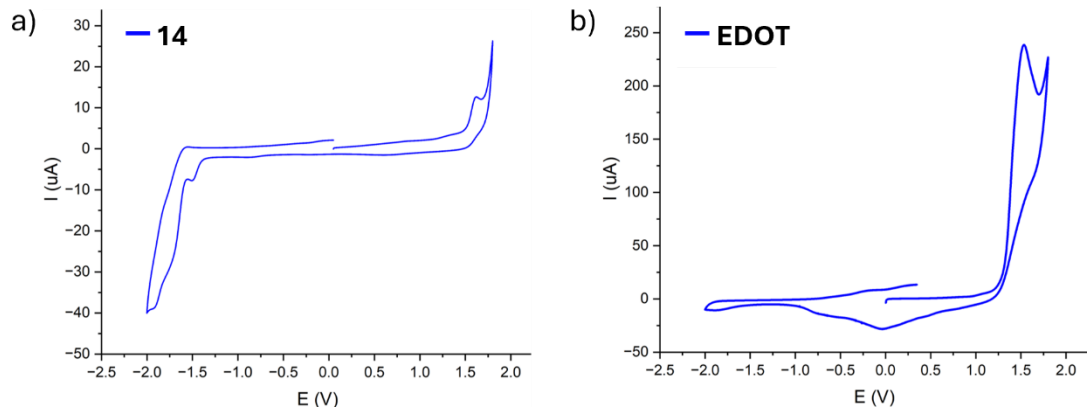

Figure 11. CV curves of monomers: a) Quinoxaline Cavitand **14** and b) EDOT

After measuring the individual oxidation potentials, a solution containing the two monomers was prepared in the same solvent mixture and with the same electrolyte concentration. For the polymerization, a **14 : EDOT** molar ratio of 1 : 3 was chosen, using a concentration of 0.5 mM for compound **14**. The applied potential ranged from 0.0 to +1.8 V at a scan rate of 50 mV/s for 50 scans. The graphs in Figure 12 show the first two scans (a and b) and the total CV of the copolymerization reaction (c).

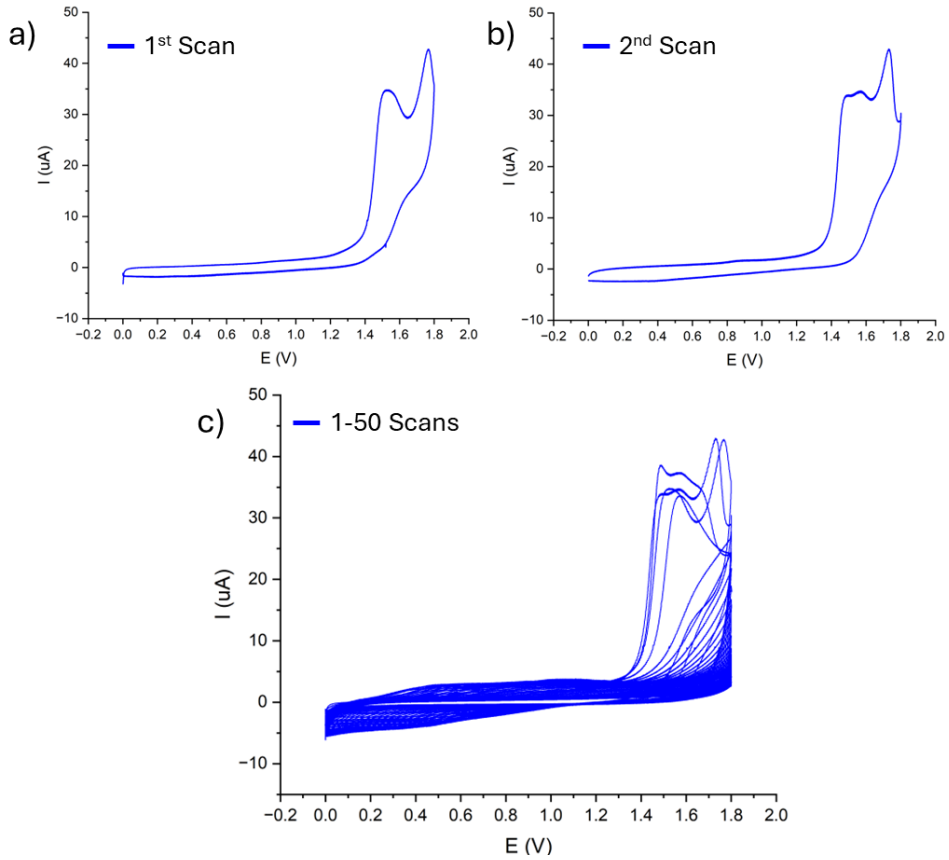

Figure 12. CV of the polymerization reaction: a) first scan; b) second scan; c) full CV.

From figure 12 a) and b), it is possible to notice that when the potential is scanned from 0.0 to +1.8V, the curve shows 2 clear oxidation peaks which might be related to the oxidation of the two monomers. On the other hand, when the potential is scanned backwords to complete the cycle, any new peak is observed meaning that no polymer is growing on the working electrode. This means that is not possible to co-polymerized the quinoxaline cavitand **14**, probably due to the high steric hindrance of the macrocycle and because of the very high oxidation potential required to ensure the oxidation of the thiophene moieties. Such high oxidation potential could indeed lead to the degradation of the conductive polymer that should form on the electrode, thus preventing its formation from the outset.

3.4 Synthesis of Quinoxaline Cavitand 17

Given all the issues encountered with the polymerization of the quinoxaline cavitand functionalized with EDOT, it was decided to change the monomeric unit by introducing a pyrrole at the upper rim of the cavitand. The introduction of pyrrole is expected to lower the oxidation potential, giving a monomer that requires milder reaction conditions for its electrochemical polymerization.

The preparation process for a conductive copolymer based on polypyrrole containing a tetraquinoxaline cavitand can be divided into two primary stages: the synthesis of the receptor with appropriate functionalization at the upper rim, and the copolymerization reaction between the macrocyclic compound and the commercial co-monomer.
The pyrrole-functionalized cavitand **17** was synthesized via a convergent synthetic strategy. This approach involves the well-established preparation of the triquinoxaline cavitand scaffold **13**, as previously described, followed by a bridging reaction with a suitably functionalized 2,3-dichloroquinoxaline moiety, as reported in Scheme 5.

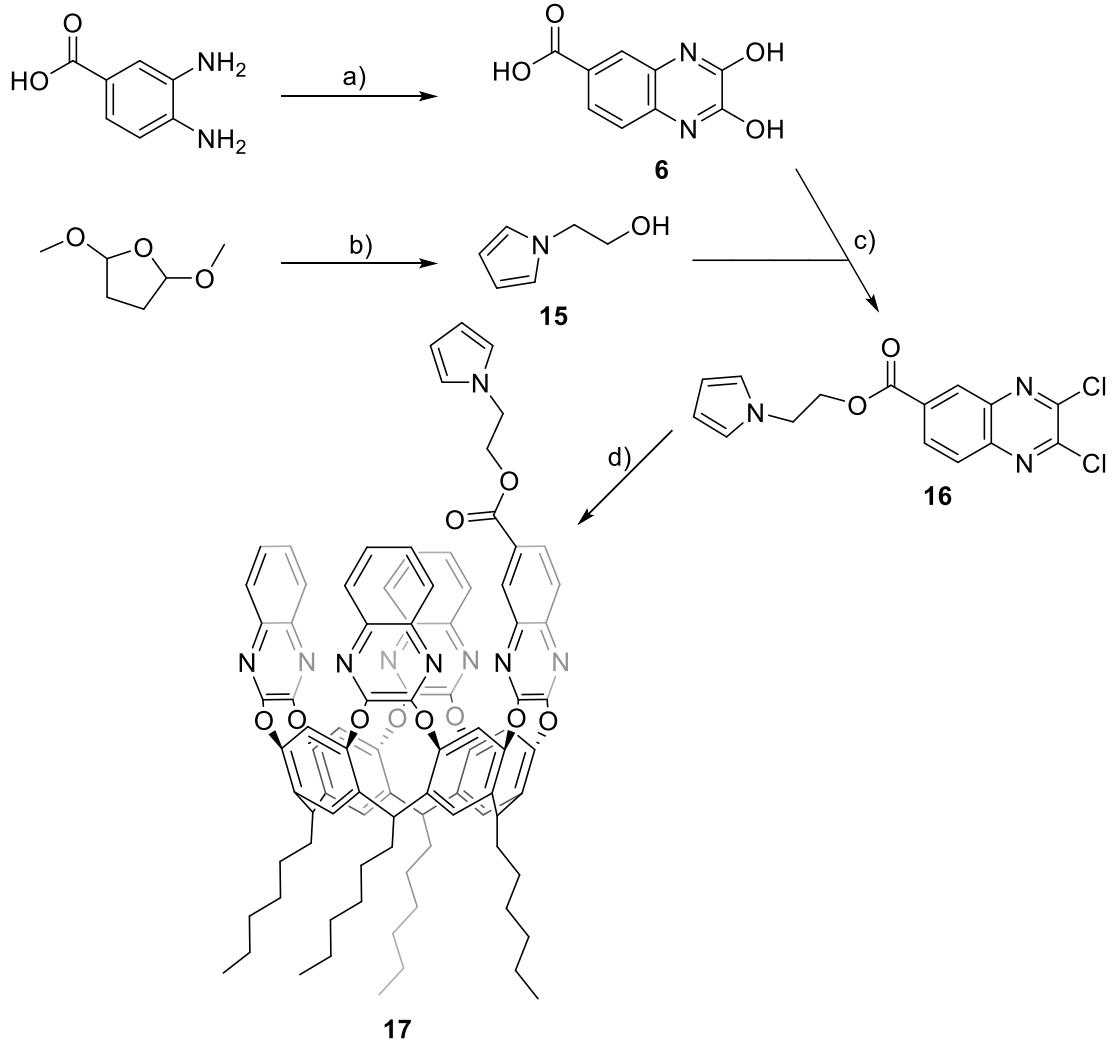

Scheme 5. *a) Oxalic acid, HCl 4N, 100°C, 18h, 74% yield; b) ethanolamine, glacial acetic acid, 115°C, 16h, 15% yield; c) 1. $SOCl_2$, Dry DMF, 70°C, 5h. 2. Dry DCM, Et_3N, **16**, RT, 16h, 46%; d) K_2CO_3, **13**, Dry DMF, 80°C, 18h, 59% yield.*

2,3-Dihydroquinoxaline-6-carboxylic acid **6** was prepared using a previously reported methodology already presented in Scheme **3**.[27] Separately, 2-(1H-pyrrol-1-yl)ethan-1-ol **15**

was synthesized following a known literature procedure,[31] where 2,5-dimethoxytetrahydrofuran was reacted with an excess of ethanolamine in glacial acetic acid. Subsequent basic treatment and alkaline work-up facilitated the recovery of the target pyrrole **15** as a brown oil with a 15% yield. Compounds **6** and **15** were then used as precursors for the synthesis of the modified quinoxaline **16**. This involved a two-step reaction: first, the quinoxaline scaffold was fully chlorinated by reaction with thionyl chloride. After solvent removal, the resulting acyl chloride on the quinoxaline scaffold was allowed to react with the hydroxyl moiety on pyrrole **15**, forming the corresponding ester. Purification via flash chromatography afforded the desired pyrrole-functionalized quinoxaline, as a yellow solid with a 46% yield. Compound **16** was characterized by ^{1}H (Figure 13), ^{13}C, COSY and HSQC NMR spectroscopy (Figures S8-10).

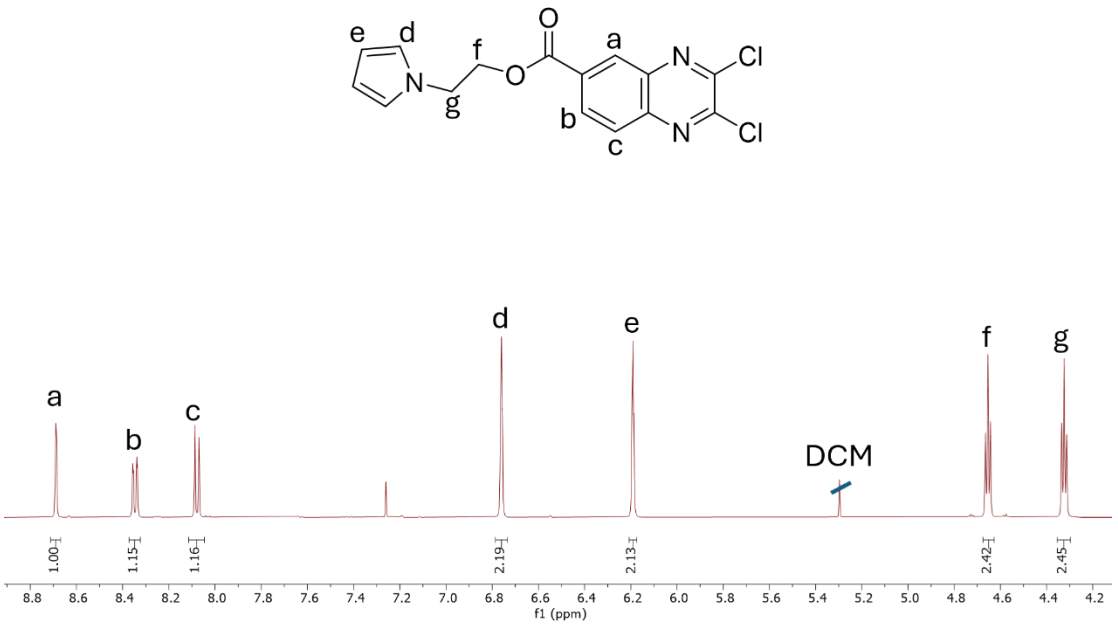

Figure 13. ^{1}H-NMR spectrum ($CDCl_3$, 25 °C, 500MHz) of compound **16**.

The spectrum shows all the peaks belonging to the desired product: the aromatic quinoxaline pattern of protons H**a**, H**b** and H**c**, the two signals of pyrrole at 6.76 and 6.19 ppm of H**d** and H**e**, and the two triplets belonging to protons H**f** and H**g** of the alkyl chain.
The final step is the bridging reaction between the pyrrole-modified quinoxaline **16** and the triquinoxaline cavitand **13**. The reaction was performed in in dry DMF under basic conditions. After purification by flash chromatography, the target pyrrole-functionalized quinoxaline cavitand (**17**) was obtained as a white solid with a 59% yield. Derivative **17** was

fully characterized by ^{1}H (Figure 14), ^{13}C, COSY, HSQC, and HMBC NMR spectroscopy (Figures S11-14), as well as MALDI-TOF mass spectrometry (Figure 15).

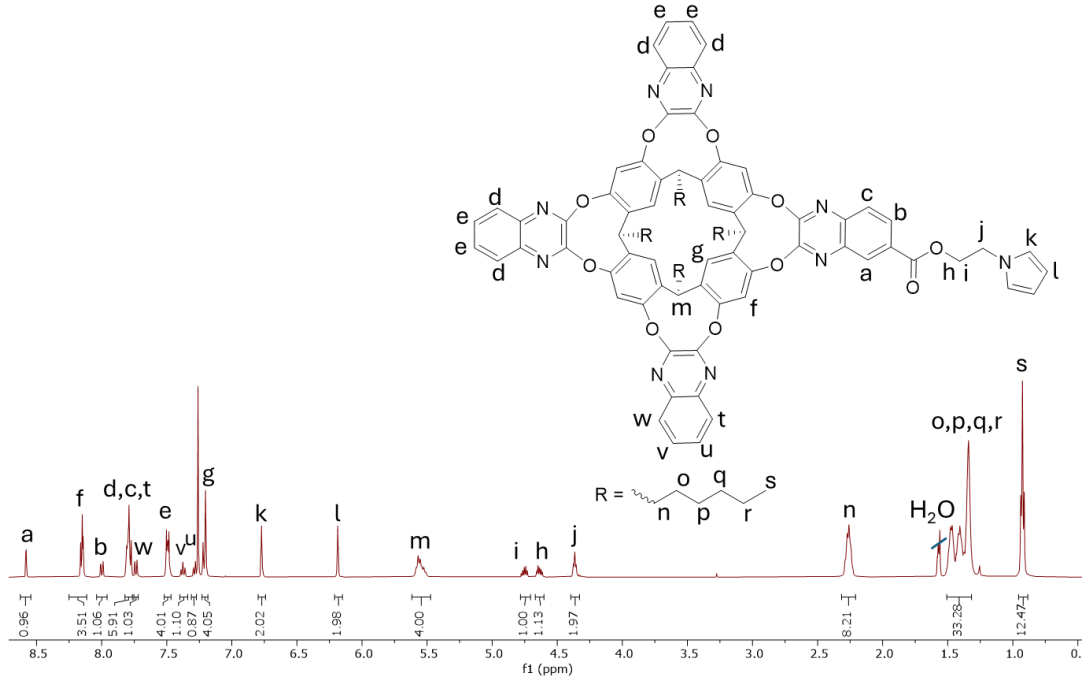

Figure 14. ^{1}H-NMR spectrum ($CDCl_3$, 25°C, 500MHz) of compound **17**.

The ^{1}H-NMR spectrum displayed all the diagnostic signals characteristic of the target molecule. Notably, the proton associated with the modified quinoxaline wall (H**a**) resonated at 8.58 ppm. The pyrrole moiety's protons (H**k** and H**l**) were detected at 6.77 and 6.22 ppm, respectively, alongside the signals corresponding to the ethylene chain protons (H**i**, H**h**, and H**j**). Importantly, the two protons H**i** and H**h**, in α position to the ester functionality, displayed distinct signals, with one proton located within the hydrophobic cavity of the macrocycle, resulting in a shielded environment. Additionally, the chemical shift of the bridging proton H**m** at 5.56 ppm indicates that the cavitand is present in the vase conformation.

The identity of the target molecule was confirmed by MALDI-TOF analysis (Figure 15), with the spectrum displaying both the proton and sodium adducts. The isotopic pattern of the proton adduct was found to be in excellent agreement with the simulated spectrum.

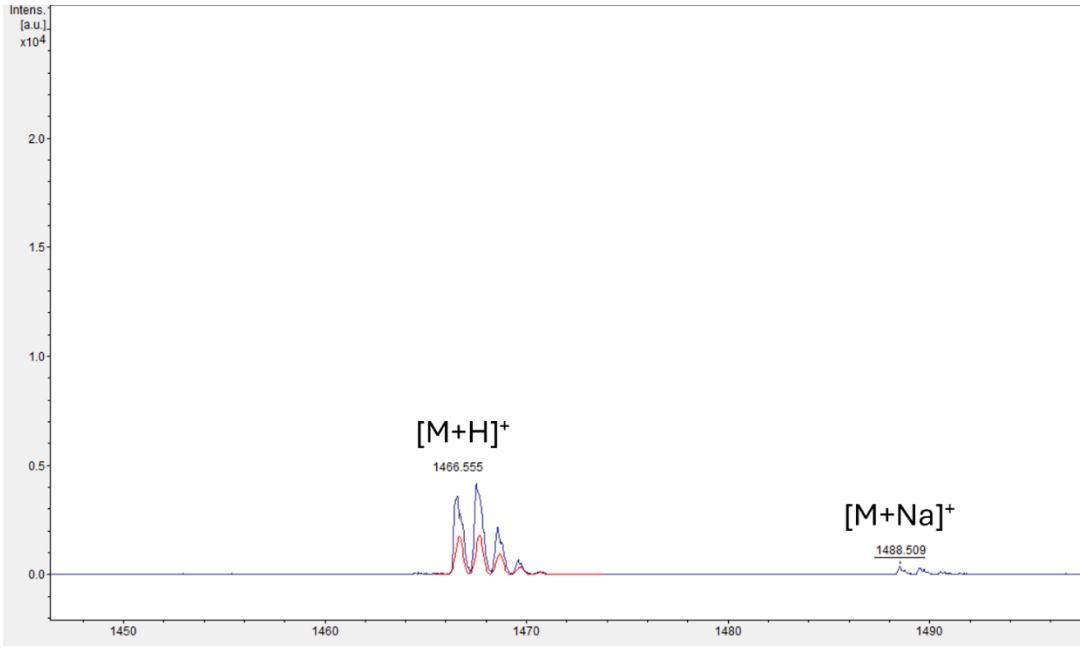

Figure 5. MALDI-TOF spectrum of target cavitand **17**.

3.5 Electrochemical polymerization of Quinoxaline Cavitand 17

A first co-polymerization attempt was carried out using N-Methyl pyrrole (N-MePy) as co-monomer. Initially, electrochemical polymerization was chosen as the polymerization method due to its low material consumption and mild reaction conditions.

The electrochemical copolymerization was performed in a solvent mixture of dichloromethane (DCM) and acetonitrile (ACN) in a 5:1 ratio, utilizing a 0.1M concentration of tetrabutylammonium hexafluorophosphate as the electrolyte. For the electrodes, a combination of Ag/AgCl as the reference electrode, a Pt rod as the counter electrode, and glassy carbon as the working electrode was selected. As a reference, the reversible oxidation/reduction potential of ferrocene/ferrocenium+ (Fc/Fc^{+}) was measured, giving an $E_{1/2}$ = +0.44 V, calculated from the oxidation-reduction peak.

Following the same approach used for cavitand **14**, the cyclic voltammetry (CV) of the individual monomers was measured (Figure 16) to determine the oxidation potential required for the electrochemical reaction between the two monomers.

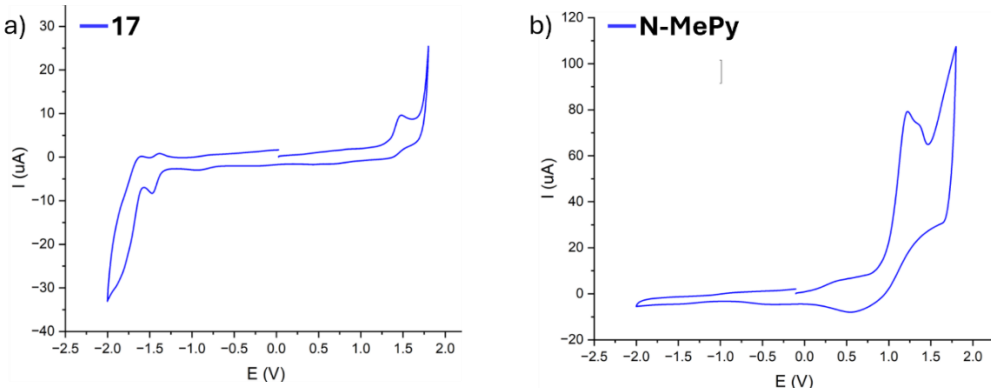

Figure 16. Cyclic Voltammetry of a) quinoxaline cavitand **17** and b) N-Methyl pyrrole

The oxidation peaks, calculated from the maximum of the anodic current of the two CVs, resulted to be +1.42 V and +1.22 V for the quinoxaline cavitand **12** and the N-Methyl pyrrole, respectively. these values are slightly lower compared to the oxidation peaks measured in the previous approach, which involved using EDOT as the monomer.
Once determined the oxidation potential of the two partners for the reaction, a first co-polymerization attempt was performed (Scheme 6).

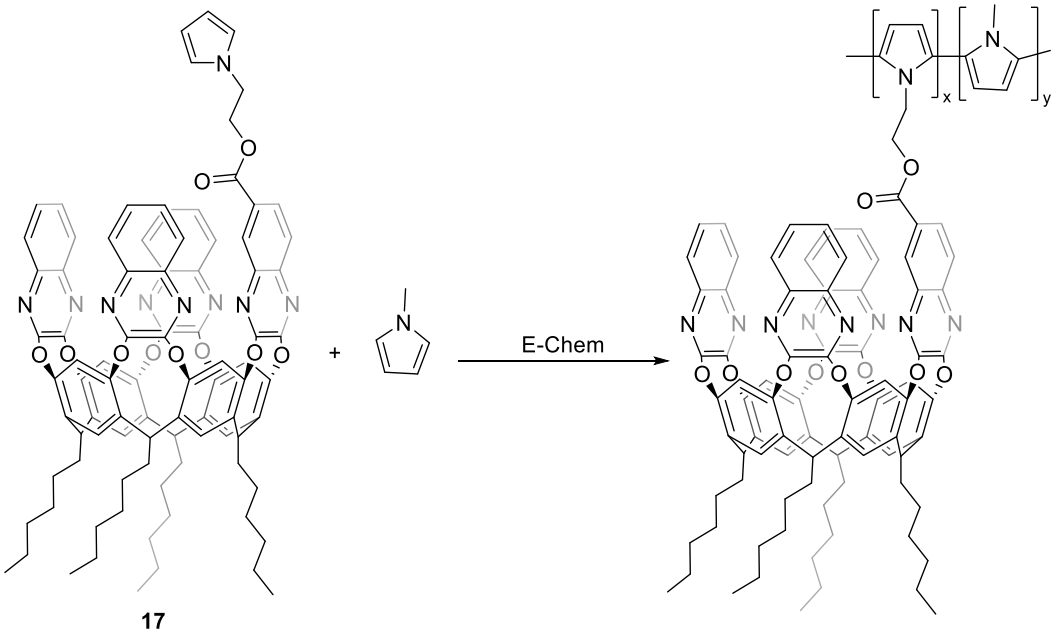

Scheme 6. Electrochemical co-polymerization of cavitand **17** with N-Methyl pyrrole (N-MePy).

For the reaction, a ratio of 1 : 3 between cavitand **17** and N-Methyl pyrrole was chosen, with a concentration of 0.5 mM relative to the macrocycle. To ensure the oxidation of both monomers, the potential was scanned between 0.0 and +1.6 V for 50 scans with a scan rate of 50 mV/s. Figure 17 shows the first, the second and the overall scans performed.

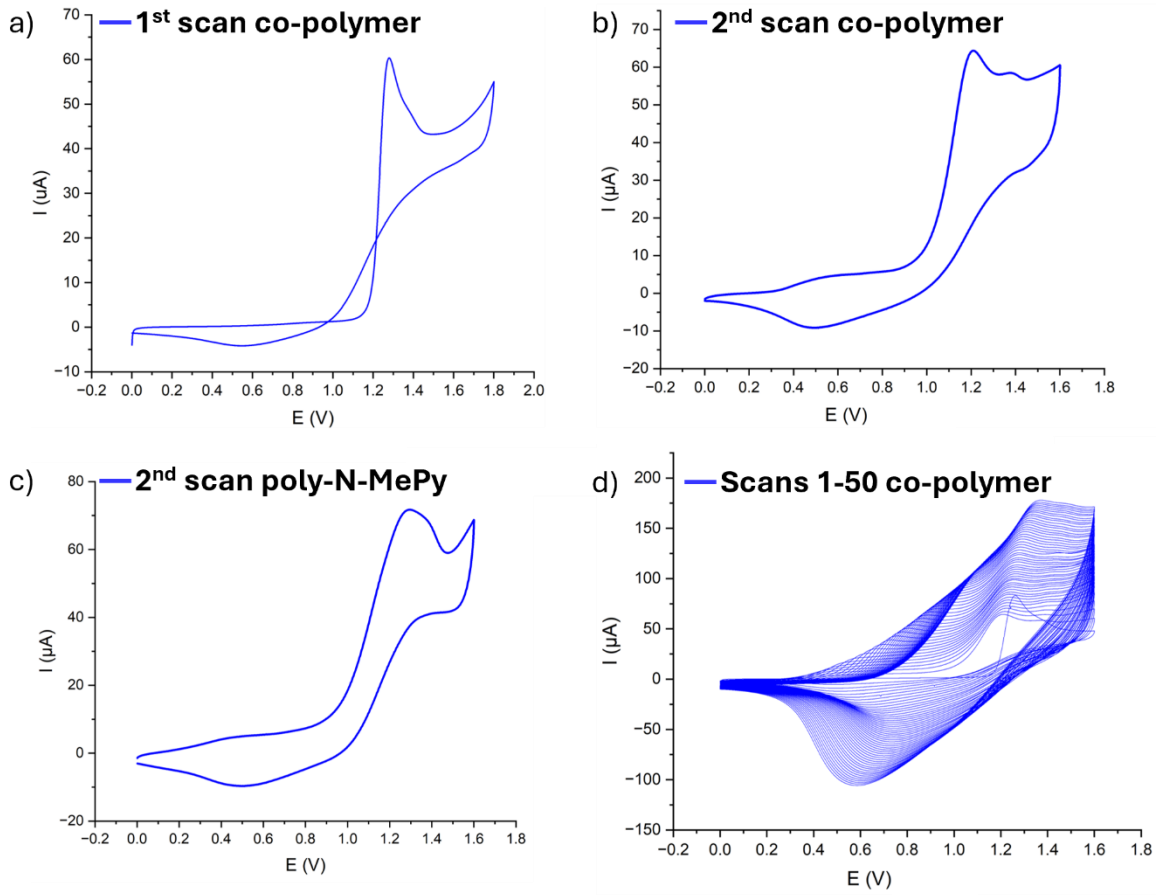

Figure 17. a) first co-polymerization scan; b) second co-polymerization scan; c) second scan homo-polymerization of poly-N-MePy; d) CV of co-polymerization scan.

From the second scan, it is evident that there are two distinct oxidation peaks: the first, more intense, around +1.2 V, which likely corresponds to N-Methyl pyrrole, and the second, less intense, around +1.4 V, which can be attributed to the quinoxaline cavitand. This was confirmed by comparing the second scan of the copolymerization with that of N-Methyl pyrrole homo-polymerization under identical conditions, where only the oxidation peak at +1.2 V was observed.

Moreover, when the potential is scanned backwards from +1.6 V to 0.0 V, a reduction peak appears and increases with successive scans. This can be attributed to the formation and growth of a conductive polymer that deposits on the glassy carbon electrode as the cycles progress.

Encouraged by these promising results, additional copolymerization attempts were conducted to assess the reproducibility of the system. Unfortunately, the replicates revealed challenges in obtaining a consistent polymerization method with these monomers. Figure 18 illustrates the high variability in shape and peak intensity across different polymerization

curves. In some reactions, both the oxidation and reduction peaks grow as the number of scans increases (Figure 18a), while in others, the oxidation peak tends to disappear with successive scans, though the reduction peak continues to grow (Figure 18b). In certain cases, both peaks diminish after a few scans, and the curves become completely flat (Figure 18c).

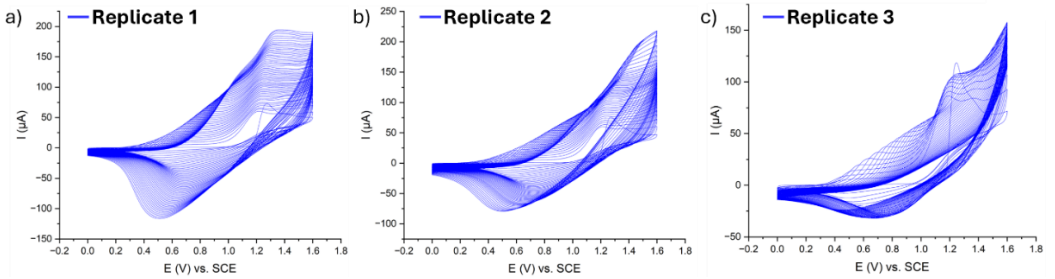

Figure 18. Three different replicates of cavitand **17** co-polymerization reaction in 1:3 ratio.

The low reproducibility could be attributed to several possible factors. First, the bulkiness of macrocycle **17** could cause perturbations in the system, making the polymerization reaction significantly more difficult, especially considering the much smaller size of the comonomer. A second issue could stem from the very high oxidation potential of the cavitand. In general, for successful electrochemical co-polymerization, not only should the oxidation potential of the two monomers be lower, but ideally, the bulkier and less reactive compound should have a lower oxidation potential compared to the co-monomer. This would facilitate better control of the copolymerization reaction and maximize the reactivity of both monomers.

In our case, the higher oxidation potential of the cavitand hinders precise control of its reactivity relative to the co-monomer. The high oxidation potential required to oxidize both monomers may be too elevated to allow proper growth of the conductive polymer and could also result in side reactions leading to degradation.

To address this, another attempt was made by increasing the cavitand/N-Methyl pyrrole ratio in favour of the commercial monomer, from 1 : 3 to 1 : 6. The aim was to co-polymerize the cavitand into the conductive polymer without inhibiting the reactivity of N-Methyl pyrrole. Unfortunately, although a better reproducibility of the reaction was observed, a certain degree of variability persisted (Figure 19).

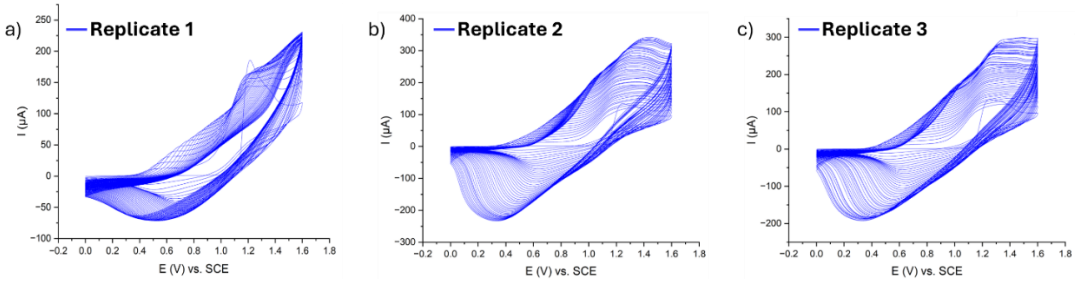

Figure 19. Three different replicates of cavitand **17** copolymerization reaction in 1:6 ratio.

Indeed, looking at the three replicates reported in Figure 19, we can see that in the first case (a), at the beginning of the reaction, both the oxidation and reduction peaks increase. However, as the number of scans progresses, the oxidation peaks disappear, while the reduction peaks stop growing and begin to decrease. This could be due to the progressive degradation of the conductive polymer formed on the electrode. On the other hand, in cases (b) and (c), both the oxidation and reduction peaks continue to grow with the increasing number of scans, which is consistent with the ongoing polymerization of the two monomers and the growth of the conductive polymer.
Even though the reproducibility of the reaction was quite low, preliminary sensing studies have been performed to determine if, upon finding good reaction conditions, the system could be suitable for the realization of a sensor.

To investigate whether this polymer could have potential applications as a sensor for detecting PFAS, the CV of the polymer was measured in a fresh solution of supporting electrolyte after polymerization. Then, the electrode coated with the polymer was immersed in deionized (DI) water for 45 minutes, and the CV was measured again. Finally, the electrode was dipped in a 100 ppm water solution of PFOA, and the CV was measured once more.
In theory, after exposure to DI water, the CV of the polymer should overlap with the original curve. Upon exposure to the pollutant, a difference in the oxidation and reduction peaks should be observed, such as a shift in potential or a change in peak intensity (Figure 20).

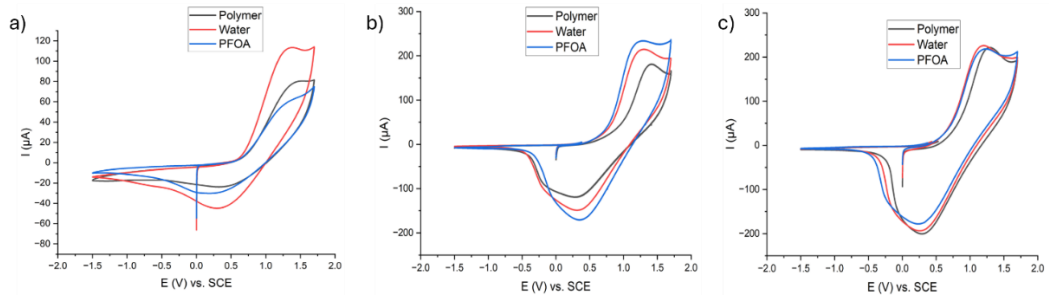

Figure 20. Cyclic Voltammetry of three different cavitand **17** copolymers as synthesized (grey trace), after exposure to DI water (red trace) and after exposure to 100ppm PFOA.

From Figure 20, it can be observed that not only does the polymer exhibit variation when exposed to DI water, but the changes in CV after different exposures are completely random. In some cases, both the oxidation and reduction peaks increase in intensity upon exposure, while in others, they decrease. This random variation is incompatible with the development of a sensor, which should provide consistent responses to the same trigger.
Once determined that the system is not suitable for the realization of a sensor for PFAS, it was decided to change approach to verify if the receptor, upon polymerization, can form a material with potential applications as absorbent for PFAS removal.

3.6 Oxidative Polymerization of quinoxaline cavitand 17

For the development of a material with potential applications as an adsorbent for pollutants removal, a change in the polymerization strategy is necessary. The goal requires a robust polymerization method that allows to produce sufficient quantities of material with a good batch-to-batch reproducibility.

To pursue this, the standard oxidative polymerization of pyrrole using iron(III) chloride as oxidizing agent was chosen.[32]

This reaction involves the dehydrogenation and the oxidative coupling of the monomer precursor pyrrole (Py) in which iron(III) chloride ($FeCl_3$) acts as catalyst for the process. The anions Cl^- formed during the reaction process will act as dopants for the formation of polarons and bipolarons, the charge carriers which are responsible for materials conductivity.[32]

Initially, a homopolymerization of cavitand **17** was attempted using chloroform as the solvent and 2.33 equivalents of iron(III) chloride per equivalent of cavitand, as this is known to be the optimal ratio between monomer and oxidant for these types of polymerization (Scheme 7).[33]

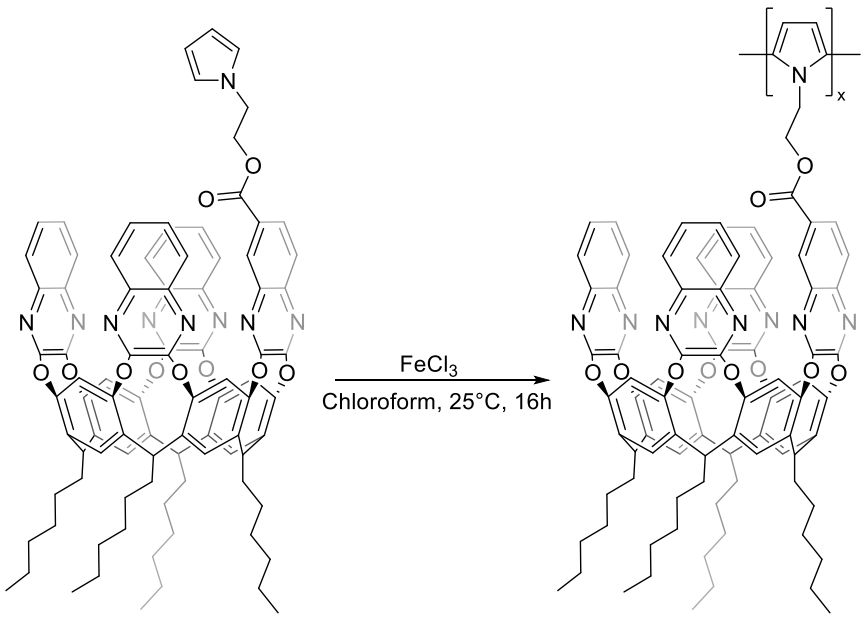

17

Scheme 7. Cavitand **17** oxidative homo-polymerization reaction.

The reaction was kept at room temperature for 16 hours and monitored by TLC. Upon confirming the complete disappearance of cavitand **17**, the solvent was evaporated under vacuum and the crude was recovered using water. The solid was then washed 3 times with water, twice with acetone and twice with DCM, with separation performed via centrifugation after each washing step. The product was recovered as black powder and the presence of the

cavitand was checked by FT-IR comparing the spectrum of the polymer with the one of the monomer (Figure 21).

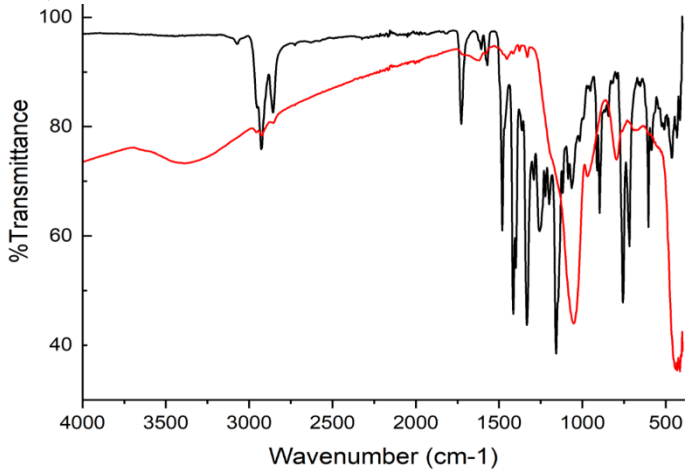

Figure 21. Comparison of FT-IR of cavitand 12 (black trace) and poly-cavitand (red trace).

From the comparison of the two spectra, it is evident that after polymerization, all the key diagnostic peaks of the cavitand disappeared, particularly the ester signal at 1750 cm^{-1}. Only a few broad signals below 1000 cm^{-1} were visible. The FT-IR analysis suggests that the solid obtained does not contain the cavitand, likely because the bulkiness of the macrocycle prevents the pyrrole functionality from undergoing proper polymerization.

To address the issue of the bulkiness of cavitand **17**, a co-polymerization reaction with N-Methyl pyrrole was attempted. This approach aims to facilitate polymer chain formation through the comonomer while incorporating some cavitand units into the polymer (Scheme 8).

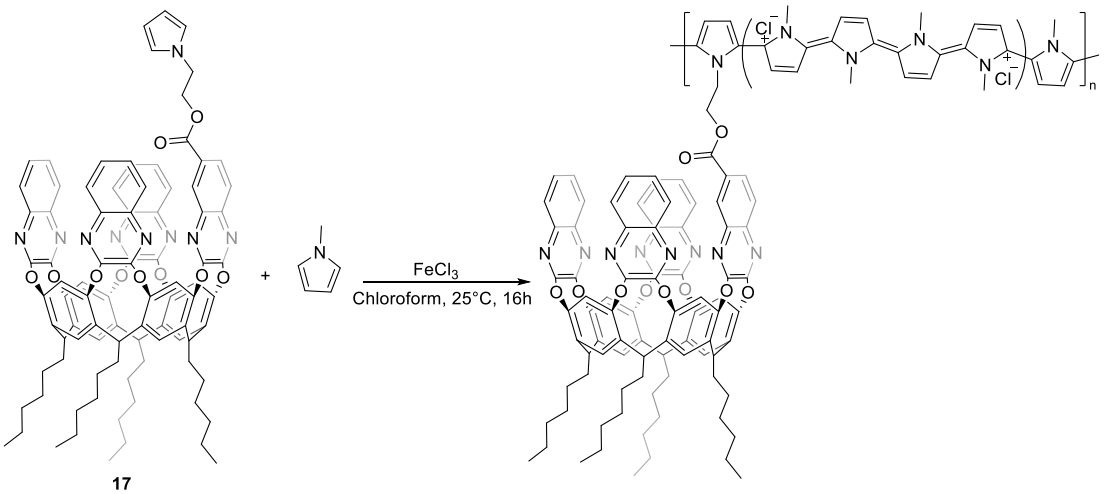

Scheme 8. Cavitand **17** oxidative copolymerization reaction

Two different reactions were performed using different ratios of cavitand **17** to N-Methyl pyrrole, specifically 1:5 and 1:10. Both reactions were carried out in chloroform at room temperature, using 2.33 equivalents of iron(III) chloride as the oxidant with respect to the total amount of monomers. The reaction progress was monitored by TLC, and once the complete disappearance of the cavitand was observed, the solvent was evaporated under high vacuum. As before, the resulting black solid was recovered using water, washed three times with water, twice with acetone, twice with DCM, and then dried under high vacuum.
The amount of polymer recovered increased significantly decreasing the amount of cavitand in the reaction environment. Specifically, starting with 100 mg of cavitand **17**, 20 mg of polymer have been recovered when using the 1:5 ratio. The increase of the co-monomer in the reaction stoichiometry allowed to recover up to 90 mg of polymer upon purification. The two polymers were then characterized by FT-IR, and their spectra were compared with those of the two monomers (Figure 22).

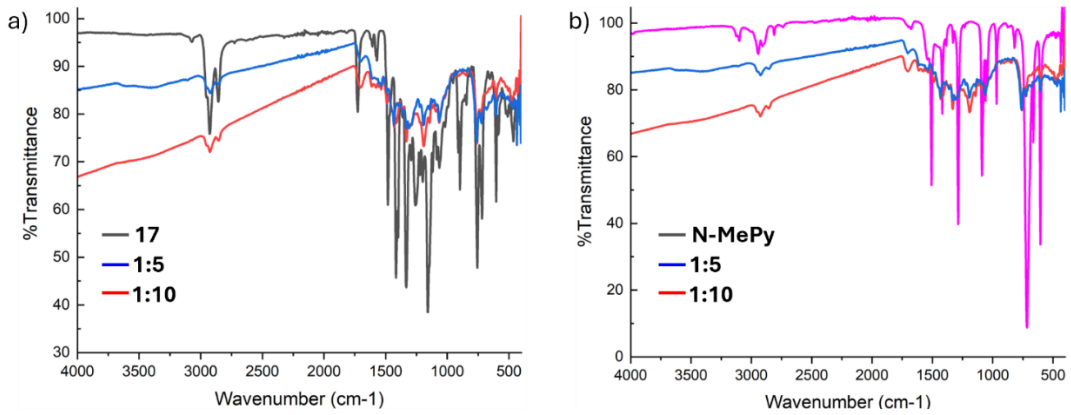

Figure 22. FT-IR spectra stacking of a) cavitand **17** with two copolymers and b) N-MePy with two copolymers.

As observed, the spectra of the two polymers are identical and both exhibit peaks corresponding to cavitand **17** and N-Methyl pyrrole. This indicates that the size of the cavitand hinders direct polymerization, making the copolymerization approach with N-Methyl pyrrole as the co-monomer the appropriate strategy. Due to the better polymerization performances, the co-polymer with a cavitand : N-MePy stoichiometry of 1 : 10 was chosen as material for further characterization and as an absorbent for PFAS. The characterization of the obtained product was carried out by ^{13}C Solid-state NMR, and its spectrum was compared with the solid-state spectrum of cavitand **17** and with poly-N-Methyl pyrrole (Figure 23).

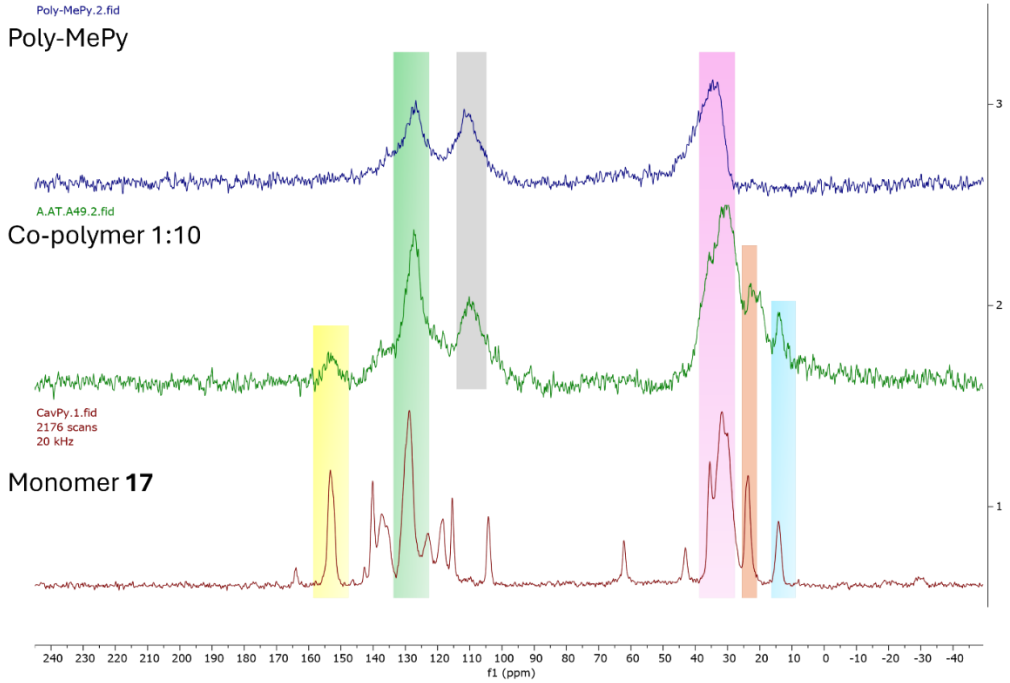

Figure 23. Stacking of solid-state NMR spectra (^{13}C, 25 °C, 125 MHz) of cavitand **17** (red trace), co-polymer 1:10 (green trace) and Poly-N-MePy (blue trace).

Comparing the three spectra, it is possible to confirm the effective formation of the copolymer and the presence of the cavitand inside the polymer due to the presence of the signals highlighted in yellow, in orange and blue. The copolymer presents also the signals of the poly-N-MePy homo-polymer (green, grey and pink) thus demonstrating the formation of the poly-pyrrole backbone.

Once the presence of the cavitand inside the copolymer was demonstrated, we tested the capability of the polymer to trap the target PFOA. To do so, the chosen approach was to expose the polymer matrix to different solutions of PFOA, measuring by LC-MS the difference in concentration of the pollutant in the mother solution before and after the exposure to the polymer, thus mimicking the working principle of a membrane (Figure 24). As control experiment, the same approach was applied to the homopolymer Poly-N-Methyl pyrrole.

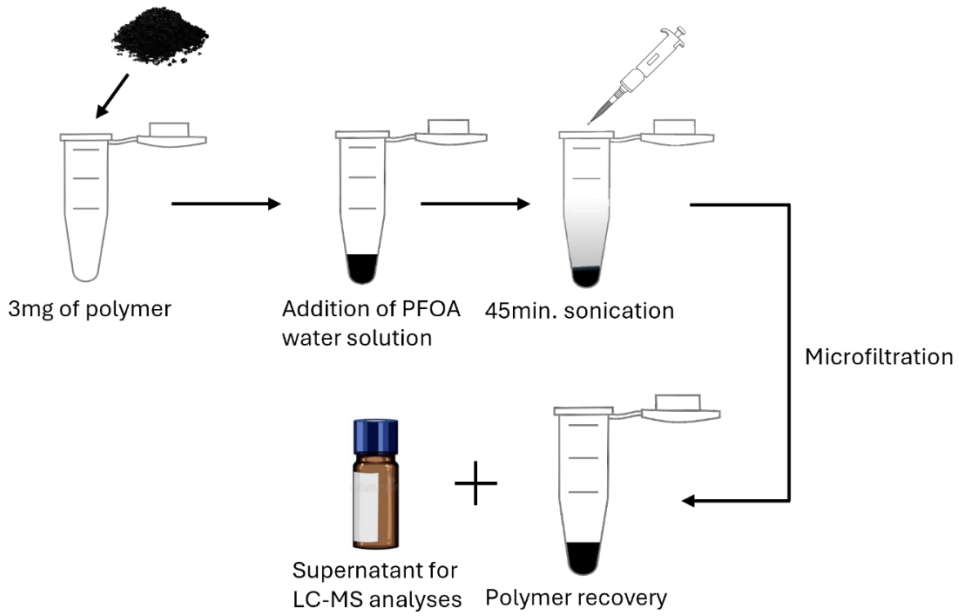

Figure 24. Schematic representation of the preparation of the LC-MS samples.

For the LC-MS measurements we adapted a known literature procedure which is specific for the analysis of some perfluoroalkyl substances, including PFOA which gave a limit of detection (LOD) in the ng/kg level.[34]
The removal capability of the copolymer was tested exposing 3 mg of material to 1 mL of a solution of PFOA in water. The mixture was sonicated for 30 minutes, then the polymer was filtered off, and the mother liquors were recovered and subjected to LC-MS analysis. The LC-MS analysis was performed using a C18 column and a mixture of water (A) and acetonitrile (B) as eluent with the following elution profile: 0-3 min: 30-65% B; 3-4 min: 65% B; 4-5 min: 65-100% B; 5-8 min: 100% B. These conditions allowed the elution of the analyte with a retention time of 6.60 minutes. Three different concentrations of PFOA have been tested: 200ppb, 20ppb and 2ppb measuring three replicates for each concentration. To calculate the removal efficiency of the polymer, the calculation was made comparing the integrals of the peak of the analyte before and after the exposure to the polymer.
The efficiency of PFOA removal can be calculated as follows:

$$Removal\ \% = \left(1 - \frac{I_{post\ exposure}}{I_{pre\ exposure}}\right) * 100$$

Results obtained with the active copolymer and the control polymer are summarized in Figure 25:

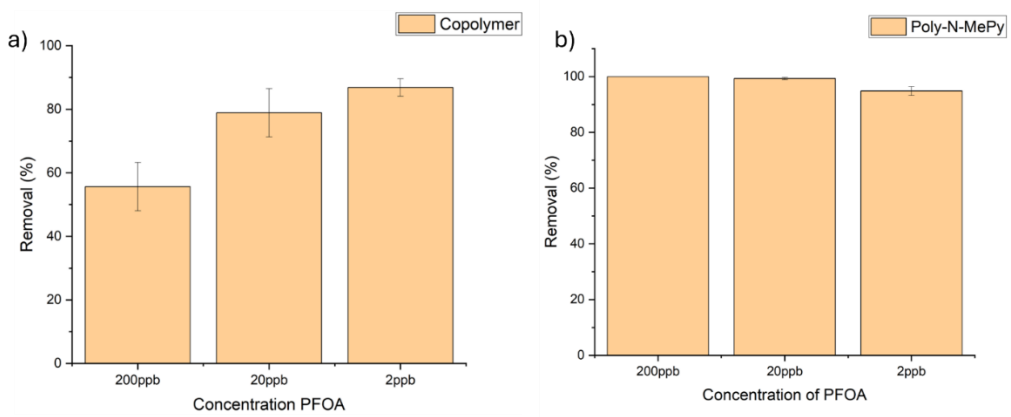

Figure 25. PFOA removal capacity of a) copolymer; b) control Poly-N-Methyl pyrrole.

From the two graph is possible to notice that the control polymer possesses higher performances than the active co-polymer.
Probably, the steric hindrance of the cavitand likely decreases the efficiency of the polymerization reaction, resulting in a material with lower molecular weight. Consequently, since both matrices are positively charged, the higher molecular weight control material will present a greater number of positive charges, thus forming ion pairs with a larger number of PFOA molecules, leading to a higher removal capacity. Probably, the amount of cavitand in the polymer matrix is too low pro produce a significant effect in removing the pollutant.

4. Conclusion

Different methods were investigated for the synthesis of a quinoxaline cavitand, properly functionalized at the upper or lower rim, which could be used as a co-monomer in the synthesis of a conductive polymer or grafted onto a preformed conductive polymer via a post-functionalization reaction. Even though the functionalization of the lower rim was unsuccessful, the upper rim modification allowed the synthesis of two new different quinoxaline cavitands suitable for the purpose: cavitand **14** functionalized with a thiophene moiety, and cavitand **17**, bearing a pyrrole moiety. Both cavitands **14** and **17** have been fully characterized by NMR spectroscopy and by MALDI-TOF analysis.
Efforts were made to co-polymerize cavitands **14** and **17** via electrochemical reactions to develop a sensor for PFAS detection. While cavitand **14** could not be successfully co-polymerized, cavitand **17** exhibited the ability to form a conductive co-polymer with N-Methyl pyrrole, albeit with limited reaction reproducibility. Preliminary studies, however, demonstrated that this co-polymer was unsuitable for sensor development due to random variations in response when exposed to both deionized water and a 100 ppm PFOA solution. As a result, an alternative co-polymerization strategy was explored to synthesize a conductive polymer incorporating cavitand **17** as side-chain pendant with the goal of producing a material suitable for PFAS adsorption. Cavitand **17** was successfully co-

polymerized, and the characterization through solid-state NMR confirmed the incorporation of the macrocycle into the co-polymer. Nevertheless, LC/MS analysis aimed at assessing the co-polymer adsorption capacity revealed worse performances when compared to the control material, the pure poly-N-MePy.
Future studies will focus on the optimization of cavitand **17** co-polymerization process to enhance the material adsorption capabilities. Additionally, analyses will be conducted on real water and marine samples spiked with small amounts of PFAS. In real water samples, which typically contain higher ion concentrations compared to deionized water, the purely positively charged conductive polymer may become saturated with these ions, thereby reducing its ability to detect negatively charged analytes. Conversely, the incorporation of cavitand into the polymer matrix is expected to facilitate the insertion of the lipophilic chains of PFAS into its cavity, thus enhancing adsorption performances.

5. Experimental

Resorcinare [ResC_3H_6OH; H] (1)

To a solution of resorcinol (10g, 90.8mmol, 1 eq) and 2,3-dihydrofuran (6.78mL, 90.8mmol, 1eq) in methanol (60mL), 17.2mL of HCl are added dropwise at 0°C in 30 minutes. Then the mixture was magnetically stirred at 50°C for 5 days. The obtained yellow solution is then poured into 300mL of cold water and obtained yellow precipitate is filtered on büchner funnel and dried under high vacuum. The target product is obtained as a pale-yellow solid in 70% yield and characterized by NMR in DMSO-d_6.
^{1}H-NMR (DMSO-d_6, 400 MHz): δ (ppm) = 8.89 (s, 8H, ArOH), 7.22 (s, 4H, ArHup), 6.14 (s, 4H, ArHdown), 4.31 (bs, 4H, CH_2O**H**), 4.19 (t, 4H, J = 8Hz, C**H**CH_2), 3.41 (t, 8H, J = 8Hz, C**H$_2$**OH), 2.09 (m, 8H, CHC**H$_2$**), 1.32 (m, 8H, CH_2C**H$_2$**CH_2OH).

Tetraquinoxaline Cavitand [C_3H_6OH; H] (2)

2,3-dichloroquinoxaline (350mg, 1.76mmol, 4.4 eq.) is added to a suspension of Resorcinarene 1 (288mg, 0.399mmol, 1 eq.) and K_2CO_3 (464mg, 3.35mmol, 8.4 eq.) in dry DMF (10mL), then the reaction is stirred at 80°C for 16 hours. After 16 hours, the mixture is cooled to room temperature and poured into 200mL of HCl 1M. The obtained pale yellow precipitate is filtered on büchner funnel and dried under high vacuum. Purification by recrystallization in MeOH allowed the recovery of the pure target quinoxaline cavitand in 70% yield.
^{1}H-NMR (DMSO-d_6, 400 MHz): 8.03 (s, 4H, ArHup), 7.88 (m, 8H, ArH), 7.84 (s, 4H, ArHdown), 7.61 (m, 8H, ArH), 5.51 (t, 4H, J = 8Hz, C**H**CH2), 4.53 (t, 4H, J = 4Hz, CH2O**H**), 3.56 (m, 8H, C**H2**OH), 1.50 (m, 8H, J = 8Hz, CH2C**H2**CH2OH).

Tetraquinoxaline Cavitand [C_3H_6Cl; H] (3)

Thionyl chloride (1.20 mL, 16.323 mmol, 20 eq.) is slowly added to a suspension of Tetraquinoxaline Cavitand [C_3H_6OH; H] (1.00 g, 0.816 mmol, 1 eq.) in dry DMF (20mL) and the reaction mixture was then kept under stirring at 55°C for 36 hours. The reaction solution is then cooled to room temperature and then quenched with 250mL of DI water. The target compound was recovered in 80% yield upon filtration of the precipitate on büchner funnel and drying under high vacuum.

^{1}H-NMR (DMSO-d_6, 400 MHz): 8.07 (s, 4H, ArHup), 7.90 (m, 8H, ArH), 7.84 (s, 4H, ArHdown), 7.63 (m, 8H, ArH), 5.56 (t, 4H, J = 8Hz, C**H**CH_2), 3.78 (t, 8H, J = 8Hz, C**H$_2$**Cl), 2.58 (m, 8H, CHC**H$_2$**), 1.81 (m, 8H, CH_2C**H$_2$**CH_2Cl).

MALDI-TOF: calculated for $C_{72}H_{53}Cl_4N_8O_8$ $[M+H]^+$ *m/z* = 1297.27, found = 1297.2735

2,3-dihydroquinoxaline-6-caboxylic acid (6)

A solution of oxalic acid (1.97g, 21.9mmol, 1.1 eq) in 20mL of HCl 4N is slowly added to a solution of 3,4-diaminobenzoic acid (3g, 19.7mmol, 1 eq) in 30mL of HCl 4N. The resulting purple mixture is refluxed under mechanical stirring for 24 hours. After 24 hours the purple precipitate is filtered, washed with deionized water and dried under high vacuum to give product 4 with 74% yield (3g, 14.55mmol).

^{1}H-NMR ($CDCl_3$, 400 MHz): δ (ppm) = 12.88 (bs, 1H, COO**H**), 12.15 (s, 1H, ArO**H**), 12.03 (s,1H, ArO**H**), 7.73 (s, 1H, Ar**H**), 7.66 (dd, 1H, J_o = 8.0 Hz, Ar**H**), 7.18 (d, 1H, J_o = 8.0 Hz, Ar**H**).

Thieno[3,4-*b*]-1,4-dioxin-2-methanol, 2,3-dihydro-, 2-(4-methylbenzenesulfonate) (7)

Derivative **7** was synthesized adapting a procedure reported in literature.[28]

p-Toluenedulfonyl chloride (1000mg, 5.22mmol, 1.5 eq) is slowly added to a solution (2,3-Dihydrothieno[3,4-*b*][1,4]dioxin-2-yl)methanol (600mg, 3.4mmol, 1 eq.) and triethylamine (1.05mL, 10.45mmol, 3 eq.) in dry dichloromethane (DCM) and the mixture is stirred at room temperature for 16 hours. The reaction is monitored by TLC (hexane/Ethyl Acetate 8:2) and when the complete disappearance of the substrate is observed, the organic phase is diluted and washed with water (3x70mL). The organic phase is dried on $MgSO_4$ and the solvent is removed under high vacuum. The crude product is purified by liquid chromatography on silica gel using a mixture of hexane/EtOAc 8:2 as eluent, affording 990mg of pure product **8** as white solid (yield = 87%).

^{1}H-NMR ($CDCl_3$, 400MHz): δ (ppm) = 7.80 (d, J = 8Hz, 2H, tosyl Ar**H**), 7.36 (d, J = 8Hz, 2H, tosyl Ar**H**), 6.32-6.26 (dd, 2H, thiophene C**H**), 4.36 (m, 1H, ethylenedioxy C**H**), 4.26-4.16 (m, 3H, methylene C**H$_2$**- ethylenedioxy C**H$_2$**), 4.03 (dd, 1H, ethylenedioxy C**H$_2$**), 2.46 (s, 3H, tosyl C**H$_3$**).

GC-MS: theoretical m/z = 326.03 $[M]^+$, experimental m/z = 326.05 $[M]^+$

2-(Azidomethyl)-2,3-dihydrothieno[3,4-b]-1,4-dioxin (8)

Compound **8** was synthesized adapting a procedure reported in literature.[29]
Sodium azide (159mg, 2.45mmol, 2 eq.) was slowly added to a solution of (Thieno[3,4-*b*]-1,4-dioxin-2-methanol, 2,3-dihydro-, 2-(4-methylbenzenesulfonate) (**8**) (400mg, 1.22mmol, 1 eq.) in dry DMF and the reaction is stirred for 16 hours. The reaction is monitored by TLC (hexane/ethyl acetate 8:2) and after 16 hours the reaction is not proceeding anymore so the organic phase is diluted with water and washed with Ethyl acetate (3x50mL). The organic phases are mixed together, dried on $MgSO_4$ and the solvent is evaporated under vacuum. The product is purified from the unreacted substrate by liquid chromatography on silica gel using a mixture of hexane/EtOAc (8.5:1.5) as eluent. The purification afforded 100mg of pure product as colourless liquid (yield = 85%).
^{1}H-NMR ($CDCl_3$, 400MHz): δ (ppm) = 6.37 (dd, 2H, thiophene C**H**), 4.32 (m, 1H, ethylenedioxy C**H**), 4.20 (dd, 1H, ethylenedioxy C**H_2**-), 4.20 (dd, 1H, ethylenedioxy C**H_2**-), 3.54 (m, 2H, azide C**H_2**-).
GC-MS: theoretical m/z = 197.03 $[M]^+$, experimental m/z = 196.97 $[M]^+$

2,3-Dihydrothieno[3,4-*b*]-1,4-dioxin-2-methanamine (9)

Compound **9** was synthesized adapting a procedure reported in literature.[30]
Triphenylphosphine (598mg, 2.28mmol, 1.8 eq.) is added to a solution of 2-(Azidomethyl)-2,3-dihydrothieno[3,4-b]-1,4-dioxin (**9**) (250mg, 1.27mmol, 1 eq.) in dry THF (15mL), then the reaction is stirred at 50°C for 45 minutes. The reaction is monitored by TLC (hexane/ethyl acetate 8:2) and when the complete disappearance of the substrate is observed, 4.04mL of a 2M aqueous solution of sodium hydroxide are added and the reaction is kept under stirring at 50°C. After 4 hours the reaction is monitored by TLC and the complete disappearance of the substrate is observed so the reaction is cooled to room temperature and the THF is evaporated under vacuum. Then the pH is adjusted with HCl 2M to pH < 3 and the aqueous phase is washed 4 times with dichloromethane (DCM). The organic phase is discarded and the pH of the aqueous phase is adjusted to pH > 8 with NaOH 2M and washed with EtOAc (3x50mL). The organic phase is dried on $MgSO_4$ and the solvent removal under vacuum afforded 180mg of pure product as yellowish oil (yield = 91%).
^{1}H-NMR ($CDCl_3$, 400MHz): δ (ppm) = 6.32 (dd, 2H, thiophene C**H**), 4.20 (dd, 1H, ethylenedioxy C**H_2**-), 4.12 (m, 1H, ethylenedioxy C**H**), 4.00 (dd, 1H, ethylenedioxy C**H_2**-), 2.97 (m, 2H, C**H_2**-NH_2).
GC-MS: theoretical m/z = 171.04 $[M]^+$, experimental m/z = 171.04 $[M]^+$.

2,3-Dichloro-*N*-((2,3-dihydrothieno[3,4-*b*][1,4]dioxin-2-yl)methyl)quinoxaline-6-carboxamide (10)

Thionyl chloride (2.5mL, 34.38mmol, 19 eq.) is added dropwise to a cold solution of 2,3-dihydroquinoxaline-6-caboxylic acid (375mg, 1.82mmol, eq.) in dry DMF (7mL) and the reaction mixture is heated at 70°C for 4 hours. Maintaining the inert atmosphere in the

reaction flask the solvent is evaporated under high vacuum and the obtained crude solid is dissolved in dry DCM (15mL) and triethylamine (7.60mL, 54.6mmol, 30 eq.). The mixture is cooled to 0°C and the 2,3-Dihydrothieno[3,4-*b*]-1,4-dioxin-2-methanamine (**10**) (280mg, 1.63mmol, 0.9 eq.) is added dropwise. The reaction mixture is stirred at room temperature for 16 hours. The reaction mixture is diluted with fresh DCM and washed three times with water. The organic phase is dried on $MgSO_4$ and the solvent is evaporated under vacuum. Purification by liquid chromatography on silica gel in hexane/EtOAc (60:40) afforded mg of pure product (yield = 30%).

^{1}H-NMR ($CDCl_3$, 400MHz): δ (ppm) = 8.38 (s, 1H, **Ha**), 8.24 (dd, 1H, **Hb**), 8.11 (d, 1H, **Hc**), 6.77 (s, 1H, **Hd**), 6.37 (dd, 2H, **Hh**), 4.42 (m, 1H, **Hf**), 4.31 (dd, 1H, **Hg**), 4.05-3.94 (m, 2H, **Hg'** + **He**), 3.73 (m, 1H, **He'**).
^{13}C-NMR ($CDCl_3$, 100MHz): δ (ppm) = 166.03, 147.27, 146.77, 141.85, 141.18, 140.90, 139.92, 136.35, 129.68, 128.97, 126.77, 100.23, 72.48, 66.22, 40.38.

^{13}C-NMR:

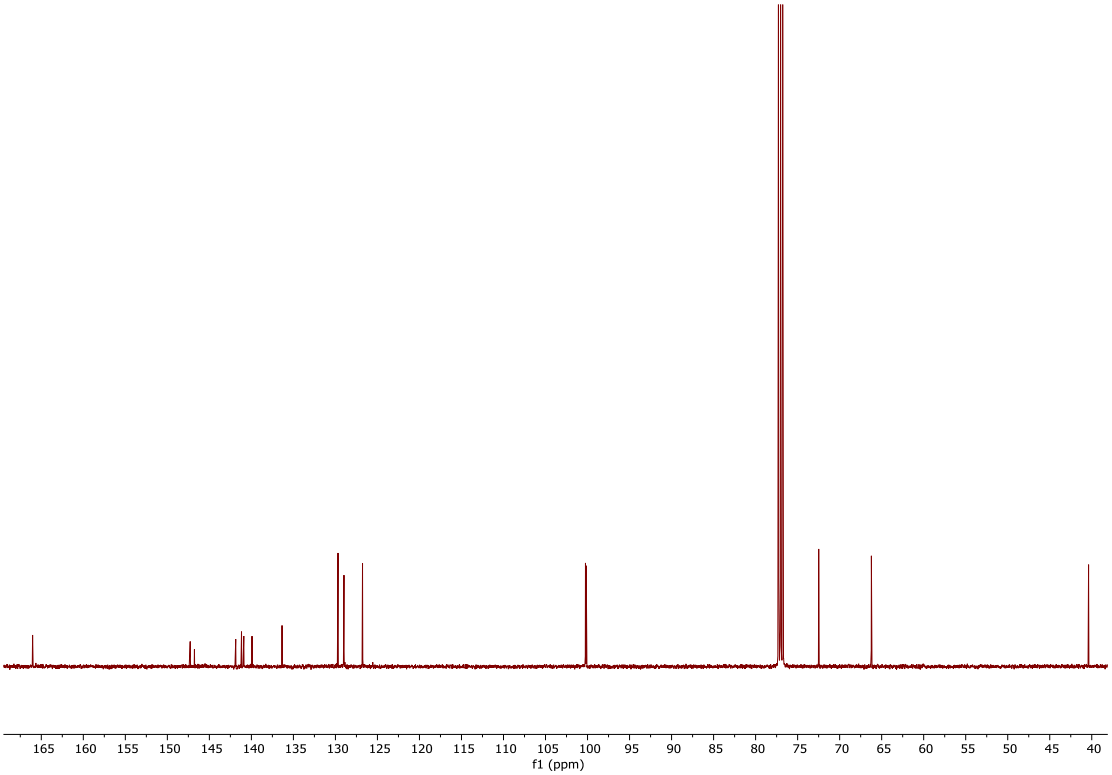

Figure S1. ^{13}C-NMR spectrum ($CDCl_3$, 25 °C, 125 MHz) of compound **10**

COSY-NMR:

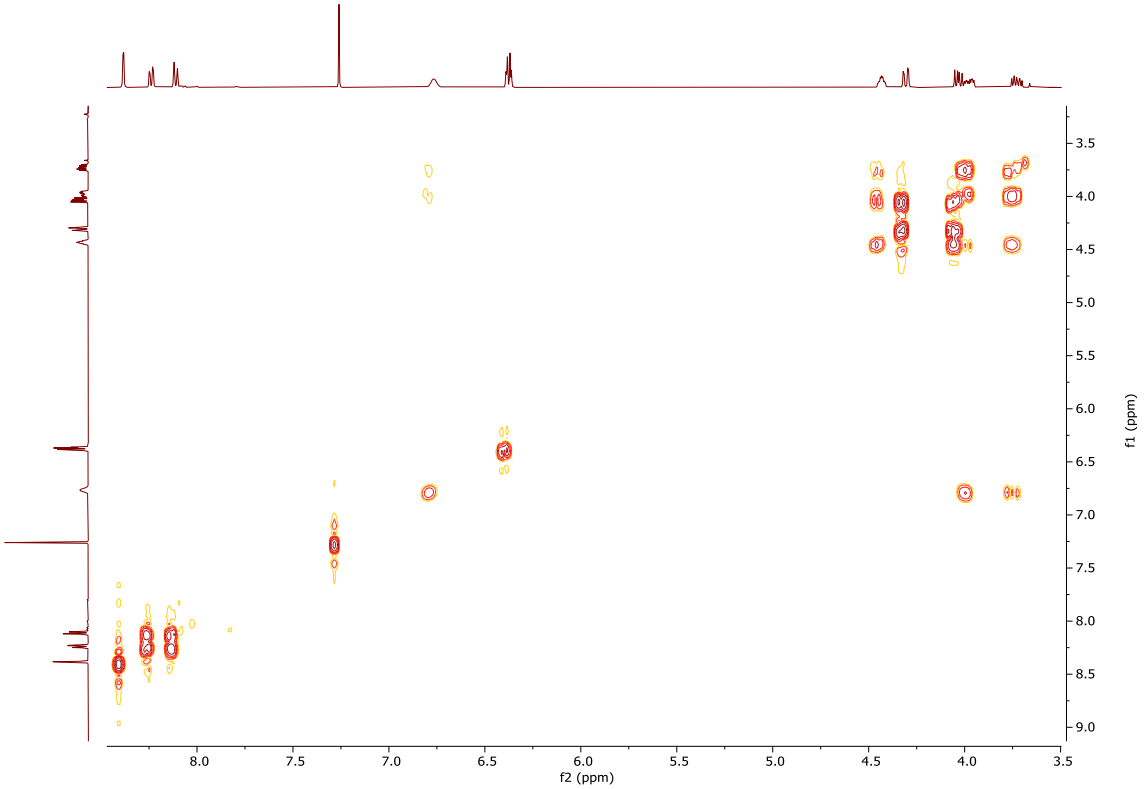

Figure S2. COSY-NMR spectrum ($CDCl_3$, 25 °C, 500 MHz) of compound **10**

HSQC-NMR:

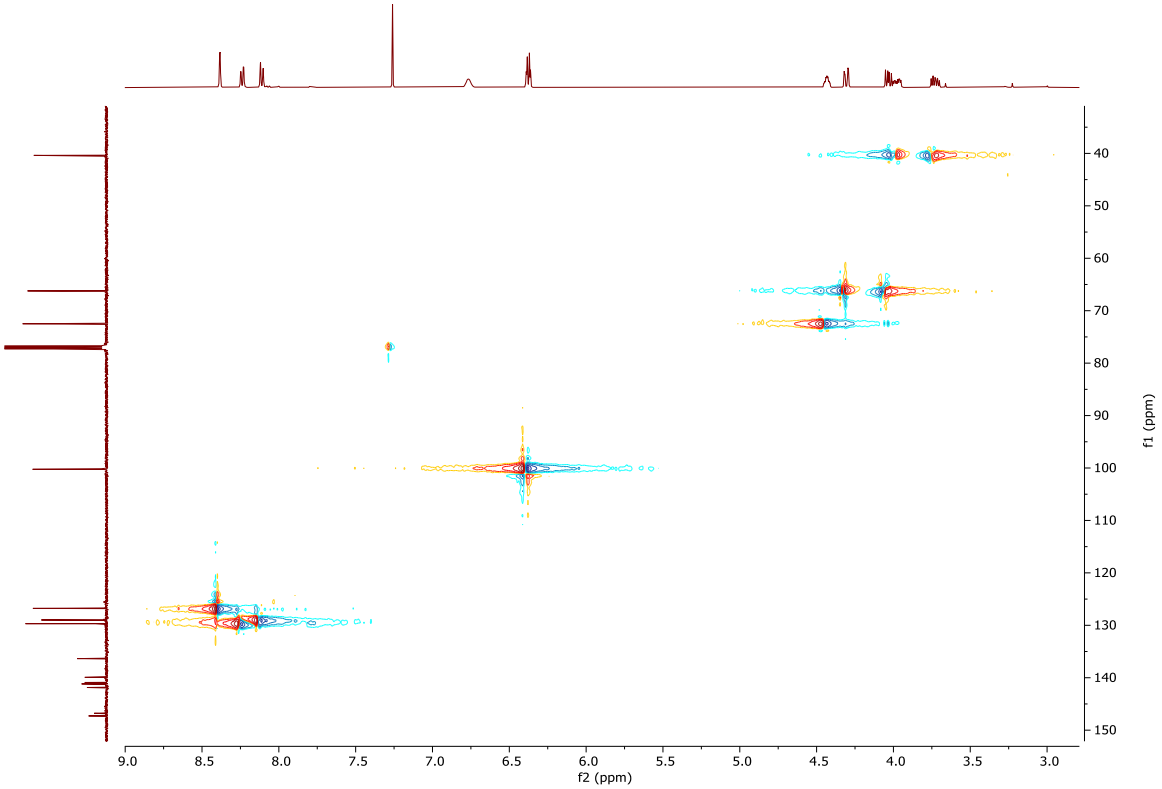

Figure S3. HSQC-NMR spectrum ($CDCl_3$, 25 °C, 500 MHz) of compound **10**

Resorcinarene [ResC_6H_{13}; H] (11)

To a solution of resorcinol (15g, 136 mmol, **4** eq.) in methanol (50mL), 20mL of HCl 12M are added dropwise at 0°C in 15 minutes, then a solution of heptanal (15.6g, 136mmol, **4** eq.) in methanol (20mL) is slowly added dropwise in 40 minutes and the obtained mixture is refluxed at 60°C for 72 hours. The cold mixture is then poured into 300mL of water and the obtained yellow precipitate is filtered and dried under high vacuum. The crude solid is recrystallized from methanol to obtain 17g of pure product in 27% yield as yellowish solid. **^{1}H-NMR** ($CDCl_3$, 400 MHz): δ (ppm) = 8.86 (s, 8H, ArO**H**), 7.15 (s, 4H, Ar**Hup**), 6.14 (s, 4H, Ar**Hdown**), 4.21 (t, 4H, J = 8Hz, C**H**CH2), 2.01 (q, 8H, J = 8Hz, C**H**CH2), 1.30-1.15 (m, 32H, -C**H2**-), 0.84 (t, 12H, J = 8Hz; CH2C**H3**).

Tetraquinoxaline Cavitand (12)

K_2CO_3 (2.6g, 19mmol, 8.4 eq.) is added to a solution of resorcinarene **1** (1.5g, 2.2mmol, 1 eq.) in 30mL of dry DMF, followed by 2,3-dichloroquinoxaline (2.0g, 9.8mmol, 4.4 eq.). The purple suspension was stirred at 80°C for 16 hours. The reaction is quenched 300mL of HCl 1M and the obtained yellow precipitate was filtered, washed with deionized water and

dried under vacuum. Recrystallization from Ethyl Acetate afforded 1.55g of cavitand **2** as white solid with 60% yield.
^{1}H-NMR ($CDCl_3$, 400 MHz): δ (ppm) = 8.17 (s, 4H, Ar**Hup**), 7.82 (m, 8H, Ar**H**), 7.82 (m, 8H, Ar**H**), 7.49 (m, 8H, Ar**H**), 7.23 (s, 4H, Ar**Hdown**), 5.58 (t, 4H, J=7.8 Hz, C**H**CH2), 2.28 (q, 8H, J=7.8 Hz, CHC**H2**), 1.55-1.31 (m, 32H, -C**H2**-), 0.95 (t, 12H, J=6.8 Hz, CH2C**H3**).

Triquinoxaline Cavitand (13)

Pyrocatechol (45.5mg, 0.414mmol, 1.1 eq.) is added to a suspension of tetraquinoxaline cavitand **2** (500mg, 0.376mmol, 1 eq.) and CsF (1.14g, 7.520mmol, 20 eq.) at 80°C. The reaction mixture is kept in temperature under mechanical stirring for 30 minutes, then the hot mixture is poured into 300mL of HCl 1M and the obtained pale-blu precipitate is filtered, washed with deionized water and dried under vacuum. The crude solid is purified by flash chromatography on silica gel (gradient from DCM 100% to DCM/EtOAc 95:5) affording 260mg of pure product **3** as white solid (60% yield).
^{1}H-NMR ($CDCl_3$, 400 MHz): δ (ppm) = 8.27 (s, 2H, **Hi**), 7.96 (d, 2H, J=8.0 Hz, **Hd**), 7.84 (m, 2H, **He**), 7.71 (d, 2H, J=8.0 Hz, **Ha**), 7.59 (td, 2H, **Hf**), 7.51 (m, 4H, **Hc** + **Hb**), 7.31 (s, 2H, **Hg**), 7.16 (s, 2H, **Hl**), 7.11 (s, 2H, **Hk**), 5.63 (t, 1H, J= 8.0 Hz, $\mathbf{H_m}$), 5.5 (t, 2H, J= 8.0 Hz **Hn**), 4.28 (t, 1H, J=8.0 Hz, **Ho**), 2.26 (m, 8H, CHC**H2**), 1.55-1.23 (m, 32H, -C**H2**-), 0.94 (m, 12H, CH2C**H3**).

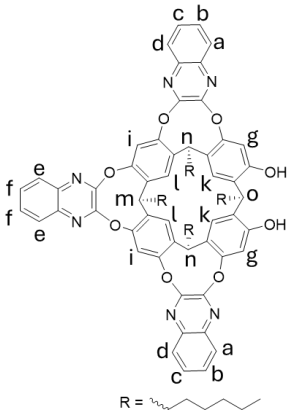

EDOT-functionalized tetraquinoxaline cavitand (14)

2,3-Dichloro-*N*-((2,3-dihydrothieno[3,4-*b*][1,4]dioxin-2-yl)methyl)quinoxaline-6-carboxamide (**10**) (40mg, 0.099 mmol, 1.1 eq.) is added to a suspension of triquinoxaline cavitand (108mg, 0.090 mmol, 1 eq.) and K_2CO_3 (15 mg, 0.108 mmol, 1.2 eq.) in dry DMF (5mL) and the reaction mixture is stirred at 80°C for 18 hours. The reaction is monitored by TLC with a mixture of hexane/ethyl acetate (8:2) as eluent. When the TLC shows the complete disappearance of the limiting substrate, the mixture is cooled to room temperature

and poured in 100mL of HCl 1M. The obtained pale-yellow precipitate is filtered, washed with water and dried under vacuum. The crude product is purified by liquid chromatography on silica gel (gradient from hexane/EtOAc (from 80:20 to 70:30) affording mg of cavitand **7** (yield = 40%).

^{1}H-NMR ($CDCl_3$, 500MHz): δ (ppm) = 8.29 (s, 1H, **Ha**), 8.15 (m, 4H, **Hf**), 7.92 (dd, 1H, **Hb**), 7.86-7.76 (m, 7H, **Hc** + **Ht** + **Hw** + **Hd**), 7.52 (m, 4H, **He**), 7.41 (m, 2H, **Hu** + **Hv**), 7.23 (m, 4H, **Hg**), 6.69 (s, 1H, **Hi**), 6.41 (s, 2H, **Hm**), 5.56 (m, 4H, **Hh**), 4.52 (m, 1H, **Hl**), 4.38 (dt, 1H, **Hk**), 4.14-4.01 (m, 2H, **Hk** + **Hj**), 3.86-3.74 (m, 1H, **Hj**), 2.28 (m, 4H, **Hn**), 1.51-1.35 (m, 32H, **Ho** + **Hp** + **Hq** + **Hr**), 0.95 (t, 12H, **Hs**).

^{13}C-NMR ($CDCl_3$, 125MHz): δ (ppm) = 166.53, 153.37, 152.65, 152.55, 152.54, 152.50, 152.47, 152.39, 152.35, 152.30, 152.13, 141.33, 141.17, 140.89, 140.85, 139.60, 139.58, 139.55, 138.91, 135.97, 135.71, 135.64, 135.61, 135.56, 134.14, 129.14, 128.25, 127.85, 127.72, 127.64, 127.50, 127.30, 126.51, 123.66, 123.48, 123.27, 123.21, 118.69, 118.45, 100.35, 72.66, 72.60, 66.30. 40.52, 40.41, 34.36, 32.47, 32.42, 32.35, 31.88, 29.38, 27.92, 22.68, 14.09.

^{13}C-NMR:

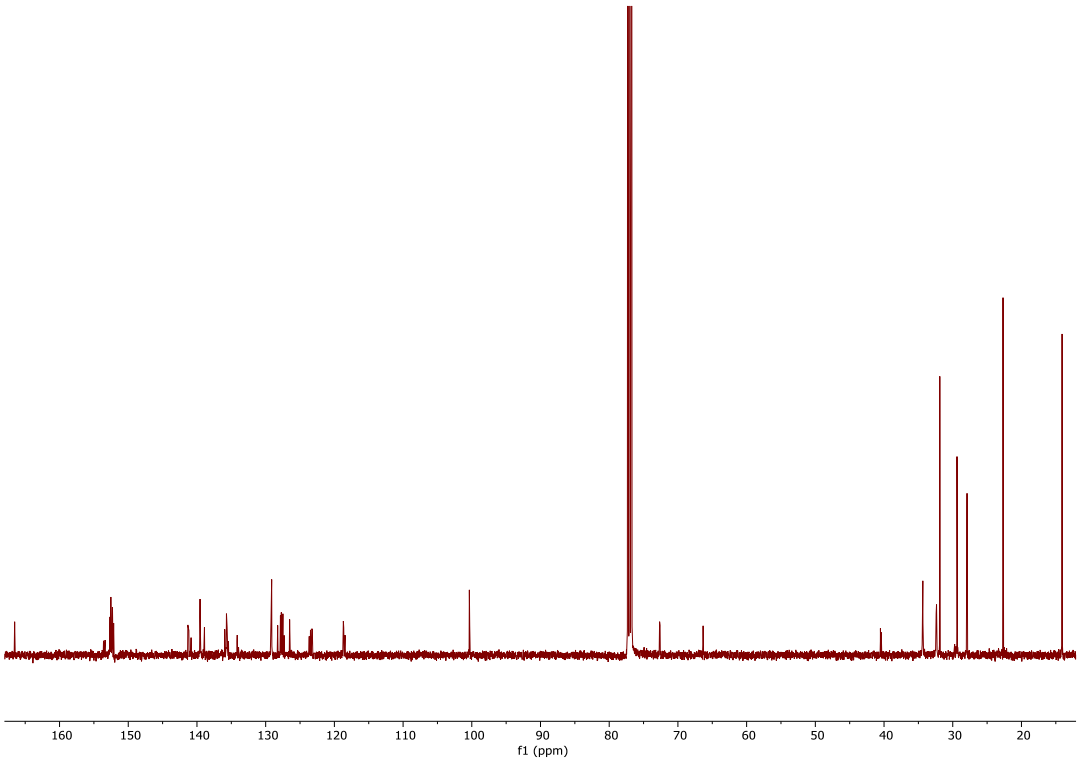

Figure S4. ^{13}C-NMR spectrum ($CDCl_3$, 25 °C, 125 MHz) of compound **14**

COSY-NMR:

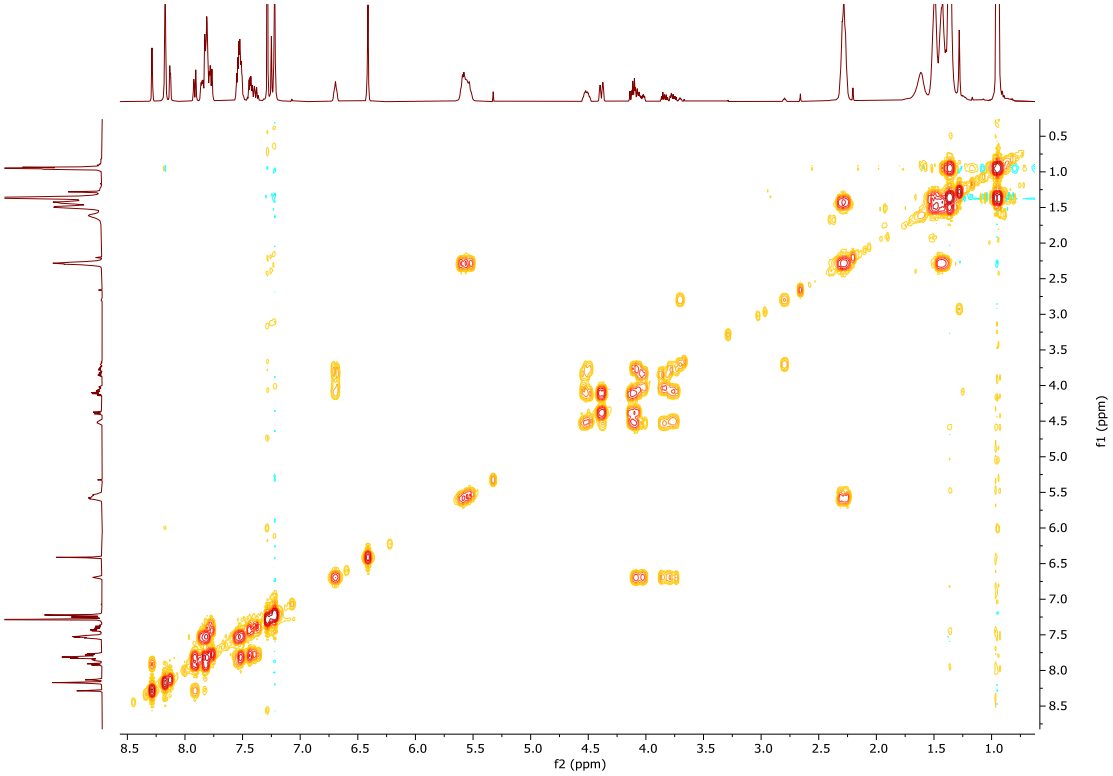

Figure S5. COSY-NMR spectrum ($CDCl_3$, 25 °C, 125 MHz) of compound **14**

HSQC-NMR:

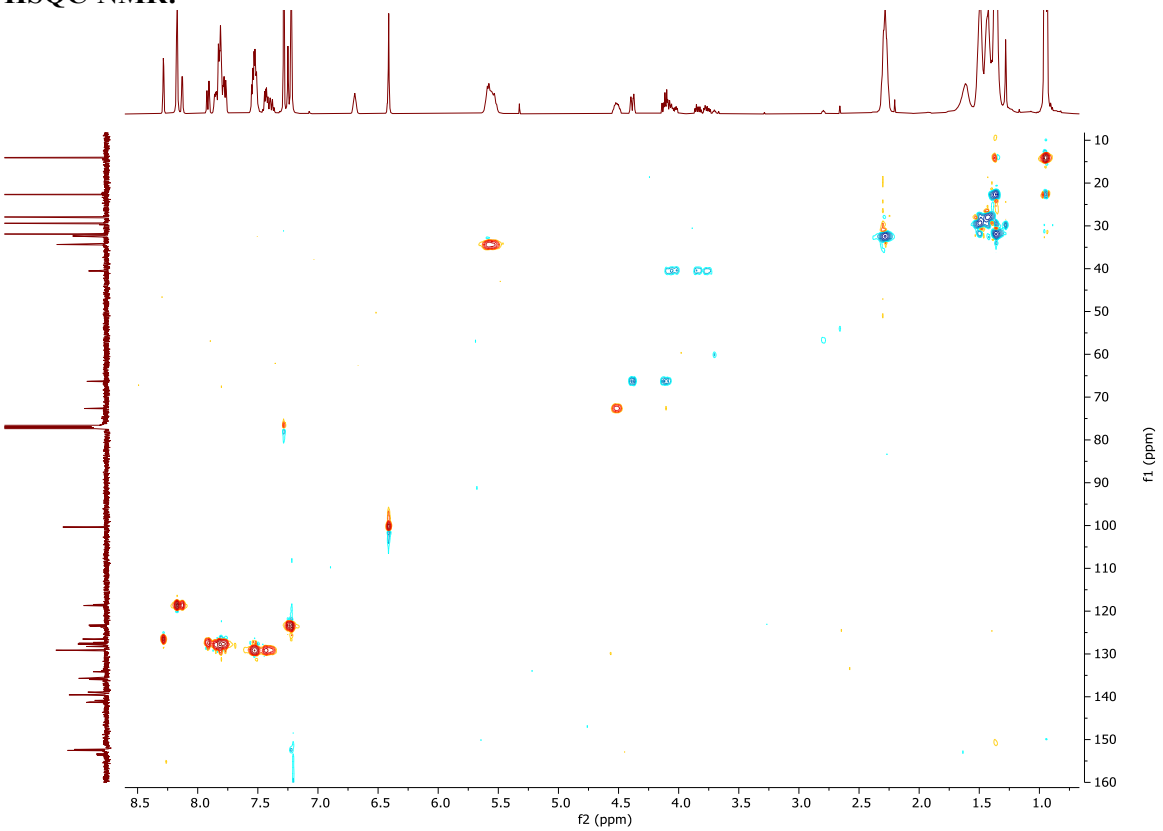

Figure S6. HSQC-NMR spectrum ($CDCl_3$, 25 °C, 125 MHz) of compound **14**

HMBC-NMR:

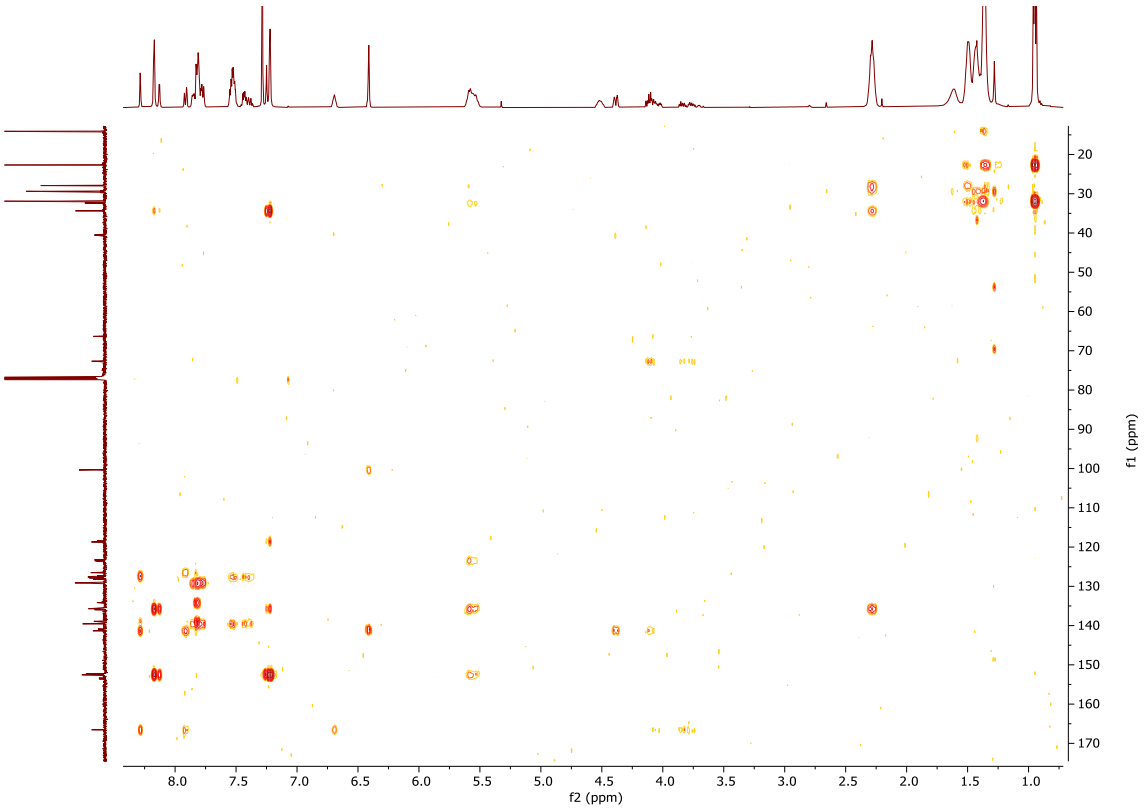

Figure S7. HSQC-NMR spectrum ($CDCl_3$, 25 °C, 125 MHz) of compound **14**

2-(1H-pyrrol-1-yl)ethan-1-ol (15)

The synthesis of compound 15 was performed following a literature procedure.[31]
2,5-dimethoxytetrahydrofuran (5 mL, 38.59 mmol, 1 eq.) is added to a solution of ethanolamine (10 mL, 165.93 mmol, 4.3 eq.) in glacial acetic acid at 0°C. The reaction mixture is the then stirred and heated up to 115°C for 16 hours. The reaction is then cooled to room temperature, diluted with deionized water and washed 3 times with DCM. The organic phase is then washed with brine and a saturated solution of K_2CO_3. The organic phase is then dried on $MgSO_4$ and the solvent is removed under high vacuum. The crude dark oil is dissolved in methanol (10mL) and a solution (5mL) of NaOH 20% wt% is added. The mixture is kept under mechanical stirring at room temperature for 90 minutes. The crude mixture is then poured into cold brine and washed 3 times with DCM. The organic phase is dried on $MgSO_4$ and the solvent is removed under vacuum to recover 1.78g of product as dark-brown oil (yield = 15%).

^{1}H-NMR ($CDCl_3$, 400 MHz): δ (ppm) = 6.71 (t, 2H, J = 4Hz, Ar**H**), 6.19 (t, 2H, J = 4Hz, Ar**H**), 4.04 (t, 2H, J = 8Hz, N-C**H$_2$**), 3.87 (q, 2H, CH_2-C**H$_2$**-OH), 1.56 (bs, 1H, CH_2O**H**).

2-(1H-pyrrol-1-yl)ethyl 2,3-dichloroquinoxaline-6-carboxylate (16)

Thionyl chloride (14.15mL, 194.02 mmol, 40 eq.) is added dropwise to a cold solution of 2,3-dihydroquinoxaline-6-caboxylic acid (1000mg, 4.85 mmol, 1 eq.) in dry DMF (7mL) and the reaction mixture is heated at 70°C for 16 hours. Maintaining the inert atmosphere in the reaction flask the solvent is evaporated under high vacuum and the obtained crude solid is dissolved in dry DCM (15mL) and triethylamine (6.8 mL, 48.5 mmol, 10 eq.). The mixture is cooled to 0°C and the 2-(1H-pyrrol-1-yl)ethan-1-ol (540 mg, 4.85 mmol, 1eq.) is added dropwise. The reaction mixture is stirred at room temperature for 16 hours. The reaction mixture is diluted with fresh DCM and washed firstly with saturated K_2CO_3, secondly with HCl 1M and then with brine. The organic phase is dried on $MgSO_4$ and the solvent is evaporated under vacuum. Purification by liquid chromatography on silica gel in hexane/EtOAc (90:10) afforded 750mg of pure product (yield = 46%).

^{1}H-NMR ($CDCl_3$, 400MHz): δ (ppm) = 8.70 (s, 1H, **Ha**), 8.35 (dd, 1H, J = 8Hz, **Hb**), 8.09 (d, 1H, J = 8Hz, **Hc**), 6.76 (s, 2H, **Hd**), 6.19 (s, 2H, **He**), 4.66 (t, 2H, J = 8Hz, **Hf**), 4.32 (t, 2H, J = 8Hz, **Hg**).

^{13}C-NMR: 164.69, 147.69, 146.71, 142.58, 139.88, 132.07, 130.83, 130.69, 128.67, 120.91, 108.98, 65.44, 48.25.

GC-MS: theoretical m/z = 335.02 $[M]^+$, experimental m/z = 334.98 $[M]^+$

^{13}C-NMR:

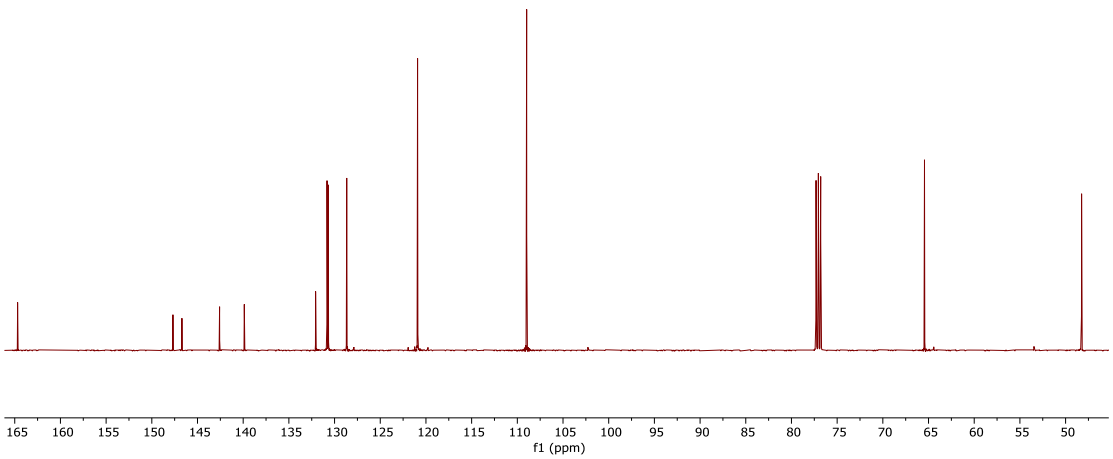

Figure S8. ^{13}C-NMR spectrum ($CDCl_3$, 25 °C, 500MHz) of compound **16**

COSY-NMR:

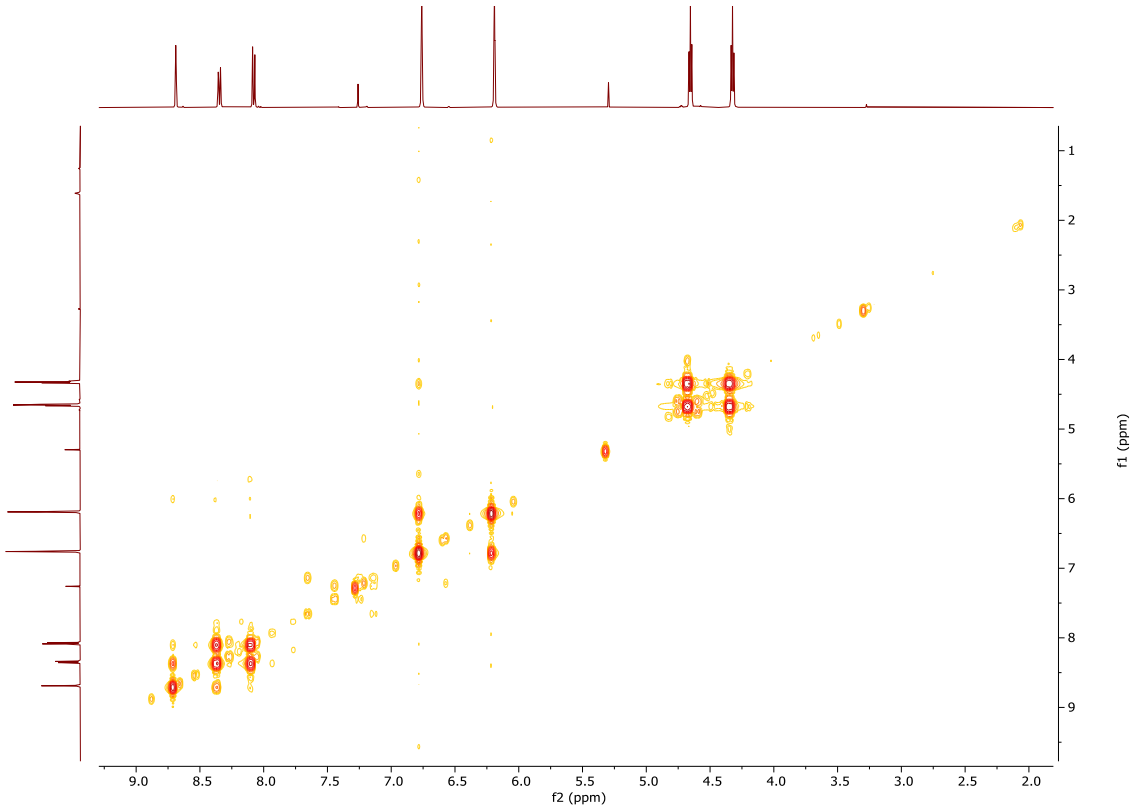

Figure S9. COSY-NMR spectrum (CDCl3, 25 °C, 500MHz) of compound **16**

HSQC-NMR:

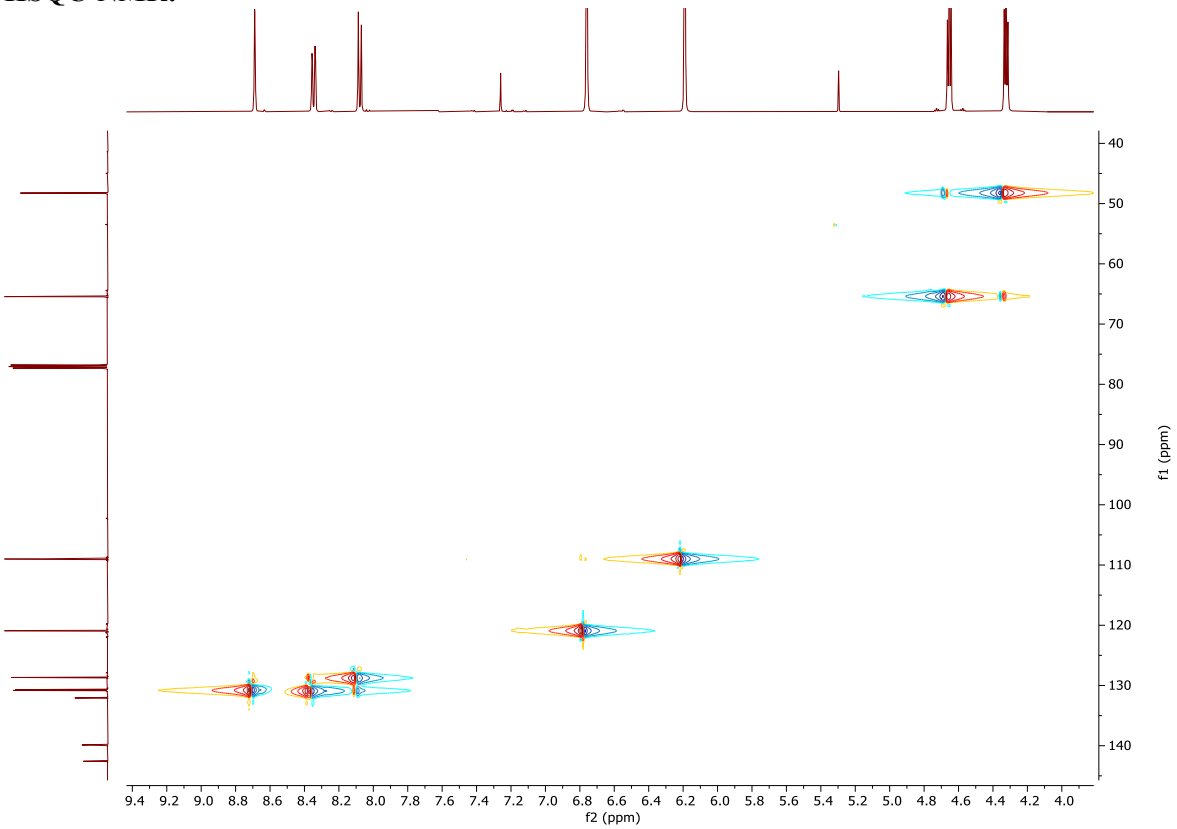

Figure S10. COSY-NMR spectrum (CDCl3, 25 °C, 500MHz) of compound **16**

Pyrrole-functionalized tetraquinoxaline cavitand (17)

2-(1H-pyrrol-1-yl)ethyl 2,3-dichloroquinoxaline-6-carboxylate (**16**) (184 mg, 0.546 mmol, 1.1 eq.) is added to a suspension of triquinoxaline cavitand (600mg, 0.498 mmol, 1 eq.) and K_2CO_3 (83 mg, 0.600 mmol, 1.2 eq.) in dry DMF (12mL) and the reaction mixture is stirred at 80°C for 18 hours. The cold mixture is then cooled to room temperature and poured in 250mL of HCl 1M. The obtained pale-yellow precipitate is filtered, washed with water and dried under vacuum. The crude product is purified by liquid chromatography on silica gel (gradient from hexane/EtOAc 85:15 to 80:20) affording 430mg of cavitand **7** (yield = 59%). **^{1}H-NMR** ($CDCl_3$, 500MHz): δ (ppm) = 8.58 (s, 1H, **Ha**), 8.15 (m, 4H, **Hf**), 8.00 (dd, 1H, **Hb**), 7.81-7.77 (m, 6H, **Hd** + **Hc** + **Ht**), 7.74 (d, 1H, **Hw**), 7.49 (m, 4H, **He**), 7.38 (t, 1H, **Hv**), 7.28 (t, 1H, **Hu**), 7.21 (m, 4H, **Hg**), 6.77 (t, 2H, **Hk**), 6.19 (t, 2H, **Hl**), 5.56 (m, 4H, **Hm**), 4.76 (m, 1H, **Hi**), 4.63 (m, 1H, **Hh**), 4.36 (t, 2H, **Hj**), 2.27 (m, 4H, **Hn**), 1.48-1.33 (m, 32H, **Ho** + **Hp** + **Hq** + **Hr**), 0.93 (t, 12H, **Hs**).

^{13}C-NMR ($CDCl_3$, 125MHz): δ (ppm) = 165.09, 153.95, 153.35, 152.68, 152.58, 152.51, 152.49, 152.46, 152.37, 152.27, 152.13, 142.17, 139.57, 138.89, 135.98, 135.76, 135.69, 135.64, 135.62, 135.45, 130.54, 129.94, 129.08, 129.00, 128.52, 127.98, 127.88, 127.80, 127.71, 127.57, 123.48, 123.39, 123.30, 120.92, 118.72, 118.68, 118.53, 109.07, 65.24, 48.34, 34.40, 34.33, 32.50, 32.38, 32.36, 31.89, 29.38, 27.93, 22.69, 14.09.
MALDI-TOF: calculated for $C_{91}H_{88}N_9O_{10}$ $[M+H]^+$ *m/z* = 1466.67, found *m/z* = 1466.53.

^{13}C-NMR:

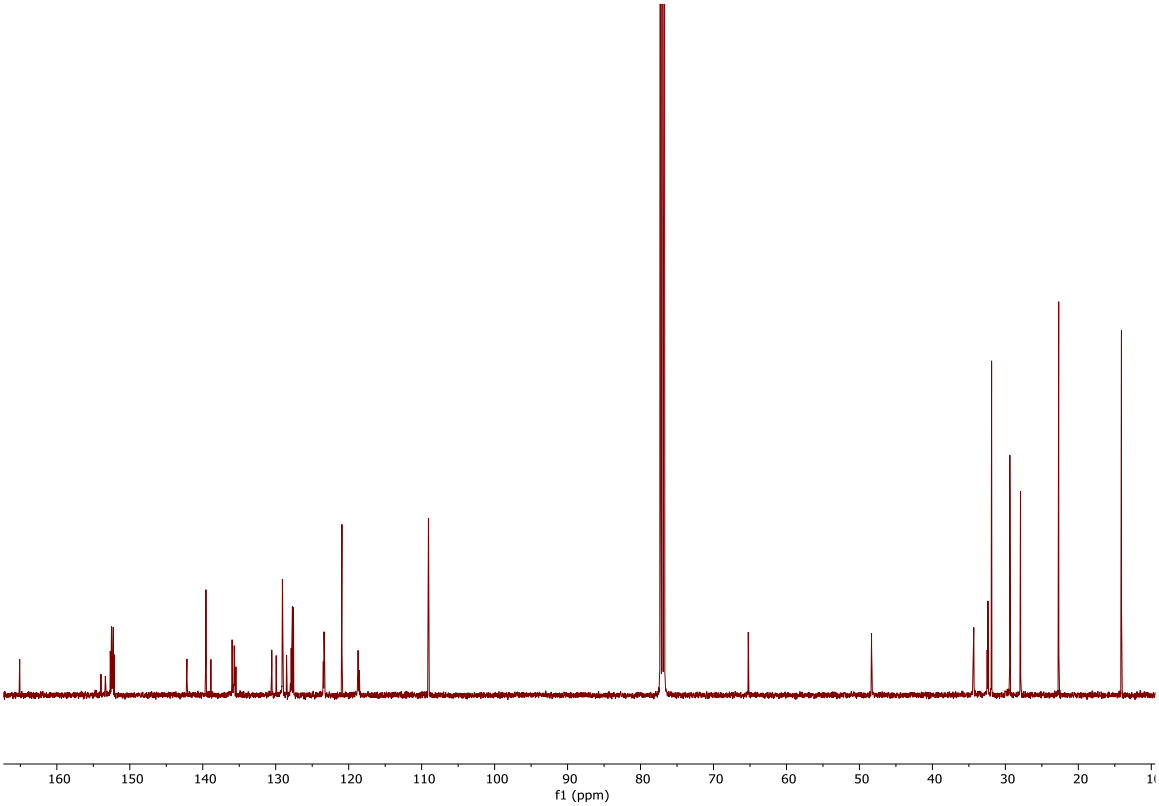

Figure S11. ^{13}C-NMR spectrum ($CDCl_3$, 25 °C, 125 MHz) of compound **17**

COSY-NMR:

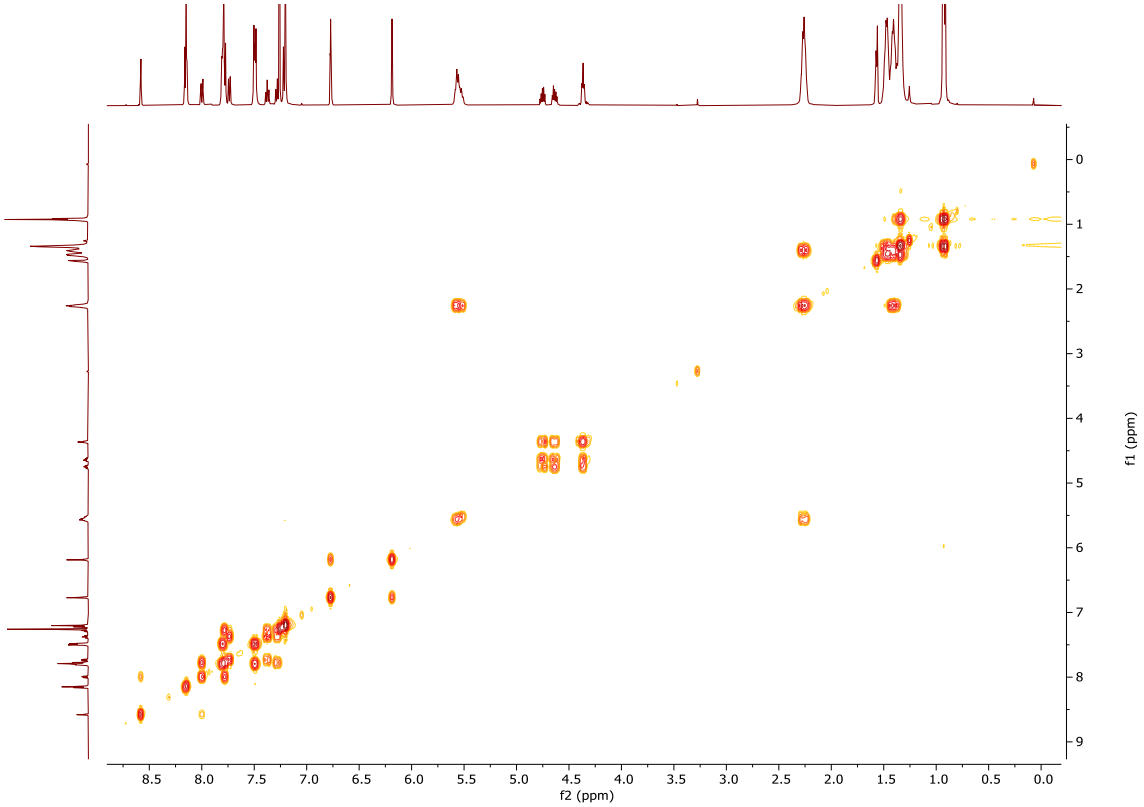

Figure S12. COSY-NMR spectrum ($CDCl_3$, 25 °C, 125 MHz) of compound **17**

HSQC-NMR:

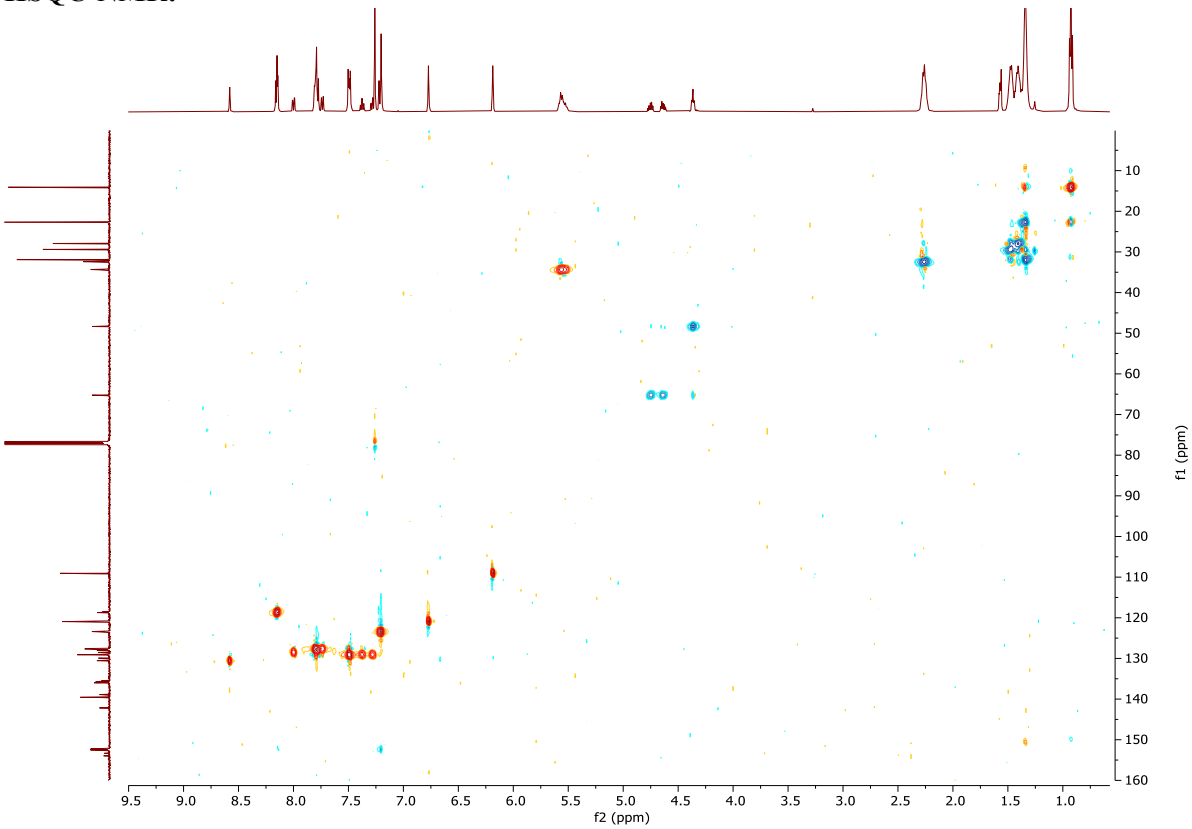

Figure S13. HSQC-NMR spectrum ($CDCl_3$, 25 °C, 125 MHz) of compound **17**

HMBC-NMR:

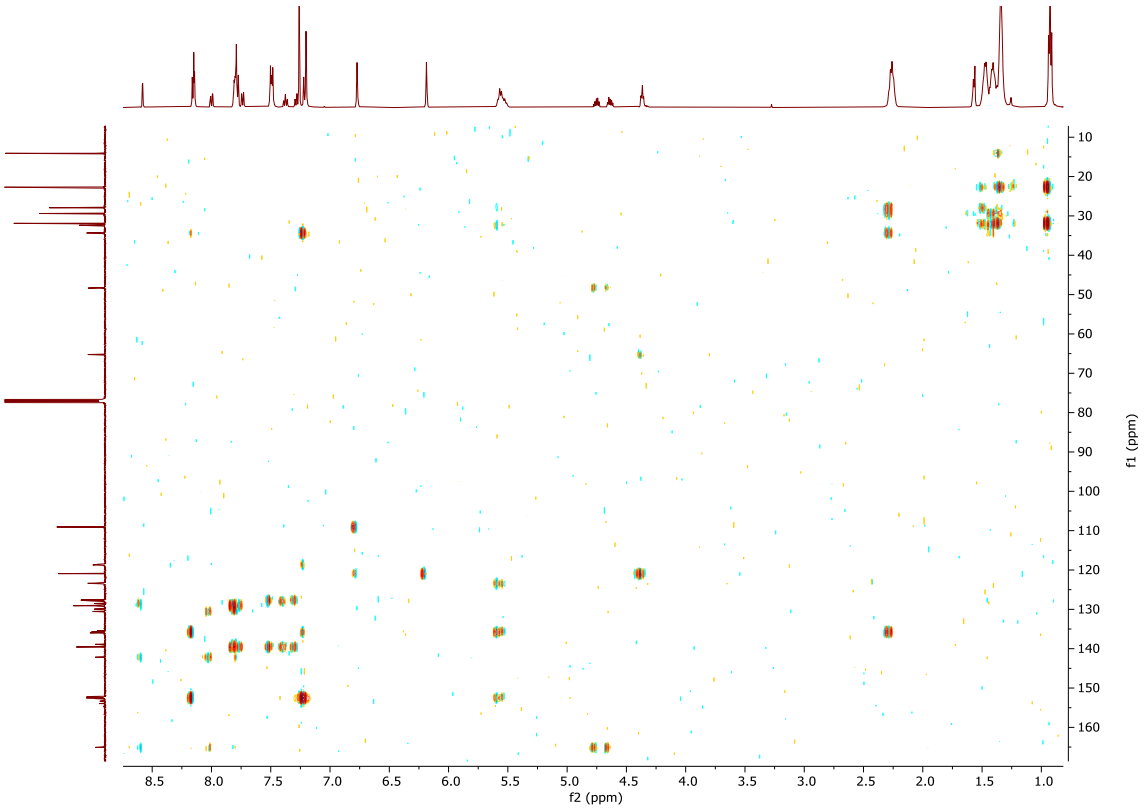

Figure S14. HMBC-NMR spectrum ($CDCl_3$, 25 °C, 125 MHz) of compound **17**

6. References

[1] *EFSA Journal*, **2011**, 9(2).

[2] Appleman, T.D., Dickenson, E.R.V., Bellona, C., Higgins, C.P., *J. Hazard. Mater.*, **2013**, 260, 740–746.

[3] Hang, X., Chen, X., Luo, J., Cao, W., Wan, Y., *Sep. Purif. Technol.,* **2015**, 145, 120–129.

[4] Deng, S., Yu, Q., Huang, J., Yu, G., *Water Res.*, **2010**, 44, 5188–5195.

[5] Wang, T., Zhao, C., Li, P., Li, Y., Wang, J., *J. Membr. Sci.*, **2015**, 477, 74–85.

[6] Dauchy X., *Curr. Opin. Environ. Sci. Health*, **2019**, 7, 8–12.

[7] Al Amin M., Sobhani Z., Liu Y., Dharmaraja R., Chadalavada S., Naidu R., Chalker J. M., Fang C., *Environ. Technol. Inno.*, **2020**, 19, 100879.

[8] Trojanowicz M., Koc M., *Microchim. Acta,* **2013**, 180, 957–971

[9] Shoemaker J. A., Grimmett P. E., Boutin B. K., *U.S. Environmental Protection Agency*, **2018**.

[10] Rosenblum L., Wendelken S. C., Menger U. R. F. et al., *Chemical Engineering Journal*, **2021**, 417, 129133.

[11] EPA Pfas Action Plan, Program Update, U.S. Environmental Protection Agency, Washingt, **2020**

[12] Gao T-N., Huang S., Nooijen R., Zhu Y., Kociok-Köhn G., Stuerzer T., et al., *Angew. Chem. Int. Ed.,* **2024,** 63, e202403474.

[13] Cram D. J., *Science* **1979**, *219*, 1177-1183

[14] Masseroni D., Mosca S., Mower M. P., Blackmond D. G., Rebeck J. J., *Angew. Chem. Int. Ed.*, **2016**, 55, 8290-8293

[15] Azov V. A., Beeby A., Cacciarini M., Cheetham A. G., Diedrich F., Frei M., Gimzewski J. K., Gramlich V., Hecht B., Jaun B., Latychevskaia T., Lieb A., Lill Y., Marotti F., Schlegel A., Schlitter R. R., Skinner P. J., Seiler P., Yamakoshi Y., *Adv. Funct. Mater.* **2006**, *16*, 148.

[16] Hooley R. J., Van Anda H. J. and Rebek J., *J. Am. Chem. Soc.*, **2007**, 129, 44, 13464–13473

[17] Skinner P. J., Cheetham A. G., Beeby A., Gramlich V., Diederich F., *Helv. Chim. Acta.* **2001**, *84*, 2146.

[18] Frei M., Marotti F., Diedrich F., *ChemComm.,* **2004**, *4*, 1362-1363.

[19] Skorjanc T., Shetty D., Trabolsi A., *Chem* **2021**, 7, 882-918.

[20] Amorini M., Riboni N., Pesenti L., Dini V. A., Pedrini A., Massera C., Gualandi C., Bianchi F., Pinalli R., Dalcanale E., *Small* **2022**, 18, 2104946.

[21] Giannetto M., Pedrini A., Fortunati S., Brando D., Milano S., Massera C., Tatti R., Verucchi R., Careri M., Dalcanale E., Pinalli R., *Sensors and Actuators B: Chemical*, **2018**, 276, 340-348.

[22] Nezakati T., Seifalian A., Tan A., Sefalian A. M., *Chem. Rev.*, **2018**, 118, 6766−6843

[23] Li X.-G., Wei F., Huang M.-R., Xie Y.-B., *J. Phys. Chem. B,* **2007**, 111, 5829−5836.

[24] Li X.-G., Hou Z.-Z., Huang M.-R., Moloney M. G., *J. Phys. Chem. C,* **2009**, 113, 21586−21595.
[25] Tran H. D., Shin K., Hong W. G., D'Arcy J. M., Kojima R. W., Weiller B. H., Kaner R. B., *Macromol. Rapid Commun.*, **2007**, 28, 2289− 2293.
[26] Park S., Gordon C. T., and Swager T. M., *PNAS*, **2024**, 121 (12).
[27] Romer D. R., *J. Heterocyclic Chem.*, **2009**, 46, 317-319.
[28] Hopkins J. et al., *Chemistry of Materials,* **2022**, 34, 140-151
[29] Daugaard A. E. et al., *Macromolecules*, **2008**, 41, 4321-4327
[30] Karlsson C. et al., *ACS Appl. Energy Mater.*, **2018**, 1, 11, 6451–6462
[31] Mecerreyes D. et al., *Macromolecules*, **2000**, 33, 5846-5849
[32] Boutry C. M., Gerber-Hörler I., Hierold C., *Polymer Engineering & Science*, **2012,** 53, 1196-1208
[33] Ansari R., *Journal of Chemistry*, **2006**, 3, 186-201
[34] https://www.agilent.com/cs/library/applications

Chapter 6

Epilogue

1. Conclusion

This work presents the synthesis, characterization, and functionalization of advanced materials with a focus on self-diagnostic, self-healing, and sensing applications. Through the integration of diverse chemical and structural innovations, significant advancements have been achieved towards the development of sustainable and multifunctional materials with applications in diverse fields, including polymer science, liquid crystal elastomers, and environmental sensing. Below, the key outcomes and their implications are summarized, followed by an outlook for future research directions.

1.1 Development of Self-Diagnostic Covalent Adaptable Networks

A novel three-component self-diagnostic system has been developed, based on core-shell nanoparticles incorporating CVL as a thermochromic dye and graphene oxide as a carbon nanostructure. Embedded in an epoxy resin matrix, this system exhibits robust self-reporting capabilities under mechanical stresses such as scratching and impact. Control experiments confirmed that the observed fluorescence emission occurs exclusively in the presence of mechanical damage, validating the system's effectiveness.

While attempts to quench CVL+ fluorescence using NIR radiation were unsuccessful, thermal treatment effectively reverted the dye to its closed, non-fluorescent state. This reversibility was further enhanced by modifying the core-shell nanoparticles with pyrene-functionalized copolymers, facilitating supramolecular interactions with graphene oxide. SEM images confirmed the successful integration of carbon nanostructures onto the nanocapsules surface, although further optimization is required to achieve significant enhancement of fluorophore activation. Future research will focus on optimizing the spatial arrangement of nanoparticles and graphene oxide to improve quenching efficiency, aiming to expand the material's potential applications in damage monitoring and repair.

Furthermore, mechanophores such as Rhodamine **3**, when appropriately functionalized, have proven to be effective crosslinking agents. This approach enables the fabrication of reprocessable thermosetting materials with inherent self-diagnostic capabilities, preserving their desirable properties after reprocessing. This comprehensive process, encompassing the application of mechanical stress, the detection of induced damage, the subsequent reprocessing of the material accompanied by mechanophore quenching, and the final reactivation of the system upon renewed stress application, is visually depicted in Figure 5 of Chapter 3 (also shown below).

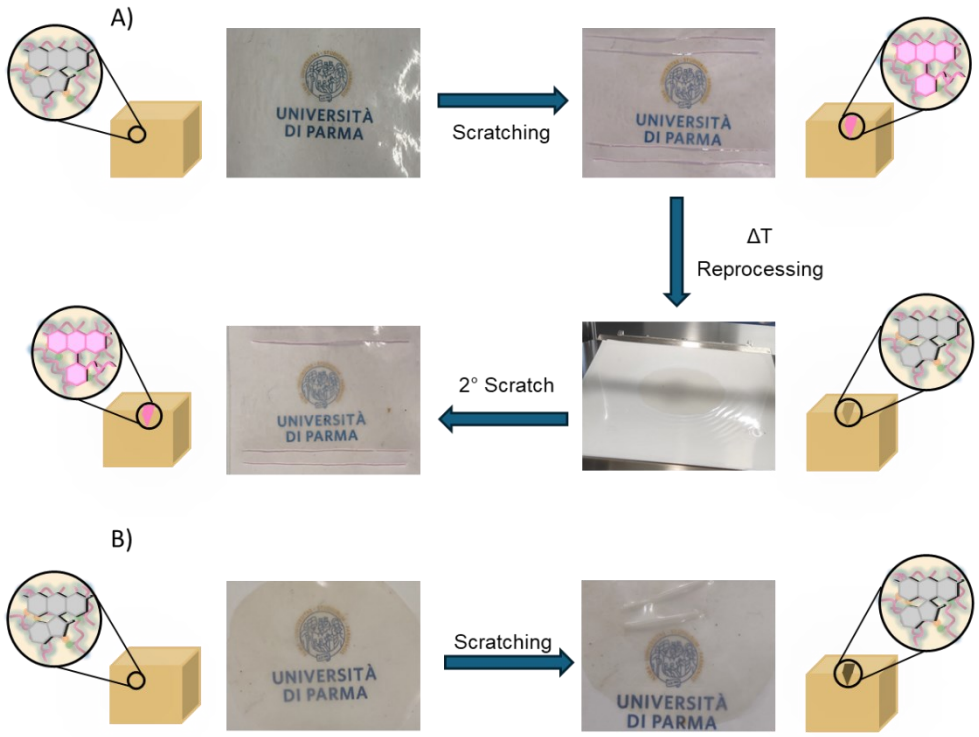

Figure 1. A) XLPE**Rh-CAN** scratching and quenching test, B) control experiment on XLPE**TMSPEDA-Rhdisp**.

1.2 Advancements in Reprocessable Liquid Crystal Elastomers

The pursuit of photoactivated liquid crystal elastomers (LCEs) has significantly advanced our understanding of material design principles. While side-chain-based materials demonstrated limitations in achieving desired properties due to constraints in molecular weight and mobility, main-chain-based materials exhibited superior performance. Specifically, a polyurethane matrix exhibited excellent fiber-forming ability during electrospinning, demonstrating promising photoactuation under UV irradiation. However, the absence of liquid crystalline order within the matrix rendered the photoactuation irreversible.

To address these challenges, a novel liquid crystalline monomer featuring a rigid core of three aromatic rings was synthesized and subsequently copolymerized. The resulting polymers exhibited a well-balanced degree of crystallinity and a broad liquid crystalline mesophase range, with polymer **20** demonstrating the most promising characteristics. Future research efforts will focus on evaluating its electrospinning capabilities and exploring the

potential for reversible photoactuation, with the aim of developing responsive materials for advanced applications.

1.3 Sensing Materials for PFAS Detection

This research focused on synthesizing functionalized quinoxaline cavitands for integration into conductive polymers to enhance PFAS detection capabilities. While attempts to functionalize the lower rim of the cavitands proved unsuccessful, modifications at the upper rim resulted in the successful synthesis of cavitands **14** and **17**. Cavitand **17** was successfully copolymerized with N-methyl pyrrole, yielding a novel conductive polymer. Despite encountering initial challenges with reaction reproducibility and suboptimal sensing performance, the successful incorporation of cavitand **17** into the polymer matrix was confirmed through solid-state NMR analysis.

Preliminary studies suggested that the incorporation of cavitands into the polymer matrix could enhance PFAS adsorption by leveraging their inherent lipophilicity and cavity structures. However, the absorption performance of the synthesized co-polymer did not yet surpass that of pure poly-N-MePy. Future research efforts will focus on refining the co-polymerization process, evaluating adsorption performance in real water samples, and exploring strategies to mitigate the detrimental effects of competing ions in complex environmental matrices.

2. Outlook

This thesis highlights the transformative potential of advanced materials in addressing critical challenges related to sustainability, functionality, and environmental sensing. The development of self-diagnostic materials presented herein offers a promising pathway for real-time damage detection and repair, aligning with the principles of a circular economy. Furthermore, advancements in LCEs and PFAS-sensing polymers demonstrate the versatility of functional materials in addressing a wide range of societal needs.

Future research efforts will focus on expanding upon these findings by optimizing material properties, exploring novel chemistries, and developing scalable manufacturing processes for practical applications. Through the continued integration of dynamic chemistries, supramolecular interactions, and innovative fabrication techniques, these materials have the potential to achieve unprecedented levels of performance, enabling safer, more sustainable, and highly functional systems across various industrial and environmental applications.